School of Science
Department of Physics and Astronomy

Optimising Geopolymer Formation

Ross Peter Williams

This thesis is presented for the Degree of
Doctor of Philosophy
of
Curtin University

December 2015

Declaration

To the best of my knowledge and belief this thesis contains no material previously published by any other person except where due acknowledgment has been made.

This thesis contains no material which has been accepted for the award of any other degree or diploma in any university.

Signature: Original Signed

Date: 23/11/2015

EXECUTIVE SUMMARY

Geopolymers are versatile materials, often made with ash from coal Power Stations. Applications include low green-house-gas emissions cement, fireproof barriers and many more. This thesis furthered the understanding of geopolymer formulation, or mixture design, by:

- Demonstrating novel methods for mixture design and determining the degree of reaction during and after curing.
- Analysing the role of formulation on cost and green-house-gas emissions.
- Developing a new material that can be used for structural neutron shielding.

ABSTRACT

Geopolymers are a class of versatile materials that have the potential for utilisation as a cement replacement, fireproof barriers, materials for high temperatures and biological implant applications. Prior to this study the typical method for formulating geopolymers was to use the bulk composition as measured by x-ray fluorescence spectroscopy of the solid feedstocks. The method fails when using flyash from coal fired power stations as the solid feedstock, as there is significant crystalline component which is essentially inert during chemical activation.

In Chapter 4, it is shown that considering only the amorphous composition of the flyash when formulating geopolymers provides more consistent geopolymer properties over the range of flyash and metakaolin starting materials, compared to using the bulk compositions.

Quantitative x-ray scattering studies (Chapter 6) showed that for metakaolin based geopolymers the initial amorphous material and subsequent amorphous geopolymer matrix could be independently measured. This allows the degree of dissolution of the solid starting materials to be determined providing a significant insight into why the physical properties are so sensitive to changes in composition. It is proposed that the degree of dissolution affects the physical properties predominately by changing the resulting composition of the geopolymer matrix, rather than changing the quantity of geopolymer matrix. It is clear that the commonly measured ‘shift’ in the amorphous hump position is insensitive and nonlinear with the degree of reaction of the geopolymer.

In Chapter 5, life cycle analysis was applied to determine if factors other than compressive strength should influence choices of geopolymer formulation; for instance cost and green-house-gas emissions. It was found the requirements to reduce costs and green-house-gas emissions both promote the decrease of Si/Al and Na/Al ratio. Changes in the Na/Al ratio has strongest effect on the final cost and green-house-gas emission rate, as the major cost and emission sources are the sodium hydroxide and sodium silicate solutions.

In Chapter 7, time resolved quantitative x-ray scattering studies were applied to flyash geopolymers, allowing determination of the degree of flyash amorphous phase dissolution as a function of time. The time resolved Wide Angle X-ray Scattering (WAXS) was conducted at the Australian Synchrotron. The data was analysed with a hybrid PONCKS and Rietveld method, allowing the determination of the dissolution and formation of phases during the reaction. The results were found to be correlated with the compressive strength of the samples.

During the thesis research a novel material was identified (Chapter 8), formulated and tested using an extension of methodology used for alkali aluminosilicate geopolymers, producing a sodium borosilicate inorganic polymer. This new inorganic polymer shows promise for use as neutron shielding material with impressive structural properties. The pastes made with this new material ($Na_{1.10}BSi_{1.70}O_{8.88}.4.65(H_2O)$) were found to have a compressive strength of up to 56(7) MPa.

The outcomes from this thesis have provided a significant increase to the understanding of formulating geopolymer from flyash, metakaolin, and borax.

ACKNOWLEDGEMENTS

The continuous support and mentorship of my primary supervisor Prof. Arie van Riessen has made significant improvements to my candidature and professional skills – leaving me in a great position for the future. I cannot thank you enough Arie.

Thank you to Dr William Rickard for assistance with reviewing the final manuscript. I would also like thank (in alphabetical order) my mentors for their advice and assistance during my candidature: Dr Geoff Carter, Dr Robert Hart, Mr Glen Lawson, Emeritus Professor Brian O'Connor, Professor Li Deyu and Dr Jadambaa Temuujin.

I am thankful for the collaboration, discussions, support and friendship of my fellow CSRP Geopolymer program candidates, particularly Dr Nigel Chen-Tan and Dr William Rickard.

I have learnt much and thank dearly all my collaborators who contributed to 9 peer reviewed publications associated with my candidature, particularly (in alphabetical order): Prof. Glen Corder, Dr Robert Hart, Dr Janine Lay, Assoc. Prof. Benjamin McLellan, Dr William Rickard, Dr Jadambaa Temuujin and Prof. Arie van Riessen.

I would like to acknowledge and thank Craig Heidrich (ADAA) and Hans Fairhurst (Cockburn Cement Ltd) for assistance in procuring flyash samples.

I would like to thank my manager, Ian Hollingworth, at Rio Tinto for supporting my work on this thesis since 2013.

I would like to thank my parents, Karl and Alicia for their support during the extended duration my candidature.

The enduring love and support of my wife, Genevieve, has made this journey much easier and enjoyable.

LIST OF PUBLICATIONS DIRECTLY FROM THIS THESIS

WILLIAMS, R. P. & VAN RIESSEN, A. 2010. Determination of the reactive component of fly ashes for geopolymer production using XRF and XRD. *Fuel,* 89**,** 3683-3692. http://dx.doi.org/10.1016/j.fuel.2010.07.031.

WILLIAMS, R. P., HART, R. D. & VAN RIESSEN, A. 2011. Quantification of the Extent of Reaction of Metakaolin-Based Geopolymers Using X-Ray Diffraction, Scanning Electron Microscopy, and Energy-Dispersive Spectroscopy. *Journal of the American Ceramic Society,* 94**,** 2663-2670. http://dx.doi.org/10.1111/j.1551-2916.2011.04410.x.

WILLIAMS, R. P. & VAN RIESSEN, A. 2011. Development of alkali activated borosilicate inorganic polymers (AABSIP). *Journal of the European Ceramic Society,* 31**,** 1513-1516. http://dx.doi.org/10.1016/j.jeurceramsoc.2011.02.021.

WILLIAMS, R. P. & VAN RIESSEN, A. (submitted). The first 20 hours of Geopolymerisation: an in situ WAXS study of flyash based geopolymers. Journal of Cement and Concrete Research.

LIST OF PUBLICATIONS RELATED TO THIS THESIS, CONTRIBUTED TO DURING CANDIDATURE.

VAN RIESSEN, A., JAMIESON, E., KEALLEY, C. S., HART, R. D. & **WILLIAMS, R. P.** 2013. Bayer-geopolymers: An exploration of synergy between the alumina and geopolymer industries. *Cement and Concrete Composites,* 41**,** 29-33. http://dx.doi.org/10.1016/j.cemconcomp.2013.04.010.

MCLELLAN, B. C., **WILLIAMS, R. P.,** LAY, J., VAN RIESSEN, A. & CORDER, G. D. 2011. Costs and carbon emissions for geopolymer pastes in comparison to ordinary portland cement. *Journal of Cleaner Production,* 19**,** 1080-1090. http://dx.doi.org/10.1016/j.jclepro.2011.02.010.

RICKARD, W. D. A., **WILLIAMS, R.,** TEMUUJIN, J. & VAN RIESSEN, A. 2011. Assessing the suitability of three Australian fly ashes as an aluminosilicate source for geopolymers in high temperature applications. *Materials Science and Engineering: A,* 528**,** 3390-3397. http://dx.doi.org/10.1016/j.msea.2011.01.005.

TEMUUJIN, J., VAN RIESSEN, A. & **WILLIAMS, R.** 2009. Influence of calcium compounds on the mechanical properties of fly ash geopolymer pastes. *Journal of Hazardous Materials,* 167**,** 82-88. http://dx.doi.org/10.1016/j.jhazmat.2008.12.121.

TEMUUJIN, J., **WILLIAMS, R. P.** & VAN RIESSEN, A. 2009. Effect of mechanical activation of fly ash on the properties of geopolymer cured at ambient temperature. *Journal of Materials Processing Technology,* 209**,** 5276-5280. http://dx.doi.org/10.1016/j.jmatprotec.2009.03.016.

LIST OF ABBREVIATIONS/ACRONYMS

Abbreviation	Term
AABSIP	Alkali Activated Borosilicate Inorganic Polymer.
AAC	Alkali Activated Cement
CI	Confidence Interval
$CO_{2\text{-Equiv}}$	CO_2 equivalent
EDS	Energy Dispersive Spectroscopy
EDXRD	Energy Dispersive X-ray Diffraction
FTIR	Fourier Transform Infrared (Spectroscopy)
GBFS	Granulated Blast Furnace Slag
GHG	Green-House-Gas
ICDD	International Centre for Diffraction Data
ICSD	Inorganic Crystal Structure Database
LOI	Loss on Ignition
NMR	Nuclear Magnetic Resonance
OPC	Ordinary Portland Cement
PDF	Pair Distribution Function
PONKCS	Partial Or No Known Crystal Structure
QPA	Quantitative Phase Analysis
RIR	Reference Intensity Ratio
SAS	Sodium Aluminate Solution
SAXS	Small Angle X-ray Scattering
SCM	Supplementary Cementitious Material
SEM	Scanning Electron Microscopy
SSS	Sodium Silicate Solution
TEM	Transmission Electron Microscopy
WAXS	Wide Angle X-ray Scattering
XRD	X-ray diffraction
XRF	X-ray Fluorescence (Spectroscopy)

STATEMENT OF CONTRIBUTION FROM OTHERS

To Whom It May Concern

I, Ross Peter Williams, contributed to below mentioned 4 publications by:

- Leading conception and design of the project
- Leading analysis and interpretation of research data
- Drafting majority parts of the work

[1] **WILLIAMS, R. P.** & VAN RIESSEN, A. 2010. Determination of the reactive component of fly ashes for geopolymer production using XRF and XRD. *Fuel,* 89**,** 3683-3692. http://dx.doi.org/10.1016/j.fuel.2010.07.031.

[2] **WILLIAMS, R. P.,** HART, R. D. & VAN RIESSEN, A. 2011. Quantification of the Extent of Reaction of Metakaolin-Based Geopolymers Using X-Ray Diffraction, Scanning Electron Microscopy, and Energy-Dispersive Spectroscopy. *Journal of the American Ceramic Society,* 94**,** 2663-2670. http://dx.doi.org/10.1111/j.1551-2916.2011.04410.x.

[3] **WILLIAMS, R. P.** & VAN RIESSEN, A. 2011. Development of alkali activated borosilicate inorganic polymers (AABSIP). *Journal of the European Ceramic Society,* 31**,** 1513-1516. http://dx.doi.org/10.1016/j.jeurceramsoc.2011.02.021.

[4] **WILLIAMS, R. P.** & VAN RIESSEN, A. (submitted). The first 20 hours of Geopolymerisation: an in situ WAXS study of flyash based geopolymers. Journal of Cement and Concrete Research.

Original Signed

Ross Peter Williams

I, as a Co-Author of publications [1] to [4], endorse that this level of contribution by the candidate indicated above is appropriate.

Original Signed

Prof. Arie van Riessen

I, as a Co-Author of publication [2], endorse that this level of contribution by the candidate indicated above is appropriate.

Original Signed

Dr Robert Hart

TABLE OF CHAPTERS

1	Introduction	25
2	Literature Review	32
3	Materials and Characterisation Methods	67
4	Determination of the reactive component of flyashes for geopolymer production using XRF and XRD	95
5	Geopolymer formulation: effects on strength, cost and carbon emissions	123
6	Quantification of the extent of reaction of metakaolin based geopolymers using XRD, SEM and EDS.	151
7	The first 20 hours of geopolymerisation: an in situ WAXS study of flyash based geopolymers	178
8	Development of alkali activated borosilicate inorganic polymers (AABSIP)	208
9	Concluding remarks	220
	References	226
	Appendix 1 – MYHIST CMR tech note	235
	Appendix 2 – Copyright clearances	241

TABLE OF CONTENTS

Chapter 1: Introduction 25

1.1. CO_2 production and Portland cements 26
1.2. Introduction to geopolymers 29
1.2.1. History of geopolymers 29
1.3. Objectives of thesis 31

Chapter 2: Literature Review 32

2.1. Chemistry of geopolymers 33
2.1.1. Dissolution of aluminosilicates 37
2.1.2. Role of alkali soluble silica 39
2.1.3. Role of alkali soluble alumina 42
2.1.4. Role of alkali 42
2.1.5. Alkali earths 44
2.1.6. Alkali activated cement (AAC) 44
2.1.7. Boron 46
2.1.8. Iron 47
2.1.9. Role of insoluble phases 47
2.2. Structure of geopolymers 49
2.3. Properties of geopolymers 51
2.3.1. Mechanical strength 51
2.3.2. Room temperature setting 51
2.3.3. Chemical resistance 52
2.3.4. Durability (longevity) 53
2.3.5. Fireproof and Thermal properties 54
2.3.6. Controllable porosity and strong capillary force 54
2.3.7. Low free aluminium 56
2.3.8. Low CO_2-eq emissions 56
2.4. Sodium hydroxide availability 61
2.5. Applications of geopolymer 62
2.6. Portland cement chemistry 63
2.6.1. Clinker and cement production 63
2.6.2. Cement hydration 65

Chapter 3: Materials and Characterisation Methods 67

3.1. Raw materials selection 68
3.1.1. Flyashes 68
3.1.2. Metakaolin (dehydroxylated kaolinite) 69
3.1.3. Silica fume (amorphous silica) 70
3.1.4. Sodium hydroxide, silicate and aluminate solutions 70
3.1.5. Borax 70
3.2. Methods and mixing 71
3.3. Geopolymer formulations 72
3.4. X-ray powder diffraction 75
3.4.1. X-ray diffraction / scattering 75
3.4.2. X-ray diffraction 75
3.4.3. Modelling methods 77
3.4.4. Curtin x-ray laboratory – D8 Advance 79
3.4.5. Australian Synchrotron – powder diffraction beamline. 83
3.4.6. Data processing – PD beamline 85
3.4.7. Australian Synchrotron – SAXS/WAXS beamline 86
3.4.8. Data processing – WAXS data 87
3.4.9. Data conversion from ASCII xy to RAW for search/match 88

3.4.10. Diffraction modelling 88
3.5. Scanning electron microscopy 89
3.5.1. Contrast mechanisms 89
3.5.2. Energy Dispersive x-ray Spectroscopy (EDS) 89
3.5.3. Simulation methods 91
3.5.4. Scanning electron microscopy analysis 91
3.5.5. Imaging 92
3.6. X-ray fluorescence 93
3.7. Compressive strength testing 94

Chapter 4: Determination of the reactive component of flyashes for geopolymer production using XRF and XRD 95

4.1. Abstract 96
4.2. Introduction 97
4.3. Materials and methods 99
4.3.1. Determination of bulk composition 99
4.3.2. Determination of the crystalline composition 100
4.3.3. Determination of amorphous composition 106
4.3.4. Testing of formulation methodologies 106
4.3.5. Fracture surface morphology 108
4.4. Results 109
4.4.1. Bulk composition 109
4.4.2. Crystalline phase composition - Quantitative phase analysis 109
4.4.3. Amorphous composition 111
4.4.4. Morphology of geopolymer fracture surfaces 112
4.4.5. Compressive strength of geopolymers 114
4.5. Discussion 115
4.5.1. Geopolymer mixture formulation 115
4.5.2. Dissolution rates and solubility 115
4.5.3. Quartz composition 116
4.5.4. Mullite composition 117
4.5.5. Cubic iron oxides phases 118
4.5.6. Rietveld refinement background modelling 119
4.5.7. Uncertainties in amorphous composition determination 120
4.6. Chapter conclusions 122

Chapter 5: Geopolymer formulation: effects on strength, cost and carbon emissions 123

5.1. Abstract 124
5.2. Introduction 125
5.2.1. Geopolymers 125
5.2.2. Life cycle analysis 126
5.2.3. CO_2 equivalence 126
5.2.4. Emissions trading schemes – a price on Carbon 127
5.3. Materials and methods 128
5.3.1. Geopolymer formulation and synthesis 128
5.3.2. Compressive strength of geopolymer pastes 129
5.3.3. Life cycle analysis of pastes 129
5.4. Results 132
5.4.1. Compressive properties 132
5.4.2. Energy utilisation 134
5.4.3. Green-House-Gas emissions 136
5.4.4. Cost without a carbon tax 138
5.4.5. Carbon taxes 139
5.4.6. Carbon tax effect on total cost of geopolymers. 142

5.5. Discussion ... *145*
5.5.1. Physical strength stability ... 145
5.5.2. Reducing the cost and carbon ... 146
5.5.3. Cost of carbon in the future ... 148
5.6. Chapter conclusions ... *150*

Chapter 6: Quantification of the extent of reaction of metakaolin based geopolymers using XRD, SEM and EDS. ... 151

6.1. Abstract ... *152*
6.2. Introduction ... *153*
6.3. Materials and methods ... *156*
6.3.1. Sample preparation ... 156
6.3.2. Compressive strength testing ... 156
6.3.3. XRD data collection ... 157
6.3.4. XRD analysis ... 157
6.3.5. Area ratio method analysis ... 157
6.3.6. PONKCS method analysis ... 159
6.3.7. Determination of water content ... 160
6.3.8. Energy dispersive spectroscopy ... 160
6.3.9. Point counting analysis ... 160
6.3.10. Calculation of fraction of metakaolin reacted ... 161
6.4. Results and Discussion ... *162*
6.4.1. XRD data analysis ... 162
6.4.2. Area ratio method analysis (x-ray diffraction) ... 164
6.4.3. PONKCS method analysis (x-ray diffraction) ... 168
6.4.4. Point counting analysis (scanning electron microscopy) ... 168
6.4.5. Calculation of fraction of metakaolin reacted ... 170
6.4.6. Energy dispersive spectroscopy (scanning electron microscopy) ... 172
6.4.7. Sampling volume ... 174
6.4.8. Total matrix content ... 175
6.5. Chapter conclusions ... *177*

Chapter 7: The first 20 hours of geopolymerisation: an in situ WAXS study of flyash based geopolymers 178

7.1. Abstract ... *179*
7.2. Introduction ... *180*
7.2.1. Geopolymer kinetics ... 180
7.3. Materials and methods ... *182*
7.3.1. Geopolymer synthesis ... 182
7.3.2. WAXS data Collection ... 183
7.3.3. WAXS data Processing ... 183
7.3.4. WAXS phase Identification ... 185
7.3.5. WAXS data Analysis ... 185
7.3.6. SAXS data Collection ... 187
7.3.7. SAXS data processing ... 187
7.4. Results and Discussion ... *189*
7.4.1. WAXS results ... 189
7.4.2. SAXS results ... 204
7.5. Chapter conclusions ... *207*

Chapter 8: Development of alkali activated borosilicate inorganic polymers (AABSIP) ... 208

8.1. Abstract ... *209*
8.2. Introduction ... *210*

8.3. Materials and methods 213
8.4. Results and discussion 215
8.5. Chapter conclusions 219

Chapter 9: Concluding remarks 220

9.1. Conclusions 221
9.2. Significance of the thesis 224
9.3. Future work 225

Chapter 10: References 226

Appendix 1 – MYHIST CMR tech note 235

Appendix 2 – Copyright clearances 241

LIST OF FIGURES

FIGURE 1-1 WORLD CEMENT PRODUCTION IN BILLIONS OF TONNES PER ANNUM, AND THE PRODUCTION SHARE OF CHINA IN THE SAME PERIOD. DATA (USGS, 2005, USGS, 2007, USGS, 2009, USGS, 2011, USGS, 2013B, USGS, 2015A)..... 26

FIGURE 1-2 WORLD CEMENT PRODUCTION SINCE 1945, THE GROWTH HAS BEEN APPROXIMATELY EXPONENTIAL. DATA FROM (USGS, 2013A)..... 27

FIGURE 1-3 THE REDUCTION IN GHG EMISSIONS FOR BOTH GREY CEMENT CLINKER AND ALL CEMENTITIOUS MATERIALS IN THE LAST 25 YEARS. DATA FROM (WBCSD, 2012)..... 28

FIGURE 1-4 THE REDUCTION IN GHG EMISSIONS FOR BOTH GREY CEMENT CLINKER AND ALL CEMENTITIOUS MATERIALS RELATIVE TO 1990 VALUES; I.E. EACH SERIES HAS BEEN NORMALISED TO 1990 VALUES. DATA FROM (WBCSD, 2012)..... 28

FIGURE 1-5 THE NUMBER OF 'GEOPOLYMER' PAPERS PER PUBLICATION YEAR, AS INDEXED BY SCIVERSE SCOPUS, INDICATIVE THAT THERE WAS A LONG INDUCTION TIME BEFORE GEOPOLYMER RESEARCH INCREASED EXPONENTIALLY. 30

FIGURE 2-1 THE REACTION SEQUENCE OF GEOPOLYMERISATION, DIVIDED INTO DISSOLUTION, REORIENTATION AND SOLIDIFICATION SECTIONS. AFTER (PROVIS AND VAN DEVENTER, 2007A). 33

FIGURE 2-2 THE MODELLED REACTION PROCESS FOR A PARTICULAR FLYASH GEOPOLYMER; UNDERSTANDING THE KINETICS OF THE DIFFERENT SPECIES IS IMPORTANT IN OPTIMISING THE GEOPOLYMERISATION PROCESS (SEE TEXT AND FIGURE 2-1 FOR DETAILS). THE LOWER PLOT IS THE SAME DATA AS SHOWN ON THE UPPER PLOT, BUT WITH A SHORTER TIME SCALE TO ALLOW DETAIL TO BE OBSERVED. T-SITES ARE THE TETRAHEDRAL SITES. AFTER (PROVIS AND VAN DEVENTER, 2007A)..... 35

FIGURE 2-3 A DESCRIPTIVE MODEL OF THE ALKALI ACTIVATION OF FLYASH. AFTER FERNÁNDEZ-JIMÉNEZ ET AL. (2005)..... 37

FIGURE 2-4 COMPRESSIVE STRENGTH OF A FLYASH GEOPOLYMER AS A FUNCTION OF ACTIVATING SOLUTION SIO2/NA2O AND NA2O/FLYASH WT (RFA) RATIO AND % RESPECTIVELY. AFTER SKVÁRA ET AL. (2009). 40

FIGURE 2-5 VARIATION IN COMPRESSIVE STRENGTH OF METAKAOLIN GEOPOLYMER WITH CHANGE IN BULK NA/AL AND BULK SI/AL. BLACK DOTS REPRESENT DATA POINTS AND CONTOUR LINES HAVE BEEN EXTRAPOLATED FROM THESE POINTS. AFTER ROWLES AND O'CONNOR (2003). 41

FIGURE 2-6 COMPRESSIVE STRENGTH OF GROUND BLAST FURNACE SLAG (GBFS) MORTARS WITH VARIOUS ACTIVATORS. DATA FROM PURDON (1940)..... 45

FIGURE 2-7 THE STRUCTURE OF GEOPOLYMER AS PROPOSED BY BARBOSA ET AL. (2000) 50

FIGURE 2-8 GEOPOLYMER STRUCTURE PROPOSED BY ROWLES ET AL. (2007), A) PROPOSED LOCATION OF CHARGE-BALANCING NA+ CATION WHICH ARE ASSUMED TO BE FROM SODIUM ALUMINATE SPECIES; B) PROPOSED LOCATION OF THE CHARGE-BALANCING NA+ CATION ASSUMING THE FORM OF A MODIFIED BRIDGING NETWORK; C) SCHEMATIC, BASED ON THE MODEL BY BARBOSA ET AL. (2000) (FIGURE 2-7), WITH MODIFICATION ATTEMPTING TO INCORPORATE THE CHARGE-BALANCING NA+ IN THE FORM OF SODIUM ALUMINATE SPECIES AND MODIFIED BRIDGING NETWORKS INTO THE STRUCTURE. 50

FIGURE 2-9 VARIATION IN COMPRESSIVE STRENGTH WITH GEOPOLYMER MATRIX CHEMISTRY, AS MEASURED BY ENERGY DISPERSIVE SPECTROSCOPY ON A SCANNING ELECTRON MICROSCOPE. BLACK DOTS REPRESENT ACTUAL DATA POINTS. THIS IS THE SAME COMPRESSIVE STRENGTH DATA AS IN FIGURE 2-5, BUT WITH THE MEASURED MATRIX COMPOSITION OPPOSED TO THE BULK COMPOSITION. THE PINK REGION HIGHLIGHTS THE 4 STRONG SAMPLES WITH STRENGTHS BETWEEN 45 TO 65 MPA. AFTER ROWLES AND O'CONNOR (2003, 2009). 52

FIGURE 2-10 THE SCHEMATIC SHOWS HOW INTRODUCING POROSITY REDUCES THE MAXIMUM WATER DIFFUSION DISTANCE COMPARING A) A SOLID SAMPLE, B) A FOAMED SAMPLE. AFTER BELL AND KRIVEN (2009). 55

FIGURE 2-11 THE TYPICAL RATE OF HYDRATION OF ALITE AS MEASURED BY ISOTHERMAL CALORIMETRY. REGION A) INITIAL REACTION; B) PERIOD OF SLOW REACTION; C) ACCELERATION PERIOD; AND D) DECELERATION PERIOD. AFTER BULLARD ET AL. (2011).... 66

FIGURE 3-1 SCHEMATIC REPRESENTATION OF THE BRAGG-BRENTANO DIFFRACTION GEOMETRY. THE DIVERGENT X-RAY BEAM FROM X-RAY TUBE, COLLIMATED BY DIVERGENCE SLITS, IMPINGE ON THE SAMPLE AT AN ANGLE Θ, SOME OF THE X-RAYS DIFFRACT AT AN ANGLE Θ FROM THE SAMPLE. THESE DIFFRACTED X-RAYS ARE 'SEEN' BY POINT ON THE GONIOMETER RADIUS AT AN ANGLE 2Θ RELATIVE TO THE INCIDENT BEAM. 76

FIGURE 3-2 THE DIFFRACTION PROFILE FROM ONE BRAGG REFLECTION (I.E. 1 D-SPACING), THE DISTRIBUTION OF WAVELENGTHS RESULTS IN SEVERAL MEASURED PEAKS. N.B. THE SAME DATA IS DISPLAYED TWICE ON DIFFERENT SCALES-LINEAR SCALE = GREEN AND LOG SCALE = BLUE. 80

FIGURE 3-3 MEASURED DIFFRACTION PATTERNS FROM A 50% HEMATITE (Fe_2O_3) + 50% MAGNETITE (Fe_3O_4) SAMPLE USING THE DEFAULT DETECTOR DISCRIMINATOR SETTINGS AND THE TIGHTER SETTINGS. THE PATTERNS ARE NOT OFFSET, SHOWING THAT THE BACKGROUND MEASURED WITH THE DEFAULT SETTINGS IS MUCH HIGHER, RESULTING IN POOR SIGNAL-TO-NOISE RELATIVE TO THE PATTERN MEASURED WITH TIGHTER DISCRIMINATOR SETTINGS. 82

FIGURE 3-4 THE DIFFRACTION PATTERN OF A BENTONITE ($Na_{0.2}Ca_{0.1}Al_2Si_4O_{10}(OH)_2(H_2O)_{10}$) SAMPLE MEASURED WITH AND WITHOUT THE KNIFE-EDGE COLLIMATOR INSTALLED. ADDITIONALLY THE SAMPLE WAS MEASURED WITH THE KNIFE-EDGE POORLY INSTALLED TO QUALITATIVELY ASSESS THE SENSITIVITY OF THE ALIGNMENT. NOTE THE SIGNIFICANT REDUCTION IN MEASURED AIR-SCATTER (NOISE) AT 2Θ BELOW APPROXIMATELY 7° 2Θ, WHICH IMPROVES THE SIGNAL TO NOISE RATIO FOR THE BRAGG PEAK AT 5.7° 2Θ. 83

FIGURE 3-5 PHOTOGRAPH THE KNIFE EDGE COLLIMATOR INSTALLED ON THE D8 ADVANCE AT CURTIN UNIVERSITY. 83

FIGURE 3-6 A SCHEMATIC OF THE MYTHEN DETECTOR SYSTEM SHOWING THE 16 MYTHEN DETECTOR MODULES IN A LINEAR ARRAY COLLECTING APPROXIMATELY 80° 2Θ WITH 0.2° 2Θ GAPS BETWEEN MODULES. 84

FIGURE 3-7 POWDER DIFFRACTION DATA OF A SMALL REGION SHOWING THE GAP IN THE SECOND PATTERN (SILICON_P2). THE SAMPLE IS NIST SRM 640, THERE IS NO BRAGG PEAK NEAR THIS ANGLE. NOTE THE INCREASE IN THE SIGNAL CLOSE TO THE EDGES OF GAP IN THE DATA. 85

FIGURE 3-8 EXPERIMENTAL GEOMETRY FOR THE IN SITU GEOPOLYMERISATION EXPERIMENT. NOMINALLY 6 GEOPOLYMER SAMPLES IN 1.5 MM PEEK TUBES WERE HELD IN THE 35 CAPILLARY HEATING STAGE. 87

FIGURE 4-1 MASS ATTENUATION COEFFICIENT OF TYPICAL PHASES (FLYASH), COMPARED WITH POSSIBLE INTERNAL STANDARDS (STD). MINIMISING THE DIFFERENCE BETWEEN THE INTERNAL STANDARDS WILL REDUCE THE BIAS DUE TO MICRO-ABSORPTION, HENCE FLUORITE OR RUTILE WOULD BE SUITABLE, BUT RUTILE WAS EXCLUDED AS IT COULD BE PRESENT IN THE SAMPLES. THE DATA WERE CALCULATED USING TOPAS 4.2 (BRUKER-AXS, GERMANY) 102

FIGURE 4-2 SIMULATED CALIBRATION OF THE RATIO OF I210 AND I120 AND X PARAMETER FOR THE SYNCHROTRON X-RAY DIFFRACTION DATA USED IN THIS STUDY (WITH POLARISED X-RAYS WITH A WAVELENGTH OF Λ= 0.100 NM)..... 103

FIGURE 4-3 COMPARING TWO METHODS FOR ESTIMATING THE COMPOSITION OF MULLITE; IF BOTH METHODS WERE CONSISTENT THERE WOULD BE 1 TO 1 RELATIONSHIP. 105

FIGURE 4-4 REPRESENTATIVE FRACTURE SURFACE MORPHOLOGY FOR GEOPOLYMERS SAMPLES FORMULATED USING THE BULK COMPOSITION OF FLYASH: A) COLLIE FLYASH; B) BAYSWATER FLYASH; AND C) PORT AUGUSTA FLYASH. THE GEOPOLYMER SAMPLES FORMULATED USING THE AMORPHOUS COMPOSITION OF FLYASH: D) COLLIE FLYASH; E) BAYSWATER FLYASH; AND F) PORT AUGUSTA FLYASH. 113

FIGURE 4-5 SEM MICROGRAPH OF SiO_2 PARTICLES (LABELLED Q) LIKELY TO BE PRIMARY QUARTZ FROM THE >45 AND <75 μM SIZE FRACTION OF COLLIE FLYASH. 117

FIGURE 5-1 COMPRESSIVE STRENGTH AS A FUNCTION OF ELEMENTAL COMPOSITION. THE SHADED REGION REPRESENTS THE OPTIMAL COMPOSITION FOR A ROBUST FORMULATION WITH GOOD MECHANICAL STRENGTH. 133

FIGURE 5-2 YOUNG'S MODULUS AS A FUNCTION OF ELEMENTAL COMPOSITION. THE SHADED REGION REPRESENTS THE OPTIMAL COMPOSITION FOR A ROBUST FORMULATION WITH GOOD MECHANICAL STRENGTH. 133

FIGURE 5-3 THE ELECTRICAL ENERGY CONSUMED IN THE PRODUCTION OF THE FEEDSTOCKS FOR GEOPOLYMER SYNTHESIS. THE GREEN ARROW HIGHLIGHTS THE DIRECTION OF DECREASING ENERGY CONSUMPTION. 134

FIGURE 5-4 THE FUEL ENERGY CONSUMED IN THE PRODUCTION OF THE FEEDSTOCK'S FOR GEOPOLYMER SYNTHESIS. THE GREEN ARROW HIGHLIGHTS THE DIRECTION OF DECREASING ENERGY CONSUMPTION. 135

FIGURE 5-5 THE ENERGY CONSUMED IN THE TRANSPORTATION OF THE FEEDSTOCK'S FOR GEOPOLYMER SYNTHESIS. THE GREEN ARROW HIGHLIGHTS THE DIRECTION OF DECREASING ENERGY CONSUMPTION. 135

FIGURE 5-6 THE TOTAL ENERGY CONSUMED IN THE PRODUCTION AND TRANSPORTATION OF FEEDSTOCKS OF ONE TONNE OF GEOPOLYMER PASTE. THE GREEN ARROW HIGHLIGHTS THE DIRECTION OF DECREASING ENERGY CONSUMPTION. 136

FIGURE 5-7 THE GHG EMISSIONS FROM THE PRODUCTION OF THE FEEDSTOCKS FOR GEOPOLYMER SYNTHESIS. THE GREEN ARROW HIGHLIGHTS THE DIRECTION OF DECREASING GHG EMISSIONS..... 137

FIGURE 5-8 THE GHG EMISSIONS FROM THE TRANSPORTATION OF THE FEEDSTOCKS FOR GEOPOLYMER SYNTHESIS. THE GREEN ARROW HIGHLIGHTS THE DIRECTION OF DECREASING GHG EMISSIONS..... 137

FIGURE 5-9 THE TOTAL GHG EMISSIONS FROM THE PRODUCTION AND TRANSPORT OF THE FEEDSTOCKS FOR GEOPOLYMER SYNTHESIS. THE GREEN ARROW HIGHLIGHTS THE DIRECTION OF DECREASING GHG EMISSIONS..... 138

FIGURE 5-10 THE CALCULATED COST OF GEOPOLYMER PRODUCTION. THE GREEN LINE HIGHLIGHTS THE DIRECTION OF DECREASING COST. 139

FIGURE 5-11 THE CARBON TAX PER TONNE OF GEOPOLYMER PASTE ASSUMING A PRICE ON CARBON OF $10 PER TONNE OF CO_2-EQIV. THE GREEN ARROW HIGHLIGHTS THE DIRECTION OF DECREASING TAX. 140

FIGURE 5-12 THE CARBON TAX PER TONNE OF GEOPOLYMER PASTE ASSUMING A PRICE ON CARBON OF $20 PER TONNE OF CO_2-EQIV. THE GREEN ARROW HIGHLIGHTS THE DIRECTION OF DECREASING TAX. 140

FIGURE 5-13 THE CARBON TAX PER TONNE OF GEOPOLYMER PASTE ASSUMING A PRICE ON CARBON OF $30 PER TONNE OF CO_2-EQIV. THE GREEN ARROW HIGHLIGHTS THE DIRECTION OF DECREASING TAX. 141

FIGURE 5-14 THE CARBON TAX PER TONNE OF GEOPOLYMER PASTE ASSUMING A PRICE ON CARBON OF $40 PER TONNE OF CO2-EQIV. THE GREEN ARROW HIGHLIGHTS THE DIRECTION OF DECREASING TAX. 141

FIGURE 5-15 THE CALCULATED COST OF GEOPOLYMER PRODUCTION WITH AU$10 PER TONNE CO_2-EQUIV. THE GREEN LINE HIGHLIGHTS THE DIRECTION OF DECREASING COST. 142

FIGURE 5-16 THE CALCULATED COST OF GEOPOLYMER PRODUCTION WITH AU$20 PER TONNE CO_2-EQUIV. THE GREEN LINE HIGHLIGHTS THE DIRECTION OF DECREASING COST. 143

FIGURE 5-17 THE CALCULATED COST OF GEOPOLYMER PRODUCTION WITH AU$30 PER TONNE CO2-EQUIV. THE GREEN LINE HIGHLIGHTS THE DIRECTION OF DECREASING COST. 143

FIGURE 5-18 THE CALCULATED COST OF GEOPOLYMER PRODUCTION WITH AU$40 PER TONNE CO2-EQUIV. THE GREEN LINE HIGHLIGHTS THE DIRECTION OF DECREASING COST. 144

FIGURE 5-19 THE TOTAL OF COST OF GEOPOLYMER PRODUCTION PER TONNE OF PASTE WITH AN EXCESSIVELY HIGH CARBON TAX OF $500 PER TONNE OF CO_2-EQ. NOTE THAT THE DIRECTION

of decreasing cost has rotated 45° anti-clockwise compared to Figure 5-18; this indicates that with a ridiculously high carbon tax the key parameter to optimise for lower cost is the Na/Al ratio, the Si/Al ratio now has almost no effect on the cost. 149

Figure 5-20 The effect of increasing price on carbon on the optimal geopolymer composition. The following prices of carbon were used: A = no carbon tax; B = \$20 t^{-1}; C = \$40 t^{-1} and D = \$500 t^{-1}; Assuming the shaded area is a constraint based on suitable physical specifications and then finding the lowest cost after applying the carbon tax. 149

Figure 6-1 XRD patterns of metakaolin and the four geopolymer samples. Patterns have been offset for clarity. 163

Figure 6-2 Selected XRD patterns of geopolymer sample 1 and the series of metakaolin spiked geopolymers (sample 1). 163

Figure 6-3 Peak shift of a single peak for all four series of geopolymer samples. Note the saturation of the peak shift when a <20 wt% metakaolin is added. 164

Figure 6-4 Typical area ratio method (ARM) XRD refinement – sample 1 (S1) with 20% metakaolin, modelled Bragg peaks for quartz and anatase and modelled diffuse peaks for metakaolin spiked geopolymer samples. 165

Figure 6-5 Calculated mass fraction of metakaolin (YMK) vs. mass fraction of metakaolin spike (SMK). The y-intercept indicates the concentration of metakaolin remaining in the geopolymer (CMK/GP). 167

Figure 6-6 Typical microstructure of geopolymer samples 1 to 4. The unreacted metakaolin is encapsulated by the glassy geopolymer matrix. 169

Figure 6-7 Degree of dissolution of the metakaolin compared to OH^- concentration (Mole/L) of the activating solution. 171

Figure 6-8 Degree of dissolution of the metakaolin compared to Si/Na ratio of the activating solution. 172

Figure 6-9 A cross section view of the sample 1, this surface has been exposed by milling with a focused ion beam (FIB). The image illustrates the difficulty with quantitative EDS of geopolymer, although there may appear to be no unreacted particles from the surface there are very few regions of 2x2 µM below the surface without metakaolin, hence EDS measurement of only matrix (GP) or only metakaolin (MK) will be unlikely. 174

Figure 6-10 the compressive strength compared to matrix mass fraction. The matrix mass fraction is the sum of solution plus dissolved solids. 176

Figure 7-1 Cropped view of the 2D WAXS diffraction pattern from a geopolymer sample. The circled annotations on the left image show the pixel overflow in the columns where a large quartz (Q) crystal saturated the detector, overflowing into adjacent pixels. This effect was reduced by applying the masking process to remove saturated pixels. The square annotations show the quartz peaks where it is clear there is a distribution of quartz d-spacings. Note the hematite (H 011) and mullite (M 120 and M 210) peaks are smooth continuous rings, indicating the crystallite size is small compared to the diffraction information volume, hence there are thousands to millions of crystallites. 184

Figure 7-2 Time resolved diffraction pattern of CFA-1.8-0.8-5.5. Features include the evolution of low angle intensity ($Q < 1$ Å^{-1}), formation of two zeolite phases and the 'shift' in the amorphous peak position. The peak positions of significant identified phases are shown at the top of the figure for [1] Quartz (SiO_2), [2] Mullite ($Al_{4.64}5Si_{1.36}O_{9.68}$), [3] Hematite ($Fe_2O_3$), [4] Magnetite ($Fe_3O_4$), [5] unspecified zeolite 1, [6] unspecified zeolite 2 and [7] small angle scattering. 190

Figure 7-3 Time resolved diffraction pattern of CFA-2.0-0.8-5.5. Features include the evolution of low angle intensity ($Q < 1$ Å^{-1}) and the 'shift' in the amorphous peak position. The peak positions of significant identified phases are shown at the top

of the figure for [1] Quartz (SiO_2), [2] Mullite ($Al_{4.64}5Si_{1.36}O_{9.68}$), [3] Hematite ($Fe_2O_3$), [4] Magnetite ($Fe_3O_4$) and [5] small angle scattering..... 191

Figure 7-4 Time resolved diffraction pattern of CFA-2.0-1.2-5.5. Features include the evolution of low angle intensity ($Q < 1$ Å^{-1}), formation of a zeolite phase and the 'shift' in the amorphous peak position. The peak positions of significant identified phases are shown at the top of the figure for [1] Quartz (SiO_2), [2] Mullite ($Al_{4.64}5Si_{1.36}O_{9.68}$), [3] Hematite ($Fe_2O_3$), [4] Magnetite ($Fe_3O_4$), [5] unspecified zeolite 3 and [6] small angle scattering. 191

Figure 7-5 Time resolved diffraction pattern of CFA-2.0-0.8-5.5. Features include the evolution of low angle intensity ($Q < 1$ Å^{-1}), formation of a zeolite phase and the 'shift' in the amorphous peak position. The peak positions of significant identified phases are shown at the top of the figure for [1] Quartz (SiO_2), [2] Mullite ($Al_{4.64}5Si_{1.36}O_{9.68}$), [3] Hematite ($Fe_2O_3$), [4] Magnetite ($Fe_3O_4$), [5] unspecified zeolite 4 and [6] small angle scattering. 192

Figure 7-6 SAXS patterns confirm that the increased intensity at low angle (<3° 2Θ) seen in the WAXS data is from small angle scattering phenomenon rather than a broad Bragg peak of a large zeolite. The useful limit of the WAXS data was $Q = 0.18$ Å^{-1}. Although there are Bragg peaks in the SAXS data, they are not source of the majority of the intensity. Note: cross section is a calibrated representation of intensity. 193

Figure 7-7 [A] The relative peak area and crystallite size for a zeolite peak at $Q = 1.97$ Å^{-1}for sample CFA-1.8-0.8-5.5. The plateau of the crystallite size as the relative peak intensity reach ~90% indicates there is nucleation period like the formation of typical zeolites, but with no crystal growth subsequently. Note: It is a fitting artifact that crystallite size randomly fluctuates when relative peak area is <5%, as there is insufficient intensity to fit the peak, hence the peaks are omitted for clarity. [B] Is zoomed in on 0.45 to 3 hr region. The error bars represent 1 estimated standard error from the refinement process..... 194

Figure 7-8 Relative peak area and crystallite sizes of a zeolite peak at $Q = 1.82$ Å^{-1} for sample CFA-1.8-0.8-5.5. The peak is of low intensity compared to the background, hence the noisy signal. The error bars represent 1 estimated standard error from the refinement process. 195

Figure 7-9 Quantitative phase results from the refinement[A] CFA-1.8-0.8-5.5 [B] CFA-2.0-1.2-5.5 [C] CFA-2.0-0.8-5.5 [D] CFA-2.2-0.8-5.5. The concentration of the flyash (FA) amorphous phase is shown on the right hand side axis. 197

Figure 7-10 Elemental ratios of the reaction products as function of time [A] CFA-1.8-0.8-5.5 [B] CFA-2.0-1.2-5.5 [C] CFA-2.0-0.8-5.5 [D] CFA-2.2-0.8-5.5. Note: that the elemental ratio levels out 4-5 hours into the reaction..... 199

Figure 7-11 The relative standard deviation of calculated atomic H/Si in solution during geopolymer phase growth (between 10% and 90% of relative GP concentration). Note: The formation of geopolymer and zeolite phases was not accounted for and the inverse correlation between compressive strength and the variability of the solution. 200

Figure 7-12 Refined output from WAXS data for samples: [A] CFA-1.8-0.8-5.5; [B] CFA-2.0-1.2-5.5 [C] CFA-2.0-0.8-5.5 [D] CFA-2.2-0.8-5.5; the time evolution of the diffuse scattering peaks of flyash (FA) and geopolymer (GP) compared with the Power Law pre factor. Note for plot [A], that the induction period for zeolite 1 and geopolymer are approximately equal. 202

Figure 7-13 Integrating the area between the geopolymer formation and Power Law pre-factor, between approximately 15 minutes and the first intercept, results in a parameter that correlates with compressive strength. 203

Figure 7-14 Relationship between the area between geopolymer formation and Power Law pre-factor (WAXS data), as measured by two metrics. This limited data set (n=4) does have a strong positive linear relationship for both methods of

DETERMINING THE AREA, INDICATING GOOD CORRELATION BETWEEN THE INTEGRATED AREA AND THE COMPRESSIVE STRENGTH. AS DESCRIBED IN THE TEXT, THE AREA SHOULD BE CORRELATED TO THE QUANTITY OF FLYASH DISSOLVED BEFORE SIGNIFICANT GEOPOLYMERISATION OCCURS, THIS SUPPORTS THE FINDINGS OF ZHANG ET AL. (2012, 2013) THAT THE STRENGTH IS MAXIMISED BY PROLONGING THE DISSOLUTION STAGE COMPARED TO THE START OF THE GEOPOLYMERISATION. 204

FIGURE 7-15 THE SAXS PATTERNS OF THE SAMPLES AND THE ORIGINAL FLYASH. 205

FIGURE 7-16 [A] POWER LAW EXPONENT FROM THE SAXS DATA COMPARED WITH THE COMPRESSIVE STRENGTH OF THE SAMPLES. [B] POWER LAW PRE-FACTOR – A, COMPARED TO THE COMPRESSIVE STRENGTH OF THE SAMPLES. THE SAXS DATA WAS FITTED BETWEEN Q = 0.02 AND 0.10 $Å^{-1}$. THERE IS NO SIGNIFICANT CORRELATION BETWEEN THE EXPONENT OR THE PRE-FACTOR WITH THE COMPRESSIVE STRENGTH. 206

FIGURE 8-1 X-RAY DIFFRACTION PATTERNS OF THE SILICA FUME AND THE ANHYDROUS BORAX FEEDSTOCKS THAT WERE USED TO PRODUCE THE AABSIP SAMPLES MIX 1 AND MIX 2. THE CRYSTALLINE PEAKS IN THE SILICA FUME ARE ZIRCONIA (Z) AND QUARTZ (Q). THE CRYSTALLINE PHASE FORMED IN THE AABSIP SAMPLES WAS BORAX DECAHYDRATE (B). PATTERNS OFFSET FOR VISIBILITY. 216

FIGURE 8-2 MICROSTRUCTURE OF MIX 1, A POROUS GLASSY MATRIX, WITH A CRYSTALLISED BORAX CRYSTAL (B). 217

LIST OF TABLES

TABLE 2-1 THE ENERGY USE AND GREEN-HOUSE-GAS EMISSION RATES FOR VARIOUS MODES OF TRANSPORT. (ABS, 2006, DITRDLG, 2008, APPELBAUM CONSULTING GROUP, 2007)..... 58

TABLE 2-2 THE ENERGY USE AND GREEN-HOUSE-GAS EMISSION RATE FOR TRANSPORT OF FLYASH FROM BAYSWATER POWER STATION (NSW, AUSTRALIA) TO PORT MELBOURNE (VIC, AUSTRALIA). SOURCES: DISTANCES (SEARATES LP, 2015, GOOGLE, 2015)..... 59

TABLE 2-3 STAGES ASSESSED IN THE LIFE-CYCLE ANALYSIS FOR GEOPOLYMERS..... 59

TABLE 2-4 THE RANGE OF APPLICATIONS INVESTIGATED FOR GEOPOLYMER TECHNOLOGY. 62

TABLE 2-5 SUMMARY OF MAJOR PHASES IN PORTLAND CEMENT AND PORTLAND CEMENT PASTE. AFTER (KURDOWSKI, 2014, TAYLOR, 1997)..... 64

TABLE 2-6 TYPICAL BULK CHEMICAL COMPOSITION OF PORTLAND CEMENT CLINKER AND CEMENT PASTE (TAYLOR, 1997) COMPARED TO A TYPICAL METAKAOLIN GEOPOLYMER,. WEIGHT FRACTIONS ARE ON THE IGNITED MASS BASIS. CEMENT PASTE WAS 14 MONTH OLD, GEOPOLYMER PASTE WAS 30 DAYS OLD. THE "-" INDICATES DATA WAS NOT AVAILABLE. 65

TABLE 3-1 CHEMICAL REQUIREMENTS FOR THE VARIOUS CLASSES OF FLYASH AS PER ASTM-C618-15 (ASTM INTERNATIONAL, 2015). 69

TABLE 3-2 COMPOSITION OF SOME POSSIBLE GEOPOLYMER FEEDSTOCKS, THE '+' OR '-' INDICATES THE FEEDSTOCK CONTAINS A MAJOR OR MINOR COMPONENT OF THAT ELEMENT, RESPECTIVELY..... 72

TABLE 3-3 COMMONLY USED METHODS TO DETERMINE THE PHASE COMPOSITION FROM X-RAY DIFFRACTION DATA. ONE OR MORE OF THESE METHODS ARE OFTEN USED SIMULTANEOUSLY. 77

TABLE 3-4 THE FUNDAMENTAL PARAMETERS DESCRIBING THE DEFAULT SETTINGS OF THE D8 ADVANCE AT CURTIN..... 79

TABLE 3-5 THE RATIO OF CU K_A AND KB WAS REFINED USING NIST SRM 1976 RESULTING IN THE FOLLOWING INSTRUMENT EMISSION PROFILE (WAVELENGTH SPECTRUM)..... 81

TABLE 3-6 THE UTILISED OBJECTS MODELLED USING TOPAS V4.2. ANY NUMBER OF THESE OBJECTS CAN BE USED TO MODEL THE DIFFRACTION DATA. 88

TABLE 3-7 SUMMARY OF THE SCANNING ELECTRON MICROSCOPES USED IN THIS STUDY. ET = EVERHART-THORNLEY DETECTOR (SECONDARY ELECTRONS); 4QBSD = 4 QUADRANT BACKSCATTERED ELECTRON DETECTOR ; INLENS = IN LENS SECONDARY ELECTRON DETECTOR; ESB = ENERGY SELECTIVE BACKSCATTERED; AND SDD = SILICON DRIFT DETECTOR. 91

TABLE 3-8 THE 99% INFORMATION DEPTH UNIT OF µM, CALCULATED WITH CASINO V2.42 FOR A TYPICAL GEOPOLYMER MATRIX ($Na_{1.25}Al_{0.9}Si_{2.05}H_{9.6}O_{10.8}$). INFORMATION DEPTH IS THE DEPTH THAT 99% OF ELEMENTAL INFORMATION CAN ORIGINATES, IT ACCOUNTS FOR ELECTRON AND X-RAY SCATTERING. 90

TABLE 4-1 THE WT% OF EACH FEEDSTOCK ADDED, WHERE THE 'AMOR' AND 'BULK' REPRESENTS MIXTURES THAT WERE FORMULATED USING THE AMORPHOUS AND BULK ALUMINA AND SILICA CONTENTS, RESPECTIVELY. THE WATER AND SODIUM HYDROXIDE WAS MIXED WITH THE SODIUM SILICATE OR ALUMINATE SOLUTION PRIOR TO MIXING WITH FLYASH. DETAILS OF SILICATE AND ALUMINATE SOLUTIONS ARE IN THE TEXT..... 107

TABLE 4-2 THE BULK COMPOSITION (WT%) OF THE STUDIED FLYASHES, MEASURED BY XRF AND LOSS OF IGNITION (LOI 1000°C). UNCERTAINTIES ARE ESTIMATED BY THE VARIATION OF KNOWN STANDARDS. 109

TABLE 4-3 COMPARISON OF QUANTITATIVE PHASE ANALYSIS RESULTS FOR NIST SRM 1633B FLYASH WITH PUBLISHED RESULTS. THE UNCERTAINTIES FOR THIS STUDY AND WINBURN *ET AL.* ARE 2 TIMES THE STANDARD DEVIATION OF 3 REPLICATES AND 6 REPLICATES, RESPECTIVELY. THE CORUNDUM ARISES FROM THE MICRONISING MILLING MEDIA. THE WARD AND FRENCH *A* AND WARD AND FRENCH *B* UTILISED CORUNDUM AND ZINCITE INTERNAL

STANDARDS, RESPECTIVELY. THE AMORPHOUS CONTENT WAS DETERMINED VIA THE INTERNAL STANDARD METHOD, AS DESCRIBED IN THE TEXT. THE SUM OF MAGNETITE AND MAGHEMITE WAS UNDERTAKEN PRIOR TO ROUNDING AND CONSERVING THE FE CONTENT. 110

TABLE 4-4 STATISTICS FROM THE RIETVELD QUANTITATIVE PHASE ANALYSIS, ALL VALUES ARE AVERAGES OF THREE DATASETS. THE R_{BRAGG} IS THE AVERAGE ACROSS MANY PHASES. MAJOR PHASES INCLUDE ONLY QUARTZ AND MULLITE. 111

TABLE 4-5 CRYSTALLINE PHASE COMPOSITION, DETERMINED BY RIETVELD QUANTITATIVE PHASE ANALYSIS, EXPRESSED AS ABSOLUTE WT%. THE UNCERTAINTIES QUOTED ARE THE STANDARD DEVIATION OF REPLICATE SAMPLES MULTIPLIED BY 2 (95% CI). THE AMORPHOUS CONTENT WAS DETERMINED VIA THE INTERNAL STANDARD METHOD, AS DESCRIBED IN THE TEXT. THE VALUE OF X FOR THE MULLITE PHASES #66447, #66448 AND #66449 ARE 0.320, 0.375 AND 0.295, RESPECTIVELY. 111

TABLE 4-6 THE AMORPHOUS COMPOSITION OF FLYASHES AS DETERMINED BY DIFFERENCE BETWEEN BULK ELEMENTAL COMPOSITION (TABLE 4-2) AND CRYSTALLINE COMPOSITION (TABLE 4-5). THE TOTAL AMORPHOUS COMPOSITION DOES NOT EQUAL THE AMORPHOUS COMPOSITION IN TABLE 4-5 BECAUSE ELEMENTS HAVE BEEN EXPRESSED AS EQUIVALENT OXIDES (I.E. ALL FE IS EXPRESSED AS Fe_2O_3). THE UNCERTAINTIES ARE PROPAGATED THOUGH THE CALCULATIONS FROM TABLE 4-2 AND TABLE 4-5. 112

TABLE 4-7 THE AVERAGE COMPRESSIVE STRENGTH (MPA) OF THE GEOPOLYMERS PASTES. N=11, UNCERTAINTIES COVER 95% CI. THE REFERENCE METAKAOLIN BASED GEOPOLYMER WAS 32(6) MPA 114

TABLE 4-8 THE AVERAGE YOUNG'S MODULUS (GPA) OF THE FLYASH GEOPOLYMER PASTES. N=11, UNCERTAINTIES COVER 95% CI. THE YOUNG'S MODULUS OF THE REFERENCE METAKAOLIN SAMPLE WAS 1.73(8) GPA. 114

TABLE 4-9 CALCULATED SI/AL ELEMENTAL RATIO OF THE THREE FRACTIONS OF THE FLYASH: BULK, CRYSTALLINE AND AMORPHOUS. UNCERTAINTIES ARE ESTIMATED ON A 95% CI BASED ON REPEATABILITY. 115

TABLE 4-10 COMPARISON OF THE INTENSITIES OF BRAGG REFLECTIONS OF MAGNETITE AND MAGHEMITE C WITH THE SAME LATTICE PARAMETER FOR A WAVELENGTH OF 0.154 NM, CALCULATED USING TOPAS 4.2 119

TABLE 4-11 TRANSMISSION COEFFICIENT THOUGH AMORPHOUS FLYASH SPHERES AT 0.100 NM AND 0.154 NM (CU KA), CALCULATED ASSUMING AN AMORPHOUS DENSITY OF 2.5 G/CM3. THE LINEAR ATTENUATION COEFFICIENT (LAC) IS ALSO SHOWN FOR CONVENIENCE. 121

TABLE 5-1 THE TARGET COMPOSITION OF THE 9 SAMPLES AND THE WEIGHT PERCENTAGE OF EACH FEEDSTOCK. WHERE CFA IS COLLIE FLYASH; SODIUM SILICATE IS SODIUM SILICATE SOLUTION (GRADE D, PQ AUSTRALIA); SODIUM HYDROXIDE PELLETS (AR GRADE); AND WATER IS DEIONISED WATER. 128

TABLE 5-2 THE PRICES PER TONNE OF CO_2-EQUIVALENT (CO_2-EQ) GREEN-HOUSE-GAS USED IN THE CALCULATION. THE CARBON POLLUTION REDUCTION SCHEME (CPRS) VALUES ARE FROM COMMONWEALTH OF AUSTRALIA (2011) AND THE 'REASONABLE' LOW AND HIGH VALUES ARE FROM THE REPORT BY GARNAUT (2011). PRICES ARE IN AUSTRALIAN DOLLARS (AUD). 130

TABLE 5-3 TRANSPORT AND EMISSIONS DATA AND REFERENCES FOR GEOPOLYMER FEEDSTOCK AND OPC. 131

TABLE 5-4 COMPRESSIVE STRENGTH AND YOUNG'S MODULUS FOR DIFFERENT ELEMENTAL RATIOS OF SAMPLES FROM THIS STUDY. 132

TABLE 5-5 A SUMMARY OF STUDIES WHICH HAVE FOUND THE OPTIMAL GEOPOLYMER COMPOSITION, THE SI/AL AND NA/AL RATIO IN THIS TABLE ARE THE MEAN ± RANGE OF SI/AL AND NA/AL RATIO FROM THE LITERATURE FOR THE MIXTURES WITH 20% OF THE MAXIMUM COMPRESSIVE STRENGTH. 146

TABLE 5-6 THE GHG EMISSION RATES AND MONETARY COSTS FOR THE MAJOR GEOPOLYMER FEEDSTOCKS, AS DESCRIBED IN MCLELLAN ET AL. (2011) 147

TABLE 6-1. THE BULK GEOPOLYMER SAMPLE COMPOSITION (ELEMENTAL RATIO), COMPRESSIVE STRENGTH, STRAIN AT MAXIMUM STRESS, YOUNG'S MODULUS AND THE DEHYDRATION BETWEEN SYNTHESIS AND MEASUREMENT. 162

TABLE 6-2. LINEAR REGRESSION DATA OF MEASURED METAKAOLIN CONCENTRATION (Y_{MK}) IN THE SPIKED SAMPLE VS. CONCENTRATION OF METAKAOLIN SPIKE (S_{MK}). THE Y_{MK} INTERCEPT IS EQUAL TO THE CONCENTRATION OF METAKAOLIN REMAINING IN THE GEOPOLYMER SAMPLE. 166

TABLE 6-3. REFINED GEOPOLYMER AND METAKAOLIN PEAK POSITIONS, DEHYDRATION CORRECTED INPUT METAKAOLIN CONCENTRATION (I.E. QUANTITY OF METAKAOLIN ADDED TO SAMPLE), CALCULATED CONCENTRATION OF UNREACTED METAKAOLIN IN THE GEOPOLYMER AND ($C_{MP/GP}$) AND THE FRACTION OF ORIGINAL METAKAOLIN THAT REACTED. 166

TABLE 6-4. THE CALCULATED ELEMENTAL RATIO FOR THE BULK SAMPLE (AS SYNTHESISED) AND THE RESULTING CALCULATED MATRIX COMPOSITION AS DETERMINED BY THE AREA RATIO METHOD (ARM) XRD, PONKCS XRD METHOD AND SEM POINT COUNTING. THE GEOPOLYMER MATRIX COMPOSITION WAS CORRECTED FOR DEHYDRATION (TABLE 1) PRIOR TO MEASUREMENT AND THE FRACTION OF METAKAOLIN THAT REACTED (TABLE 6-3). SENSIBLE EDS DATA COULD NOT BE COLLECTED FOR SAMPLE 3, AS THE REGIONS OF GEOPOLYMER MATRIX WERE MUCH SMALLER THAN THE INFORMATION VOLUME OF THE EDS ANALYSIS. ... 172

TABLE 7-1 COMPOSITION OF GEOPOLYMER SAMPLES, COMPRESSIVE STRENGTH (CS) AND YOUNG'S MODULUS (YM). CALCULATIONS OF THE ELEMENTAL RATIO ONLY CONSIDER THE AMORPHOUS COMPOSITION OF THE FLYASH, I.E. THE CRYSTALLINE COMPONENT WAS CONSIDERED INERT AND THE VALUES INDICATE THE TARGET FINAL COMPOSITION ASSUMING 100% REACTION OF THE AMORPHOUS COMPONENT OF THE FLYASH. 182

TABLE 7-2 THE PARAMETER SCHEME USED IN THE REFINEMENT. NOTE: GP REPRESENTS GEOPOLYMER AND FA FLYASH 187

TABLE 7-3 SETTING TIME AS MEASURED BY THE TIME THAT THE QUARTZ SPOT POSITIONS STOPPED CHANGING. 190

TABLE 7-4 SUMMARY OF THE FLYASH AMORPHOUS PHASE CONCENTRATION; INITIAL CONCENTRATION WAS CALCULATED FROM MIX FORMULATION AND QPA RESULTS OF THE STARTING FLYASH (CHAPTER 4) AND THE FINAL CONCENTRATION WAS DETERMINED BY THE REFINEMENT OF THE WAXS DATA. THE COMPRESSIVE STRENGTH (CS) AND YOUNG'S MODULUS (YM) HAS BEEN SHOWN AGAIN FOR COMPARISON. 196

TABLE 7-5 D-SPACINGS OF THE FLYASH AND GEOPOLYMER AMORPHOUS PHASE PEAKS. THE GEOPOLYMER AMORPHOUS PHASE PEAK POSITIONS ARE SMALLER THAN FOUND FOR THE METAKAOLIN GEOPOLYMER (CHAPTER 6) WHICH WERE BETWEEN 3.15 AND 3.22 Å. THE FLYASH AMORPHOUS PHASE PEAK POSITION WAS ALLOWED VARY BETWEEN SAMPLES IN THE REFINEMENT. 196

TABLE 7-6 THE CALCULATED ATOMIC RATIO IN THE SOLUTION DURING GEOPOLYMER PHASE GROWTH (BETWEEN 10% AND 90% OF RELATIVE GP CONCENTRATION), THE MEAN AND STANDARD DEVIATION WERE WEIGHTED BY TIME. THE FINAL EXTENT RATIOS ARE CALCULATED FROM THE FINAL EXTENT OF THE FLYASH DISSOLUTION, IT IS THE MEAN OF THE LAST 15 PATTERNS. NOTE: THE FORMATION OF GEOPOLYMER AND ZEOLITE PHASES WAS NOT ACCOUNTED FOR AS THE SPECIFIC CHEMISTRY WAS NOT KNOWN. 200

TABLE 7-7 POWER LAW FIT RESULTS FOR THE FLYASH AND GEOPOLYMER SAMPLES. THE SAXS DATA WAS FITTED BETWEEN Q = 0.02 AND 0.10Å-1. *A* IS THE PRE-FACTOR AND *B* IS THE EXPONENT. 205

TABLE 8-1 FORMULATIONS OF THE AABSIP SAMPLES. 213

TABLE 8-2 COMPRESSIVE STRENGTH AND YOUNG'S MODULUS OF AABSIP SAMPLES. UNCERTAINTIES QUOTED ARE THE STANDARD DEVIATION OF 4 REPLICATE SAMPLES. 215

TABLE 8-3 COMPARISON OF THE CALCULATED NEUTRON SHIELDING PROPERTIES OF THE AABSIP AND OTHER SHIELDING MATERIALS. INCREASED MACROSCOPIC CROSS-SECTION RESULTS IN IMPROVED NEUTRON STOPPING POWER. REFERENCES ARE FOR THE COMPOSITION OF THE

MATERIAL. THE CROSS-SECTION DATA IS FROM PUBLISHED DATA (NCRP, 1971, RAUCH AND WASCHKOWSKI, 2003)..... 217

CHAPTER 1: INTRODUCTION

1.1. CO_2 PRODUCTION AND PORTLAND CEMENTS

Cement production is a significant contributor to global Green-House-Gas (GHG) emissions; at around 5-7% of global emissions (IEA, 2008, Allwood et al., 2010, Friedlingstein et al., 2010, UNSTATS, 2010). The global average GHG emission rate is 0.842 tonne of CO_2-eq per tonne of cement clinker or 0.618 tonne of CO_2-eq per tonne of cementitious material (WBCSD, 2012). The global cement production is 4.2 Gt/y (USGS, 2015a) and growing at a steady rate of 0.2 Gt/y for between 2003 and 2014 as shown in Figure 1-1 (USGS, 2005, USGS, 2007, USGS, 2009, USGS, 2011, USGS, 2013b, USGS, 2015a). China has played a dominate role in this growth, increasing its share of global production from 42 to 60% from 2003 to 2014, respectively. The longer term growth in global production has been approximately exponential between 1945 and 2012 (USGS, 2013a), as shown in Figure 1-2.

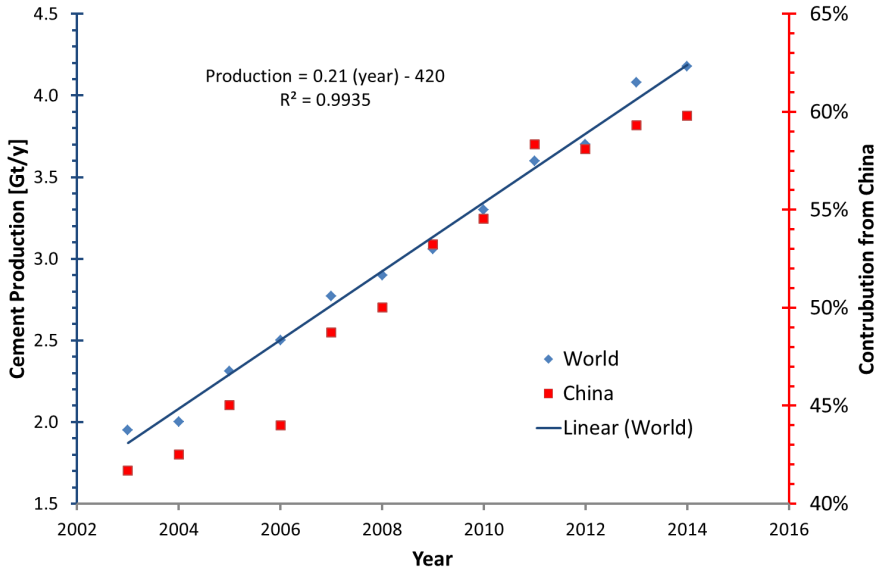

Figure 1-1 World cement production in billions of tonnes per annum, and the production share of China in the same period. Data (USGS, 2005, USGS, 2007, USGS, 2009, USGS, 2011, USGS, 2013b, USGS, 2015a).

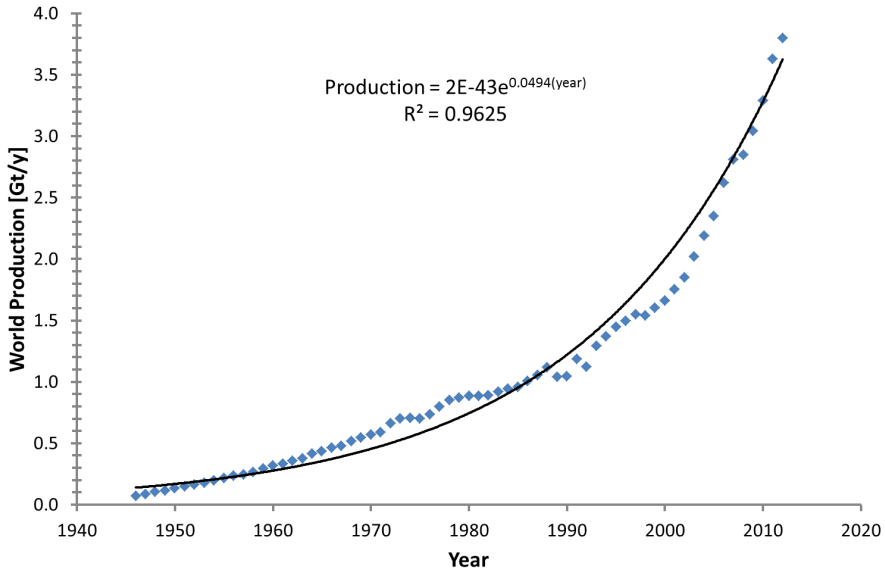

Figure 1-2 World cement production since 1945, the growth has been approximately exponential. Data from (USGS, 2013a).

The cement industry has made efforts to reduce the GHG emission rate by installation of fuel-efficient kilns, partial replacement of kiln feedstocks with non-carbonate calcium oxides sources and by the use of supplementary cementitious materials (SCM) (O'Brien et al., 2009, Petek Gursel et al., 2014, Prusinski et al., 2006, USGS, 2015a). SCMs are pozzolans, such as flyash, slag or limestone that partially replace cement clinker in cement or concrete. The reduction of the GHG emission rate for grey cement clinker and all cementitious materials (i.e. clinker, plus additives and SCMs if applicable) are shown in Figure 1-3 (WBCSD, 2012). The values shown are the global production weighted mean from cement producers contributing to the collected data. These data are not fully representative as it is from approximately 1/3 of total world production and only includes 4% of Chinese production. It also excludes emissions from electrical power used in the cement production. The reduction in the GHG emission rate for both clinker and the cementitious material indicates that the cement industry is both reducing the emission rate for clinker and reducing the fraction of clinker in the cementitious material, using SCMs. The reduction of both clinker and cementitious GHG emissions relative to 1990 levels is shown in Figure 1-4.

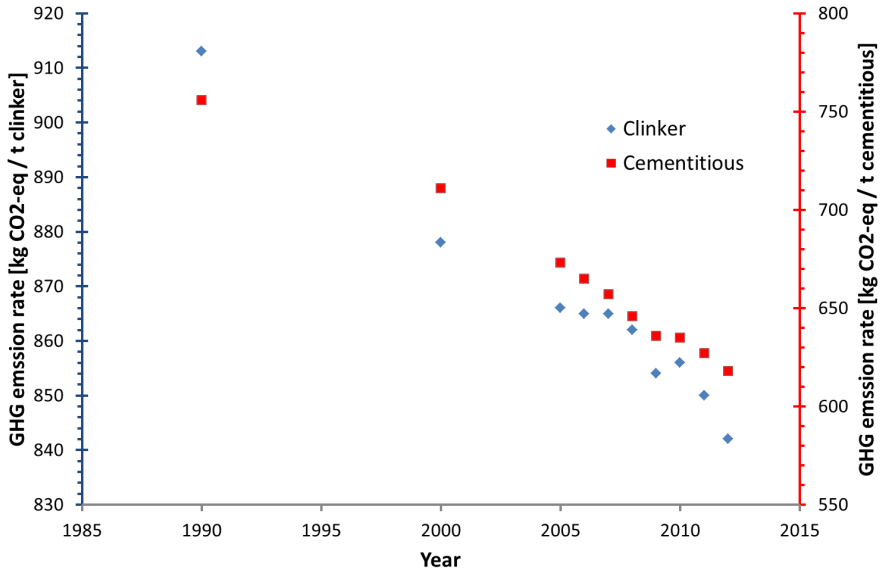

Figure 1-3 The reduction in GHG emissions for both grey cement clinker and all cementitious materials in the last 25 years. Data from (WBCSD, 2012)

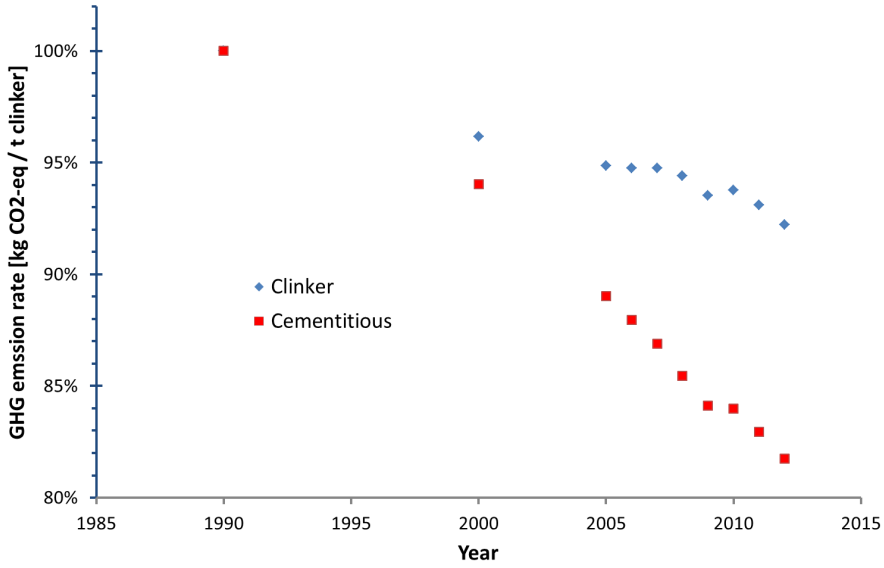

Figure 1-4 The reduction in GHG emissions for both grey cement clinker and all cementitious materials relative to 1990 values; i.e. each series has been normalised to 1990 values. Data from (WBCSD, 2012)

1.2. INTRODUCTION TO GEOPOLYMERS

Geopolymers or aluminosilicate inorganic polymers (AIP) have potential uses as alternate binders with improved physical properties compared with Portland cement. The physical properties include high compressive strength, acid resistance, fire resistance and the ability to be produced from waste streams (Rangan, 2008, Rickard et al., 2010, Hart et al., 2006) to name a few. Geopolymers have also been proposed as encapsulation materials for radioactive wastes (Blackford et al., 2007), and as precursors for refractory materials (Kriven et al., 2004).

1.2.1. History of geopolymers

Davidovits was arguably the first to work with alkali activated aluminosilicates or geopolymers as we know them today, investigating these materials as early as 1979. Unfortunately the majority of his early research and development was in his own words ‘not academic in nature’ (Davidovits, 1991) thus was mostly restricted to patent literature. Fortunately Davidovits published a ‘Geopolymer’ peer review journal publication in (1989), which was the start of series of peer reviewed papers (1991, 1991, 1993, 1994) reporting on the processing, properties, applications and environmental impact of geopolymers. The highly patented environment that Davidovits created probably contributed to the slow rate of uptake of academic research publications, indicated by the number of geopolymer publications indexed by Sciverse Scopus per publication year, Figure 1-5. Note the exponential growth in publication since the year 2001.

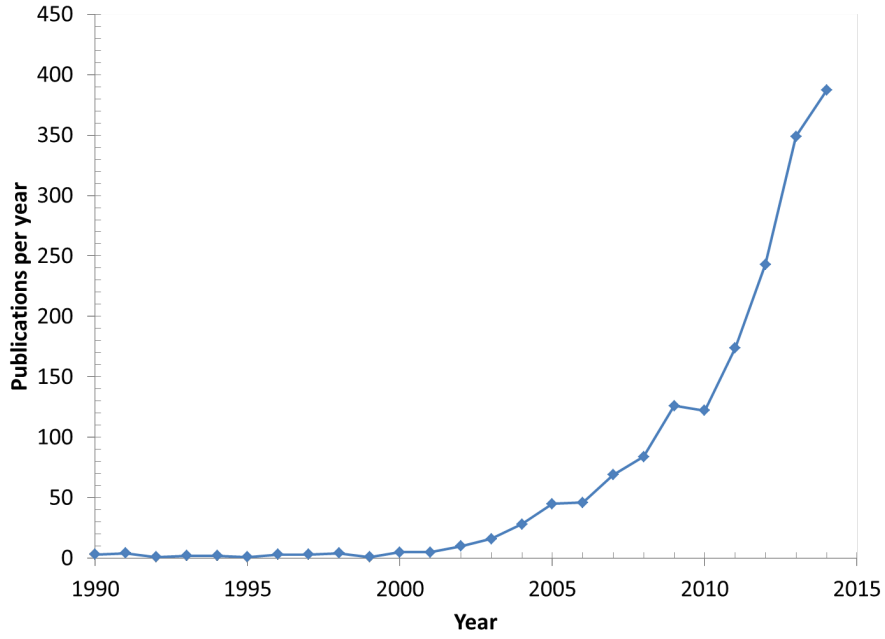

Figure 1-5 The number of 'geopolymer' papers per publication year, as indexed by SciVerse Scopus, indicative that there was a long induction time before geopolymer research increased exponentially.

Alkali activated cement (AAC) research and development started many years earlier in Europe. AAC is the alkali activation of calcium silicates or calcium aluminosilicates (Pacheco-Torgal et al., 2008), such as sodium hydroxide activation of blast furnace slag. The pioneering work was reported by Purdon (1940), who activated 30 different blast furnace slags with sodium hydroxide and/or lime solutions. Purdon found the majority of AACs produced from the slags had superior early compressive and tensile strengths compared to Portland cements. However, Purdon's work has only a few citations suggesting his work has not been widely adopted (53 and 212, in Google scholar, 10th of March 2011 and 15th of November 2015, respectively).

It is reported that in 1959 Viktor Glukhovsky in his book *Gruntosilikaty* (English translation: "Soil Silicates") described the alkali activation of calcium aluminosilicate minerals (Krivenko, 2005, Skvára et al., 2009). Many buildings have been built with these alkali-activated cements in Eastern Europe and are still standing today. Now there are hundreds of geopolymer researchers worldwide, spread across every inhabited continent.

1.3. OBJECTIVES OF THESIS

The objective of this thesis is to understand how to formulate flyash or metakaolin geopolymer mixtures. The specific aims or questions addressed are listed below:

- Develop a measurement protocol based on the composition of precursors to create formulations to target a specific geopolymer matrix composition, i.e. composition of the reaction product.
- Develop a measurement protocol to determine the extent of solid feedstock dissolution, allowing determination of the resultant geopolymer matrix composition.
- Assess the factors that affect the choice of target geopolymer matrix composition.
- Develop a measurement protocol to monitor the dissolution, reorientation and solidification reactions of geopolymers and apply it to understand flyash geopolymer systems.
- Can boron substitute for aluminium in geopolymer?

CHAPTER 2: LITERATURE REVIEW

2.1. CHEMISTRY OF GEOPOLYMERS

The geopolymerisation reaction process is still not completely understood. The process can be simplified as a dissolution-reorientation-solidification reaction, and can be modelled with some degree of accuracy to predict the kinetics (Provis and van Deventer, 2007a). Figure 2-1 shows a schematic representation which has been annotated to highlight the dissolution-reorientation-solidification steps.

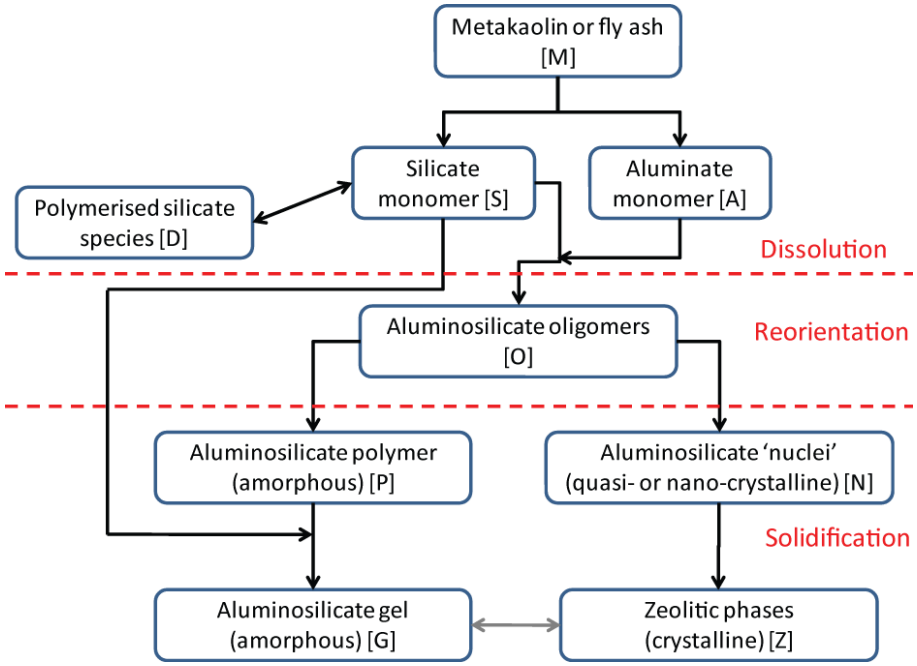

Figure 2-1 The reaction sequence of geopolymerisation, divided into dissolution, reorientation and solidification sections. After (Provis and van Deventer, 2007a).

During the dissolution stage the solid aluminosilicates [M] are dissolved by the [OH^-], the Si and Al forms monomers [S] and [M] in the solution. Before the dissolution stage finishes globally, the reorientation begins with the monomers, [S] and [M], quickly reorientating into larger oligomers [O]. However, this step is contentious, because Barbosa et al. (2000) could not observe Al in solution using liquid state ^{27}Al NMR, concluding there were little dissolution of Al from solid to liquid state. The larger aluminosilicate oligomers form either an aluminosilicate polymer [P] or aluminosilicate 'nuclei' [N]. Once a critical amount of [P] forms the reaction is autocatalytic. The aluminosilicate polymer [P] then slowly converts to aluminosilicate gel [G] and the aluminosilicate 'nuclei' [N] may crystallise to zeolitic phases [Z].

Over an even longer time scale [G] may crystallise to [Z] (Provis and van Deventer, 2007a). The abovementioned reactions can be modelled for both flyash and metakaolin geopolymer systems (Provis and van Deventer, 2007a), the kinetics of a typical flyash geopolymer system are shown in Figure 2-2**.** The reaction rates are modelled based on the pH, silica concentration and quantity of solution and the concentration of reactive silica and alumina in the solid feedstocks. However, there are other parameters that would control the kinetics such as solid particle size and reaction temperature; although the model does not cover these aspects.

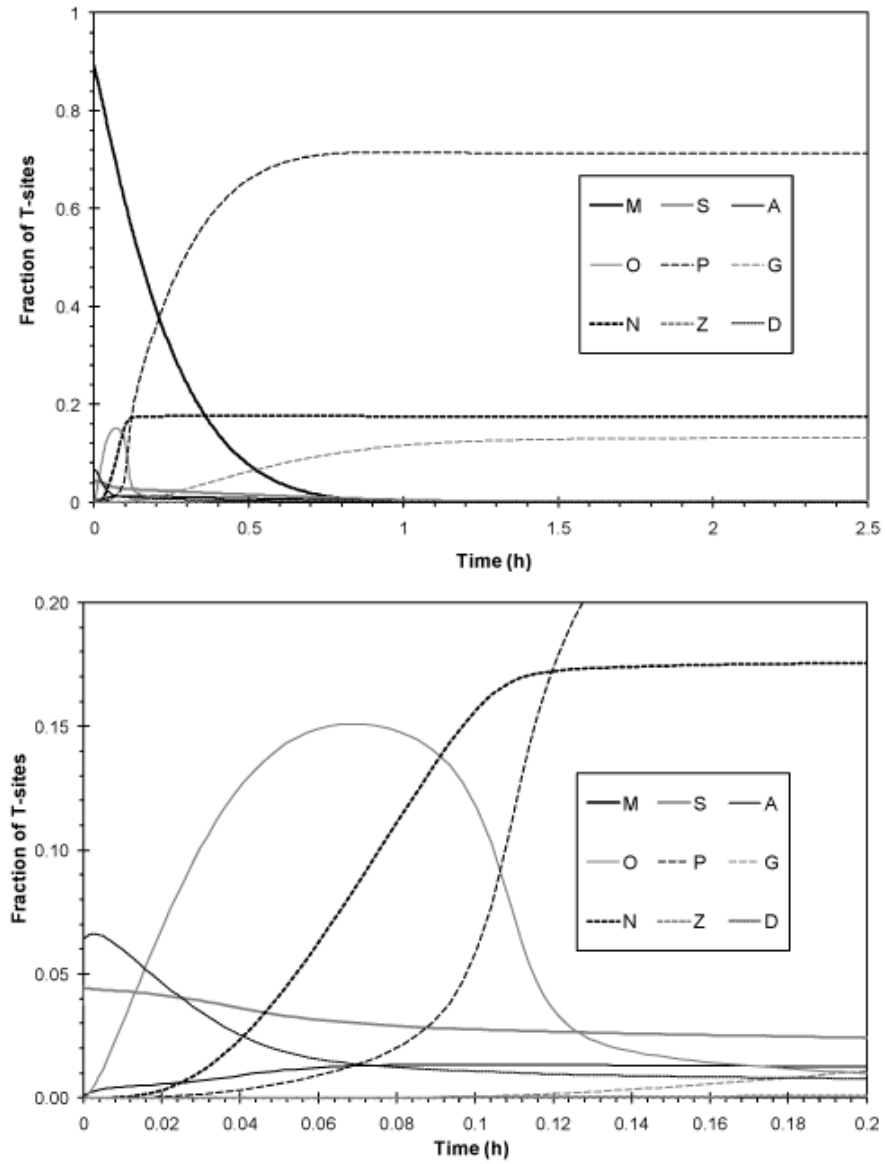

Figure 2-2 The modelled reaction process for a particular flyash geopolymer; understanding the kinetics of the different species is important in optimising the geopolymerisation process (see text and Figure 2-1 for details). The lower plot is the same data as shown on the upper plot, but with a shorter time scale to allow detail to be observed. T-sites are the tetrahedral sites. After (Provis and van Deventer, 2007a).[1]

A descriptive geopolymerisation model was proposed for flyash geopolymerisation (Fernández-Jiménez et al., 2005). This model is based on a more mechanical description of the process with less specific comments on speciation than the Provis and van Deventer model, Figure 2-3. It only applies to hollow spheres.

[1] I would like to acknowledge Prof. John Provis for generously providing the data for these graphs.

The model (Figure 2-3) describes;

a) Partial dissolution of a flyash particle, creating a hole into the sphere
b) As dissolution continues the hole grows exposing both the inner surface and the outer surfaces of smaller encapsulated spheres. Alkali dissolution is now bi-directional, acting on the outside and inside of the particles. A thin reaction product forms on all dissolved surfaces.
c) The reaction product continues to form as the dissolution proceeds, until the particle is completely or mostly consumed. The reaction product increases in thickness and density, reducing the diffusion rate, decreasing the speed of dissolution and forming the matrix which is responsible for strength.
d) The process is not uniform and varies locally depending on particle size and local chemistry (e.g. pH). Several morphologies co-exist within the sample: unreacted particles, partially reacted particles which retain the spherical morphology, reaction product and other particles.
e) The precipitation of reaction product on the small encapsulated spheres acts as a barrier inhibiting further dissolution.

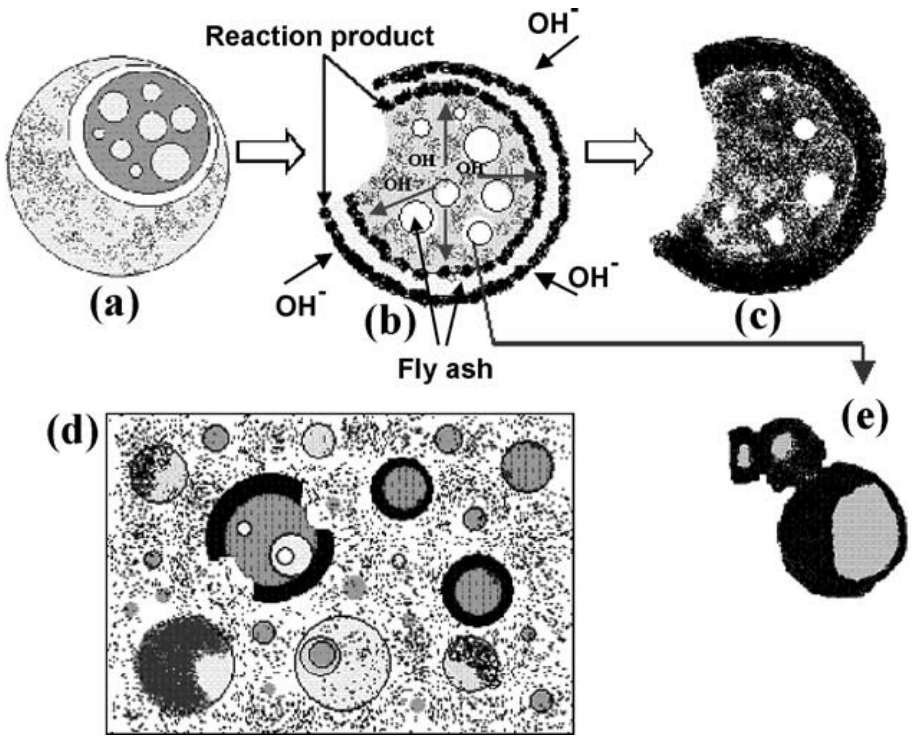

Figure 2-3 A descriptive model of the alkali activation of flyash. After Fernández-Jiménez et al. (2005) [2]

The key aspects of the Fernández-Jiménez et al. model that are not covered by the Provis and van Deventer model are that the aluminosilicate polymer [P] covers the exposed surface, gradually getting thicker and denser, resulting in slowing the further dissolution of those particles (Figure 2-3 c and e). Both models agree that the [P] phase is Al rich compared to the final [G] phase, i.e. $(Si/Al)_{[P]} < (Si/Al)_{[G]}$ not that $(Si/Al)_{[P]} < 1$ as could be misconstrued. The presence of an Al rich phase is supported by experimental observations (Rees et al., 2007a, Rees et al., 2007b).

2.1.1. Dissolution of aluminosilicates

The majority of early studies used only the bulk or total composition of each feedstock when calculating the target element ratio of the geopolymer. However, nearly all studies which report on the microstructure of

[2] Reprinted from Cement and Concrete Research, 35/6, A. Fernández-Jiménez, A. Palomo, M. Criado, Microstructure development of alkali-activated fly ash cement: a descriptive model, 1204-1209, Copyright (2005), with permission from Elsevier.

geopolymers conclude there is incomplete solid feedstock dissolution; this is especially the case for metakaolin and flyash studies. Many studies have found crystalline phases do not react, hence for the metakaolin example the silica from quartz impurities could not contribute to the geopolymer matrix; and for flyash the quartz, mullite and iron oxide phases would also not play a role in forming the matrix. Hence it is sensible to quantify the amount of unreactive material and exclude it from geopolymer composition calculations; this leads to the studies of Chapters 4 and 6. However, even then some of the amorphous material does not completely react – which is much harder to estimate. The effect of incomplete aluminosilicate dissolution for the case of metakaolin or flyash activated with sodium silicate is to decrease the silica and alumina that forms the geopolymer matrix, this has the effect of increasing the matrix Si/Al and Na/Al ratio compared to the calculated bulk Si/Al and Na/Al ratio. In this thesis the following terms are defined as follows:

Bulk composition – the complete composition of everything in the sample;

Amorphous composition – starting material composition which ignores crystalline phases.

Target Composition – the composition of geopolymer matrix trying to be achieved based on the amorphous composition of the solid feedstocks.

The dissolution rate of Si and Al from aluminosilicates in alkali solution is complex. There is data in the literature that supports incongruent dissolution (i.e. Si and Al dissolve at different rates) (Duxson et al., 2005b, Rees et al., 2007a, Rowles and O'Connor, 2009). There are also studies which show a small incongruence, i.e. a variation in the Si/Al < 10% over time (Oelkers and Gislason, 2001, Oelkers et al., 1994). However, there is far more data supporting congruent dissolution of Si and Al (Feng et al., 2004a, Brouwers and Van Eijk, 2002).

The geopolymer literature supporting incongruent dissolution is based on Attenuated Total Reflectance Fourier Transform Infrared (ATR-FTIR) spectroscopy data (Rees et al., 2007a) and Energy Dispersive x-ray Spectrometry (EDS) data (Rowles and O'Connor, 2009).

Although Rowles and O'Connor (2009), reported incongruent dissolution of Al and Si from metakaolin, with more Al dissolving than Si, this is only based on EDS of unreacted metakaolin particles. Their result cannot be reconciled with the EDS results of the geopolymer matrix in the same study and the authors' NMR studies (Rowles et al., 2007). Careful reanalysis of the published EDS data for the geopolymer matrix of Rowles and O'Connor (Rowles and O'Connor, 2009) suggests there was congruent metakaolin dissolution with some Na leaching during polishing. The measured composition of unreacted metakaolin (Si/Al > 1, rather than Si/Al =1) could be an artefact of measuring particles of a similar size to the information volume of EDS (at 20 kV) in a matrix with Si/Al > 1.

Leaching studies of kaolinite in potassium hydroxide solutions, with a liquid to solid ratio of 1 g to 80-240 ml of 0.1-4 M/l KOH, shows initially congruent dissolution, followed by a small incongruence with Al dissolving slightly more readily than Si, particularly when Al is added to the leaching solution (Bauer and Berger, 1998, Bauer et al., 1998). At lower pH of 12.4 with a high liquid to solid ratio an incongruence of approximately 20% in preference to Al was observed in the early stages of illite dissolution, followed by approximately 20% preference to Si dissolution, followed by congruent dissolution (Köhler et al., 2003).

2.1.2. Role of alkali soluble silica

For a typical geopolymer composition ($Na_{1.0\pm0.2}Al_{1.0\pm0.2}Si_{2\pm0.4}O_{7\pm2}$-$5.5\pm1.0(H_2O)$), Si is present with the highest concentration by weight. The silica is usually sourced from either an alkali silicate solution and a solid aluminosilicate from metakaolin or the amorphous part of flyash. The silica not only forms part of the short-range-ordered network of AlO_4^- and SiO_4 tetrahedra linked alternately by sharing oxygen atoms (Lecomte et al., 2003, Duxson et al., 2005c), but also plays a role while in solution (alkali silicate solution) by changing dissolution and network formation kinetics depending on the concentration and speciation (Rees et al., 2007a).

There is a distribution in the number Al units bonded to the silica tetrahedra, for a typical geopolymer, $NaAlSi_{1.9}O_{5.8}$-5.5(H_2O); the distribution was approximately 45% $SiQ^4(2Al)$, 31% $SiQ^4(3Al)$, 19% $SiQ^4(1Al)$ and 5% $SiQ^4(4Al)$, as measured by ^{29}Si NMR (Duxson et al., 2005c). This distribution has been observed to change with variation in Si/Al, Alkali/Al and for changes in Na/(Na+K).

Increasing Si/Al for metakaolin geopolymers increases the compressive strength, Young's Modulus and apparent density before reaching a small region of stability (Si/Al ~ 1.8 to 2.4) (Duxson et al., 2005b, Steveson and Sagoe-Crentsil, 2005a, Steveson and Sagoe-Crentsil, 2005b). Studies that have investigated higher Si/Al observe that these properties then decrease with increasing Si/Al ratio (Rowles and O'Connor, 2003, Subaer and van Riessen, 2007). However, a flyash study at constant water/solid ratio identified that at constant Na_2O content the compressive strength is insensitive to changes in silica content (Skvára et al., 2009), see Figure 2-4.

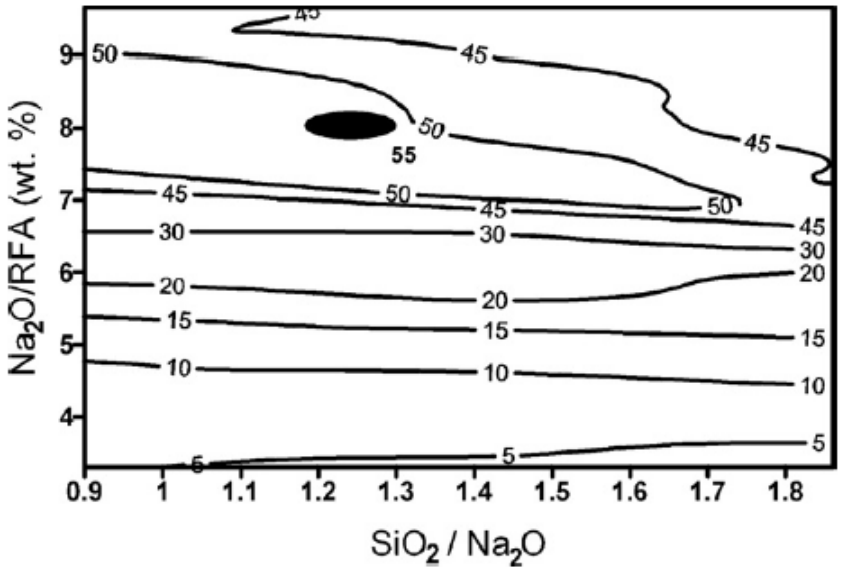

Figure 2-4 Compressive strength of a flyash geopolymer as a function of activating solution SiO2/Na2O and Na2O/flyash wt (RFA) ratio and % respectively. After Skvára et al. (2009).[3]

[3] Reprinted from Journal of Hazardous Materials, 168/2-3, František Škvára, Lubomír Kopecký, Vít Šmilauer, Zdeněk Bittnar, Material and structural characterization of alkali activated low calcium brown coal fly ash, 711-720, Copyright (2009), with permission from Elsevier.

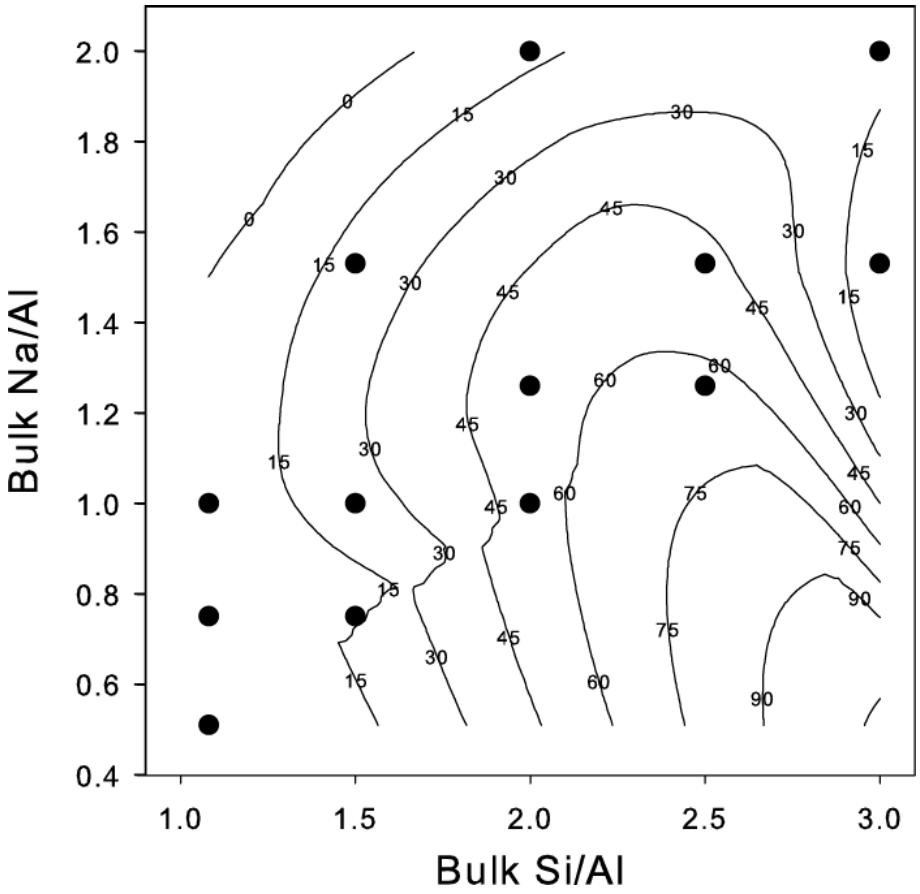

Figure 2-5 Variation in compressive strength of metakaolin geopolymer with change in bulk Na/Al and bulk Si/Al. Black dots represent data points and contour lines have been extrapolated from these points. After Rowles and O'Connor (2003).

Increases in the Si/Al ratio decreases the rate of dissolution of metakaolin, as observed by Energy Dispersive X-ray Diffraction (EDXRD) in the first few hours of reaction (Provis and van Deventer, 2007b). This is also supported by differential scanning calorimetry (DSC) observation, where an increased duration of the exothermic signal for geopolymer was observed with increasing Si/Al (Rahier et al., 1997). A range of monoliths with very high target Si/Al ratio (Si/Al = 12 to 150; with Na/Al ~ 0.6) were observed to set but were 'rubbery' exhibiting plastic deformation (Fletcher et al., 2005); although to what extent the fine amorphous silica or metakaolin dissolved for those samples is questionable which in turn raises an uncertainty about the geopolymer matrix composition.

2.1.3. Role of alkali soluble alumina

As described in Section 2.1.2, the dissolved alumina species reorientate with tetrahedral (AlQ^4) coordination and form part of the short-range-ordered aluminosilicate network in the geopolymer. The local bonding environment depends strongly on the composition (Duxson et al., 2005c, Barbosa et al., 2000) and formation conditions, however Al tends to form Al-O-Si bonds, as these are more thermodynamically stable than Al-O-Al bonds. In a synthetic metakaolin geopolymer study Tsai et al. (2010) showed that the Al Q^6/Q^4 coordination ratio of the solid aluminosilicate precursor, in a range of 1.38 to 1.92, did not affect the final Q^6/Q^4 ratio of the geopolymer, remaining relatively constant for a given geopolymer composition.

At high alumina levels (Si/Al < 1) the resulting monoliths were found to have very poor mechanical properties (Fletcher et al., 2005, Rowles and O'Connor, 2003) for which there are two explanations; 1] that the Al-O-Al bonds are unfavourable (Lowenstein's rule) hence no long range polymeric network can form (Fletcher et al., 2005), 2] that the absences of silicate in the solution retards aluminosilicate polymer formation (Rees et al., 2007a). Fletcher et al. (2005) produced samples with Si/Al = 0.25, 0.5 and 1.0 using ρ-alumina and sodium silicate solution. These monoliths with Si/Al < 1 tend to form discrete crystalline solids (zeolites and other similar species) rather than an amorphous aluminosilicate phase.

The rate of release (dissolution) the alumina has a significant impact on the homogeneity of the geopolymer matrix and extent of silica dissolution (Hajimohammadi et al., 2010). Hajimohammadi et al. found that at high release rates the matrix were more spatially homogenous and silica had a lower extent of dissolution compared to a sample with a lower rate of alumina release.

2.1.4. Role of alkali

The alkali is usually added as a hydroxide, silicate or aluminate solution. The choice of alkali depends on the application; sodium is the most widely used alkali (Fletcher et al., 2005, Rowles and O'Connor, 2003) due mainly to

availability and cost. However, partial replacement of sodium with potassium increases the compressive strength, density and improves the thermal properties (Duxson, 2006). Caesium and potassium hydroxides can be used to produce ceramic precursors (pollucite and leucite, respectively). Geopolymerisation is a useful route to forming these crystalline ceramics because, there is high degree of dissolution of the precursor; there is little or no zeolite formation and they have higher melting points than sodium-based systems (Bell et al., 2009a, Bell et al., 2009b, Barbosa and MacKenzie, 2003).

The alkali cation itself acts to charge balance the AlO_4 i.e. Na/Al = 1 is required for stability of typical geopolymer. Any excess alkali migrates to the pores (Duxson et al., 2005a, Duxson et al., 2006, Rowles et al., 2007) and combines with water (Skvára et al., 2009, Fletcher et al., 2005, Barbosa et al., 2000, Ly et al., 2006), leading to efflorescence when moisture gradients are present. Excess alkali can be fixed in the structure, such that it does not leach out in water, by heating the geopolymer to between 250° and 600° C (Oudadesse et al., 2007a, MacKenzie et al., 2010).

The coordination of sodium is difficult to measure by NMR as the peak shift from changes in coordination is small, this is due to the ionic nature of Na^+ and the inability of sodium to form bonds of covalent character (Rowles et al., 2007). The coordination of potassium is also difficult to measure for the same reasons however there is the added problem that the low frequency and high sensitivity required for K is out of reach of many solid state NMR spectrometers.

Steins et al. (2014) found that pore size, shape and distribution differ depending on the alkali type for the sodium and potassium based activators. Samples activated with potassium silicate have a higher specific surface area compared to those activated with sodium silicate, due to a large distribution of very small pores.

2.1.5. Alkali earths

Addition of calcium and/or magnesium in the form of blast furnace slag, lime or hydrated lime increases the compressive strength and reduces the setting time and in some cases allows curing at ambient temperature for flyash geopolymers (Li and Liu, 2007, Dombrowski et al., 2007, Temuujin et al., 2009). When calcium containing compounds are added at low concentrations they are found mixed throughout the geopolymer matrix, but when added at high concentrations a calcium silicate hydrate phase is found segregated from the geopolymer matrix (Yip et al., 2005).

2.1.6. Alkali activated cement (AAC)

Before the early work Purdon (1940), it was known that that Ground Blast-Furnace Slag (GBFS) when mixed with water produced very strong pastes, mortars and concretes but the very slow reaction made this impractical for most applications. To try and overcome this limitation, Purdon activated 30 different blast furnace slags with sodium hydroxide and/or lime solutions. Purdon found the majority of slags had superior early compressive and tensile strengths compared to Portland cements, and that the heat of hydration was extremely low. In addition concrete made from GBFS was found to be practically water tight with low solubility in pure and aggressive water. The key disadvantage Purdon found was the inconvenience of not being able to pre-mix the alkali or lime with the slag due to excess carbonation. The mean composition of slags studied by Purdon were CaO = 43.6 wt%, SiO_2 = 29.8 wt%, Al_2O_3 = 19.5 wt%; these GBFSs are usually almost completely x-ray amorphous.

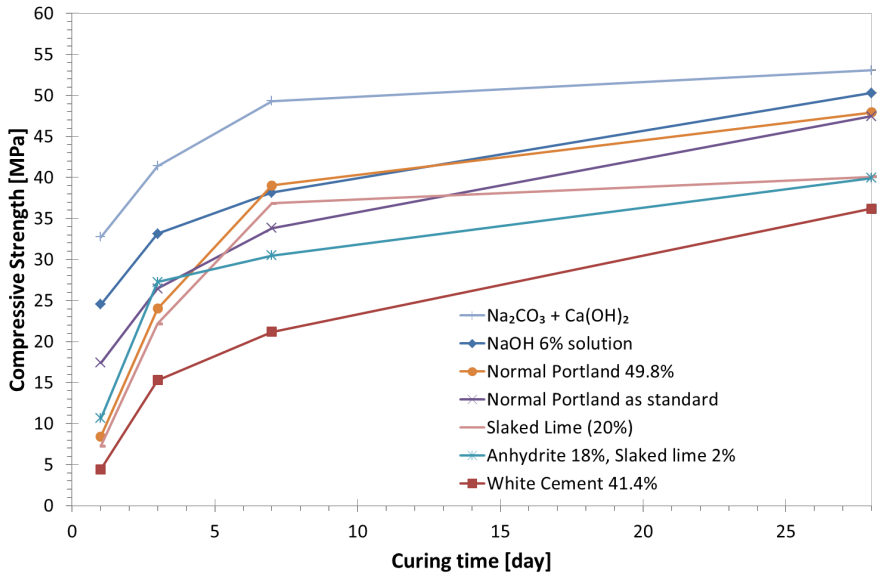

Figure 2-6 Compressive strength of ground blast furnace slag (GBFS) mortars with various activators. Data from Purdon (1940)

Krivenko (2005) reports that there were numerous small and large scale implementations of alkali activated cements in Eastern Europe since the 1960's including applications in hydropower engineering, road, agricultural, industrial, civil engineering and mining; most of which were still in service in 2005.

Studies have shown that the reaction products of alkali activated GBFSs are a combination of calcium silicate hydrate (C-S-H), calcium aluminosilicate hydrate (C-A-S-H) and/or calcium (-sodium) aluminosilicate hydrate (C-(N)-A-S-H) gels (Krivenko, 2005, White et al., 2015), depending on the activator. The fraction of cross-linked/non-cross-linked C-(N)-A-S-H was found to vary significantly, particularly between 28 and 200 days, when the fraction of cross-linked C-(N)-A-S-H decreased (Myers et al., 2015). The C-S-H and C-A-S-H gel phases of OPC are nanocrystalline with a structure similar to tobermorite with short range ordering out to about 40 Å which is equal to the crystallite size. Whereas the C-(N)-A-S-H phase derived from the alkali activation of GBFS has similar short range order, but only out to about 8 Å, hence is predominantly amorphous (White et al., 2015). In this context nanocrystalline means that a bulk crystal structure roughly describes the observed short range order until a particular radial value.

2.1.7. Boron

The addition of small quantities of boron as borax ($Na_2B_4O_7$-$10H_2O$) to 'typical' geopolymers has been patented as a means of prolonging the setting time (Palomo and Lopez de la Fuente, 2003, Nicholson and Fletcher, 2005). However, as explored in Chapter 8, total substitution of B for Al is possible with acceptable kinetics leading to a new material with high neutron attenuation making it suitable for shielding panels in reactors etc. This was achieved by activating silica fume with a sodium borate solution.

Inspired by the journal publication from Chapter 8 (Williams and van Riessen, 2011), Nazari et al. (2014) reported compressive strength of up to 64 MPa in paste samples by activating flyash with a sodium borate solution. The study of the microstructure, with SEM, revealed very few remnant flyash particles compared to typical sodium silicate activated flyash geopolymer, indicating a high degree of flyash dissolution. Even in the lower strength samples, Nazari et al. reported very few macro or microstructural cracks on the fracture surfaces. The study of speciation, with FT-IR, indicated that the presence of B-O bonds was crucial to the high strength development. Nazari et al. (2015a) found that the B-O bonds form when cured at 70° and 90°C but not when cured at 25° or 40°C, because at lower temperatures the sodium borate solution crystallises as sodium perborate ($NaBO_2$) consuming the activating solution. The flexural strength of this type of material was found to be suitable for structural application, 9.5 ± 0.4 and 11.8 ± 0.9 MPa for non-reinforced and reinforced pastes, respectively (Nazari et al., 2015b).

Nazari et al. (2015a) reported paste samples with a compressive strength >35 MPa with only 5.2 wt% NaOH, which on the lower range for aluminosilicate geopolymers. A typical metakaolin or flyash geopolymer has 13 wt% or 8 wt% NaOH, respectively. The low NaOH content has significant consequence to the CO_2-eqivalent emissions, as the rate for NaOH is the highest of the geopolymer feedstocks, hence this material might be of interest as a construction material with low CO_2 emissions. See Section 2.3.8 for more discussion on CO_2 emissions.

2.1.8. Iron

When added as hematite or goethite, iron does not react in the geopolymerisation reaction (Perera et al., 2007, Fernandez Jiminez et al., 2004). However, iron in flyash does dissolve into solution and is part of or mixed with the geopolymer hydration product (Fernandez Jiminez et al., 2004). It is not clear which phases of iron will dissolve; in particular to dissolution rate as a function of Fe substitution for Al in soluble aluminosilicate glasses. Iron's role is important to geopolymerisation depending on the chemical form that it is present in, due to the effects on reaction kinetics. Increases in iron substitution in the aluminosilicate glass of flyash leads to a reduction of alkali solubility of the aluminosilicates (Chen-Tan et al., 2009), which obviously affects the resulting material. Very small iron oxide particles, which are alkali insoluble, may acts a nucleation seed similar to corundum (Rees et al., 2008) and is described in more detail in Section 2.1.9.

2.1.9. Role of insoluble phases

The majority of insoluble phases will have no effect on the chemistry of the resulting geopolymer matrix, however if there is a high enough surface area the particles can act as nucleation seeds promoting either geopolymer matrix formation or zeolite formation as observed when corundum with a surface area of 275 m^2/g is used to produce a geopolymer-corundum mortar (Rees et al., 2008).

The microstructural role of insoluble or undissolved phases is vital – this is a major difference between flyash and metakaolin geopolymers. Flyash has 20 to 40 wt% inert crystalline phases such as quartz and mullite while metakaolin typically does not. Within flyash there are two types of insoluble phases, those that are present but separate from flyash spheres, such as carbon and quartz and those generally smaller particles within the spheres which are predominantly mullite, quartz and iron oxides. The quartz and mullite act as fillers. Mullite is also responsible for the improved thermal

stability of flyash geopolymers compared to metakaolin geopolymers (Rickard et al., 2010).

2.2. STRUCTURE OF GEOPOLYMERS

To-date there are only a few studies reporting predicted structures for geopolymers (Barbosa et al., 2000, Rowles et al., 2007), however the current understanding and the amorphous nature of geopolymers are such that the structures are schematic generalisations, not quantitative models. What is clear from NMR studies is that the geopolymer consists of a network of tetrahedrally coordinated Si and Al, with the distribution of the number of Al units bonded to the Si tetrahedral changing with composition, particularly the Si/Al ratio (Barbosa et al., 2000, Rowles et al., 2007, Duxson et al., 2005c). In the model proposed by Barbosa et al. (Figure 2-7) the alkali and free water sites are within the pores of the tetrahedral aluminosilicate network. Rowles et al. proposed modification of this model (Figure 2-8c) based on more extensive NMR data. The key difference is the location of the alkali for charge balancing. Rowles et al. proposed that the alkali form as hydrated alkali aluminates (Figure 2-8a) and as hydrated alkali silicates (Figure 2-8b) to achieve charge balance. Although these models are contentious because they do not fully account for electro-neutrality of the network and the location of the water is inconsistent with thermal gravimetric analysis, but consistent with ^{2}H NMR (Duxson, 2006).

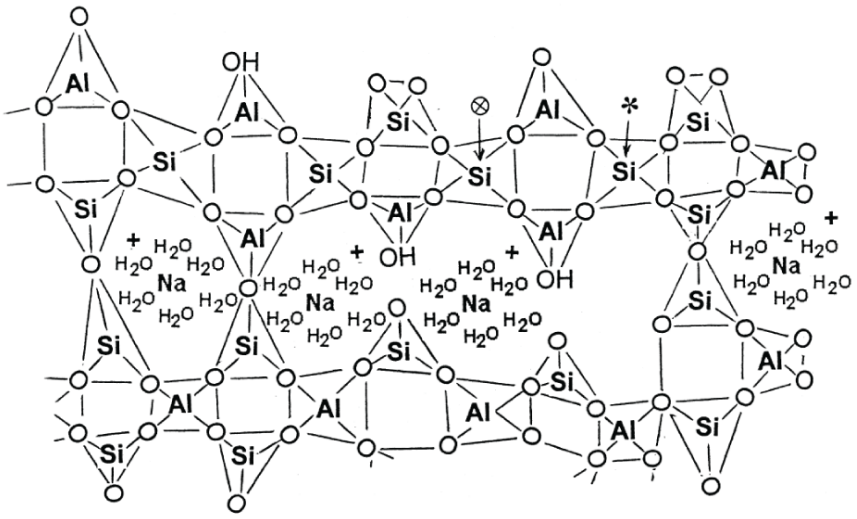

Figure 2-7 The structure of geopolymer as proposed by Barbosa et al. (2000)[4].

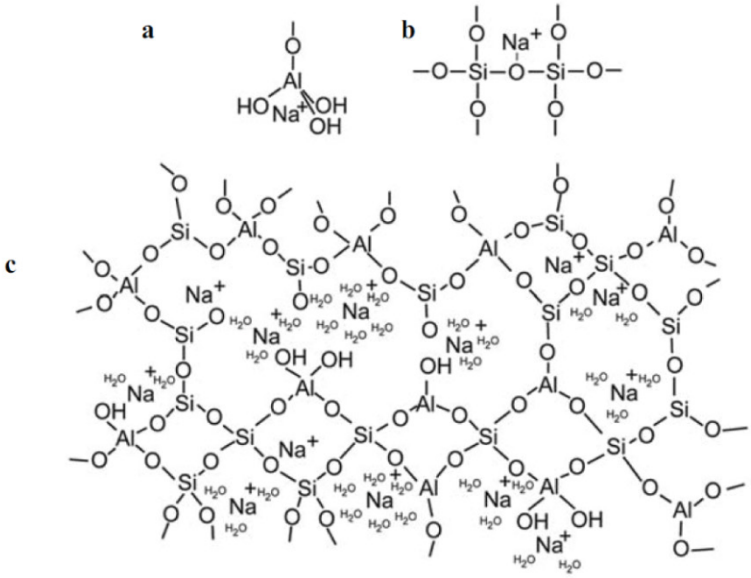

Figure 2-8 Geopolymer structure proposed by Rowles et al. (2007), a) proposed location of charge-balancing Na+ cation which are assumed to be from sodium aluminate species; b) proposed location of the charge-balancing Na+ cation assuming the form of a modified bridging network; c) schematic, based on the model by Barbosa et al. (2000) (Figure 2-7), with modification attempting to incorporate the charge-balancing Na+ in the form of sodium aluminate species and modified bridging networks into the structure[5].

[4] Reprinted from International Journal of Inorganic Materials, 2/4, Valeria F. F. Barbosa, Kenneth J. D. MacKenzie, Clelio Thaumaturgo, Synthesis and characterisation of materials based on inorganic polymers of alumina and silica: sodium polysialate polymers, 309, Copyright (2000), with permission from Elsevier.

[5] With kind permission from Springer Science+Business Media: Applied Magnetic Resonance, ^{29}Si, ^{27}Al, ^{1}H and ^{23}Na MAS NMR Study of the Bonding Character in Aluminosilicate Inorganic Polymers, 32, 2007, 663, M.R. Rowles, J.V. Hanna, B.H. O'Connor, K.J. Pike, M.E. Smith and E.R. Vance, Figure 9.

2.3. PROPERTIES OF GEOPOLYMERS

Geopolymers are generally characterised as having high compressive and tensile strength and superior acid resistance and thermal properties, relative to Portland cements.

2.3.1. Mechanical strength

The compressive strength of geopolymer samples depends on both intrinsic strength of the geopolymer matrix, morphology of the microstructure and the macrostructure (cracks and voids etc.). Unfortunately to-date, very few studies have investigated geopolymer microchemistry. Rowles and O'Connor (2009) is one such study for which the compressive strength and microchemistry for the same samples is available (Rowles and O'Connor, 2003). In Figure 2-9 the compressive strength data and the matrix compositions are plotted, it is clear that there is more variation as a function of matrix composition than as a function of the bulk composition shown in Figure 2-5. There is large region of high compressive strength (45 to 65 MPa), shown on Figure 2-9, the sample with maximum compressive strength had a bulk composition Si/Al = 2.5, Na/Al =1.25 and a matrix composition of Si/Al = 3.2 and Na/Al = 1.4.

2.3.2. Room temperature setting

Many authors have reported room temperature setting can be achieved by adding a small percentage of ground blast furnace slag to geopolymer mixture (Li and Liu, 2007, Dombrowski et al., 2007, Temuujin et al., 2009) . However, Vijai et al. (2012) simply replaced 10% of the flyash with cement powder to achieve room temperature setting.

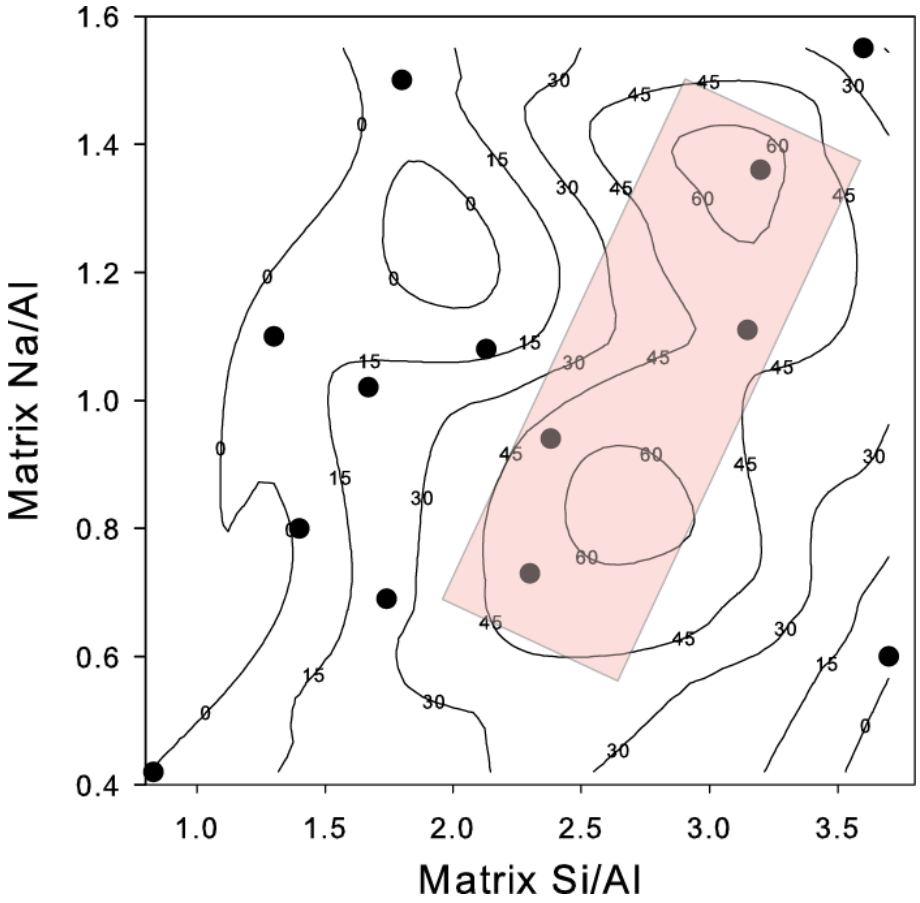

Figure 2-9 Variation in compressive strength with geopolymer matrix chemistry, as measured by energy dispersive spectroscopy on a scanning electron microscope. Black dots represent actual data points. This is the same compressive strength data as in Figure 2-5, but with the measured matrix composition opposed to the bulk composition. The pink region highlights the 4 strong samples with strengths between 45 to 65 MPa. After Rowles and O'Connor (2003, 2009).

2.3.3. Chemical resistance

Wallah et al. (2005) showed that flyash geopolymer concrete samples were not significantly affected by 1 year exposure to 5% sodium sulphate solution or 0.5% nitric acid solution (Wallah and Rangan, 2006). Whereas exposure to 1% and 2% nitric acid solutions led to significant degradation in compressive strength (Wallah et al., 2005, Wallah and Rangan, 2006).

Bakharev (2005) also found that flyash geopolymer pastes are resistant to nitric or sulphuric acid dissolution at pH 1 to 3, and much more so than OPC (0.5% nitric acid solution has a pH of approximately 1).The nitric acid attacks by depletion and exchange of the alkali and alkali rare earth ions by H^+ or H_3O^+ ions and by an electrophilic attack on the polymeric Si-O-Al bonds

(Allahverdi and Skvara, 2001a). This results in a silica rich framework which is brittle and hard (Allahverdi and Skvara, 2001b).

The lifetime of sewer pipes is governed by the time taken to erode the physical properties to a threshold value, the major factors affecting this for OPC sewer pipes are exposure to weak acids from bacterial action and ground water, sulphates, water and atmospheric CO_2 (Oualit et al., 2012). Rocla Technology have developed a range of geopolymer sewer pipes that exploit the chemical resistive properties (Gourley and Johnson, 2005). They report that the University of Mississippi test for sulphuric acid dissolution predict the lifetime of geopolymer sewer pipes is around 900 years compared to 50 years for a similar sized OPC pipe. The University of Mississippi test is an accelerated test that cycle between acid and water to simulate real world use as sewage pipe.

2.3.4. Durability (longevity)

Geopolymers perform well in accelerated tests, such as University of Mississippi test for chemical resistance (Gourley and Johnson, 2005), indicating a very long service life (>900 year). However, there are a limited number of long term laboratory tests (Wallah and Rangan, 2006) and very few reported long term in-service field tests i.e. tested in the normal application. The number of these studies are increasing, and are very necessary. For example, in a 2-year study of AAC's, Myers et al found that mean-chain-length (MCL) of C-(N)-A-S-H was stable until 28 days, and then reduced (Myers et al., 2015). While this reduction in MCL may or may-not not have significant impact on the physical properties, it highlights that there could be adverse reactions over longer time scales than typical study durations reported in the literature, hence the need for longer term studies. Wallah et al. studied geopolymer over the period of 1 year, finding that most properties were consistent or steadily improved. However, for example mass loss due to exposure to 1% sulfuric acid started to rapidly increase (degrade more rapidly) after 36 weeks. It is positive that some in-service studies are underway, such as paving (Van Deventer et al., 2012), it would be good see

the results in the future. There are also in-service long term studies underway for railway sleepers and sewage pipes (Gourley and Johnson, 2005).

2.3.5. Fireproof and Thermal properties

Geopolymers generally have superior high temperature fire resistant properties compared to OPC (Vickers et al., 2015). The factors that decrease the thermal stability of geopolymers are: phases undergo transformation with significant volumetric changes; melting of phases which then act as a flux; and escaping gases (Rickard et al., 2011). The phases with problematic phase transformation include quartz, disordered iron oxides and hydrated species (Rickard et al., 2011). Any unreacted alkali in the pores is of concern as it may melt and act as a fluxing agent. When used as a coating, variation of the Si/Al and water content can be adjusted to match coefficient of expansion that more closely matches that of steel substrate – also excess water escapes keeping the material cooler for longer and leaves a porous structure (Temuujin et al., 2012, Temuujin et al., 2010).

2.3.6. Controllable porosity and strong capillary force

The macro porosity (>1 μm size scale) of geopolymers can be tailored to specific applications by either producing a composite with sacrificial fibres, the addition of reactive foaming agents or the addition of inactive foaming agents.

For the application of passive cooling, where a strong capillary force is required to transport water, temporary geopolymer-fibre composites were produced and then the fibres were subsequently removed via alkali, hydrothermal, heat or a combination thereof (Okada et al., 2011, Okada et al., 2009). Okada et al. (2011) reported significant increases in porosity and capillary rise heights by the addition and subsequent removal of polylactic acid (PLA) fibres, particular for alkali and heated geopolymers-PLA fibre composites. A similar process was found to reduce the crack size in flyash geopolymer reinforced with Polyvinyl Alcohol (PVA) fibres compared to basalt fibres during a fire test (Masi et al., 2015). During the simulated fire exposure

the PVA fibres decompose, leaving a path for steam to escape, reducing large scale damage.

For the applications with specific thermal property requirements, such as building materials with insulting properties, fireproof materials and ceramic precursors the use of reactive and inactive foaming additives have been investigated to increase the macro porosity. The intent of the increased macro porosity decrease the thermal conductivity and create a pore network that also enables moisture, including steam, to escape without structurally damaging the material (Bell and Kriven, 2009). Introducing pores reduces the maximum diffusion distance within the geopolymer (Figure 2-10) which reduces the capillary force produced to remove the water thus decreasing the probability of cracks forming.

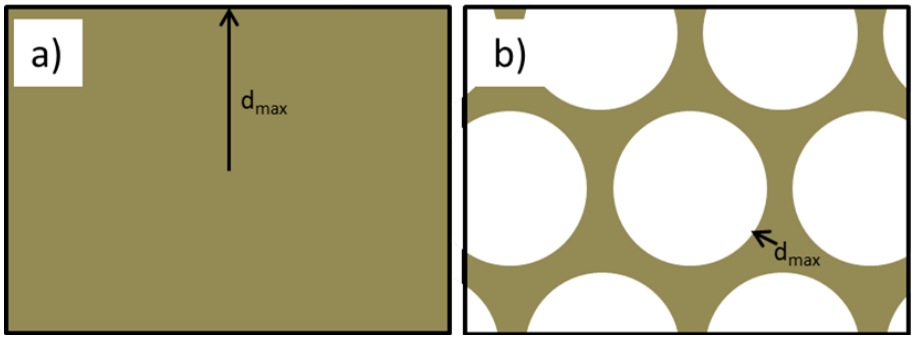

Figure 2-10 The schematic shows how introducing porosity reduces the maximum water diffusion distance comparing a) a solid sample, b) a foamed sample. After Bell and Kriven (2009).

Bell and Kriven (2009) reported using both hydrogen peroxide (H_2O_2) and Al metal powder to produce a foamed geopolymer. Both additives reacted in the alkali environment and decompose producing gas shown in Equations 2-1 and 2-2 (Bell and Kriven, 2009). The pore size was selected by controlling the pressure during curing considering the Young-Laplace Equation (2-3) where γ is the surface energy of the liquid vapour interface and is equal to 7.29 x 10^{-2} J/m^2 for water.

$$\boldsymbol{H_2O_2 \rightarrow 2H_2O + O_2} \quad \textbf{(2-1)}$$

$$\boldsymbol{2Al + 6H_2O + 2NaOH \rightarrow 2Na[Al(OH)_4] + 3H_2} \quad \textbf{(2-2)}$$

$$\boldsymbol{\Delta P = 2\,\gamma/radius} \quad \textbf{(2-3)}$$

The H_2O_2 foamed geopolymer exhibited strong compressive strength with a low bulk density, making it suitable for ambient temperature structural

applications. However, the specimens were not suitable for making ceramics or other refractory applications as the removal of moisture still resulted in cracking. This was because the pore network was non-percolating. The Al foamed geopolymer produced a percolating pore network, hence on heating the moisture could escape causing less cracking, resulting in strong ceramics. However, given the Al powder was added at rate of 60 wt% and resulted in multiple phases forming on heating (Al_2O_3, Si, AlN) this method is probably not ideal for production of ceramic precursors.

2.3.7. Low aluminium leachability in simulated body fluids

Due to the nature of the incorporation of Al into the tetrahedral sites of the geopolymer structure, geopolymers have been found to be very resistant to leaching in simulated body fluid (SBF) (MacKenzie et al., 2010, Oudadesse et al., 2007a, Oudadesse et al., 2007b). For the application of biological implants Al leach-ability in SBF is of interest because Al can be biologically toxic. Both groups of authors reported on heat treated potassium aluminosilicate geopolymers. MacKenzie et al. reported on samples with compositions of Si/Al = 1.6, K/Al = 0.62 and H/Si = 4.6; and heat treated at 400°C. Oudadesse et al. reported on samples with Si/Al = 31, K/Al = 33-50 and H/Si = 0.8; and heat treated at 250°C. MacKenzie et al. found that the addition of 10 wt% $Ca_3(PO_4)_2$ or Ca silicate reduced the leach-ability of Al in SBF, whereas the addition of 10 wt% $Ca(OH)_2$ increased the leach-ability of Al in SBF. The results clearly showed that heat treatment significantly reduces leachability both the K and Al in SBF.

2.3.8. Low CO_2-eq emissions

The chemistry of geopolymers is such that the CO_2-eq emissions can be much lower compared to Portland cements. There are two reasons why; namely the lack of direct CO_2 emissions from geopolymer production and that the majority of starting materials are typically industrial by-products (McLellan et al., 2011, Provis, 2014, Weil et al., 2009).

Cement production has one major intrinsic source of CO_2 - the decomposition of calcium carbonate, whereas there are no intrinsic sources of CO_2 for geopolymers. i.e. theoretically if renewable energy sources were used for all energy supply there would be almost no CO_2-eq emissions.

However, given that it is not feasible currently for either cement or geopolymers to be only produced with non-emitting energy sources these must be considered. A life cycle approach much be taken which assesses the total emissions released during the life of the product (McLellan et al., 2011). When comparing two products, a functional unit that is comparable between products must be defined and assessed, for example 100 years of in-track and regularly used railway sleepers (ties) that meet physical performance specification required. i.e. this could include several repairs or replacements for both geopolymer and OPC sleepers. The scope of the analysis has to have a common start and end point for both products, i.e. assess both from mining of raw materials to disposal of the product. Where the initial steps are similar and specific information is not available the start point of the analysis could be much later in the life cycle. When conducting a life-cycle analysis all processes that produce emissions should be assessed, such as mining, processing, refining and transport. This makes the analysis complicated as it does need to be specific on what starting materials are used, how they are treated and transported and where they are located compared to where they will be used. The net result for the product with lower emissions, geopolymer or OPC, is highly dependent on where the product is to be used compared to the flyash sources (McLellan et al., 2011).

One complication with assessing a product that is not yet commercialised is that emissions actually released on a small scale (laboratory or pilot scale) are compared to those released on a large scale (commercial). These emissions may be significantly different, especially when transport is a major contributor to emissions. For example if flyash geopolymer was to be used in Melbourne, Victoria Australia, the lack of a suitable local flyash dictates that flyash might need to be imported from power stations near Sydney, New South Wales Australia. As the scale of commercialisation increase more efficient transport modes can be used. Table 2-1 summarises the energy use

and green-house-gas emission rates of the various transport modes. Table 2-2 show the energy use and green-house-gas emission rates per tonne of flyash transported from Bayswater Power Station (NSW, Australia) to Port Melbourne (Vic, Australia). It is quite clear that at pilot scale, when only utilising small trucks the impact is quite high compared to using rail or sea freight.

Table 2-1 The energy use and green-house-gas emission rates for various modes of transport. (ABS, 2006, DITRDLG, 2008, Appelbaum Consulting Group, 2007)

Transport Type	Energy [MJ/(km t)]	Green-house-gases [kg CO2-eq/(km t)]
Road - Rigid trucks	2.9	0.28
Road - Articulated Trucks	1.0	0.09
Rail - Ancillary	0.08	0.01
Rail - Hire and Reward	0.23	0.04
Sea Freight	0.17	0.02

Table 2-2 The energy use and green-house-gas emission rate for transport of flyash from Bayswater power station (NSW, Australia) to Port Melbourne (Vic, Australia). Sources: Distances (SeaRates LP, 2015, Google, 2015).

Scale of commercialisation	Mode of transport	Distance [km]	Energy [GJ/t]	Green-house-gases [kg CO2-eq/t]
Pilot scale	Road (rigid trucks)	1,116	3.2	310
Small	Road (articulated trucks)	1,116	1.1	97
Medium/Large	Rail	1,228	0.28	46
Massive	Sea plus articulated trucks	1192 + 124	0.32	36
	Sea (only)	1,192	0.20	25

For the geopolymer feedstocks that are industrial by-products, the life-cycle is assessed from point of disposal i.e. flyash is assessed once it is collected from the power station and includes the bulk handling, processing (screening) and transport. Whereas virgin feedstock material, such as kaolin (for converting to metakaolin), are assessed from the mining stage. Table 2-3 summarises the stages included in the life-cycle analysis of geopolymers (McLellan et al., 2011).

Table 2-3 Stages assessed in the life-cycle analysis for geopolymers.

Feedstock	Stages assess by life-cycle analysis
Flyash	Bulk handling, screening and transport
Metakaolin	Mining, screening, dehydroxylation (700-800°C), bulk handling and transport.
Silica part of sodium silicate (dissolution method)	Mining, screening, bulk handling and transport.
Sodium hydroxide	Mining, screening, bulk handling and transport

The cement clinker is produced by mixing the limestone, clay, bauxite and/or iron ore together in a rotary kiln while heating to 1300-1400°C, resulting in a solid state reaction. This process releases 785 kg of CO_2 per tonne of calcium oxide, resulting in 385 kg of CO_2 per tonne of cement. An additional 315 kg of CO_2 per tonne of cement is produced from use of fuel and electricity, i.e. a total of 700 kg of CO_2 per tonne of cement (CIF, 2013), on average for Australian cement producers. This includes the significant

contribution from grinding the clinker to a fine particle size. The cement industry does try to utilise alternative fuels from industrial by-products that have suitable calorific value, such waste tyres, timber or oils. The cement industry also mixes supplementary cementitious materials (SCMs) with the clinker to produce cement, such as granulated blast furnace slag. SCMs generally do not require as much energy for processing compared to the clinker, as they often do not need to be crushed/ground.

2.4. SODIUM HYDROXIDE AVAILABILITY

One challenge for full scale deployment of geopolymers is the global sodium hydroxide production capacity. Assuming 10% replacement of the 4 Gt/y (USGS, 2015a) of cement with geopolymer, the sodium hydroxide requirement would be 0.03-0.05 Gt/y, this compared to the estimated 2012 global production rate of 0.08 Gt/y (Alkali Manufacturers' Association of India, 2012), hence a 30% to 80% increase in production would be required. Sodium hydroxide is primarily produced from salt brines, co-producing chlorine and hydrogen gases. The sodium chloride requirement would be 0.03-0.07 Gt/y, compared to the 2015 global production rate of 0.27 Gt/y (USGS, 2015a). This significant increase in salt requirements can probably be safely collected from the ocean, it is estimated that the ocean has 5×10^7 Gt of sodium chloride (USGS, 2015b). The 30% to 80% increase to hydrogen production may find a market as an energy vector in the hydrogen economy (US Department of Energy, 2015), i.e. as a intermediate fuel source to power equipment such as cars. However, the 30% to 80% increase in chlorine gas production may not find a market hence needs to be disposed of as a waste-product. The requirement to dispose of the chlorine gas would have a significant impact on the cost and carbon calculations.

Utilisation of alkali by-products such as Bayer Liquor (sodium aluminate solution) from the alumina refining industry, have the potential to fill this gap (van Riessen et al., 2013). This is discussed in more detail in Section 5.5.2.

2.5. APPLICATIONS OF GEOPOLYMER

Geopolymers have been investigated for a wide range of applications ranging from large scale bulk applications such as mine back fill to niche low volume applications such as drug delivery. Table 2-4 lists some of the applications for which geopolymers have been designed and the relevant properties exploited for each application.

Table 2-4 The range of applications investigated for geopolymer technology.

Application	Geopolymer Properties Required	Literature
Cast and Cured Concrete	Moderate to high compressive strength	(CSRP, 2010, Rangan, 2008, Hardjito et al., 2004, Chang et al., 2007, Sumajouw et al., 2007, Davidovits and Sawyer, 1985)
Ready-mix concrete	Moderate to low compressive strength. Room temperature setting	(CSRP, 2010) (Li and Liu, 2007, Dombrowski et al., 2007, Temuujin et al., 2009)
Sewage Pipes	Chemical resistance High flexural strength	(CSRP, 2010)
Railway sleepers	Very High flexural and compressive Strength	(CSRP, 2010)
Fireproof / high temperature concrete	Dimensional stability at high temperatures Low thermal conductivity Non flammable	(van Riessen et al., 2009, CSRP, 2010, Dombrowski et al., 2007, Davidovits et al., 1989)
Ceramic Precursor	High degree of homogeneity High density	(Bell et al., 2009a, Bell et al., 2009b)
Neutron Shielding	High boron content Mechanically stable	Chapter 8
Cooling (reducing heat island effect)	High water pump-up ability Controllable porosity Mechanically stable	(Okada et al., Okada et al., 2009)
Fireproof coatings	Dimensional stability at high temperatures Low thermal conductivity Non flammable	(Temuujin et al., 2010)
Medical implants	neutral pH low ‘free aluminium’ Porous	(Oudadesse et al., 2007a, MacKenzie et al., 2010)
Humidity indicators	Reversible changes in geopolymer	(MacKenzie and O'Leary, 2009)
Drug delivery	Mechanically stable Controllable permeability	(Jämstorp et al., 2010)

2.6. PORTLAND CEMENT CHEMISTRY

For the purposes of completeness and to facilitate comparison to geopolymers the following section briefly describes a simplified view of the chemistry of Portland cements.

Portland cement concrete is a composite of many compounds and is produced in a multiple step process. After mining and transport of raw materials, the raw materials are crushed, ground and reacted at high temperatures in a kiln, producing clinker. The clinker is then ground and blended with additives such as gypsum and limestone to produce cement. Mixing cement water and aggregates produces concrete. In this final step the cement undergoes a hydration reaction with the water to produce the binder.

2.6.1. Clinker and cement production

The first stage of clinker production is to produce the raw mix. The raw mix is a mixture of starting materials such that a suitable elemental composition and free CaO content is achieved. These are mixed, crushed and ground together. The starting materials vary depending on location, but typically include limestone, seashells, bauxite, clays, shales, sands, iron ores and gypsum (Taylor, 1997). Ca, Si, Al and Fe oxides dominate the composition however the Mg, S and P content also play a role (Kurdowski, 2014).

The raw mix is fed into a rotary kiln at very high temperature (1300° - 1500°C) (Taylor, 1997). The rotary kiln has a temperature gradient, such that there is controlled heating and cooling. Initially the carbonates and hydrated minerals decompose, releasing CO_2 and H_2O into the flue gases. The reaction proceeds mostly in the solid state with a small fraction of molten CaO, this step produces predominantly crystalline dicalcium silicates and dicalcium aluminates (Kurdowski, 2014). Then as the material reaches the hottest part of the kiln the reaction is dominated in the liquid phase (fluxed by molten CaO, molten alkali sulphates and chlorides, and molten Al and Fe phases), then as it cools the tricalcium silicates (such as alite) and tricalcium aluminates crystallise (Taylor, 1997, Kurdowski, 2014).

The clinker is then crushed and ground with additives to produce cement. Typically limestone, gypsum and pigments are added to control setting time and colour (Kurdowski, 2014).

The major phases found in clinker are alite, belite, aluminate and ferrite; and with several other phases including alkali sulfate (Taylor, 1997, Kurdowski, 2014). The compositions of these phases and typical abundances are summarised in Table 2-5.

Table 2-5 Summary of major phases in Portland cement and Portland cement paste. After (Kurdowski, 2014, Taylor, 1997).

Cement notation	Phase name	Chemical Name	Chemical formula	Abundance
Cements				
C_3S	Alite	tricalcium silicate	Ca_3SiO_5	50-70%
C_2S	Belite	dicalcium silicate	Ca_2SiO_4	15-30%
C_3A	Aluminate	tricalcium aluminate	$Ca_3Al_2O_6$	5-10%
C_4AF	Ferrite	Tetra-calcium aluminoferrite	$Ca_2(Al_xFe_{(1-x)})O_5$ where $0 < x < 0.7$	5-15%
C$\underline{S}$H	gypsum	gypsum	$CaSO_4 \cdot 2H_2O$	2-5%
C$\underline{S}$	anhydrite	anhydrite	$CaSO_4$	
Pastes				
C-S-H	Calcium silicate hydrate gel	-		~50%
CH	Portlandite	Calcium Hydroxide	$Ca(OH)_2$	~20%
AFm	Al_2O_3-Fe_2O_3-mono		$Ca2(Al,Fe)(OH)_6 \cdot X \cdot x\ H_2O$ where X is formula unit of a singly charged anion or half a formulate of a doubly charged anion. Commonly OH^-, SO_4^{2-} or CO_3^{2-}	~15%

The typical bulk chemical compositions of OPC clinker and cement are shown in Table 2-6. The key point of note is that clinkers and cement pastes are mostly calcium oxide based (65.6 and 65.3 wt%, respectively) compared to typical geopolymer pastes, which are mostly SiO_2 and Al_2O_3 based (58 wt% and 21 wt%, respectively), with a relatively small fraction of alkali (16 wt% Na_2O).

Table 2-6 Typical bulk chemical composition of Portland cement clinker and cement paste (Taylor, 1997) compared to a typical metakaolin geopolymer,. Weight fractions are on the ignited mass basis. Cement paste was 14 month old, geopolymer paste was 30 days old. The "-" indicates data was not available.

Oxide	Portland Cement Clinker	Portland Cement Paste	Metakaolin Geopolymer Paste
CaO	65.6	65.3	-
SiO_2	21.6	21.0	58.1
Al_2O_3	5.3	5.6	26.1
Na_2O	0.3	0.2	15.8
Fe_2O_3	3.1	3.1	-
SO_3	1.0	2.6	-
K_2O	1.0	0.4	-
MgO	1.6	1.2	-
H_2O (chemically bound)	-	29.3	-
H_2O (Total non-evaporable)	-	40.6	-
H_2O (Total)	-	-	38.4
Minor elements	0.5	0.6	-

2.6.2. Cement hydration

A complex set of reactions are triggered when water is added to the cement. The alite, belite, aluminate and ferrite phases dissolve at different rates and the reaction products react with each other and the undissolved cement phases to produce a range of final reaction products. The belite phase can take many years to completely dissolve. The final reaction product is predominantly an amorphous calcium silicate hydrate gel (C-S-H gel), calcium hydroxide (CH), calcium aluminate ferrite mono (AFm) and pore water (Taylor, 1997, Kurdowski, 2014). The C-S-H gel has no specific composition, however Allen et al. (2007) found that the composition in the samples analysed had composition of $(CaO)_{1.7}(SiO_2)(H_2O)_{1.80}$ as measured

by SAXS and SANS. In many cases the AFm phase is transient; forming and then redissolving and forming the C-S-H phase.

Alite is the most abundant phase in cement clinker. In pure alite paste samples it is well established that there are four distinct regions of reactivity (Figure 2-11): Region A) Initial reaction; B) Period of slow reaction; C) Acceleration period; and D) Deceleration period (Bullard et al., 2011). The reaction rate peaks at around 9 hours, and remains very exothermic until about 15 hours.

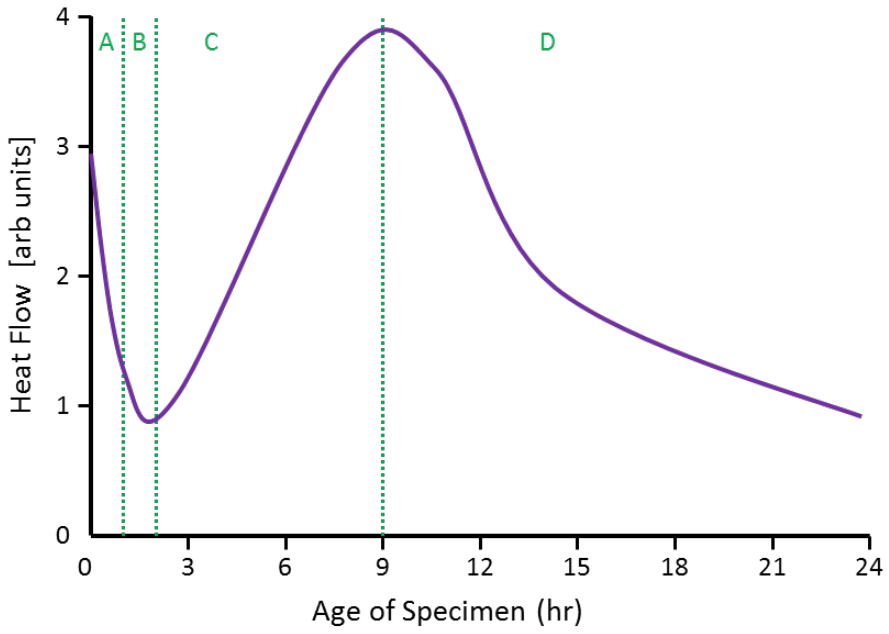

Figure 2-11 The typical rate of hydration of alite as measured by isothermal calorimetry. Region A) Initial reaction; B) Period of slow reaction; C) Acceleration period; and D) Deceleration period. After Bullard et al. (2011)

The rate that the aluminate phase reacts is highly dependent on the gypsum or anhydrite content; without the sulphate the aluminate phase reacts extremely quickly resulting in premature setting of the paste (Taylor, 1997, Bullard et al., 2011, Kurdowski, 2014). The presence of sulphate provides precise control of the setting time for the pastes.

CHAPTER 3: MATERIALS AND CHARACTERISATION METHODS

3.1. RAW MATERIALS SELECTION

3.1.1. Flyashes

Flyash is the fine particle residue transported by flue gas after the combustion of coal in a coal fired power station. This flyash is typically captured by electrostatic precipitators (ESP) or a bag filter. The chemical composition of the flyash depends on the initial coal composition, and the mineralogical composition depends on the power station design and the power station operating conditions. Flyash is an aluminosilicate with some Fe and/or Ca oxides, with minor concentrations of Na, Mg, P, S, K, Ti, Sr and Ba. The chemical form of these elements can vary although flyashes normally have quartz and mullite as major crystalline phases, and 40 to 80 wt% amorphous (non-crystalline) phases. The quartz in flyash originates from both the source coal (primary quartz) and that formed during combustion (secondary quartz) (Vassilev and Vassileva, 1996). The mullite forms during combustion by solid state reaction of decomposed clays and/or crystallization of the aluminosilicate melt (Pietersen et al., 1989, Vassilev and Vassileva, 1996). When mullite forms by crystallisation of a melt the Al/Si ratio has a greater variation than when it is formed by a solid state reaction (Li et al., 2004). Flyash is generally regarded as a waste product and as such it is not produced to a particular chemical specification. Flyash has been observed to be heterogeneous and variable (Vassilev and Vassileva, 1996), this is due to the variability of the composition of the incombustibles in coal and variable burn conditions. The variability of the different constituent phases within these flyashes is such that they may not produce geopolymers with the same properties, hence the purpose of this study.

The flyashes chosen for this study are all available in bulk quantities and are widely utilised as supplementary cementitious material (SCM) for Portland and blended cements, and are reported to be suitable to produce geopolymer (Provis et al., 2009, Rangan, 2008, van Jaarsveld et al., 2003). The flyashes were sampled in 4th quarter of 2007 from the Australian power stations in Collie (Western Australia), Port Augusta (South Australia) and Bayswater

(New South Wales). Unfortunately Port Augusta power station is scheduled for closure in 2016/2017 (Alinta Energy, 2015).

Flyash extracted from the electrostatic precipitators (ESP) of Port Augusta's power station has a small particle size that does not need to be further classified. The other flyashes in this study were classified prior to delivery with standard methods (with a cyclone device) to produce fine flyash as defined by Australian Standards (AS 3582.1 - 1998), which is 75 wt% passing <45 μm. The 20 kg samples of flyash supplied were split with multiple rotatory splitting devices to produce representative samples of different quantities, in particular ~3 g samples for all microanalysis (XRD, XRF, various synchrotron studies and electron microscopy), ~100 g for geopolymer paste synthesis and 2.5 kg samples for larger geopolymer sample synthesis. The flyashes used in this thesis are classified as Class F flyash according to ASTM-C618 (ASTM International, 2015), as they have low calcium content. ASTM-C618 defines 3 classes of flyash, N, F and C. The key differences between the classes is the SiO_2+Al_2O_3+Fe_2O_3 content, Class N and F must have > 70 wt% and Class C > 50 wt%, with full chemical requirements provided in Table 3-1.

Table 3-1 Chemical Requirements for the various classes of flyash as per ASTM-C618-15 (ASTM International, 2015).

	Class N	Class F	Class C
SiO_2+Al_2O_3+Fe_2O_3	> 70 wt%	> 70 wt%	> 50 wt%
SO_3	< 4.0 wt%	< 5.0 wt%	< 5.0 wt%
Moisture	< 3.0 wt%	< 3.0 wt%	< 3.0 wt%
Loss on ignition	< 10 wt%	< 10 wt%	< 10 wt%

Further analyses of the flyashes are presented in the results chapters, particularly Chapter 4.

3.1.2. Metakaolin (dehydroxylated kaolinite)

A commercially available kaolinite (Snobrite 65, Unimin) was chosen because of its fine particle size and high phase purity. The kaolinite was dehydroxylated at 750°C for 24 hours producing metakaolin in approximately

2 kg batches. The low level of impurities (Fe and Ti) and low levels of crystalline (quartz and anatase <2 wt%) phases makes the metakaolin ideal for the production of geopolymers.

3.1.3. Silica fume (amorphous silica)

A commercially available silica fume (SF98, Australian Fused Materials) was chosen because it had a fine particle size and high phase purity. The SF98 is produced as a by-product of zirconia production from mineral sands. The presence of low levels of ZrO_2 impurities is not problematic for geopolymer production as it is almost completely liberated from the silica and is inert under high pH conditions.

3.1.4. Sodium hydroxide, silicate and aluminate solutions

All sodium hydroxide used was AR grade pellets from a commercial supplier, either Unilab or Sigma Aldrich. The pellets were dissolved in deionised water to the specified concentration. In a few cases the sodium hydroxide pellets were dissolved in the sodium silicate solution, when no extra water was required.

The sodium silicate solution used was obtained from PQ Australia (Grade D). The sodium aluminate solution used was obtained from Coogee Chemicals.

3.1.5. Borax

The sodium tetraborate decahydrate, 99.5% purity, powder was sourced from Sigma Aldrich.

3.2. METHODS AND MIXING

The sodium hydroxide was combined with the sodium silicate, sodium aluminate or sodium borate solutions and allowed to cool prior to mixing with the flyash, metakaolin and/or silica fume. Silica fume was only used as a solid for alkali activated borosilicate inorganic polymer (AABSIP) samples (Chapter 8). In all other cases the silica fume was pre-dissolved in the alkali solution.

The solid was added to the solution and mixed either in the ARE-250 Planetary orbital mixer (Thinky Corporation, Japan), a Kenwood house-hold mixer or the rotary tool mixer (synchrotron experiment, Chapter 7). The mixing times are specified in each relevant section of the thesis.

After mixing, the samples were poured into polypropylene vials or syringes and cured at 70°C or 75°C for 24 hours. Polypropylene was chosen as it has good dimensional stability and chemical durability at 70°C even for strong caustic solutions.

3.3. GEOPOLYMER FORMULATIONS

The quantity of each feedstock required for a mixture (the formulation) was calculated based on selected elemental ratios Si/*Y*, *Z*/*Y* and H/Si, where *Y* is Al or B and *Z* is Na or K. This approach was used as the properties of geopolymers have been found to vary with Si/Al, Na/Al and the water content (Duxson et al., 2005b, Rowles and O'Connor, 2003).

The physical, chemical and microstructural properties of geopolymer depend significantly on the formulation. A simple geopolymer could be formulated by mixing a fine 'pure' metakaolin, sodium silicate solution, sodium hydroxide pellets and water. The sodium hydroxide is dissolved in the water and then mixed with the sodium silicate solution. This combined solution is then mixed with the metakaolin resulting in a geopolymer. This approach assumes that the entire feedstock is available to react thus formulating a specific composition is relatively simple.

Working with metakaolin and synthetic feedstocks the mix calculations are straight forward, however when industrial waste products and by-products are utilised such as flyash, slag and Bayer liquor the calculation becomes more complicated. Table 3-2 summarises elements that are typically in selected feedstocks. If a geopolymer was to be formulated using the method detailed above with all of these feedstocks at a particular composition the calculation would be rather tedious and complicated. Accordingly, a more efficient approach for formulation development has been designed which is described below.

Table 3-2 Composition of some possible geopolymer feedstocks, the '+' or '-' indicates the feedstock contains a major or minor component of that element, respectively.

	Si	Al	Na	Ca	H
Flyash (FA)	+	+	-	-	
Sodium Aluminate Solution (SAS)		+	+		+
Sodium Silicate Solution (SSS)	+		+		+
Granulated blast furnace slag (Slag)	+	+	-	+	-
NaOH			+		+
Water					+

The proportion of each feedstock required can be calculated with a set of simultaneous equations; enabling a matrix method to be adopted to find the solution to these equations. The simultaneous equations 3.1 to 3.5, calculate the number of moles of each element per unit weight (Si, Al, Na, Ca and H), using the proportion of each $feedstock_{wt}$ and the number of moles per unit weight of each element for each $feedstock_{element}$. These were formulised as equations 3.6 to 3.8 for the 5 elements of interest (Williams and van Riessen, 2010). Where F1 to F5 are feedstocks, Fn_{wt} in vector W is the weight fraction of each feedstock n, and F is a matrix with the number of moles of Si, Al, Na and H per unit weight of each feedstock, and matrix R is a column matrix with the desired elemental concentration, which is expressed as elemental ratio by setting the Al =1, then other elements are expressed as the ratio i.e. R = [Si/Al, Al/Al, Na/Al, Ca/Al, H/Al]. Note: H is used rather than H_2O to be consistent with using elemental ratios. However, it is obvious there are 5 equations and 6 unknowns so two of the feedstocks must be constrained together at a specified ratio.

$$\mathrm{Si} = \mathrm{FA_{wt}FA_{Si}} + \mathrm{SAS_{wt}SAS_{Si}} + \mathrm{SSS_{wt}SSS_{Si}} + \mathrm{SLAG_{wt}SLAG_{Si}} + \mathrm{NaOH_{wt}NaOH_{Si}} + \mathrm{Water_{wt}Water_{Si}} \quad (3.1)$$

$$\mathrm{Al} = \mathrm{FA_{wt}FA_{Al}} + \mathrm{SAS_{wt}SAS_{Al}} + \mathrm{SSS_{wt}SSS_{Al}} + \mathrm{SLAG_{wt}SLAG_{Al}} + \mathrm{NaOH_{wt}NaOH_{Al}} + \mathrm{Water_{wt}Water_{Al}} \quad (3.2)$$

$$\mathrm{Na} = \mathrm{FA_{wt}FA_{Na}} + \mathrm{SAS_{wt}SAS_{Na}} + \mathrm{SSS_{wt}SSS_{Na}} + \mathrm{SLAG_{wt}SLAG_{Na}} + \mathrm{NaOH_{wt}NaOH_{Na}} + \mathrm{Water_{wt}Water_{Na}} \quad (3.3)$$

$$\mathrm{Ca} = \mathrm{FA_{wt}FA_{Ca}} + \mathrm{SAS_{wt}SAS_{Ca}} + \mathrm{SSS_{wt}SSS_{Ca}} + \mathrm{SLAG_{wt}SLAG_{Ca}} + \mathrm{NaOH_{wt}NaOH_{Ca}} + \mathrm{Water_{wt}Water_{Ca}} \quad (3.4)$$

$$\mathrm{H} = \mathrm{FA_{wt}FA_{H}} + \mathrm{SAS_{wt}SAS_{H}} + \mathrm{SSS_{wt}SSS_{H}} + \mathrm{SLAG_{wt}SLAG_{H}} + \mathrm{NaOH_{wt}NaOH_{H}} + \mathrm{Water_{wt}Water_{H}} \quad (3.5)$$

$$\mathrm{W} = \begin{bmatrix} \mathrm{F1_{wt}} \\ \mathrm{F2_{wt}} \\ \mathrm{F3_{wt}} \\ \mathrm{F4_{wt}} \\ \mathrm{F5_{wt}} \end{bmatrix} = \mathrm{F^{-1}} \cdot \mathrm{R} \quad (3.6)$$

$$\mathrm{F} = \begin{bmatrix} \mathrm{F1_{Si}} & \mathrm{F2_{Si}} & \mathrm{F3_{Si}} & \mathrm{F4_{Si}} & \mathrm{F5_{Si}} \\ \mathrm{F1_{Al}} & \mathrm{F2_{Al}} & \mathrm{F3_{Al}} & \mathrm{F4_{Al}} & \mathrm{F5_{Al}} \\ \mathrm{F1_{Na}} & \mathrm{F2_{Na}} & \mathrm{F3_{Na}} & \mathrm{F4_{Na}} & \mathrm{F5_{Na}} \\ \mathrm{F1_{Ca}} & \mathrm{F2_{Ca}} & \mathrm{F3_{Ca}} & \mathrm{F4_{Ca}} & \mathrm{F5_{Ca}} \\ \mathrm{F1_{H}} & \mathrm{F2_{H}} & \mathrm{F3_{H}} & \mathrm{F4_{H}} & \mathrm{F5_{H}} \end{bmatrix} \quad (3.7)$$

$$\mathrm{R} = \begin{bmatrix} \mathrm{Si} \\ \mathrm{Al} \\ \mathrm{Na} \\ \mathrm{Ca} \\ \mathrm{H} \end{bmatrix} \quad (3.8)$$

The calculation to solve the matrix is long but there are many software packages that make this easy, in this case the calculation was completed

symbolically using Maple 11 (Waterloo Maple Inc.). The formula was then converted to Visual Basic for Applications (VBA, Microsoft) code to allow calculation within Microsoft Excel. The solution for the 4 element case can be directly used as a formula in Microsoft Excel 2007, but the solution for the 5 element case is too long for Excel and has to be a VBA calculation.

However to actually make a geopolymer that is workable there are other constraints such as the quantity of solution, pH, solubility and stability of the sodium silicate solution and many others.

Within the thesis there are range of geopolymer compositions used, showing a progression in understanding and adaption to requirements for each study. In chapter 4, geopolymers were synthesised with flyashes from 3 power stations: Collie, Port Augusta and Bayswater. These were produced with a composition similar to typical metakaolin geopolymers, differing by considering bulk and amorphous composition to formulate the geopolymers for each flyash, to show that using the amorphous composition was appropriate for the rest of thesis. In chapter 6, metakaolin geopolymers were synthesised to provide a simpler system to develop the techniques described within the chapter, to be used subsequently in chapter 7. In chapter 5 and 7, a range of compositions were synthesised with Collie flyash to understand the effect of formulation. Due to constraints with experimental beam time, only a subset of samples in chapter 5 were analysed in chapter 7. In Chapter 8, borosilicate geopolymer were synthesised to evaluate a new possible starting material.

3.4. X-RAY POWDER DIFFRACTION

3.4.1. X-ray diffraction / scattering

X-ray diffraction (XRD) is a well-established technique suitable for characterising crystalline materials. Recently XRD has also been applied to poorly ordered and x-ray amorphous systems providing useful atomic and nano-scale information.

3.4.2. X-ray diffraction

The Bragg's equation (Equation 3.9) can be used to describe the diffraction of wave-like radiation from a crystalline material, where λ is the wavelength of the radiation, d is the distance between atomic planes (or d-spacing), and θ is half the scattering angle (Cullity and Weymouth, 1957). Rearranging Bragg's equation (equation 3.10) it is apparent that the distribution of d-spacing can be elucidated with fixed wavelength by scanning the angle (angle dispersive) or with a fixed angle scanning the wavelength (energy dispersive).

$$\lambda = 2d \sin\theta \tag{3.9}$$

$$d = \frac{\lambda}{2 \sin\theta} \tag{3.10}$$

The most common type of diffraction for powders in the laboratory is the angle dispersive, Bragg-Brentano geometry (Figure 3-1). For Bragg-Brentano geometry the divergent "monochromatic" x-ray beam from the x-ray tube is collimated by divergence slits to impinge the sample (at an angle θ) (Cullity and Weymouth, 1957). Diffracted x-rays are collected by the detector which is at the same angle θ relative to the sample surface - hence the scattering angle is 2θ. There are slight variations to this geometry such as the addition of pre or post sample optics to improve the diffraction pattern or the addition of small arrays of detectors i.e. position sensitive detectors which allow collection of the same intensity in a fraction of the time. Due to the Bragg-Brentano geometry, when the sample is sufficiently thick, the information volume is constant at all angles. This condition occurs because both beam foot print and information depths have an inverse relationship resulting in a

constant volume. The result is that the intensity of Bragg peaks at any angle represents the same size volume allowing quantification of phases without volume-angle corrections.

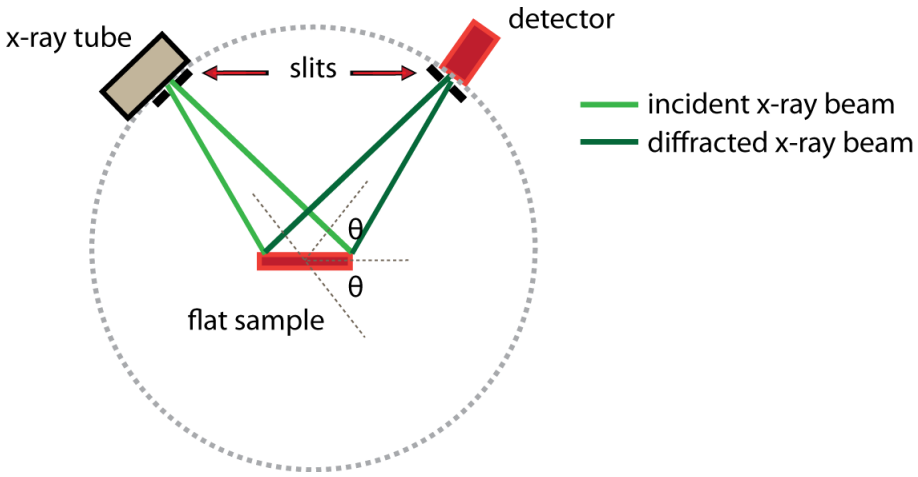

Figure 3-1 Schematic representation of the Bragg-Brentano diffraction geometry. The divergent x-ray beam from x-ray tube, collimated by divergence slits, impinge on the sample at an angle θ, some of the x-rays diffract at an angle θ from the sample. These diffracted x-rays are 'seen' by point on the goniometer radius at an angle 2θ relative to the incident beam.

The more common geometry used at a synchrotron beamline is Debye-Scherrer geometry. This is when a parallel, monochromatic photon beam impinges the sample, either in a capillary or as a thin flat plate. The diffracted photons transmitted through the sample are measured by a detector; there are many options for detectors the key differences being the angular resolution and range they detect; the energy resolution and the dynamic range of the detector. Improved energy resolution of a detector improves the signal to noise ratio, because the useful diffraction data is the energy of the incident x-ray beam - all other energies are 'noise'. Due to inelastic scattering events such as fluorescence and Compton scatter, some of incident x-rays will generate secondary x-rays of a lower energies than the incident x-ray energy. These secondary x-rays are not useful in Bragg scattering, hence are filtered out by using a detector with a good energy resolution.

The x-rays scatter from the electrons in the material, thus scattered intensity increases with atomic number, this allows determination of both structure and

composition of a phase to be determined (Von Dreele and Rodriguez-Carvajal, 2008).

3.4.3. Modelling methods

In order to get the most information out of x-ray diffraction data, including quantitative phase abundance results, a model needs to be refined to fit the data. In an attempt to understand the most appropriate methods to determine the phase composition from the diffraction data the commonly used methods have been summarised in Table 3-3. The main differences between methods is the number of peaks used, the calculation of intensity calibration constants, calculation of peak positions and how they can deal with diffraction peak overlap.

Table 3-3 Commonly used methods to determine the phase composition from x-ray diffraction data. One or more of these methods are often used simultaneously.

Type of model	Intensity calibration	Peak intensities	Peak positions	Other data
Single peaks	Measured compared to a reference	Individual peak intensities	Individual peak positions	
Multiple peaks	Measured compared to a reference	Individual or linked peak intensities	Individual peak positions	
Pawley models	Measured compared to a reference	A phase scale and refinable relative intensities	Lattice parameters	space group
Rietveld models	Crystal structure models	a phase scale, relative intensities constrained by structure factor	Lattice parameters	space group, Atomic position, atomic displacement parameters

The reference-intensity-ratio (RIR) method historically has been widely used. In this method the ratio of intensity of a particular phase and the intensity of a reference phase, often corundum, at the same concentration is used. This method is more commonly used with the background-subtracted integrated area rather than fitting a peak. The integration is used partly because it easier to do so and partly as it remove the systematic uncertainty of incorrectly modelling the peak shape. Careful peak shape modelling does accommodate peak overlap. The RIR values either determined by measuring

a pure sample of a particular phase with a known amount of reference material, or the value is calculated with knowledge of the crystal structure. Researchers commonly use the tabulated values from databases such as the Powder Diffraction File (PDF) from the International Centre for Diffraction Data (ICDD). The area of each peak of interest is simply summed, usually after the subtraction of background. The main issues with these types of methods are the difficulty with dealing with peak overlaps, determination of the background, and the absence of a published RIR values or phase pure samples of each phase present in the analysed sample. This method does have the advantage that no software is required and for some samples very high accuracy and precision can be achieved.

Rietveld based quantitative phase analysis method is a full pattern method, the intensity calibration is calculated based on the crystal structure and allows the intensity of all peaks in the phase to be scaled based on the concentration of the phase. in this situation calibration means calculating the scaling factor between the Bragg peak intensity and the concentration of the phase. The peak positions are refinable lattice parameters, and the peak shapes are modelled for each phase separately. The software packages available for Rietveld analysis differ in features but usually allow other parameters such as atomic displacement parameters, crystallite size and crystallite strain to be refined.

Although the crystal structure of a phase can be refined using data from a composite sample that is also used for quantitative phase analysis it is not ideal, usually a phase pure sample or almost pure sample with a contaminant of known crystal structure is required to allow a ‘good quality’ structure to be refined (Scarlett and Madsen, 2006).

With these methods there is choice of adding an internal standard (also referred to a spike), this allows the phase concentration to be calculated on an absolute scale, rather than a relative scale. This is an important point, as determination of the concentration of crystalline phases on an absolute scale allows the calculation of non-crystalline remainder (i.e. the amorphous fraction).

3.4.4. Curtin x-ray laboratory – D8 Advance

Laboratory based x-ray diffraction patterns were collected with a D8 Advance diffractometer (Bruker-AXS) using copper radiation and a LynxEye position sensitive detector. The collection conditions are specified in each chapter.

The data from the D8 Advance diffractometer can be readily modelled using TOPAS v4.2 (Bruker AXS, 2008) using the Fundamental Parameters convolution approach (Cheary and Coelho, 1992, Cheary et al., 2004). The typical fundamental parameters specified in TOPAS 4.2 are shown in Table 3-4. This approach allows you to model the instrumental peak shapes based on the aperture sizes used at the time of data collection.

Table 3-4 The fundamental parameters describing the default settings of the D8 advance at Curtin.

Parameter	Value
Goniometer radii	
Primary radius (mm)	250
Secondary radius (mm)	250
Equatorial Convolutions	
Linear PSD Settings	
2Th angular range of LPSD (°)	3
FDS angle (°)	0.3
Beam spill, sample length (mm)	20
Axial Convolutions	
Full Axial Model	
Source length (mm)	12
Sample length (mm)	25
Receive slit length (mm)	17
Primary Soller (°)	2.5
Secondary Soller (°)	2.5

X-rays produced from an x-ray tube are not monochromatic; there is a broad energy spectrum extending up to the tube accelerating potential (i.e. 40 kV) called Bremsstrahlung radiation. Superimposed on the Bremsstrahlung are intense peaks from the characteristic x-rays of the target material. In the case of Cu the significant energies are the Kα and Kβ emission lines at 8.04 and 8.9 keV, respectively. The Lynxeye position sensitive detector has ~20% energy resolution, so when it is set to measure 8.04 keV it will measure x-ray energies approximately from 6.4 to 9.6 keV. Thus most of the x-rays from the tube spectrum will not be measured although both the Kα and Kβ x-rays will be measured. A 0.5 mm thick Ni filter is used to selectively attenuate the Cu Kβ compared to the Cu Kα. The resulting energy spectrum that the detector measures is mostly Cu Kα1, Cu Kα2 and a small quantity of Cu Kβ and a

step change in intensity caused by the Ni absorption edge. Table 3-5 lists the emission profile that was used in TOPAS. The Kα:Kβ ratio was refined using a standard silicon sample (NIST SRM 640). Inspection of one of the Bragg peaks of silicon shows the impact of these wavelength artefacts, Figure 3-2.

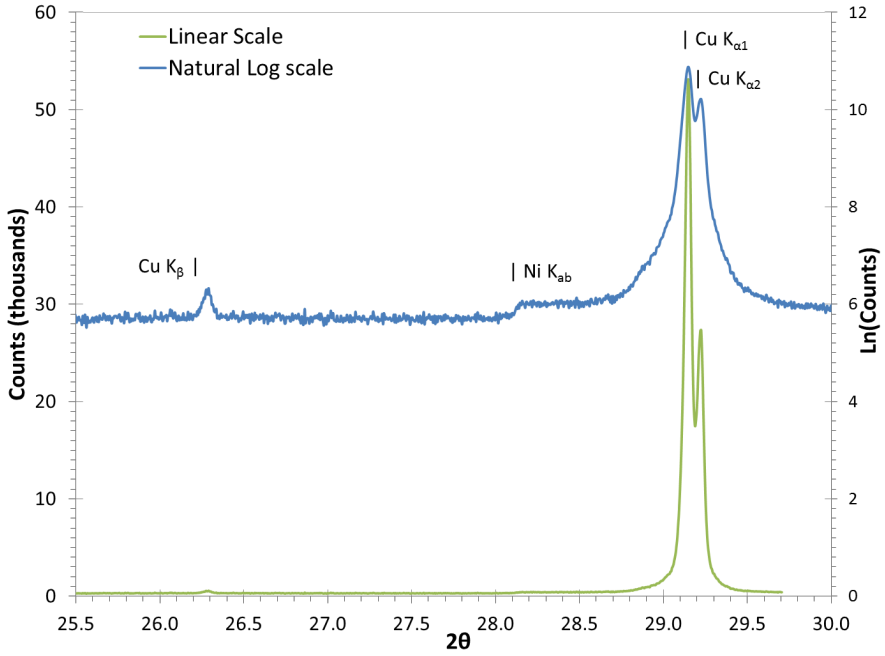

Figure 3-2 The diffraction profile from one Bragg reflection (i.e. 1 d-spacing), the distribution of wavelengths results in several measured peaks. N.B. The same data is displayed twice on different scales-linear scale = green and log scale = blue.

Table 3-5 The ratio of Cu K_α and Kβ was refined using NIST SRM 1976 resulting in the following instrument emission profile (wavelength spectrum).

Area (arb. Units)	WL (Å)	Lorentzian Half width (mÅ)
0.0159	1.534753	3.6854
0.5691	1.540596	0.437
0.0762	1.541058	0.6
0.2517	1.544410	0.52
0.0871	1.544721	0.62
0.00162349	1.392216	0.5502872
0.0008301554	1.392595	0.5505868
0.000368214	1.391758	0.5546122
0.0003347409	1.393491	1.265473
0.0003347409	1.391300	0.8290293

In addition to diffraction some of the x-rays impinging on the sample will produce fluorescent x-rays via the photoelectric effect. The photoelectric effect is when x-rays interact with bound electrons, exciting these electrons to a higher energy level. The atom relaxes and when an electron falls back to the ground state an x-ray is released with an energy that is equal to the energy difference between the excited level and relaxed state, this x-ray energy is unique and characteristic to the element. The laboratory x-ray beam will interact with all elements in the sample by the photoelectric effect to some extent. However, the elements of particular concern are those with characteristic x-rays of similar energy to that of copper (Kα = 8.04 keV) as these x-rays will be measured as signal by the detector, resulting in an isotropic increase in the measured background. Iron is of particular concern, with its characteristic x-ray energy of 6.4 keV (Fe Kα), 20% lower energy than Cu Kα. For samples with an iron content of >3 wt% (e.g. Fe_2O_3) tighter detector discriminator settings were used, reducing the x-ray energy range that the detector measured, so as to reduce the Fe Kα x-rays measured. The usual measured range is 0.11 V to 0.25 V, whereas the tighter settings are 0.18 V to 0.23 V. The tighter settings result in a significant reduction in the background and thus an improved signal-to-noise ratio for samples with an elevated Fe content, see Figure 3-3.

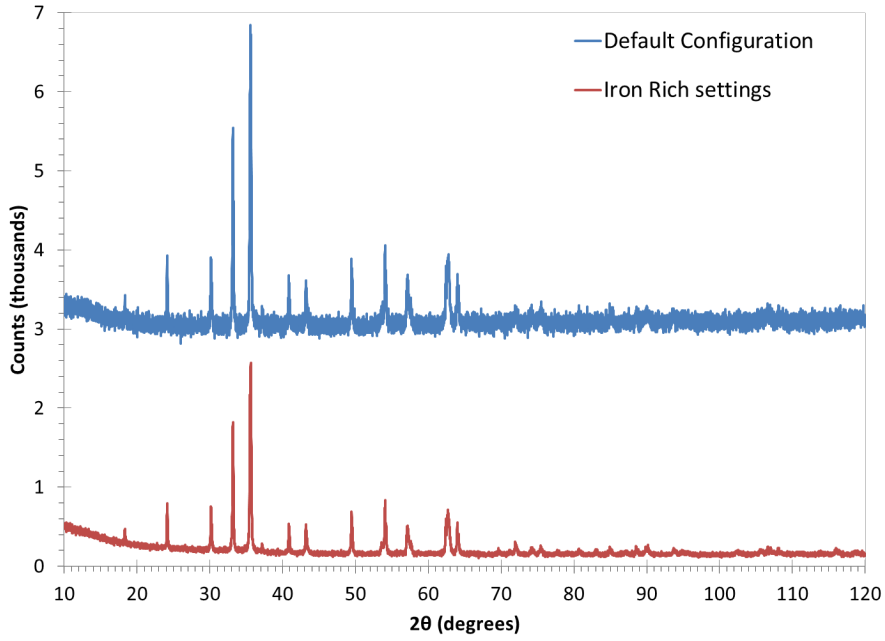

Figure 3-3 Measured diffraction patterns from a 50% Hematite (Fe_2O_3) + 50% Magnetite (Fe_3O_4) sample using the default detector discriminator settings and the tighter settings. The patterns are NOT offset, showing that the background measured with the default settings is much higher, resulting in poor signal-to-noise relative to the pattern measured with tighter discriminator settings.

When using the LynxEye detector, at angles below about 7° 2θ, the contribution from air scatter is very significant. An anti-scatter knife edge slit can be fitted to reduce the air scatter, Figure 3-5. This expands the useable lower angle from about 5 – 6° to 3 – 4° 2θ. For example Figure 3-4, shows the diffraction pattern of a bentonite ($Na_{0.2}Ca_{0.1}Al_2Si4O_{10}(OH)_2(H_2O)_{10}$) clay sample measured with and without the knife-edge collimator installed. It is clear that the knife-edge collimator results in a significant reduction in measured air-scatter (noise) at 2θ below approximately 5° 2θ improving the signal to noise ratio for the Bragg peak at 5.7° 2θ. The knife-edge collimator is highly effective at reducing the air-scatter at low angles and was found to be insensitive to poor alignment at low angles. The major disadvantage of using the knife edge collimator is that it must be removed to measure 2θ above 100° 2θ without very careful alignment, as it can block the scattered beam.

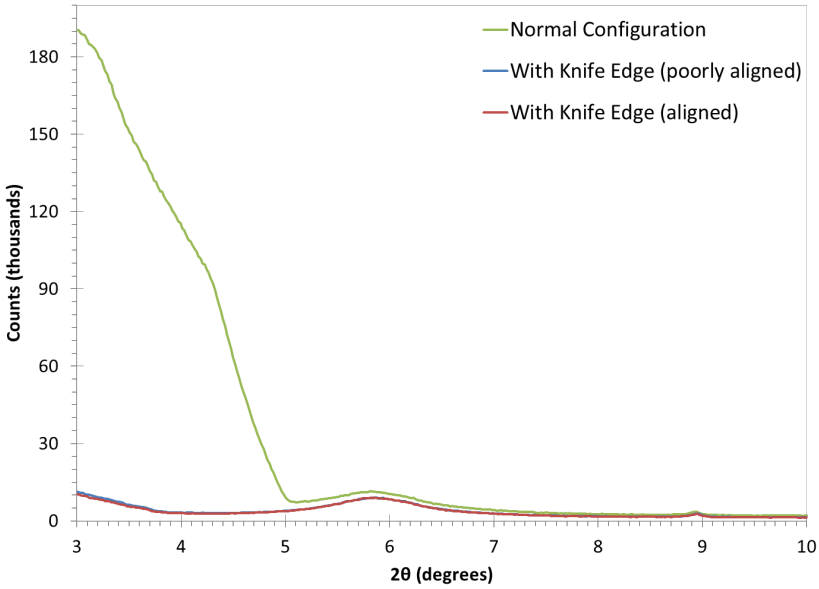

Figure 3-4 The diffraction pattern of a bentonite ($Na_{0.2}Ca_{0.1}Al_2Si4O_{10}(OH)_2(H_2O)_{10}$) sample measured with and without the knife-edge collimator installed. Additionally the sample was measured with the knife-edge poorly installed to qualitatively assess the sensitivity of the alignment. Note the significant reduction in measured air-scatter (noise) at 2θ below approximately 7° 2θ, which improves the signal to noise ratio for the Bragg peak at 5.7° 2θ.

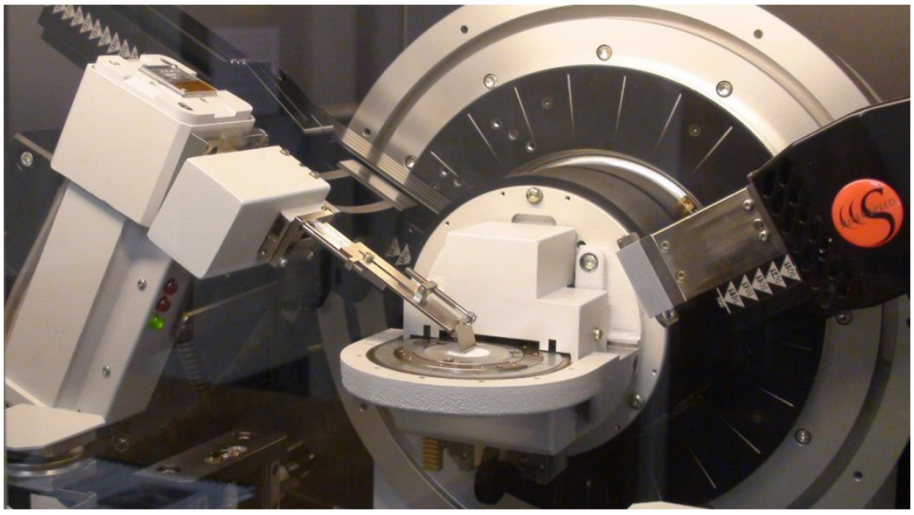

Figure 3-5 Photograph the Knife Edge Collimator installed on the D8 Advance at Curtin University.

3.4.5. Australian Synchrotron – powder diffraction beamline.

The diffraction data for the quantitative phase analysis in Chapter 4 were collected at the Powder Diffraction (PD) beamline (BL4) at the Australian

Synchrotron. A MYTHEN detector system (**m**icrostrip s**y**stem for **t**ime r**e**solved experime**n**ts) was used. The MYTHEN detector system at the PD beamline consists of 16 detectors, each covering approximately 4.8° 2θ with approximately 0.2° 2θ gap between modules. The experimental setup (Chapter 4) on the PD beamline results in each pixel covering approximately 0.00375° (2θ) resulting in a total collection angle of ~80°. To overcome the gap between modules the diffraction pattern is collected as two or more histograms, the second histogram is collected after moving the detector an arbitrary angle x, such that 0.2°<x<4.8°. There is also a very minor artefact in the data which manifests itself as a slight increase in signal in the first and last few pixel of the each module (Figure 3-7).

This detector system is primarily designed, as it name suggests, for time resolved experiments. Due to its design the resolution and instrumental signal to noise ratio is rather poor compared to more traditional single or double monochromator detector systems, with well-defined detector slits. The benefit of this detector system is excellent counting statistics due to the parallel angular collection, which results in typical acquisition times of between 2 and 1800 seconds, depending on the application.

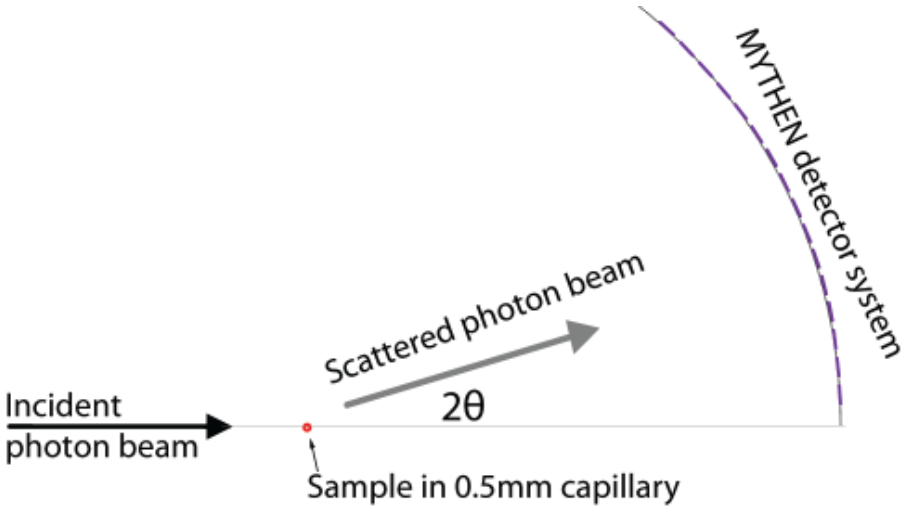

Figure 3-6 A schematic of the MYTHEN detector system showing the 16 MYTHEN detector modules in a linear array collecting approximately 80° 2θ with 0.2° 2θ gaps between modules.

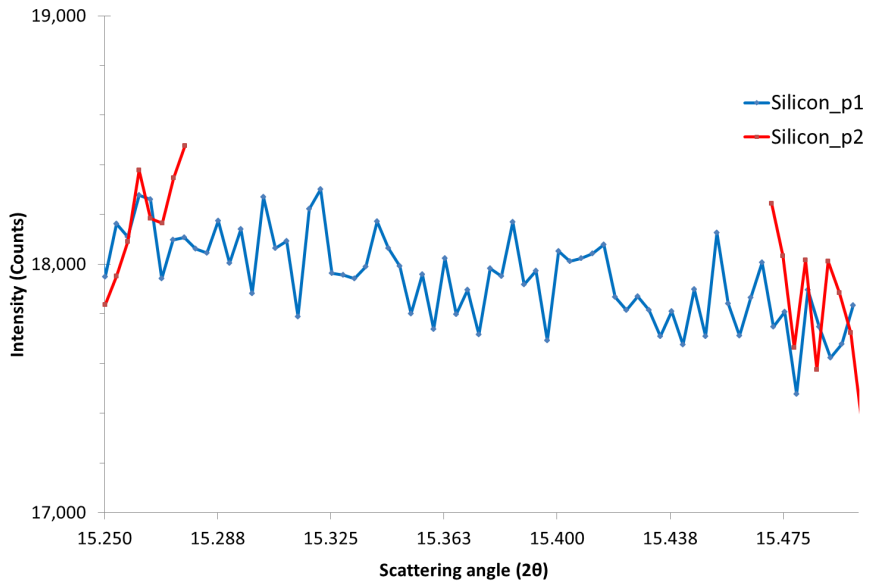

Figure 3-7 Powder diffraction data of a small region showing the gap in the second pattern (silicon_p2). The sample is NIST SRM 640, there is no Bragg peak near this angle. Note the increase in the signal close to the edges of gap in the data.

3.4.6. Data processing – PD beamline

Initially flood fill and angular corrections/calibrations are applied to the data at the beamline, producing data files for each of the histograms. These data files (.xy) are whitespace (one space) delimited ASCII text files, i.e. they can be opened directly in Notepad or Excel. More specifically, there is no header, with angle in the first column and counts in the second column, with the angle being recorded as a floating point number (with 6 decimal point precision, unknown accuracy) and counts as an integer. Due to the nature of the angular calibration the step size is irregular (~0.00375°).

A small application was written using IDL Workbench (ITT Visual Information Solutions) to align the histograms and join the data. It is has been named the **MY**THEN detector system **h**istogram **s**plice **t**ool (MyHST). The data was joined by filling the gaps (plus a little overlap) in the first histogram from the second histogram, cut and paste style, see Appendix 1 for more details.

More specifically, initially the data is linearly interpolated onto a common grid with constant step size of 0.00375°2θ. The cross-correlation product is then calculated for a 'lag' of -50 to +50 pixels (i.e. a relative zero error of

±0.1875°), the position of the maximum value for this function represents the relative zero-offset between histograms for which there is maximum cross correlation. The maximum value is determined by fitting a Gaussian to the cross correlation product as a function of pixel 'lag', this allows a relative zero error to be determined with better than a pixel precision. This calculated relative zero offset is applied to the raw data of the second histogram which is then interpolated again on the same constant step size grid as histogram 1. The gaps (plus overlap of 0.05°) are filled with data from histogram 2. The data is then saved in an ASCII xy text file that can be opened directly in TOPAS-4.2 or converted to another format.

3.4.7. Australian Synchrotron – SAXS/WAXS beamline

The insitu experiment (Chapter 7) was conducted on the SAXS/WAXS beamline (BL4) at the Australian Synchrotron. A 20.000 keV photon beam was focused to a ~100 μm square spot. A MAR-165 camera was used to measure the 2D diffraction patterns at a camera length of approximately 235 mm. The camera was placed such that the beam centre was near the edge of the detector to maximise the angular range in one direction (Figure 3-8). Using these conditions the measured q-range was approximately 0.2 to 4.5 $Å^{-1}$ which is equivalent to measuring from 3 to 55° 2θ using copper Kα radiation. A 35 position capillary sample holder, with water-bath heating, was used to hold the samples at 70° C. The diffraction patterns of approximately 6 samples were collected sequentially; this was repeated for ~21 hours, such that the time resolution was ~ 3 minutes, resulting in ~500 patterns for each sample.

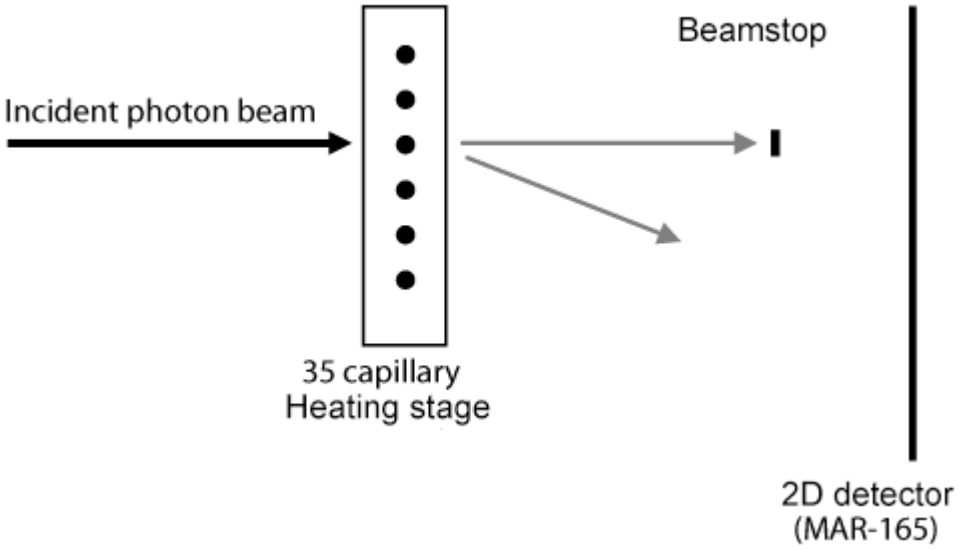

Figure 3-8 Experimental geometry for the in situ geopolymerisation experiment. Nominally 6 geopolymer samples in 1.5 mm PEEK tubes were held in the 35 capillary heating stage.

The sample capillaries for this experiment needed to be resistant to strong sodium hydroxide solution at 70°C for 24 hours and be available as thin tubing, with an appropriate wall thickness as to allow good x-ray transmission. Polyetheretherketone (PEEK) was the logical choice as it is highly resistant to hot caustic solutions (NetMotion Inc. , 2003), has a low average atomic number and is available in a 1.59 mm diameter capillary with 0.01 mm wall thickness (SUPERLCO Analytical, USA). This tubing was pressure rated to 1000 psi, hence should not deform appreciably during the experiment.

3.4.8. Data processing – WAXS data

The camera length and camera tilt was refined using a LaB_6 (NIST SRM 660b) standard and calibration with beamline software 15-ID SAXS/WAXS ver3.299. The sample datasets were radially averaged to produce a 1D diffraction pattern. The intensity and error were the average and standard deviation of each radial sector. The patterns were normalised to the incident beam intensity; corrected for the transmission factor of each sample and the PEEK capillary 'blank' was subtracted. All the ~500 diffraction patterns were

exported as an ASCII file in the format of 1 column of 2θ's, ~500 columns of intensity and ~500 columns of error in intensity. A visual basic for applications (VBA) script was used to convert this to ASCII *.xy and *.xye data files.

3.4.9. Data conversion from ASCII xy to RAW for search/match

The ASCII xy files were converted to the 'Diffrac AT raw version 1' file-format using FileExchange v.1.2.28 (Bruker-AXS). The wavelength determined by relevant standards was embedded into the files to facilitate phase identification using EVA (Bruker-AXS).

3.4.10. Diffraction modelling

All diffraction modelling in this thesis was conducted with TOPAS v4.2 (Bruker-AXS). TOPAS v4.2 is very versatile and allows the modelling of an unlimited number of single peaks, Pawley method phases and/or Rietveld method phases. For example, for a particular sample phase 1 could be modelled with a Rietveld method phase, phase 2 with a Pawley method phase and the amorphous 'hump' could be modelled by one or more single peaks. Details of these refinement types are listed in Table 3-6. All of these objects can be calibrated for quantitative phase analysis. The calibration constant for Rietveld method phases are automatically calculated based on the specified atoms and unit cell volume (i.e. average atomic mass of the unit cell (Z), mass of the unit cell (M), and volume of the unit cell(V)) (Scarlett and Madsen, 2006).

Table 3-6 The utilised objects modelled using TOPAS v4.2. Any number of these objects can be used to model the diffraction data.

Object	Refinable parameters	Peak shape parameters
Single Peak	Position and shape	1 of 5 peak shape types
Pawley method Phase	Lattice parameters, intensity of each reflection and peak profile parameters	1 of 4 peak profile types
Rietveld method Phase	Lattice parameters, scale factor, peak profile parameters, atomic positions etc.	1 of 4 peak profile types

3.5. SCANNING ELECTRON MICROSCOPY

Scanning Electron Microscopy is a widely used technique where a focused electron beam is rastered across the surface of a sample and a subsequent signal is collected by one or more detectors. The contrast mechanism depends on the detector in use, the most common detectors collect signals from secondary electrons (<50 eV), backscattered electrons (~primary electron beam energy) and characteristic x-rays.

3.5.1. Contrast mechanisms

An Everhart-Thornley detector is used to collect secondary electrons that have escaped from the surface of the sample. As secondary electrons can only escape from approximately 5 nm below the surface (Wells, 1974) using this type of detector results in a contrast mechanism dominated by surface morphology and the work function of the material. However, samples are usually coated with a conductive coating with a high work function, such as gold, so the surface morphology is the dominate contrast mechanism.

All the SEM instruments at Curtin University are also equipped with 4 quadrant backscattered electron detectors. Backscattered electrons are elastically scattered electrons; the contrast mechanism is the product of atomic number and density. Increased atomic number and density results in increased elastic scattering thus increased signal (Wells, 1974).

3.5.2. Energy Dispersive x-ray Spectroscopy (EDS)

Energy dispersive x-ray spectroscopy (EDS) on the SEM can be used to analyse the elemental composition of a selected area or used to create a spatial map showing the elemental distribution in a given region. The area selected can be a point, a series of points on a line or a rectangular region of interest. The EDS method can be used to identify elements $Z \geq 6$ (carbon); and with careful sample preparation and calibration can quantify elements with $Z \geq 11$ (sodium). The characteristic x-rays of elements lighter than sodium have energies < 1 keV and as such have a high probability of self-absorption. Wavelength dispersive spectroscopy attachments can be used to

quantify elements as light as B, with careful sample preparation and calibration.

Details of the energy dispersive spectroscopy (EDS) spectra are provided in each chapter. The major instrument parameters to consider for EDS analysis are the accelerating voltage, electron spot size and beam current. Changing the electron accelerating voltage (V_{acc}) has two significant effects: decreases in V_{acc} result in decreased information volume from EDS and a reduced ionisation cross section resulting in lower photon emissions. The optimum V_{acc} (assuming constant number of electrons) for each element can be estimated as the relevant absorption edge (keV) multiplied by e^1 (~2.71), the ratio of the electron energy and the absorption edge energy is termed the overvoltage ratio. Choice of overvoltage is important but must be increased for SEM's with a tungsten filament as the electron flux decreases significantly with decreasing V_{acc} due to lower gun brightness. CASINO v2.42 (Drouin et al., 2007) was used to simulate the information volume for two geopolymer samples (Table 3-7). The information depth is the depth for which contributes 99% of the measured signal for each element, it takes into account electron and x-ray scattering within the material. For the case of flyash based geopolymers where there is a significant content of unreacted material the information volume must be minimised hence a V_{acc} = 7 kV was chosen to provide a small information volume while still allowing the measurement of all elements of interest.

Table 3-7 The 99% information depth unit of µm, calculated with CASINO v2.42 for a typical geopolymer matrix ($Na_{1.25}Al_{0.9}Si_{2.05}H_{9.6}O_{10.8}$). Information depth is the depth that 99% of elemental information can originates, it accounts for electron and x-ray scattering.

V_{acc} (kV)	Depth (µm)
5	0.25
7	0.5
8	0.6
10	0.9
15	2.0
20	3.5

Increasing the spot size or aperture size increases the number electrons interacting with the specimen resulting in more signal to all detectors but

increases the physical size of the electron beam on the sample which often reduces the spatial resolution. However, the best resolution from EDS is governed by the information volume which is larger than typical sizes of the electron beam, hence the spot size can be increased without sacrificing the spatial resolution of EDS mapping.

For both the Si(Li) and SDD EDS detectors it is desirable to detect as many x-rays as possible before significant non-linear processing effects occur. The major non-linear effect is dead-time; this is the short time after measuring an x-ray that the detector is not able to measure another x-ray. Thus if the photon flux on the detector is too high the measured count rate will not be proportional to the x-ray flux, this can be corrected for as long as the total dead time is not too large. The dead-time was kept below 5% for EDS spectra and 15% for EDS mapping.

3.5.3. Simulation methods

The information volume can be readily simulated for backscattered electrons and characteristic x-rays (i.e. EDS) using the software CASINO v2.42 (Drouin et al., 2007). CASINO is a Monte Carlo based simulator which uses relevant physical models. The resulting electron and/or x-ray distributions can be analysed in a spread sheet tool to extract data such as the information volume.

3.5.4. Scanning electron microscopy analysis

Analyses were carried out on several different scanning electron microscopes (SEM), depending on the time and the purpose of the study. The SEM's are summarised in Table 3-8. The XL30 SEM was used prior to the EVO instrument installation; at this time the XL30's Si(Li) detector system was moved to the EVO, after this change the XL30 was not used again. The Neon was used for high resolution imaging and high spatial resolution EDS.

Table 3-8 Summary of the scanning electron microscopes used in this study. ET = Everhart-Thornley Detector (secondary electrons); 4QBSD = 4 quadrant backscattered electron detector ; InLens = In lens secondary electron detector; ESB = Energy Selective backscattered; and SDD = Silicon Drift Detector.

Manufacturer	Model	Electron source	Detectors used	EDS system
Zeiss	EVO 40XVP	tungsten filament	ET, 4QBSD	Si(Li)
Zeiss	Neon 40EsB	field emission gun	ET, 4QBSD, InLens, ESB	SDD
Philips	XL30	tungsten filament	ET, 4QBSD	Si(Li)

3.5.5. Imaging

Imaging conditions for micrographs are detailed in each chapter. Generally imaging was carried out with the Everhart-Thornley and 4QBSD detectors, producing micrographs for which the contrast mechanism was the topography and elemental number/density, respectively.

3.6. X-RAY FLUORESCENCE

The XRF and Loss on Ignition (LOI) were determined by a commercial laboratory (Ultratrace Geoanalytical Laboratories, Canning Vale, WA, Australia), using 12:22 fusion beads, calibrated with relevant certified standards. Quoted uncertainties were estimated by the difference between measured certified standards and the relevant certified values. After analysis the beads were returned and checked for undissolved particles via optical microscopy. Loss on Ignition (LOI) was determined between 105° and 1000°C for 60 ± 5 minutes, with results being reported on a dry weight basis.

3.7. COMPRESSIVE STRENGTH TESTING

The compressive strength results in this thesis are unconstrained compressive strength of cylinders. The maximum strength of samples is not intrinsic to an ideal sample as the maximum stress measured depends strongly on the strain rate (Harsh et al., 1990), and hence consistent experimental conditions are imperative. If the condition of the sample deviates from ideal, i.e. flat and perpendicular faces, diameter to height ratio of 2, free from cracks and large air bubbles, the compressive strength will be lower than expected.

The unconfined compressive strength was determined using a Lloyds EZ50 Universal Tester (Lloyd UK), using a 0.5% grade 50 kN load cell and 150 mm diameter compression platens. For samples described in Chapter 4 a preload of 50 N was applied followed by an extension rate of 5 mm/min. For samples tested and described in all other Chapters a preload of 50 N was applied followed by a constant stress rate of 0.25 MPa/s. The Young's modulus was taken as the gradient of the elastic portion of the stress-strain curve. The force measured by the load cell was calibrated in the factory and the measurements were conducted within the certified period (2 years). The machine extension values were cross-checked by measuring the height of brass cylinders with the instrument compared with Vernier callipers. The Young's Modulus measured platen displacement, like used in this thesis, produces values approximately an order of magnitude less than using the ultrasound methods (Vickers, 2015). However, the values of Young's Modulus are consistent and repeatable within this laboratory, as measured by repeat measurement 'standard' geopolymer samples within a measurement session and across several years.

CHAPTER 4: DETERMINATION OF THE REACTIVE COMPONENT OF FLYASHES FOR GEOPOLYMER PRODUCTION USING XRF AND XRD

This chapter is a typescript version of a published article:

Williams, R. P. and A. van Riessen (2010). "Determination of the reactive component of flyashes for geopolymer production using XRF and XRD." Fuel **89**: 3683-3692 DOI: 10.1016/j.fuel.2010.07.031.

4.1. ABSTRACT

This study investigated methods for determining the formulation for manufacturing geopolymers made with flyash from coal-fired power stations. The accepted method of determining the formulation of geopolymers to get the desired matrix chemistry uses the bulk composition of the feedstock materials. This formulation method is widely used in investigations using feedstock materials that almost completely react during processing. It is widely considered that amorphous components of flyash are the reactive components in the geopolymerisation reaction. However, quantification of the amorphous components is challenging and generally avoided with the concomitant problem that the formulation is far from optimum. For the work presented here, the composition of the amorphous part is determined accurately and this information utilised to synthesise geopolymers. The bulk composition is first determined using x-ray fluorescence spectroscopy (XRF) and then the amorphous composition determined using XRF and quantitative phase analysis (QPA) of x-ray diffraction (XRD) data. Formulating the mixture based on amorphous composition produced samples with a significantly higher compressive strength than those formulated using the bulk composition. Using the amorphous composition of flyash produced geopolymers with similar physical properties to that of metakaolin geopolymers with the same targeted composition. We demonstrated a new quantitative formulation method that is superior to the more commonly used methods.

4.2. INTRODUCTION

Empirical formulation of geopolymers made with dehydroxylated kaolinite (metakaolin) have been investigated by many researchers (Barbosa et al., 2000, Davidovits, 1987, Duxson et al., 2005b, Latella et al., 2008, Rowles and O'Connor, 2003, Steveson and Sagoe-Crentsil, 2005a, Subaer et al., 2002). The physical properties of the geopolymers depend primarily on the ratio of Si/Al, Na/Al and the water content (Duxson et al., 2005b, Rowles and O'Connor, 2003). Often these ratios are investigated indirectly for example, by varying the activation solution to solids ratio. However, even for metakaolin studies the bulk composition does not correlate to the micro chemistry of the geopolymer matrix (Rowles and O'Connor, 2009); an outcome of incomplete dissolution of Al and Si from metakaolin. The metakaolin geopolymer formulations optimised for maximum compressive strength is achieved when the nominal composition of Si/Al = 1.8 to 2.2 and Na/Al = 0.9 to 1.2 (Duxson et al., 2007a, Rowles and O'Connor, 2003, Steveson and Sagoe-Crentsil, 2005a).

Currently, the bulk composition of flyash is widely used to formulate the mixture of flyash based geopolymers. The properties of geopolymers can be varied by altering the Si/Al, Na/Al ratios and water content (Skvara et al., 2005). Many researchers also vary the ‘activating solution’ (Fernández-Jiménez and Palomo, 2005, Keyte, 2008, Steveson and Sagoe-Crentsil, 2005b) which directly alters the mixture composition. These studies have shown that for different flyashes, there is a disparity between the bulk ratios that achieve the maximum compressive strength. Despite this many studies have produced high quality flyash geopolymers pastes, mortars and concrete. The formulation method as it stands is not robust and corrections for changes in flyash bulk composition are usually not successful in maintaining the geopolymer properties. Factors that affect the flyash reactivity are changes in combustion conditions, classification settings, coal composition and transport treatment (i.e. wet or dry).

Modelling of data from Pietersen et al. (1989) showed that the dissolution of flyash is dependent on the amorphous content at very high liquid to solid ratio

(1000:1 by weight) in a strong sodium hydroxide solution (Brouwers and Van Eijk, 2002). Pietersen et al. concluded glass chemistry had little effect on the reactivity and that the dissolution rate of Al, Si and K was almost congruent. However, Brouwers and van Eijk demonstrated that the shrinking core model could be used to describe Pietersen et al.'s system and in fact the dissolution of the outer hull (of flyash spheres) is less reactive than the inner region due to different chemical composition (Brouwers and Van Eijk, 2002). With this in mind, it should be noted that dissolution of classified flyash at a lower liquid to solid ratio (50:1) did not reveal a more reactive inner hull (Chen-Tan et al., 2009). Geopolymer systems have much lower liquid to solid ratio and dissolution of flyash in these conditions has been shown to be incongruent, with amorphous alumina being more soluble than amorphous silica (Sindhunata et al., 2006) in specific cases. This is in contrast to geopolymer synthesised with large grain metakaolin, where the alumina was consistently less soluble than the silica (Rowles and O'Connor, 2009); when $Na/Al \geq 0.8$.

Given the flyash dissolution results (Brouwers and Van Eijk, 2002, Pietersen et al., 1989) and the flyash geopolymer microchemistry data (Sindhunata et al., 2006) it is reasonable to assume the amorphous aluminosilicate component of flyash is the reactive component. The assumption that the amorphous alumina and silica can be used for geopolymer mix design has been sporadically practiced in the literature, however usually with only one flyash and very little attention is focused on the method (Chen-Tan et al., 2009, Sindhunata et al., 2006). The microchemistry of strength optimised flyash geopolymers has previously been shown to have Si/Al and Na/Al ratio similar to that of metakaolin systems (Fernández-Jiménez and Palomo, 2005).

4.3. MATERIALS AND METHODS

The flyashes chosen for this study are all available in bulk quantities and are widely utilised as supplementary cementitious material (SCM) for Portland and blended cements, and are reported to be suitable to produce geopolymer (Provis et al., 2009, Rangan, 2008, van Jaarsveld et al., 2003). The flyashes were sampled in 4th quarter 2007 from the Australian power stations in Collie (Western Australia), Port Augusta (South Australia) and Bayswater (New South Wales).

Flyash extracted from the electrostatic precipitators (ESP) of Port Augusta's power station has a small particle size that does not need to be further classified. The other flyashes in this study were classified prior to delivery with standard methods (with a cyclone device) to produce fine flyash as defined by Australian Standards (AS 3582.1 - 1998), which is 75 wt% passing <45 μm. The 20 kg samples of flyash supplied were split with multiple rotary splitting devices to produce representative samples of different quantities, in particular ~3 g samples for all microanalysis (XRD, XRF, various synchrotron studies and electron microscopy), and ~100 g for geopolymer synthesis.

4.3.1. Determination of bulk composition

The bulk compositions of the flyashes was measured by XRF and Loss on Ignition (LOI), which was determined by a commercial laboratory (Ultratrace Geoanalytical Laboratories, Canning Vale, WA, Australia), using 12:22 fusion beads, calibrated with relevant certified standards. Quoted uncertainties were estimated by the difference between measured certified standards and the relevant certified values. Loss on Ignition (LOI) has been determined between 105° and 1000°C for 60 ± 5 minutes, with results being reported on a dry basis.

4.3.2. Determination of the crystalline composition

***Quantitative phase analysis sample preparation*.** The flyash samples for XRD were prepared by mixing a nominally dry weight of 3.0000 g of flyash with 0.3333 g of Fluorite (CaF_2, Sigma-Aldrich >99.5%, powder ~325 mesh) as an internal standard. By using an internal standard the concentration of the crystalline phases can be determined on an absolute basis enabling the amorphous fraction to also be determined. This powder was then added to a McCrone micronising canister with 7 mL of laboratory grade ethanol and sintered alumina milling media and milled for 5.0 minutes. The suspension was then poured into a polypropylene dish and dried at 105°C for 24 hours. The dried powder was then brushed into a polypropylene vial, and sealed until analysis.

Synchrotron powder diffraction samples were loaded into 0.5 mm diameter borosilicate capillaries (GLAS, Schönwalde, Germany). The samples were loaded by placing a small quantity of sample in the opening of the capillary and vibrating the capillary with a soft brush on a rotary tool. The capillaries were then sealed with a butane microtorch.

Synchrotron based powder diffraction. The Powder Diffraction beamline 10-BM-1 at the Australian Synchrotron was used to collect the diffraction patterns of each flyash sample. A double crystal monochromator was used to select the wavelength of 0.100073 nm, determined accurately by a Pawley Refinement of NIST SRM 660a (LaB_6) data. The beam was collimated to 7 mm width and 1 mm height. A MYTHEN detector system was used to collect patterns from 10° to 90° 2θ. This detector system consists of 16 position sensitive detectors arranged such that there is a small gap between detector modules of 0.2°. To collect the data for these gaps the pattern was collected for 5.0 minutes and then the detector bank was moved 0.5 degrees and the pattern measured for an additional 5.0 minutes. The script that was developed to splice the datasets is described elsewhere (Williams and van Riessen, 2008) and appendix A.

Selection of internal standards and micro-absorption considerations. The selection of the internal standard for quantitative x-ray diffraction of flyashes is not trivial due to the Bragg peak overlaps and micro-absorption issues. Many internal standards were considered; the phases given the most consideration were corundum (Al_2O_3), zincite (ZnO), anatase (TiO_2), rutile (TiO_2), ilmenite ($FeTiO_3$), fluorite (CaF_2) and diamond (C). The corundum, anatase, rutile and ilmenite were ruled out as it was conceivable these phases could be present in the flyash in trace quantities below the level of detection of preliminary laboratory XRD analysis.

Excessive micro-absorption differences result in biased quantitative phase abundances; this increases the measured abundances of strong absorbers and decreases the measured abundances for weak absorbers (Madsen and Scarlett, 2008). The degree of micro-absorption is related to the product of the mass attenuation coefficient, density and the particle diameter. The flyashes have quartz, mullite and assorted iron oxides encapsulated in solid amorphous spheres, so the concept of particles in the sense of Brindley corrections is invalid (Brindley, 1945). This does not mean micro-absorption is not a problem, quite the contrary, particularly if using Cu Kα where there is a major mismatch in mass attenuation coefficient between the aluminosilicates and the iron oxides. Figure 4-1 shows the mass attenuation coefficient as a function of energy calculated using TOPAS version 4.2 (Bruker-AXS). This shows that for a wavelength of 0.100 nm (12.40 keV) fluorite (CaF_2) and rutile (TiO_2) are suitable because they result in the smallest difference in mass attenuation coefficients. The most accurate quantitative phase analysis (QPA) results will be obtained if the attenuation contrast between all phases is minimised, however as there was a possibility that rutile was present in the samples, it was excluded as an internal standard leaving fluorite as the only option. Rutile was found to be present in NIST SRM 1633b and Port Augusta flyashes.

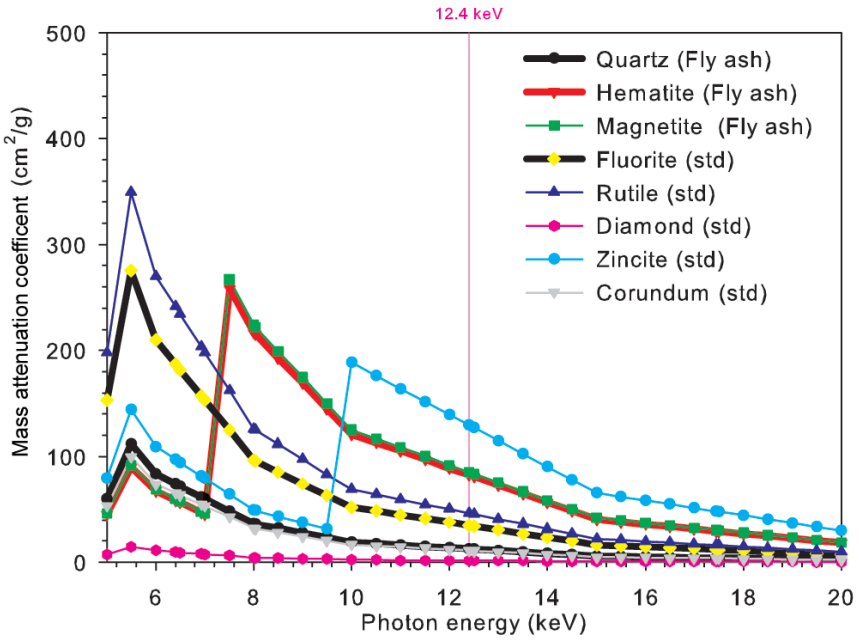

Figure 4-1 Mass attenuation coefficient of typical phases (flyash), compared with possible internal standards (std). Minimising the difference between the internal standards will reduce the bias due to micro-absorption, hence fluorite or rutile would be suitable, but rutile was excluded as it could be present in the samples. The data were calculated using TOPAS 4.2 (Bruker-AXS, Germany)

The diffraction pattern of fluorite (CaF_2) does not significantly overlap with the flyash phases identified by the laboratory analysis and will not react with the sample, making it a suitable internal standard.

Phase search/match. The spliced synchrotron diffraction pattern files were individually loaded into EVA 11.0, (Bruker-AXS, Germany) and the background was stripped. Search/match of phases present was then conducted using the Powder Diffraction File (PDF) version 2002-52. The filters used were inorganic classification and an elemental filter, using the XRF results as a guide to limit the search to elements with greater than 0.1 wt% plus hydrogen and carbon.

Special consideration must be taken to identify the correct mullite phase. The mullite is a solid solution of the general form $Al_{4+2x}Si_{2-2x}O_{10-x}$, with x typically varying from about 0.14 to 0.49, hence the value of x must be determined prior to Rietveld refinement so that the correct structure can be modelled. This change in the mullite Si/Al ratio leads to changes in the calculated amorphous Si/Al ratio. This is further complicated as there can be

substitution of Fe, Cr, Co, P and/or Ti for Al [(Al, Fe, Ti, Co, Cr, P) $_{4+2x}Si_{2-2x}O_{10-x}$] (Schneider and Komarneni, 2005). The two main methods described in the literature for estimating the value of *x* are Cameron's Law (1977) using the lattice parameter *a* and Ban and Okada's (1992) method of using the intensity ratio of the 220 and 111 reflections. Ban and Okada showed the ratio method to be more accurate than the lattice parameter method.

The 220 and 111 reflections overlap with reflections from other phases in flyash, so Ban and Okada's structures were used to calculate a similar equation to estimate *x* from the 210 and 120 reflections. TOPAS 4.2 was used to simulate the diffraction patterns of the structure determined by Ban and Okada (1992). A similar linear equation of Ban and Okada's can be used with the synchrotron diffraction data with the intensity ratio of the 210 and 120 reflections, rather than the 220 and 111. Figure 4-2 shows there is a strong linear relationship which can be used to predict *x* from the 210 and 120 intensity ratio.

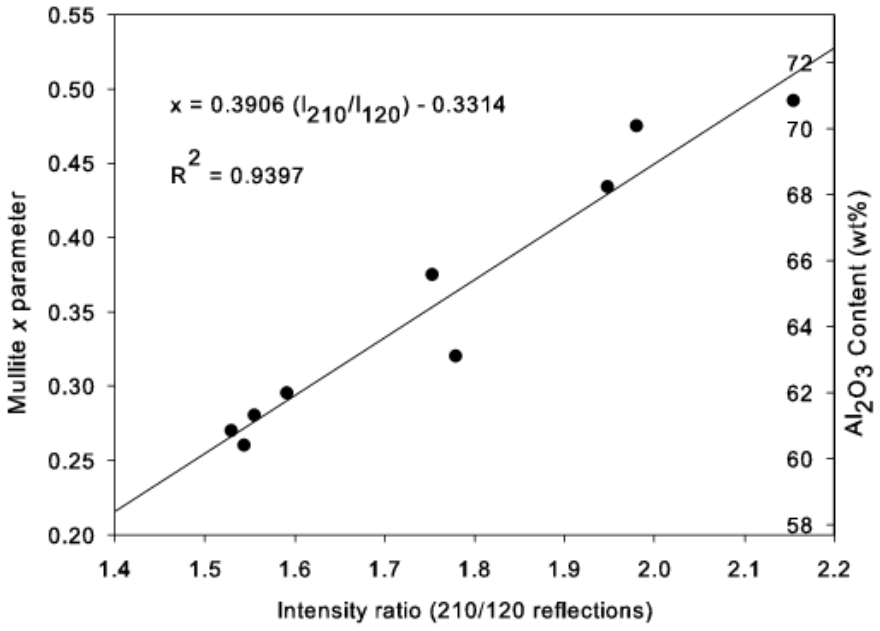

Figure 4-2 Simulated calibration of the ratio of I210 and I120 and x parameter for the synchrotron x-ray diffraction data used in this study (with polarised x-rays with a wavelength of λ= 0.100 nm).

Rietveld refinement was used with the spliced diffraction patterns to model all the phases (i.e. with crystal structures) other than mullite which was modelled

using the Pawley model (i.e. reflection position restrained by the space group Pbam, intensities allowed to refine). This allowed the intensity of the 210 and 120 reflections and the lattice parameter *a* to be determined accurately enabling estimation of the mullite *x* value by both methods. The intensity ratios of the 210 and 120 reflections were also used to estimate the composition using the linear regression (Figure 4-2) calculated from structures of Ban and Okada's method. The lattice parameter *a* was used to determine the inferred composition using Cameron's Law (Cameron, 1977). The discrepancy between the methods (Figure 4-3) indicates there is some cation substitution, such as described by Gomes et al. (2000) for mullite in flyashes. Using Figure 3 from Cameron (1977) the determined weight fraction of Fe_2O_3 + TiO_2 for each of the mullites in this study was approximately 2 wt%. The lattice parameter method was used to determine which structure should be used. The most suitable structures for the mullites in these flyashes were reported from Ban and Okada, the value of *x* varied from 0.295 to 0.375. Table 4-5 (in Section 4.4.2) reports the ICSD catalogue numbers of the phases used. Although structures of Fe, Cr, Co, Ti and/or P substituted mullites have been refined elsewhere (Parmentier et al., 1999, Popovic et al., 2007, Ronchetti et al., 2001), the crystal structure data available does not cover the composition range (Al, Si and Fe+Ti) encountered in the flyashes in this study, so the mullite structure was approximated to closest non-substituted mullite.

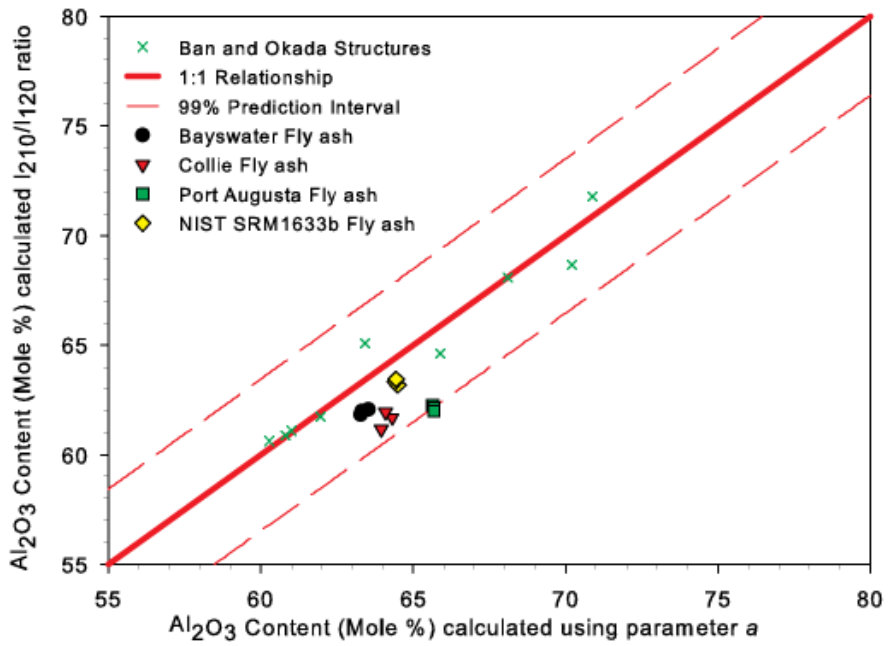

Figure 4-3 Comparing two methods for estimating the composition of mullite; if both methods were consistent there would be 1 to 1 relationship.

Rietveld Quantitative phase analysis. The instrument resolution function (IRF) and wavelength were refined by a Pawley refinement of NIST SRM 660 (LaB_6). A Pawley refinement was used rather than Rietveld refinement as modelling the intensity relative to a crystal structure was not required. The IRF was the convolution of many functions (circles, exponentials and 1/x) varied as a function of angle chosen to provide a good quality fit of the standard data. After refinement it was kept constant for all sample datasets.

Using the search/match results as a guide, appropriate structures were chosen using the ICSD database (2008/2), except for mullite, for which the structure was chosen as described previously. The Rietveld refinement with the synchrotron data were performed for each replicate starting from the ICSD structural values or best estimate where appropriate. The following parameters were refined - background, zero error and then for each phase the lattice parameters (constrained to plus or minus 0.05 the ICSD value – this was monitored to ensure refined parameters did not approach the constraints), phase scale and Lorentzian crystallite size. Then after convergence, isotropic atomic displacement parameters were refined for all phases. The background model used was an order 4 Chebychev polynomial

and three split Pseudo Voigt (SPV) at nominal positions 13°, 45° and 58° 2θ, such that the background could be modelled appropriately. The position, intensity, half width at half maximum (HWHM) left and right, and mixing function left and right were allowed to refine independently for each background peak, the only constraint was to set a minimum HWHM in each direction of 2° (i.e. minimum FWHM of 4°), such that it would not refine into an adjacent Bragg reflection.

4.3.3. Determination of amorphous composition

The amorphous composition can be calculated if the elemental and crystalline compositions are known on an absolute basis (Ward and French, 2006, Winburn et al., 2000). The crystalline components are known on an absolute basis because a known concentration of internal standard was added and all the crystalline phases are scaled from this and the remaining mass fraction is termed amorphous. In this case the composition of the amorphous was calculated as a weight fraction of equivalent oxides.

4.3.4. Testing of formulation methodologies

Geopolymer Formulation. Two different methods of formulating geopolymers were tested, the difference being the way silica and alumina weight fraction are calculated. The first set of geopolymers were prepared using the bulk weight fraction of silica and alumina as determined by XRF while the second set were prepared using the amorphous weight fraction of silica and alumina. For both cases, the quantity of sodium hydroxide, sodium silicate and/or sodium aluminate were varied such that the calculated atomic ratio were Si/Al = 2.0, Na/Al = 1.0, H/Si = 5.5. The metakaolin geopolymers prepared for comparison purposes were made using the bulk composition, to the same atomic ratios. The sodium silicate solution used was grade D A53 (PQ Australia) with a composition of 29.4 wt% SiO_2 and 14.7 wt% Na_2O. The sodium aluminate solution used was commercially available (Coogee Chemicals, Australia) with a composition of approximately 19.0 wt% Al_2O_3 and 19.8 wt% Na_2O. Although 100% of the flyash's amorphous fraction will not react, nor would 100% of the metakaolin; currently there is no satisfactory

way to determine the degree of reaction of solid feedstocks, hence the further work in Chapters 6 and 7.

The weight proportion of each feedstock (e.g. F1 = Flyash, F2 = sodium silicate solution, F3 = sodium hydroxide and F4 = water) was calculated by solving for the matrix W in Equation 4.1, where F is a matrix with the number of moles of Si, Al, Na and H per unit weight of each feedstock, and matrix R is a column matrix with the desired elemental concentration, which is expressed as elemental ratio by setting the Al =1, then other elements are expressed as the ratio i.e. R = [Si/Al, Al/Al, Na/Al, H/Al]. Note: H is used rather than H_2O to be consistent with using elemental ratio. The weight proportions calculated are rescaled to the mixture size required. This method is effective when the number of feedstocks is equal to the number of elements considered. The actual quantities of each feedstock are specified in Table 4-1.

$$W = \begin{bmatrix} F1_{wt} \\ F2_{wt} \\ F3_{wt} \\ F4_{wt} \end{bmatrix} = F^{-1} \cdot R$$

$$F = \begin{bmatrix} F1_{Si} & F2_{Si} & F3_{Si} & F4_{Si} \\ F1_{Al} & F2_{Al} & F3_{Al} & F4_{Al} \\ F1_{Na} & F2_{Na} & F3_{Na} & F4_{Na} \\ F1_{H} & F2_{H} & F3_{H} & F4_{H} \end{bmatrix}; \quad R = \begin{bmatrix} Si/Al \\ 1 \\ Na/Al \\ (Si/Al)(H/Si) \end{bmatrix} \tag{4-1}$$

Table 4-1 The wt% of each feedstock added, where the 'amor' and 'bulk' represents mixtures that were formulated using the amorphous and bulk alumina and silica contents, respectively. The water and sodium hydroxide was mixed with the sodium silicate or aluminate solution prior to mixing with flyash. Details of silicate and aluminate solutions are in the text.

Flyash (Power station)	Collie	Bayswater	Pt Augusta	Collie	Bayswater	Pt Augusta
Formulation method:	amor	amor	amor	bulk	bulk	bulk
Flyash	66.1	62.1	67.1	54.6	55.9	47.5
Sodium Silicate Solution	14.9	-	12.5	20.1	-	41.3
Sodium Aluminate Solution	-	33.9	-	-	11.7	-
Sodium Hydroxide (solid)	5.7	0.4	6.0	7.6	9.1	3.8
Water	13.4	3.5	14.4	17.8	23.3	7.4

Geopolymer synthesis. For each sample, the flyash was mixed with the activating solution at 800 rpm for 600 seconds using a planetary orbital mixer (ARE-250, Thinky Japan), followed by a 2000 rpm de-aeration cycle for 30 seconds. The samples were cast in 25 mL polypropylene (PP) vials sealed with a polyethylene (PE) screw lid and cured at 75°C for 24 hours in an electric oven. Samples were demoulded 24 hours before testing. The top surface was levelled with P80 emery paper. Each batch produced 4 samples for testing, with each formulated mixture repeated in triplicate.

Compressive strength testing. The unconfined compressive strength was determined using a Lloyds EZ50 Universal Tester (Lloyd UK), using a 0.5% grade 50 kN loadcell and 150 mm diameter compression platens. A preload of 50 N was applied followed by an extension rate of 5 mm/min. To ensure that small changes in compressive strength could be detected with statistical significance 11 repeat samples were test for each composition, and prepared in 3 different batches. The specimens were cylinders with a diameter of approximately 25mm and height of 50mm, dimension were measure with digital callipers for stress and strain calculations.

4.3.5. Fracture surface morphology

The morphology of the fracture surfaces was analysed using a Zeiss EVO-40 (Carl-Zeiss, Germany) scanning electron microscope (SEM). The fractured geopolymer samples were cut to a small size and mounted on an Al stub and sputter coated with a thin layer of gold. The samples were kept in a vacuum desiccator for 3 days prior to coating and analysis to allow out-gassing to occur.

4.4. RESULTS

4.4.1. Bulk composition

The bulk compositions of the flyashes as determined by XRF are shown in Table 4-2. The uncertainty specified is the maximum wt% difference between analysed and known values for appropriate standards.

Table 4-2 The bulk composition (wt%) of the studied flyashes, measured by XRF and loss of ignition (LOI 1000°C). Uncertainties are estimated by the variation of known standards.

Sample/Element	Bayswater	Collie	Port Augusta	uncertainty
Al_2O_3	23.5	26.6	31.2	0.1
BaO	0.05	0.39	0.08	0.01
CaO	2.26	1.72	5.82	0.05
Fe_2O_3	4.98	13.00	3.07	0.02
K_2O	1.20	0.90	1.21	0.04
MgO	0.75	1.38	2.60	0.03
MnO	0.06	0.08	0.04	0.02
Na_2O	0.23	0.42	3.92	0.05
P_2O_5	0.26	1.08	1.28	0.02
SiO_2	64.79	51.85	47.88	0.08
SO_3	0.16	0.30	0.37	0.03
SrO	0.034	0.235	0.055	0.003
TiO_2	1.19	1.48	2.10	0.01
LOI 1000°C	0.39	0.31	0.35	0.05

4.4.2. Crystalline phase composition - Quantitative phase analysis

To check the efficacy of the data collection and Rietveld quantitative phase analysis (RQPA), the crystalline phase concentration was first determined for NIST SRM 1633b flyash. The results were similar to previous studies (Ward and French, 2006, Winburn et al., 2000) (Table 4-3). Quartz was modelled as two distinct phases and these were summed for comparison with literature values. One quartz phase was modelled with a large crystallite size the other a much smaller crystallite size, this is further discussed in Section 4.4.3. The cubic iron oxides phases (magnetite and maghemite) were also summed for

comparison purposes, as the diffraction patterns of theses phases almost completely overlap. This is further discussed in Section 4.4.5. The concentration of cubic iron oxide phases may have been biased downwards in the other studies due to the increased microabsorption encountered with copper Kα radiation (0.154 nm) compared to 0.100 nm wavelength used in this study.

The mean R_{wp} and R_{Bragg} values are reported in Table 4-4. The determined crystalline phase concentrations of the 3 flyashes are reported in Table 4-5. These values are the average of 3 replicate measurements, 3 separate capillaries loaded with the same micronised sample, and the uncertainties are based on the variation of 3 repeat samples, covering the 95% CI, i.e. 2σ. The crystal structure models used in the pattern refinement do not contain substitution.

Table 4-3 Comparison of quantitative phase analysis results for NIST SRM 1633b flyash with published results. The uncertainties for this study and Winburn *et al.* are 2 times the standard deviation of 3 replicates and 6 replicates, respectively. The corundum arises from the micronising milling media. The Ward and French *a* and Ward and French *b* utilised corundum and zincite internal standards, respectively. The amorphous content was determined via the internal standard method, as described in the text. The sum of magnetite and maghemite was undertaken prior to rounding and conserving the Fe content.

Phase	This study	Winburn *et al*	Ward and French *a*	Ward and French *b*
Sum of both quartz phases	7.4(5)	6.1(4)	7.1	7.2
Primary Quartz low	2.9(2)	-	-	-
Secondary Quartz low	4.5(5)	-	-	-
Mullite	20.9(6)	21.8 (10)	22.2	22.5
Hematite	1.71(7)	2.2(4)	1.1	0.8
Sum of cubic iron oxides (as Fe_2O_3)	5.9(4)	4.0(4)	4.3	4.6
Magnetite (Fe_3O_4)	2.3(3)	3.9(4)	2.2	2.4
Maghemite (Fe_2O_3)	3.6(2)	-	2	2.1
Rutile	0.22(7)	-	-	-
Calcium Aluminate	-	-	1.1	0.7
Gypsum	-	1.0(2)	-	-
Corundum (contamination)	0.4(1)	-	-	-
Amorphous	63.5(12)	65	64.3	64.3

Table 4-4 Statistics from the Rietveld quantitative phase analysis, all values are averages of three datasets. The R_{Bragg} is the average across many phases. Major phases include only quartz and mullite.

Flyash	R_{wp}	Major Phases R_{Bragg}	Other Phases R_{Bragg}
NIST SRM 1633b	3.22	1.42	1.16
Bayswater	2.82	1.36	0.79
Collie	3.20	1.65	1.32
Port Augusta	2.59	1.28	1.03

Table 4-5 Crystalline phase composition, determined by Rietveld quantitative phase analysis, expressed as absolute wt%. The uncertainties quoted are the standard deviation of replicate samples multiplied by 2 (95% CI). The amorphous content was determined via the internal standard method, as described in the text. The value of x for the mullite phases #66447, #66448 and #66449 are 0.320, 0.375 and 0.295, respectively.

Phase Name	NIST SRM1633b	Collie	Bayswater	Port Augusta
Primary Quartz low ICSD#100341	2.9(2)	7.2(11)	6.2(3)	5.1(8)
Secondary Quartz low ICSD#100341	4.5(5)	9.0(11)	9.3(2)	5.9(8)
Mullite ICSD#66447 ($Al_{4.64}Si_{1.36}O_{9.68}$)		13.7(11)		17.5(11)
Mullite ICSD#66448 ($Al_{4.75}Si_{1.25}O_{9.63}$)	20.9(6)			
Mullite ICSD#66449($Al_{4.59}Si_{1.41}O_{9.70}$)			20.9(4)	
Hematite ICSD#82137	1.71(7)	1.9(2)	1.46(6)	
Magnetite ICSD#82237	2.3(3)	1.0(5)	2.0(4)	0.36(9)
Anhydrite ICSD#16382				0.21(4)
β-Fe_2O_3 ICSD #108905		0.27(8)		
Lime ICSD #75785			0.36(5)	
Maghemite C ICSD#87119	3.6(2)	1.85(8)		0.50(6)
Rutile ICSD #93097	0.22(7)			0.69(6)
Spinel ICSD#79000				2.3(4)
Corundum ICSD #31545 (Contamination)	0.4(1)	0.62(8)	0.60(6)	1.00(3)
Amorphous	63.5(12)	64(4)	59.3(2)	66(3)

4.4.3. Amorphous composition

The composition of the amorphous fraction was calculated based on the difference between the bulk composition and the crystalline components as oxides (Table 4-6). Quoted uncertainties are two times the standard error with uncertainties propagated assuming the input variables are independent (Kirkup, 1994).

Table 4-6 The amorphous composition of flyashes as determined by difference between bulk elemental composition (Table 4-2) and crystalline composition (Table 4-5). The total amorphous composition does not equal the amorphous composition in Table 4-5 because elements have been expressed as equivalent oxides (i.e. all Fe is expressed as Fe_2O_3). The uncertainties are propagated though the calculations from Table 4-2 and Table 4-5.

oxide	Collie	Bayswater	Port Augusta
SiO_2	32(3)	43.7(8)	32(2)
Al_2O_3	16(2)	8.2(6)	16(2)
Fe_2O_3	8(1)	1.5(8)	2.2(2)
CaO	1.7(1)	1.9(1)	5.7(1)
K_2O	0.90(8)	1.20(8)	1.21(8)
TiO_2	1.48(2)	1.19(2)	1.4(1)
MgO	1.38(6)	0.75(6)	1.8(2)
Na_2O	0.4(1)	0.2(1)	3.9(1)
P_2O_5	1.08(4)	0.26(4)	1.28(4)
SrO	0.23(1)	0.03(1)	0.05(1)
BaO	0.39(1)	0.05(1)	0.08(1)
Other	1.1(1)	0.8(1)	0.92(13)
Total	65(4)	60(1)	67(3)

4.4.4. Morphology of geopolymer fracture surfaces

Representative SEM images showing morphology of the geopolymer fracture surfaces are presented in Figure 4-4.

The geopolymer samples formulated using the bulk composition were found to have a small proportion of continuous matrix. The Collie flyash geopolymer, Figure 4-4a, has a matrix with a friable appearance and many microcracks. The Bayswater flyash geopolymer, Figure 4-4b, has some gel matrix agglomerating the flyash remnants but overall a fragile structure. The geopolymer with Port Augusta flyash, Figure 4-4c, has a continuous, dense matrix consistent with that of a strong material. The microcracks observed likely form during the compressive strength testing or the drying process (sample preparation).

The geopolymer samples formulated using the amorphous composition had a greater proportion of matrix, with a higher degree of flyash reaction, than the bulk composition samples. Large portions of the Collie flyash geopolymer, Figure 4-4d, had a matrix consistent with a brittle material and some flyash

remnants including unreacted mullite needles. The Bayswater flyash geopolymer, Figure 4-4e, had more matrix than the bulk formulated sample, but the agglomerates of flyash remnants and geopolymer gel appear to be weakly bound. The Port Augusta geopolymer, Figure 4-4f, has a continuous, dense matrix with no microcracks and a high degree of flyash reaction.

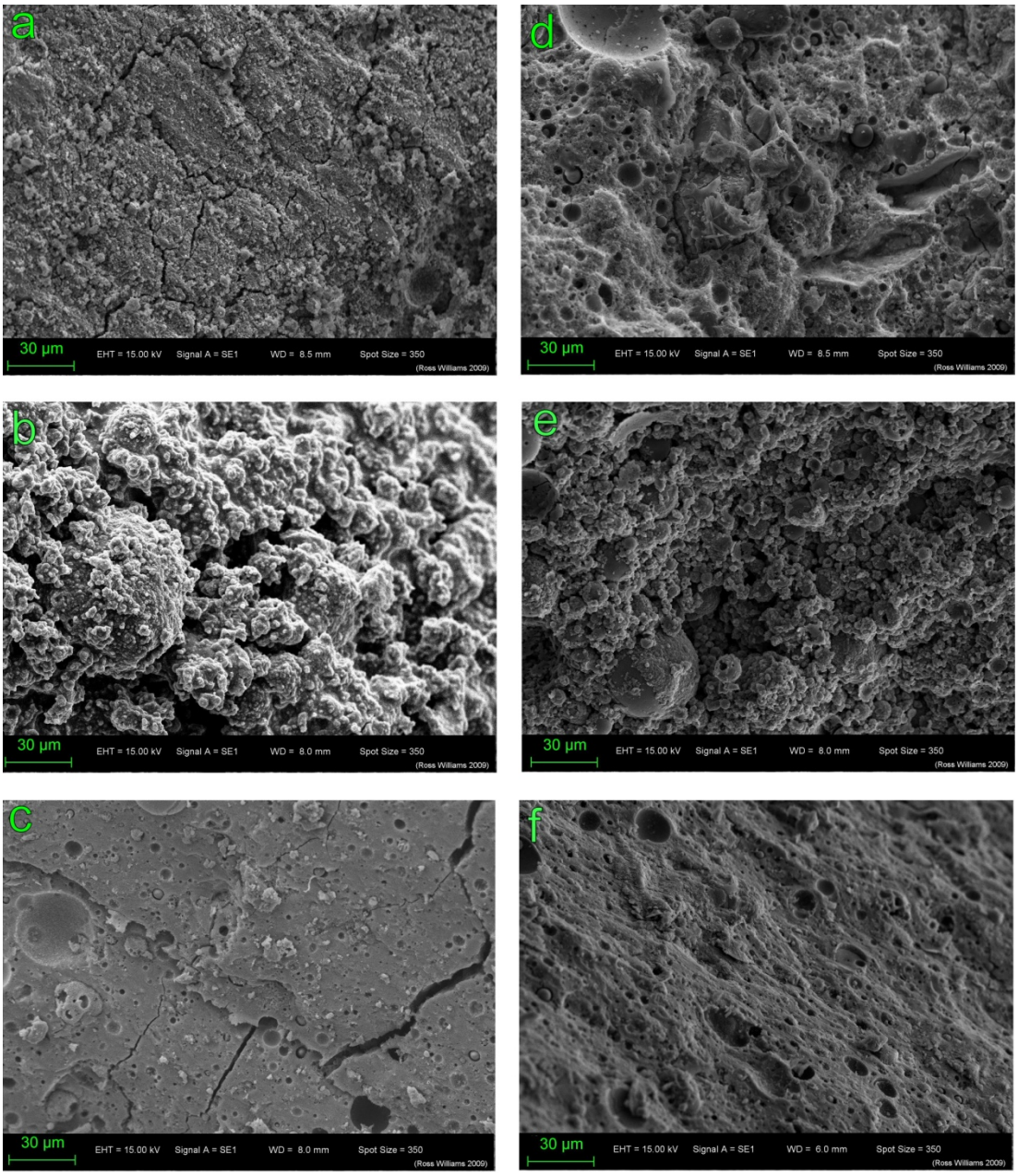

Figure 4-4 Representative fracture surface morphology for geopolymers samples formulated using the bulk composition of flyash: a) Collie flyash; b) Bayswater flyash; and c) Port Augusta flyash. The geopolymer samples formulated using the amorphous composition of flyash: d) Collie flyash; e) Bayswater flyash; and f) Port Augusta flyash.

4.4.5. Compressive strength of geopolymers

The bulk and amorphous compositions were used to synthesize two sets of geopolymer samples per flyash. The average compressive strength and Young's modulus of 11 geopolymer samples are shown in Table 4-7 and Table 4-8, respectively. Note: The Young's modulus was determined by the gradient of the stress-strain curve during compressive testing, it is repeatable between samples, but is an order of magnitude less that literature values, see section 3.7 for more details. The Bayswater flyash samples formulated using the bulk composition crumbled when removed from the moulds. The metakaolin geopolymer made with the same nominal composition was found to have a compressive strength of 32(6) MPa with a Young's modulus of 1.73(8) GPa.

Table 4-7 the average compressive strength (MPa) of the geopolymers pastes. N=11, uncertainties cover 95% CI. The reference metakaolin based geopolymer was 32(6) MPa

Flyash Source	Bulk composition	Amorphous composition
Collie	7(3)	29(7)
Port Augusta	24(8)	48(12)
Bayswater	<<1	9.5(12)

Table 4-8 The average Young's modulus (GPa) of the flyash geopolymer pastes. N=11, uncertainties cover 95% CI. The Young's modulus of the reference metakaolin sample was 1.73(8) GPa.

Flyash Source	Bulk composition	Amorphous composition
Collie	0.7(3)	1.8(2)
Port Augusta	1.4(2)	2.0(1)
Bayswater	Too weak to test	1.0(1)

4.5. DISCUSSION

4.5.1. Geopolymer mixture formulation

The determination of the amorphous composition of flyash is necessary to understand the reaction pathway when flyash reacts with alkali solutions in the geopolymerisation reaction. It may ultimately provide a method to monitor the reactivity of the flyash for both the purposes of geopolymer production and zeolite production. The elemental Si/Al ratio of the bulk, crystalline and amorphous parts of the flyash are summarised in Table 4.9.

Table 4-9 Calculated Si/Al elemental ratio of the three fractions of the flyash: bulk, crystalline and amorphous. Uncertainties are estimated on a 95% CI based on repeatability.

Fraction	NIST SRM 1633b	Collie	Bayswater	Port Augusta
bulk	1.47(1)	1.65(1)	2.34(2)	1.30(1)
crystalline	0.66(6)	1.7(3)	1.17(5)	0.9(1)
amorphous	2.5(2)	1.7(2)	4.5(3)	1.7(2)

Using the amorphous composition rather than bulk composition for mixture formulation produced geopolymers more like those synthesised with metakaolin based on the 7 day compressive strength and Young's modulus.

Calculation of the quantity of water to add is complicated; the objective is to provide the gel reaction with a similar content of water to that of pure geopolymer systems. There are many factors that are related to the role of unreacted flyash particles; size distribution, porosity, hygroscopicity and moisture content. The quantitative effect of these properties needs to be estimated and accounted for, but will be a topic for future study and is not further investigated within this study.

4.5.2. Dissolution rates and solubility

Calculation of the composition of the amorphous fraction does not provide the speciation of the amorphous phases, only the average composition. It is proposed that the amorphous part of flyash has phase separated into the immiscible parts particularly SiO_2 and $Al_6Si_2O_{13}$, however the reactivity in

alkali solution of both these glasses is similar (Provis and van Deventer, 2009), so taking the average composition will provide a good estimate of the resultant geopolymer's matrix composition. This averaging method will not be appropriate if the amorphous phases separate into other phases which do not have similar reactivity; however for this limited set of flyashes averaging is believed to provide a good estimate.

Many authors have reported on the effects of secondary metals on geopolymerisation however, in nearly all cases, the studies have investigated the addition of discrete metal species. It is not believed that these studies are relevant to the understanding of the role of metal ions that are incorporated in the amorphous phases of the flyash. The change in dissolution kinetics from small changes in glass composition can be significant (Brouwers and Van Eijk, 2002). To understand the impact of the secondary metal ions in the amorphous phase(s) aluminosilicate glasses should be synthesised with the addition of secondary metal ions in the ranges observed in flyashes. The degree of charge balancing of Al and the secondary metal ions should be investigated with various alkali earth and alkali rare earth ions over the range that is observed in flyashes. The compositional range of flyashes is significant, particularly the range of charge balancing ratios (Keyte, 2008), so a broad range of compositions must be studied.

4.5.3. Quartz composition

It was determined that there were at least two different populations of quartz (SiO_2) in the flyash samples. The first quartz is a primary constituent from the coal, with larger crystallite size (>125 nm) and pure composition with lattice parameters close to typically published values for quartz (Figure 4-5). The second quartz phase with smaller crystallite size (<125 nm), higher atomic displacement parameters (increased disorder) and larger lattice parameters (i.e. substitution) is consistent with a secondary constituent formed when the molten ash cooled forming flyash spheres. The secondary quartz is likely to have formed from the breakdown of clay into quartz and mullite. The larger size fraction of flyash within 75 and 45 μm was enriched with primary quartz (Figure 4-5). The particles are identified as quartz because they contain Si

and O by EDS; have an angular morphology and are not associated with flyash spheres.

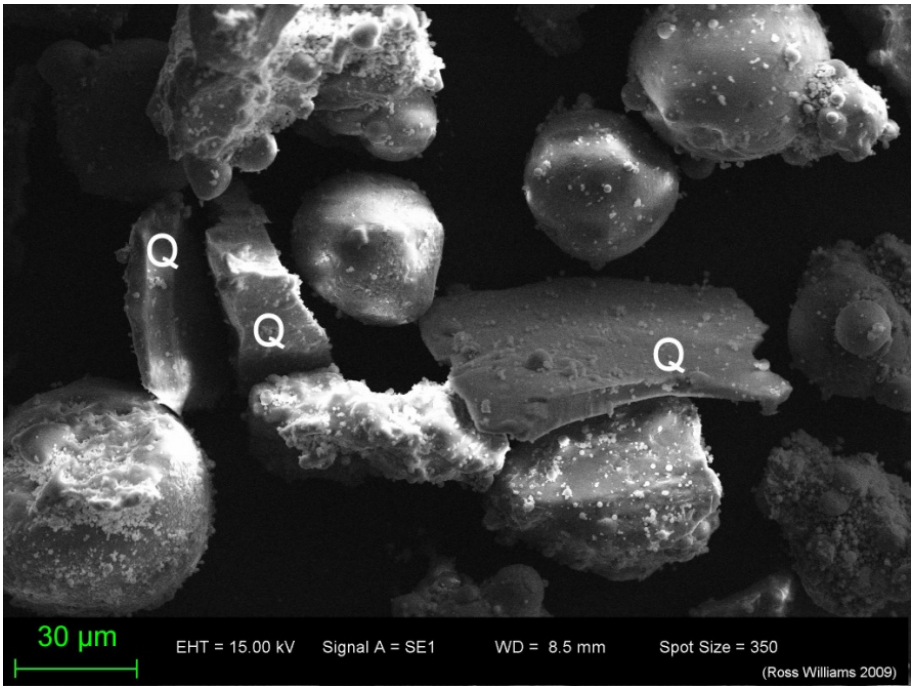

Figure 4-5 SEM micrograph of SiO_2 particles (labelled Q) likely to be primary quartz from the >45 and <75 µm size fraction of Collie flyash.

4.5.4. Mullite composition

To accurately model flyash XRD patterns the correct structure for mullite must be chosen prior to the Rietveld refinement. Mullite is a solid solution ($Al_{4+2x}Si_{2-2x}O_{10-x}$), with sillimanite ($Al_2SiO_5$) and ι-alumina (iota-alumina) as end members. The most common mullites are 3/2-mullite with x = 0.25, i.e. $Al_{4.5}Si_{1.5}O_{9.75}$ = $3(Al_2O_3)2(SiO_2)$ and 2/1-mullite with x=0.4, i.e. $Al_{4.8}Si_{1.2}O_{9.6}$ = $2(Al_2O_3)(SiO_2)$, but the composition is not restricted to these values. The two dominant methods were used to determine the composition of mullite and hence arrive at the correct structure for use in the Rietveld Refinement, which were (Ban and Okada, 1992): (i) using the lattice parameter *a* and (ii) the intensity ratio of a set of reflections (220 and 111). To reduce the effects of peak overlap the ratio of the 210 and 120 reflections are used instead. Only a small inconsistency is apparent by plotting the Al_2O_3 content (mole %) measured using both methods, this is illustrated in Figure 4-3. The

substitution of Fe and Ti for the metals can affect measured parameters. The mullite in these flyashes are within the 99% prediction interval (Figure 4-3) calculated based on the fit of the Ban and Okada structural data. This is consistent with the estimated 2 wt% Fe_2O_3 + TiO_2 for the mullite found in this study. The elemental composition of mullite in flyash cannot be directly measured, as the crystals are encapsulated, along with poorly ordered quartz, in solid amorphous aluminosilicate spheres. The composition of mullite in flyash has been measured previously by others (Gomes and Francois, 2000) using a hydrofluoric acid dissolution followed by analytical transmission electron microscopy. Although this is useful to get an indicative composition of the mullite in flyash the sampling volume is such that the measurements are not statistically representative of the bulk, particularly for a sample as heterogeneous as flyash. This is evident by the variation in the iron content found in the mullite by this method, where the standard deviation of the Fe per formula unit was larger than the average value (Gomes and Francois, 2000).

In addition to accurately modelling the diffraction pattern, the reported mullite composition range of x = 0.14 to x = 0.49 is significant, with the lower x-value having 67.9 wt% alumina and 32.1 wt% silica, compared with x at the higher range having 80.6 wt% alumina and 19.4 wt% silica. Given a typical mullite abundance of 20 wt% the impact on the calculated amorphous composition will be significant if the wrong model is used, the calculated alumina content could vary from 13.6 to 16.1 wt%. Whereas the range of substituted iron oxides (0 to 2 wt%), will only effect the alumina content by no more than 0.5 wt%.

4.5.5. Cubic iron oxides phases

The cubic iron oxide phases most commonly reported in flyash are magnetite, maghemite C and maghemite Q. However, particularly for the case of magnetite and maghemite C there is very little difference between the diffraction patterns with a constant lattice parameter. Table 4-10 shows the calculated intensities of magnetite (ICSD#82237) and maghemite C (ICSD#87119) both of which have had the lattice parameter *a* set to 0.837

nm, the main difference is the slight variation in peak intensity. Given there is typically less than 5 wt% “magnetite”, it is not possible to accurately identify the cubic iron oxides. Obviously, the reported lattice parameter for magnetite and maghemite C differs as there can be significant substitution of Mg, Al or Ti for the Fe, increasing or decreasing the lattice parameter.

Table 4-10 Comparison of the intensities of Bragg reflections of magnetite and maghemite C with the same lattice parameter for a wavelength of 0.154 nm, calculated using TOPAS 4.2

Peak (2θ)	Maghemite C	Magnetite
22.883	100.0%	100.0%
39.561	59.8%	51.2%
36.221	40.8%	37.3%
19.477	32.3%	26.7%
54.718	22.8%	17.3%
27.687	19.6%	22.4%
71.784	16.8%	9.9%
34.083	15.1%	11.0%
46.197	13.9%	11.3%
62.419	12.8%	8.6%
76.478	8.7%	5.1%
57.195	8.7%	6.2%
69.609	8.5%	5.1%
53.196	7.6%	4.7%
44.467	6.9%	4.4%
89.735	5.3%	2.4%
85.215	5.2%	2.5%
46.763	3.8%	5.3%
23.916	3.1%	7.4%
11.887	2.1%	7.2%

4.5.6. Rietveld refinement background modelling

Background modelling of x-ray diffraction patterns needs to be treated cautiously to avoid parameter correlation. It is essential to refine as few parameters as possible while adequately modelling the background. Modelling the background during Rietveld refinement removes the pattern contribution from instrumental background, elastic diffuse scattering from non-crystalline and disordered crystalline phases, and inelastic sample interactions such as Compton scattering and fluorescence. Although there

are methods that use the diffuse scattering signal such as Pair Distribution Function analysis and Partial or no Known Crystal Structure (PONKCS) method (Scarlett and Madsen, 2006), neither of these methods was applied in this analysis.

4.5.7. Uncertainties in amorphous composition determination

The usually random uncertainties associated with Rietveld quantitative phases analysis have been presented along with the data, however these statistics do not account for the systematic errors associated with the structures not including foreign cations, such as Fe substituted in mullite, and Mg or Al substituted in magnetite. A good fit can still be achieved, but quantitative phase analysis will be biased as the structure factor will be slightly changed. It is assumed that this effect is small.

X-ray microabsorption - Brindley corrections. It would be desirable to perform Brindley corrections for microabsorption, however there are significant limitations to applying these corrections to flyashes as there is a large particle size distribution and most of the phases are encapsulated in solid amorphous spheres (aluminosilicate). The encapsulation is the largest concern, particularly when there is significant concentration of iron in the amorphous matrix. Table 4-11 shows the calculated x-ray transmission coefficients through typical flyash spheres of different sizes, assuming an amorphous composition of $AlSi_2O_5$. The increased transmission achieved using synchrotron radiation with a wavelength of 0.10 nm compared with using Cu Kα with a wavelength of 0.154 nm will increase the accuracy of the QPA, as the signal from the mullite and secondary quartz will be absorbed less than if using the Cu Kα x-ray source. Furthermore, the effect of iron in the amorphous component is also clear, due to the high photoelectric cross section of Fe at both 0.154 nm and 0.100 nm, significantly reducing the transmitted signal. Increasing the transmission coefficient of the amorphous component decreases the negative bias of encapsulated mullite and secondary quartz phases. Given the flyash has been micronized the typical sphere radius would be 5 μm or less, resulting in only a slight bias for 0.100 nm x-rays.

Table 4-11 Transmission coefficient though amorphous flyash spheres at 0.100 nm and 0.154 nm (Cu Kα), calculated assuming an amorphous density of 2.5 g/cm3. The linear attenuation coefficient (LAC) is also shown for convenience.

	Synchrotron (λ = 0.10 nm)		**Cu Kα**	
LAC (cm^{-1})	23.5	55.4	84.3	187.3
Diameter (μm)	**$AlSi_2O_5$**	**$Fe_{0.5}AlSi_2O_5$**	**$AlSi_2O_5$**	**$Fe_{0.5}AlSi_2O_5$**
0.5	99.9%	99.7%	99.6%	99.1%
1.0	99.8%	99.4%	99.2%	98.1%
2.5	99.4%	98.6%	97.9%	95.4%
5.0	98.8%	97.3%	95.9%	91.1%
7.5	98.3%	95.9%	93.9%	86.9%
10	97.7%	94.6%	91.9%	82.9%

4.6. CHAPTER CONCLUSIONS

The formulation of a geopolymer mixture using the amorphous composition of flyash was compared to using just the bulk composition. Using the amorphous composition produced stronger geopolymer pastes with similar physical properties to a metakaolin geopolymer of the same target composition. Using the amorphous composition improves the development of flyash geopolymer mixture formulation and its adoption will ensure manufacture of geopolymer products with superior properties.

The bulk, crystalline and amorphous compositions of three Australian flyashes have been determined using x-ray fluorescence (XRF) and quantitative phase analysis (QPA) of x-ray diffraction (XRD) data. Significant differences in Si/Al were determined for the three flyashes particularly for the amorphous component with Bayswater = 4.5 and Collie and Port Augusta = 1.7. It is interesting to compare the Si/Al of the bulk which for Collie and Port Augusta is almost the same as for the amorphous component while for Bayswater it is 2.3. The importance of these variations cannot be underestimated if accurate mix formulations are to be generated. The Si/Al ratios could only be determined with confidence by rigorous refinement with XRD data which included taking into account variation in *x* for mullite and introducing two phases for quartz.

CHAPTER 5: GEOPOLYMER FORMULATION: EFFECTS ON STRENGTH, COST AND CARBON EMISSIONS

5.1. ABSTRACT

This chapter explores the optimum formulation for Collie flyash geopolymers, based on compressive strength and minimum cost incorporating a cost on carbon of $0 to $40 Australian dollars per tonne of CO_2-equivalent.

This CO_2-equivalent generated from producing geopolymers is mostly associated with the sodium hydroxide and sodium silicate production, thus as expected the carbon cost per tonne of geopolymer paste increases linearly with increasing Na/Al and Si/Al ratios.

The green-house-gas (GHG) emission rate was calculated as 240(50) kg of CO_2-equivalent per tonne of geopolymer paste, the 21% relative standard deviation is associated with the different compositions of geopolymer that provide similar compressive strengths. This suggests strongly that the GHG emission rate should be calculated on a mix-by-mix basis, as the different formulations have a significant effect on the carbon cost per tonne of geopolymer paste. The mean carbon tax liability per tonne of geopolymer paste was calculated as $5(1) and $7(1) for carbon tax rates of $20 and $30 per tonne of CO_2-eqivalent. The burden of the carbon tax liability is a small fraction of the unburdened cost of production, 3.6% and 5.5%, respectively for carbon tax rates of $20 and $30 per tonne of CO_2-eqivalent.

5.2. INTRODUCTION

Concrete production is a significant global activity both in terms of value, volumes and green-house-gas emissions. Cement production contributes approximately 5 – 7% of global anthropogenic emissions (Allwood et al., 2010, Friedlingstein et al., 2010, IEA, 2008, UNSTATS, 2010). This is particularly important given that the emissions can be reduced significantly using alterative cementitious binders such as geopolymer technology (Davidovits, 1993, Davidovits, 2002). This study advances the work completed with co-authors (McLellan et al., 2011) to understand the relationship of geopolymer mixture design and sustainability metrics.

5.2.1. Geopolymers

The physical, chemical and microstructural properties of geopolymer depend significantly on the quantity of each component added (Duxson et al., 2005b, Rowles and O'Connor, 2003). Hence the geopolymer composition can be optimised for a particular desirable property, such as compressive strength, encapsulation capability, fire resistance or cost. There is often a trade-off between the various properties; hence in this case we are considering a trade-off between strength, strength stability, cost and carbon production. For the purpose of this study strength stability means that if the composition of the geopolymer changes the resulting change in strength is small, i.e. less than 20%.

The formulation calculations used in this thesis only consider the fraction of the feedstocks that are likely to react, as not all of the solid feedstocks are dissolved during geopolymerisation, this is due to the chemical form and particle morphology (mostly size). For example the amorphous composition of flyash, as calculated in Chapter 4, is used to formulate flyash geopolymers, rather than the bulk composition, as it is considered that the crystalline phases will not react significantly (Williams and van Riessen, 2010).

Despite estimating the reactive components of the feedstocks the chemistry of the resulting geopolymer matrix will not equal the input composition due to

incomplete dissolution of solid feedstocks and the crystallisation of zeolite phases. When activated with sodium silicate solution, the result of incomplete metakaolin or flyash dissolution, is a geopolymer matrix with higher Si/Al, Na/Al and H/Si compared to the planned composition.

5.2.2. Life cycle analysis

A life cycle analysis allows comparison of the true cost of products that do the same task. The cost can be monetary, environmental, social or otherwise, and with the appropriate choice of analysis boundaries, products that are generated from dissimilar production routes can be compared fairly. To allow comparison of different technologies a functional unit is defined; this is a quantity that performs the same task for all products being compared. For example, with regards to railway sleeper applications, the alternative sleeper might be made from wood (Jarrah), OPC or geopolymers. In this application a suitable functional unit is a sleeper produced to a specification, not a specific volume or mass, as the physical properties of each material might be different hence a sleeper from each material will not have a common mass or volume. Additionally, if more information was known, such as the service life of each sleeper material type the functional unit could be 100 years of sleeper service.

The life cycle analysis in this chapter was conducted with three headline metrics being; energy, carbon dioxide emissions and cost. The functional units chosen for the geopolymer to geopolymer comparison is a tonne of paste. Comparison between these geopolymer and other technologies would require definition of an appropriate functional unit, such volume of binder, volume of a specific strength concrete, per sleeper or per sewage pipe. This chapter does not try to compare with other technologies such as Portland cement as this has been the topic of other investigations (McLellan et al., 2011, Weil et al., 2009).

5.2.3. CO_2 equivalence

The Kyoto protocol recognises the following gasses as green-house-gases (GHG) (United Nations, 1998): Carbon dioxide (CO_2), Methane (CH_4),

Nitrous oxide (N_2O), Hydrofluorocarbons (HFCs), Perfluorocarbons (PFCs) and Sulphur hexafluoride (SF_6). The magnitude of effect on climate change differs between the gas types, hence to allow comparisons a value termed the Carbon dioxide equivalence (CO_2-eq) is defined allowing the calculation of a single value to represent the damage associated with that GHG, relative to CO_2.

5.2.4. Emissions trading schemes – a price on Carbon

An Emissions Trading Scheme (ETS) was a proposed Australian economic scheme designed to reduce green-house-gas (GHG) emissions by attributing a price on GHG emissions. The effect of the additional price on goods and services with high emissions will reduce demand by individuals, businesses and governments, resulting in decreased emissions (Garnaut, 2011).

A cost on carbon was implemented for a short period in Australia however the scheme was repealed in November 2013. The politics of this are beyond the scope of the current study. The Australian government scheme that was in place was based on the Garnaut report, which recommended an initial price of \$20 to \$30 AUD t^{-1} CO_2-eq, based on economic factors (Garnaut, 2011). The Carbon Pollution Reduction Scheme (CPRS) was an earlier proposed scheme which was never implemented in Australia, it had an initial proposed cost on carbon of \$10 AUD t^{-1} CO_2-eq, followed by floating the price on the market (Commonwealth of Australia, 2011).

The European Union Emission Trading System (EU ETS) is similar to what was in place in Australia for the short period before November 2013 (European Commission, 2013). In the EU ETS credits are initially allocated for free to large GHG emitters, as time progresses less credits are allocated for free instead companies must purchase credits at auctions from the issuer or in a trading market from other companies. The total number of credits issued per year reduces with time, reducing the supply and thus increasing the price of credits. This increase in cost of credits, and hence GHG emissions, should promote the reduction of emissions as a business decision to maximise profits.

5.3. MATERIALS AND METHODS

5.3.1. Geopolymer formulation and synthesis

Geopolymers were formulated with varying Si/Al and Na/Al ratio using Equation 4.1 to calculate the required quantities of feedstocks to obtain the desired target composition. Table 5-1 summarises the target element ratios and quantities of each feedstock. Only the amorphous components of the flyash were considered when formulating the geopolymers, as previously discussed in Chapter 4.

Table 5-1 The target composition of the 9 samples and the weight percentage of each feedstock. Where CFA is Collie flyash; Sodium Silicate is Sodium Silicate Solution (Grade D, PQ Australia); Sodium Hydroxide Pellets (AR grade); and water is deionised water.

Si/Al	Na/Al	H/Si	CFA (wt%)	Sodium Silicate (wt%)	Sodium Hydroxide (wt%)	Water (wt%)
1.8	1.0	5.5	71.6%	4.7%	8.1%	15.6%
1.8	1.2	5.5	70.6%	4.7%	9.8%	15.0%
2.2	1.2	5.5	65.2%	21.0%	4.2%	9.6%
2.0	1.2	5.5	67.3%	13.1%	7.7%	11.9%
2.0	0.8	5.5	69.2%	13.4%	4.4%	13.0%
2.2	0.8	5.5	66.0%	21.3%	2.6%	10.1%
1.8	0.8	5.5	72.6%	4.8%	6.4%	16.2%
2.0	1.0	5.5	68.2%	13.3%	6.1%	12.4%
2.2	1.0	5.5	65.2%	21.0%	4.2%	9.6%

The activating solution was prepared by firstly dissolving sodium hydroxide pellets (AR Grade) with deionised water ensuring that any evaporated water is replaced. When the solution's temperature was less than 30°C it was added to the required quantity of commercially available sodium silicate solution (Grade D, PQ Australia), while mixing with a mechanical stirrer. The solution was then sealed and allowed to cool for approximately 2 hours. The geopolymers paste samples were synthesised by adding the flyash to the sodium silicate solution and mixing at 1500 rpm for 5 minutes with a Planetary Orbital Mixer (ARE-250, Thinky Corporation, Japan). The sample slurry was then extracted from the mixing cup using 25 mL polypropylene syringes. The syringes were then sealed in plastic bags in groups of 4, and

cured at 70°C for 24 hours, in a position such that the needle socket was upwards.

5.3.2. Compressive strength of geopolymer pastes

Thirty days after removal from 70°C the sample and syringes were cut with a diamond saw to produce cylinders with a height/diameter ratio of 2, then the remaining wall of the syringe was removed with a hot scalpel.

The cylindrical specimens were then tested for compressive strength using the Lloyds EZ50 Universal Tester (Lloyds UK), using a 0.5% grade 50 kN loadcell and 150 mm diameter compression platens. A preload of 50 N was applied followed by a constant stress rate of 0.25 MPa/s. The Young's modulus was taken as the maximum gradient of the elastic portion of the stress strain curve. The compressive strength and Young's Modulus reported here are the mean of 11 repeat compressive tests. Note: The Young's modulus was determined by the gradient of the stress-strain curve during compressive testing, it is repeatable between samples, but is an order of magnitude less that literature values, see section 3.7 for more details

5.3.3. Life cycle analysis of pastes

A range of prices for GHG emissions was chosen using the estimates provided in recommendations of an Australian Government commissioned economist (Garnaut, 2011). The prices per tonne of CO_2-equivalent GHG are shown in Table 5-2.

The life cycle analysis is based on a boundary conditions from mining raw materials to mixing concrete at Kwinana Port (Western Australia, Australia), assuming industrial quantities. The life cycle steps considered in the metric calculation for each feedstock is specified in Table 5-3. It should be stressed the life cycle analysis is on the commercial production of geopolymer concrete, not on the laboratory scale pastes samples used for physical properties analysis.

Table 5-2 The prices per tonne of CO_2-equivalent (CO_2-eq) green-house-gas used in the calculation. The Carbon Pollution Reduction Scheme (CPRS) values are from Commonwealth of Australia (2011) and the 'reasonable' low and high values are from the report by Garnaut (2011). Prices are in Australian Dollars (AUD).

	Carbon Price (AUD t^{-1} CO2-eq)
No carbon tax	0
Australian proposed CPRS initial value	10
Reasonable low value	20
Reasonable high value	30
Australian CPRS cap value	40

Table 5-3 Transport and emissions data and references for geopolymer feedstock and OPC.

Feedstock	Classification	Specification	Source Location	Life/Cycle Steps Considered	Key References
Fly ash	waste	Fine fly ash (AS 3582.1 - 1998)	Collie, Western Australia	Collection from flue gases and separation	(Heeley, 2003, Heidrich et al., 2005, Samarin, 1999)
Sodium Hydroxide	product	50 wt.% NaOH solution	Japan	Electrolysis of brine	(Van Santen, 1998, Wilson and Jones, 1994)
Sodium Silicate	product	37 wt.% sodium silicate solution	China or Kwinana, Western Australia	Soda ash production/sand mining; furnace liquor production	(Duxson et al., 2007b, Fawer et al., 1998, ICIS, 2008)
OPC	product	General Purpose	Kwinana, Western Australia	Mining; Grinding; Calcination; Re-grinding	(ABARE, 2008, CIF, 2008, Flower and Sanjayan, 2007, Huntzinger and Eatmon, 2009, Lippiatt and Ahmad, 2004, Nisbett, 2002, O'Brien et al., 2009, Worrell et al., 2001)

5.4. RESULTS

5.4.1. Compressive properties

The compressive strength and Young's Modulus of each sample are shown in Table 5-4. These results visualised as contour plots are shown in Figure 5-1 and Figure 5-2. The ultimate compressive strength of paste samples is prone to large uncertainties due to micro-cracking and imperfections in the specimens, however the Young's Modulus is less affected by these factors thus have improved precision and accuracy (Duxson, 2006). The results in this study are consistent with Duxson's findings with an average relative standard deviation of 15% and 9% for compressive strength and Young's modulus, respectively. As defined in the Section 5.2.2, the design specification for comparison is a robust formulation with a compressive strength of ≥ 50 MPa; considering this the optimal formulation is shaded green on Figure 5-1 and Figure 5-2. The contour plots are generated by cubic interpolation. The samples did not present with significant quantity of efflorescence.

Table 5-4 Compressive strength and Young's modulus for different elemental ratios of samples from this study.

Si/Al	Na/Al	H/Si	Maximum Strength [MPa]	Young's Modulus [GPa]
1.8	1.0	5.5	17(2)	2.0(3)
1.8	1.2	5.5	16(3)	2.0(3)
2.2	1.2	5.5	54(9)	3.2(3)
2.0	1.2	5.5	50(9)	3.4(3)
2.0	0.8	5.5	35(3)	2.91(8)
2.2	0.8	5.5	40(7)	3.01(7)
1.8	0.8	5.5	14(2)	2.2(4)
2.0	1.0	5.5	55(4)	3.51(7)
2.2	1.0	5.5	55(7)	3.3(2)

Values in parentheses correspond to the least significant figure in the standard deviation to the left.

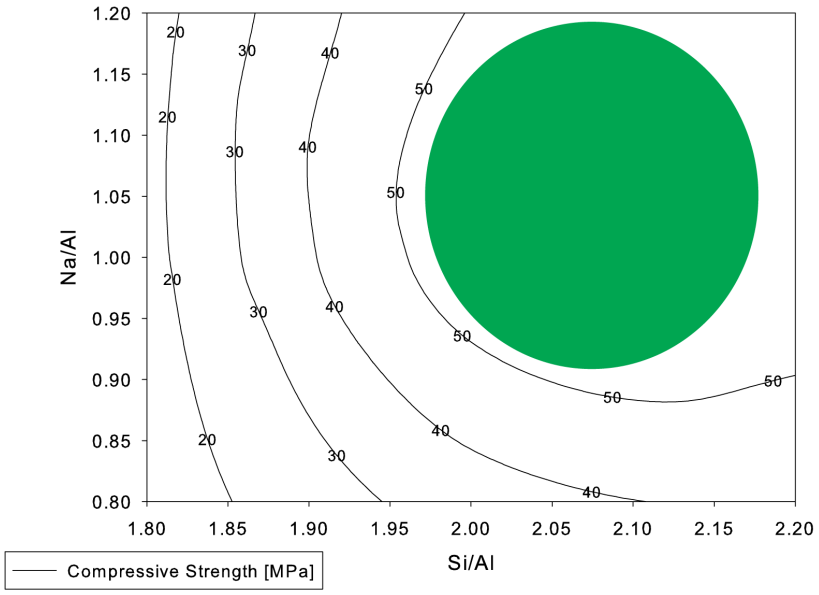

Figure 5-1 Compressive strength as a function of elemental composition. The shaded region represents the optimal composition for a robust formulation with good mechanical strength.

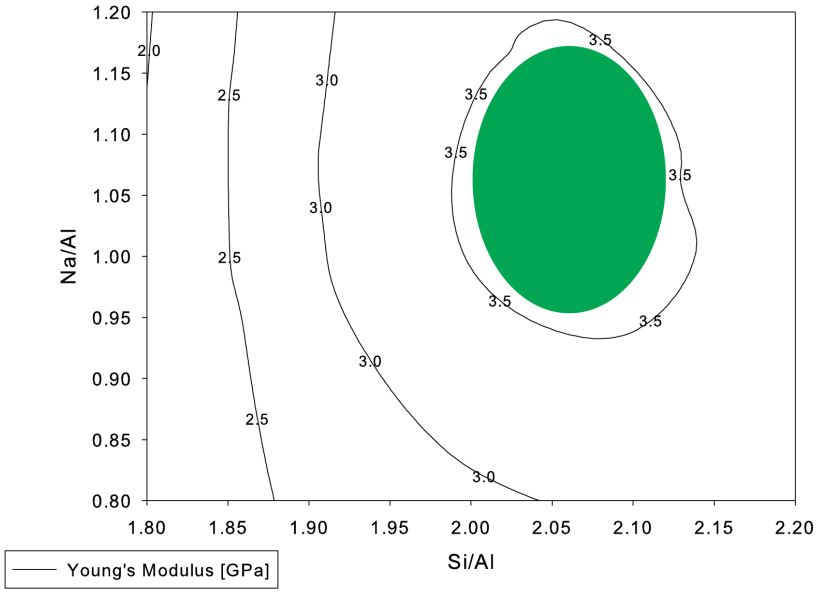

Figure 5-2 Young's Modulus as a function of elemental composition. The shaded region represents the optimal composition for a robust formulation with good mechanical strength.

5.4.2. Energy utilisation

The energy consumed in the production of the geopolymers with different formulations can be calculated. For the production, the energy used as electricity is shown in Figure 5-3 and as fuel in Figure 5-4. The mean (n=9) energy consumption from production was 0.61(30) and 0.76(25) GJ/t paste as electricity and fuel, respectively, where the bracketed value is one standard deviation expressed as the variation in the last digit(s) of the value. The large standard deviation is due to the variation in geopolymer composition. The mean energy consumed by transporting the feedstock is 0.005(1) GJ/t paste and is much less than those associated with the production of the feedstocks (Figure 5-5). The total energy utilised is shown in Figure 5-6, with a mean value of 1.4(2) GJ/t paste, which is dominated by the electricity and fuel used in the actual production of the feedstocks. This compares with the embodied energy of OPC binder at 4.9 GJ/t and Bayer geopolymer binder at 0.27 GJ/t (Jamieson et al., 2015).

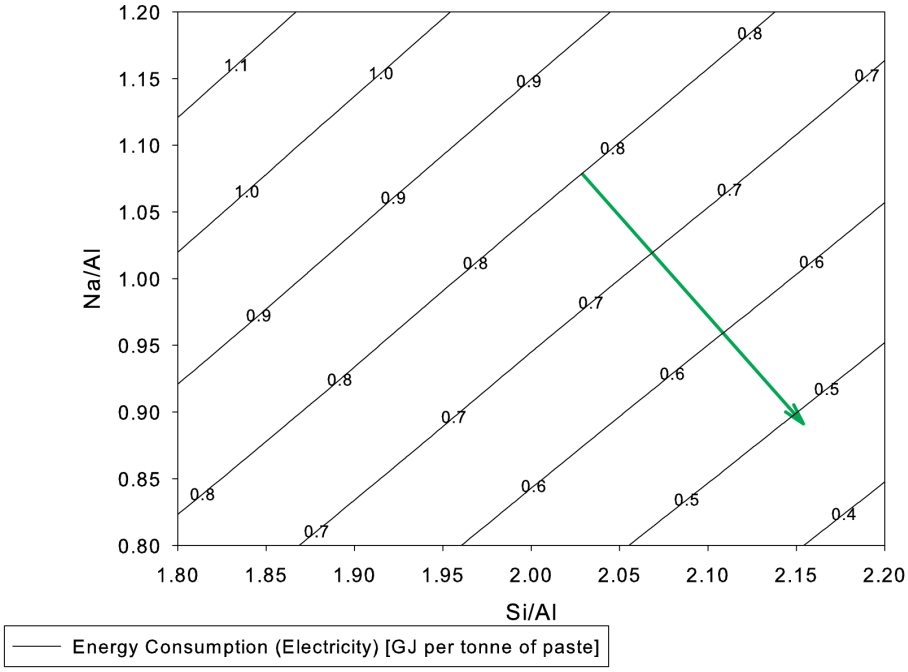

Figure 5-3 The electrical energy consumed in the production of the feedstocks for geopolymer synthesis. The green arrow highlights the direction of decreasing energy consumption.

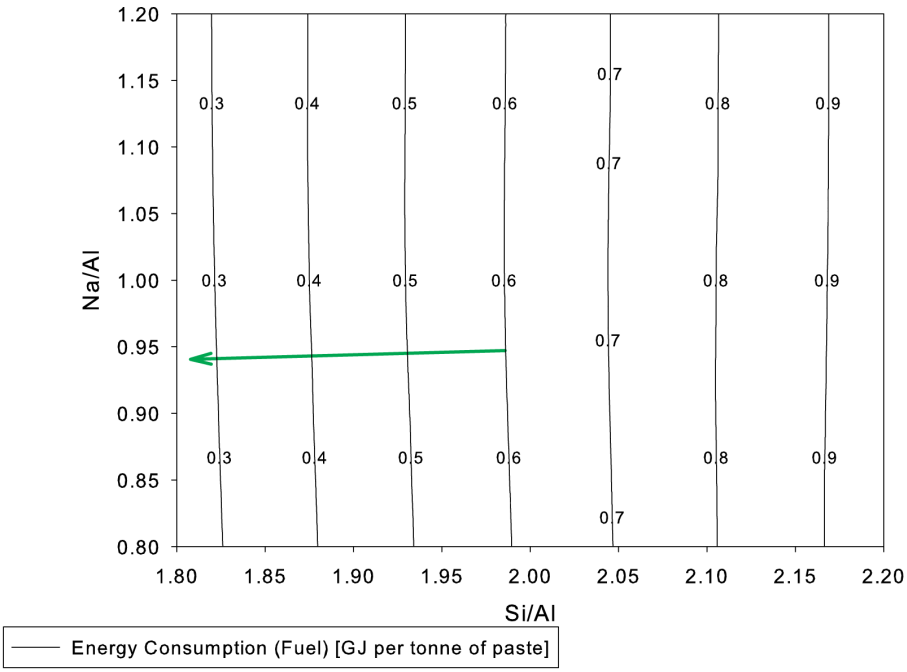

Figure 5-4 The fuel energy consumed in the production of the feedstock's for geopolymer synthesis. The green arrow highlights the direction of decreasing energy consumption.

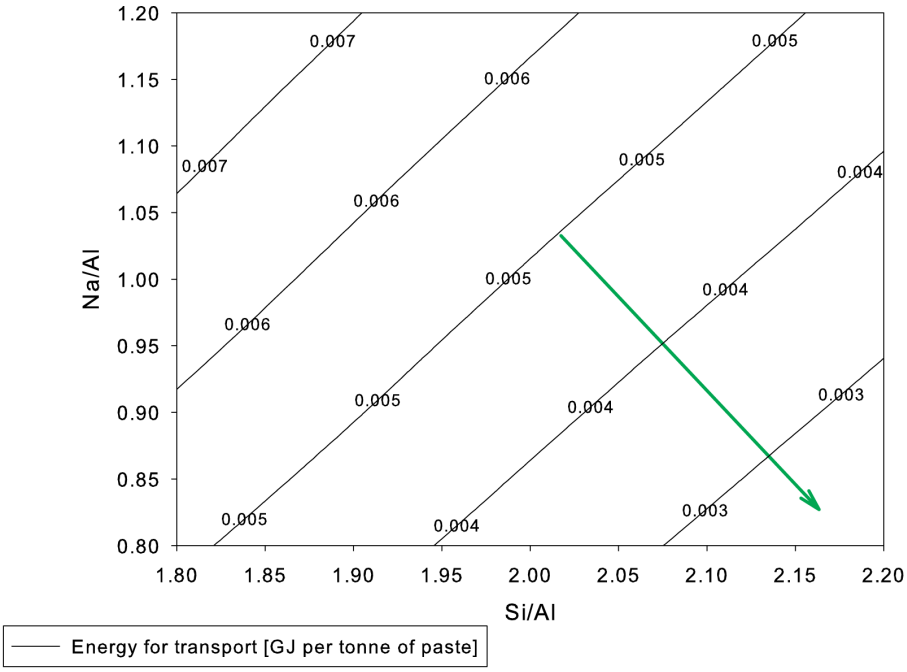

Figure 5-5 The energy consumed in the transportation of the feedstock's for geopolymer synthesis. The green arrow highlights the direction of decreasing energy consumption.

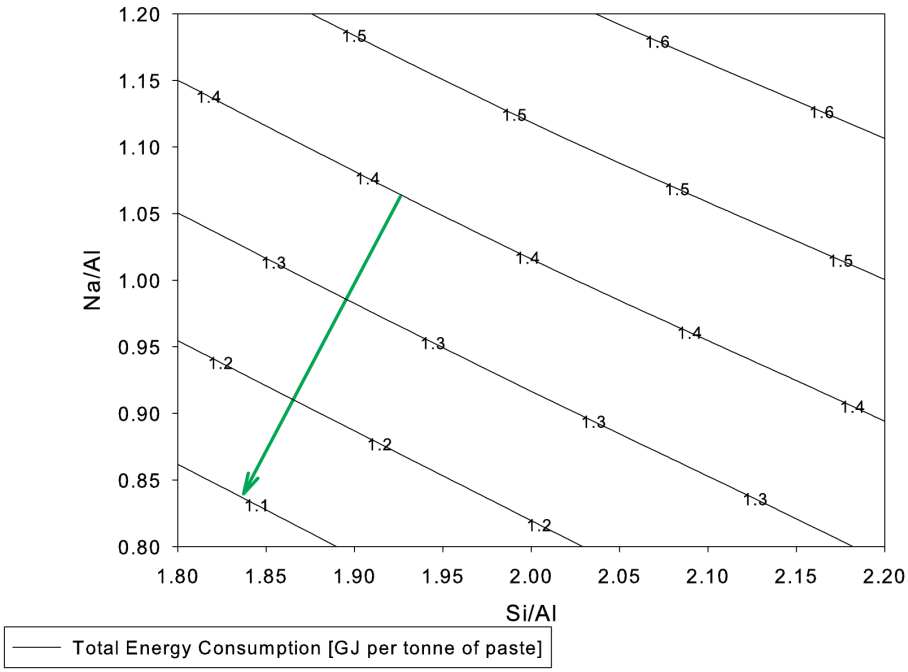

Figure 5-6 The total energy consumed in the production and transportation of feedstocks of one tonne of geopolymer paste. The green arrow highlights the direction of decreasing energy consumption.

5.4.3. Green-House-Gas emissions

The green-house-gas (GHG) emissions as measured by carbon dioxide equivalent ($CO_{2\text{-equiv}}$) for the production, the transport of the feedstock's and the total emissions are shown in Figure 5-7, Figure 5-8 and Figure 5-9, respectively. The mean GHG emissions from feedstock production and transport were 240(50) and 0.40(15) kg $CO_{2\text{-equiv}}$ / tonne paste, respectively. These values are calculated with the assumptions outlined in Section 5.2.2. This compares with the GHG emission rate of OPC binder at 387-428 kg $CO_{2\text{-equiv}}$ / tonne paste, cement emission rate from WBCSD (2012) and using a water to cement ratio of 0.45 and 0.60.

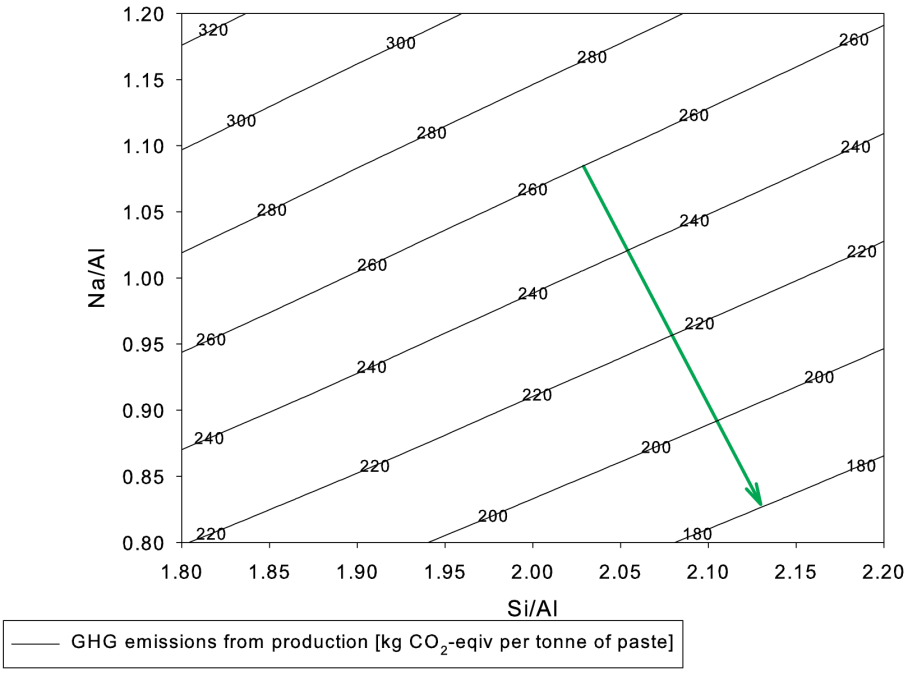

Figure 5-7 The GHG emissions from the production of the feedstocks for geopolymer synthesis. The green arrow highlights the direction of decreasing GHG emissions.

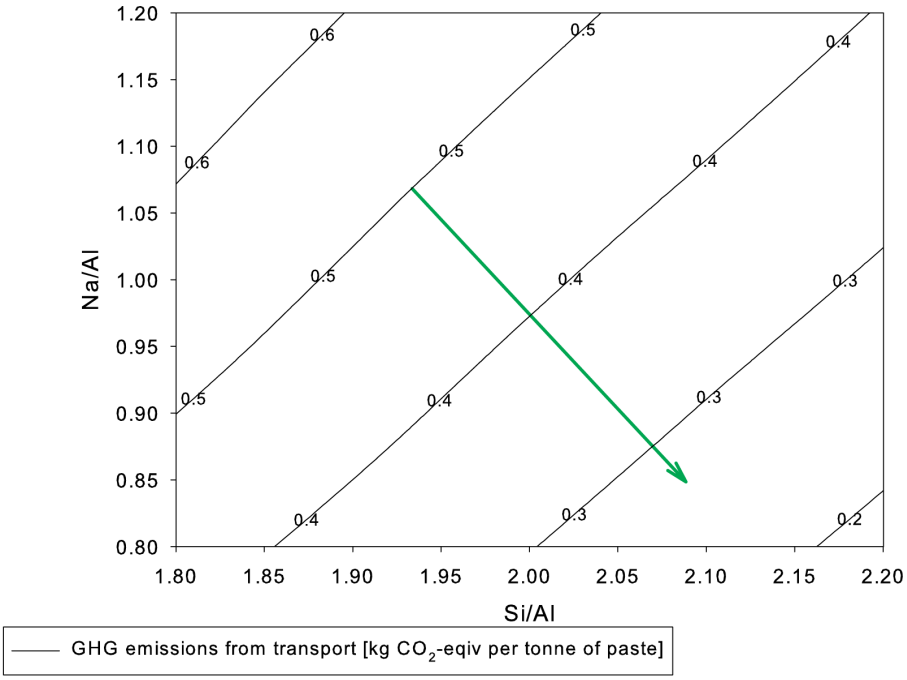

Figure 5-8 The GHG emissions from the transportation of the feedstocks for geopolymer synthesis. The green arrow highlights the direction of decreasing GHG emissions.

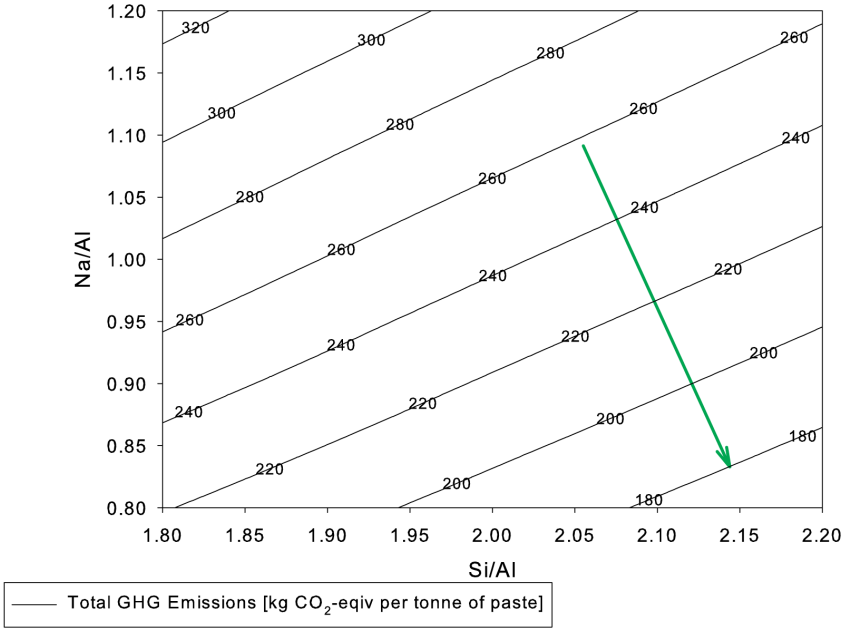

Figure 5-9 The total GHG emissions from the production and transport of the feedstocks for geopolymer synthesis. The green arrow highlights the direction of decreasing GHG emissions.

5.4.4. Cost without a carbon tax

The cost of the formulations can be calculated[6], assuming no carbon tax, and is shown in Figure 5-10. The cost of one tonne of geopolymer paste varies from AU$110 to AU$160, dependent on the composition, with the minimum cost occurring at low Na/Al and low Si/Al. The mean cost without a carbon tax is AUD $140(20).

[6] DISCLAIMER: These prices are subject to market fluctuations, minimum quantities and other commercial terms.

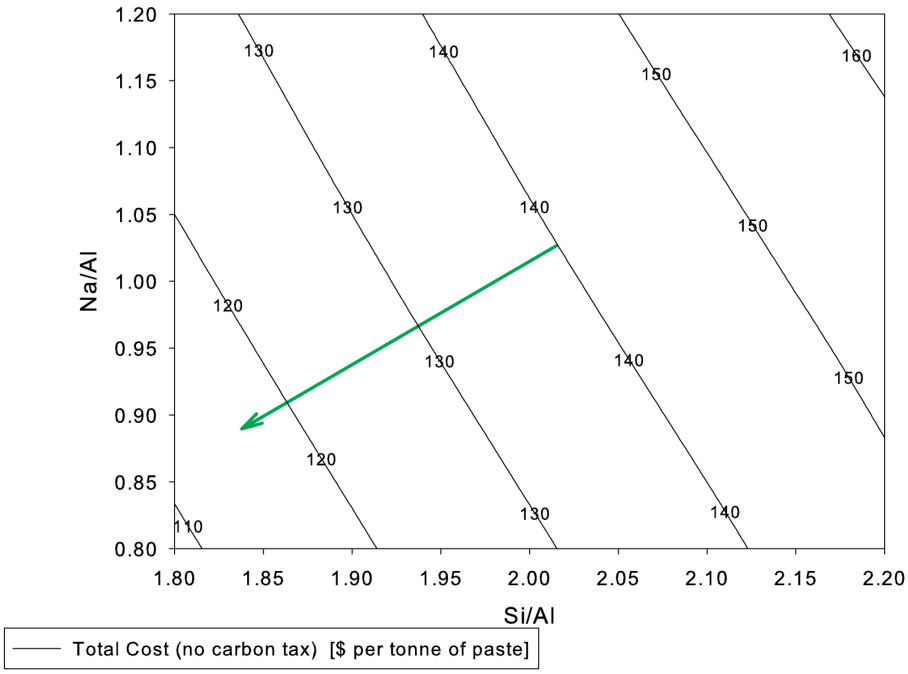

Figure 5-10 The calculated cost of geopolymer production. The green line highlights the direction of decreasing cost.

5.4.5. Carbon taxes

The calculated carbon tax per tonne of geopolymer paste assuming prices on carbon of \$10, \$20, \$30 and \$40 AUD/per tonne $CO_{2\text{-equiv}}$ are shown in Figure 5-11 to Figure 5-14. The mean tax costs are 2.4(5), 4.9(10), 7.3(15) and 9.7(21) AUD/tonne paste, respectively.

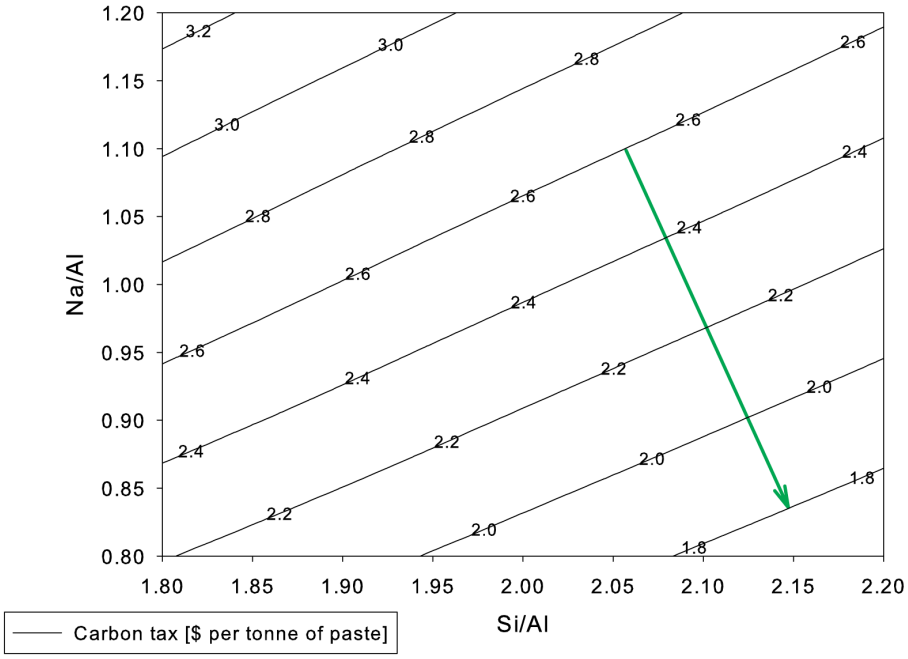

Figure 5-11 The carbon tax per tonne of geopolymer paste assuming a price on carbon of $10 per tonne of CO_2-eqiv. The green arrow highlights the direction of decreasing tax.

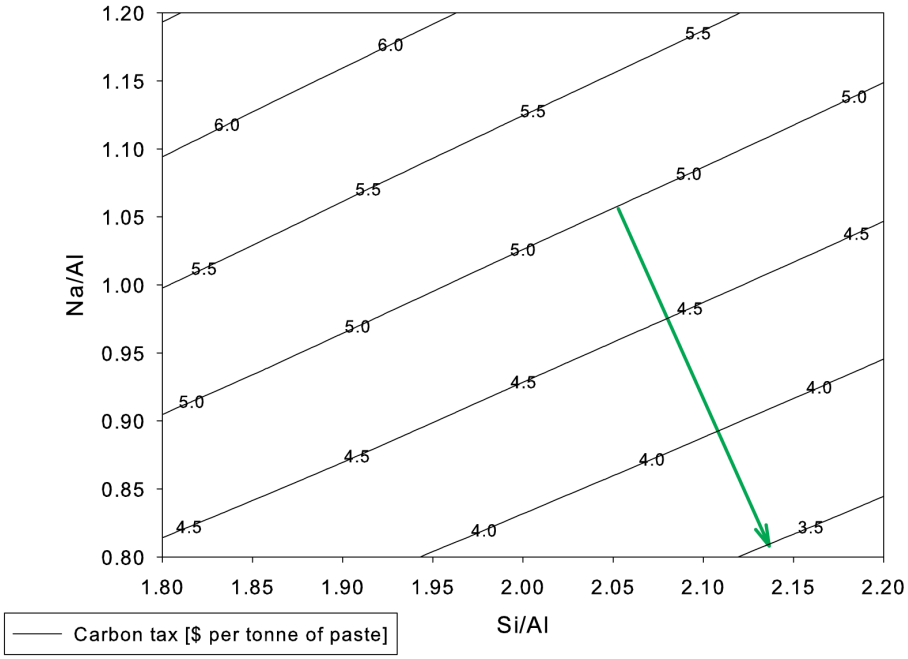

Figure 5-12 The carbon tax per tonne of geopolymer paste assuming a price on carbon of $20 per tonne of CO_2-eqiv. The green arrow highlights the direction of decreasing tax.

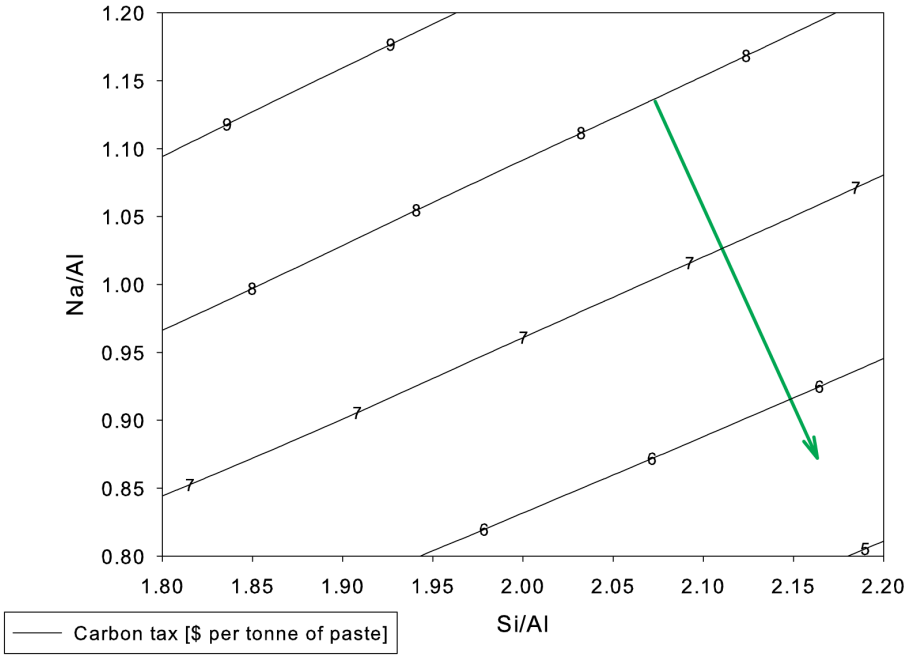

Figure 5-13 The carbon tax per tonne of geopolymer paste assuming a price on carbon of $30 per tonne of CO_2-eqiv. The green arrow highlights the direction of decreasing tax.

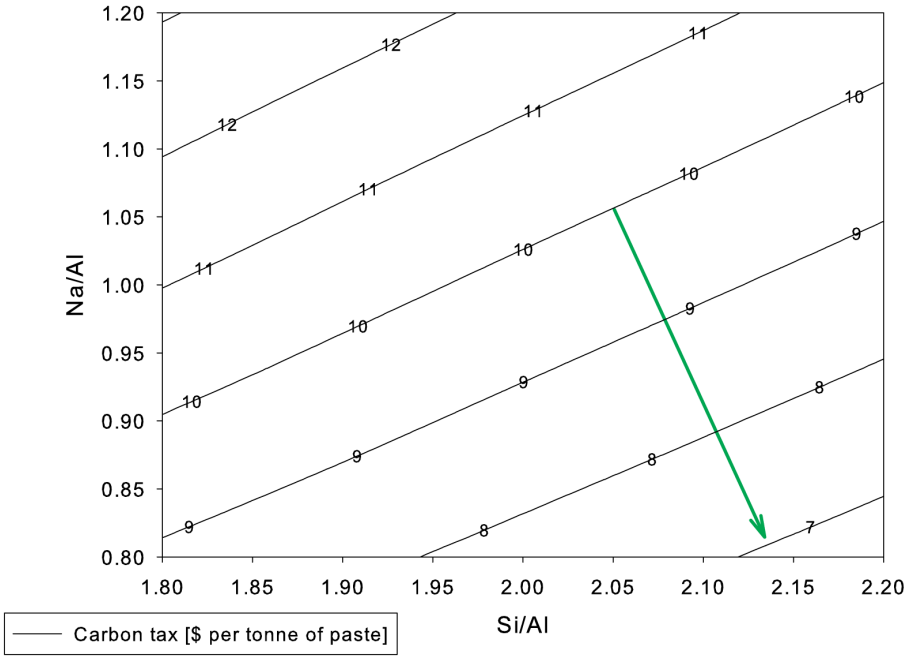

Figure 5-14 The carbon tax per tonne of geopolymer paste assuming a price on carbon of $40 per tonne of CO2-eqiv. The green arrow highlights the direction of decreasing tax.

5.4.6. Carbon tax effect on total cost of geopolymers.

The effect of the additional cost of the carbon tax at prices of 10, 20, 30 and 40 AUD/tonne $CO_{2\text{-equiv}}$ on the cost of production is shown in Figure 5-15 to Figure 5-18. The mean cost will increase by the small values specified in Section 5.4.5, to 138(17), 141(17), 143(17), 146(17) AUD/tonne paste. The increase in the average cost is smaller than the spread caused by the variation in the formulation.

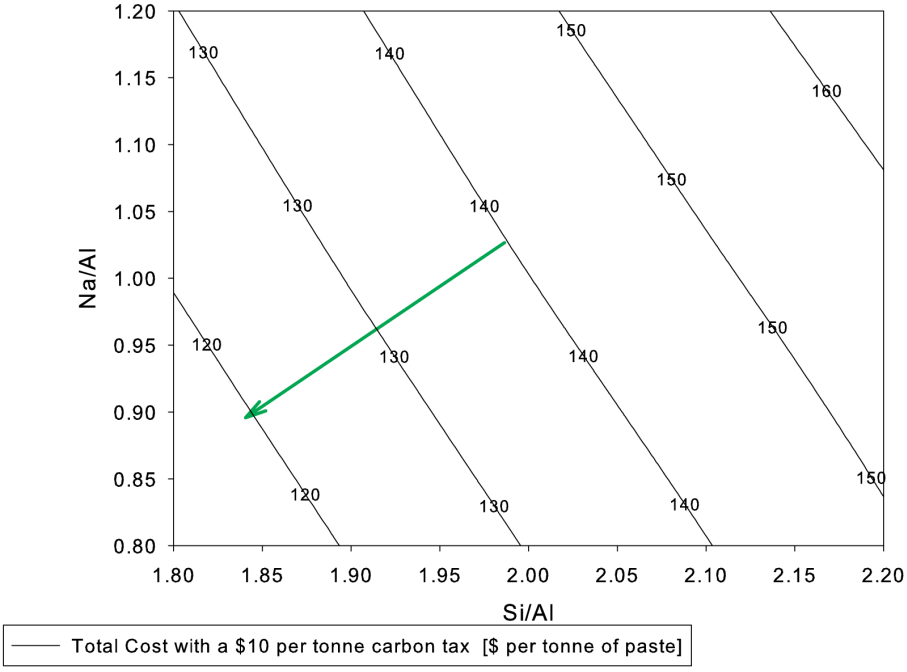

Figure 5-15 The calculated cost of geopolymer production with AU$10 per tonne $CO_{2\text{-equiv}}$. The green line highlights the direction of decreasing cost.

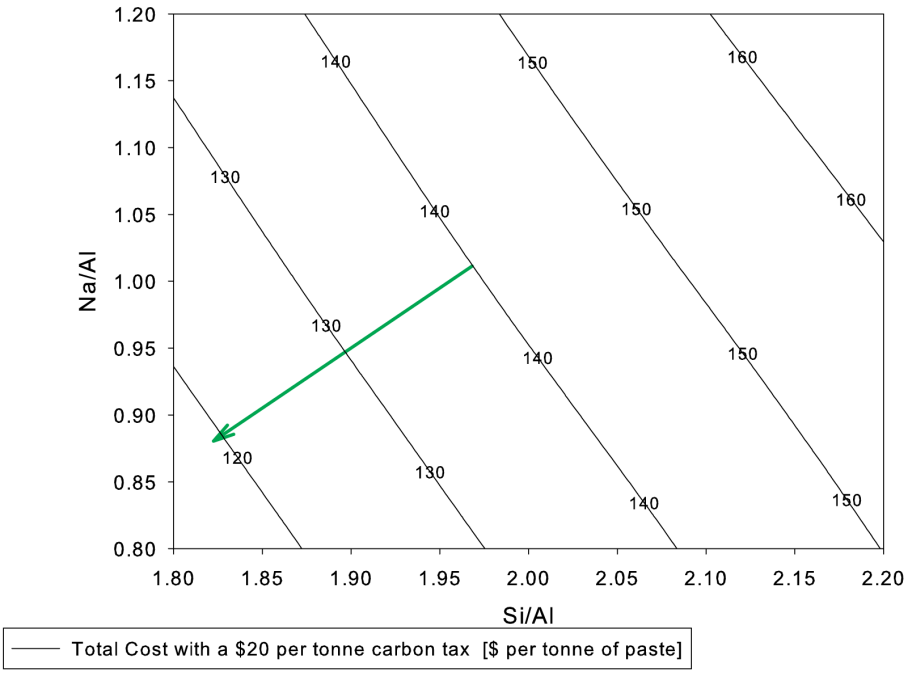

Figure 5-16 The calculated cost of geopolymer production with AU$20 per tonne $CO_{2\text{-equiv}}$. The green line highlights the direction of decreasing cost.

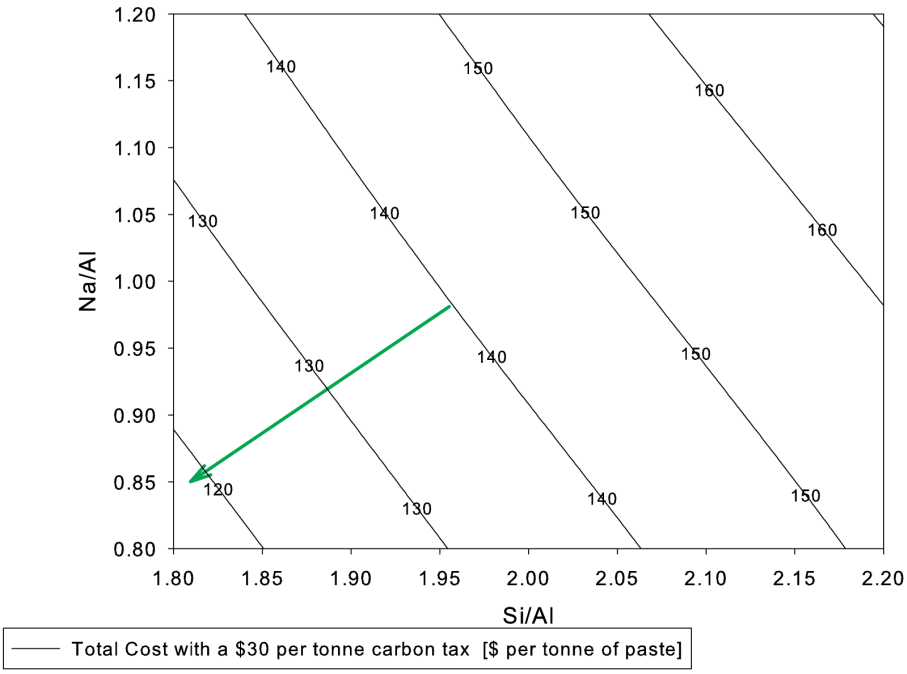

Figure 5-17 The calculated cost of geopolymer production with AU$30 per tonne CO2-equiv. The green line highlights the direction of decreasing cost.

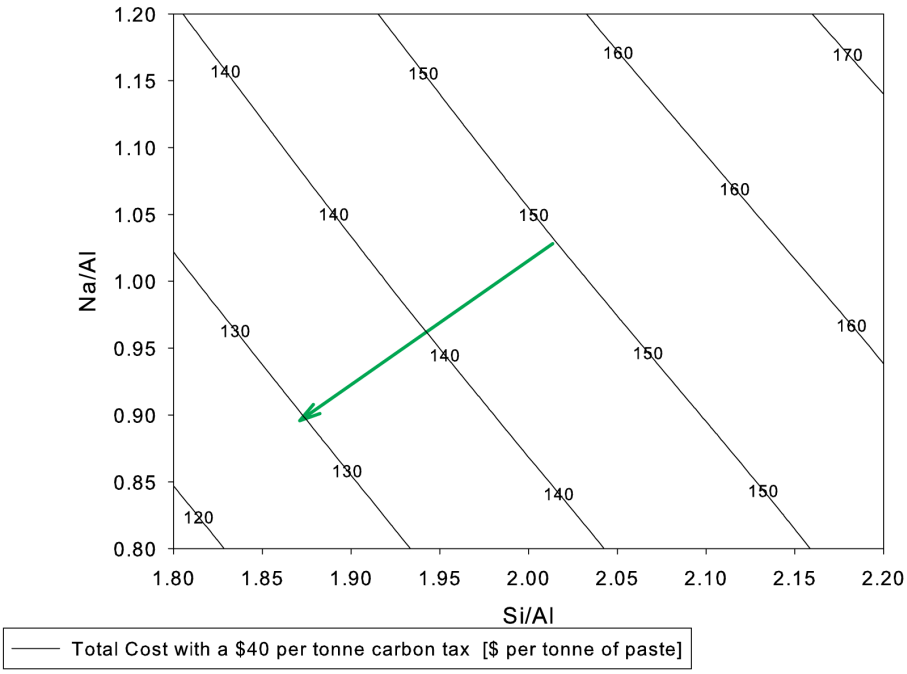

Figure 5-18 The calculated cost of geopolymer production with AU$40 per tonne CO2-equiv. The green line highlights the direction of decreasing cost.

5.5. DISCUSSION

5.5.1. Physical strength stability

The maximum physical strength as measured by the compressive strength and Young's modulus is stable between the regions shown in Figure 5-1 and Figure 5-2, which is approximately Si/Al = 2.1 ±0.1 and Na/Al = 1.1±0.1.

This can be compared with several other studies (Table 5-5) with metakaolin and flyash geopolymer formulations which had maximum compressive strengths in a similar range of Si/Al = 1.9-2.3 and Na/Al = 0.9-1.2. From the studies that performed a systematic search of Si/Al and Na/Al ratios for maximum compressive strength, the only outlier was Subaer (2004) who found optimal compressive strength around Si/Al = 1.6 and Na/Al = 0.6, this can be reconciled given the reported elemental ratios are based on the bulk composition and there was a large fraction of unreacted metakaolin meaning less Al formed the geopolymer matrix suggesting the matrix elemental ratio could have been closer to the nominal range of ratio's found in other studies.

Table 5-5 A summary of studies which have found the optimal geopolymer composition, The Si/Al and Na/Al ratio in this table are the mean ± range of Si/Al and Na/Al ratio from the literature for the mixtures with 20% of the maximum compressive strength.

Reference	Solid Feedstock	Si/Al[7]	Na/Al	Composition Type
Rowles(2003)	Metakaolin (Kingwhite)	2.3±0.5	1.2±0.5	Bulk
		2.9±0.9	0.9±0.8	Matrix (EDS)
Subaer (2004)	Metakaolin (Kingwhite)	1.5	0.6	Bulk
Steveson and Sagoe-Crentsil (2005a)	Metakaolin (Kaolin Commercial Minerals)	1.8±0.4	1.1±0.3	Bulk
Steveson and Sagoe-Crentsil (2005b)	Flyash (Pozzolanic Enterprises, Australia)	1.95	1	Bulk
Chen-Tan (2010)	Flyash (Collie)	2.6	1.2	Bulk
Current work (Chapter 5)	Flyash (Collie)	2.1±0.1	1.1±0.1	Amorphous components
Current work (Chapter 6)	Flyash (Collie)	1.90±0.06	0.66±0.06	Bulk
	Metakaolin (SnoBright 65, Unimin Pty Ltd, Australia)	1.9	1	Bulk
		2.3	1.4	Matrix (XRD Methods)

5.5.2. Reducing the cost and carbon

To reduce the CO_2-eq, it is necessary to consider the GHG emission rates for each feedstock (Table 5-6) compared to the typical weight fraction of each feedstocks as per Table 5-1. Although sodium as sodium hydroxide or sodium silicate are typically at low concentrations, the associated GHG emission rates and unit costs are both an order of magnitude larger than the flyash, hence the sodium concentration has a large effect on the total GHG emissions. Although the GHG emission rate and unit cost of flyash is low, due large mass fraction of flyash in geopolymer, the contribution to total GHG emissions and cost are substantive.

[7] The Si/Al and Na/Al ratio in this table are the mean ± range of Si/Al and Na/Al ratio from the literature for the mixtures within 20% of the maximum compressive strength.

Table 5-6 The GHG emission rates and monetary costs for the major geopolymer feedstocks, as described in McLellan et al. (2011)

Feedstock	GHG emission rate [kg of CO_2-eq per tonne of feedstock]	Cost [AUD $ per tonne][8]
Flyash	0.007	70
Sodium Hydroxide (dry solid)	3165	600
Sodium Silicate (dry solid)	634	611

The GHG emissions and monetary costs associated with the transport of the bulk materials are also significant, but difficult to accurately evaluate. In this instance the geographic region on which the case study is evaluated will be one of the most significant components. In particular, the proximity of coal fired power stations and appropriate ports for sodium hydroxides/silicates compared to the geopolymer production sites. Also important for geopolymer technology is that coal fired power stations and freight ports are in close proximity to all Australian capital cities and industrial cities reducing the transport costs, energy use and emissions.

Given the large impact of high unit costs and GHG emission rates of sodium hydroxide/silicate sources it is beneficial to find alternative by-product or waste product streams. ALCOA World Alumina have a patent for utilising spent Bayer Liquor as a substitute for sodium hydroxide in geopolymer materials (Jamieson, 2008). The Bayer Liquor is a sodium aluminate solution which is used in the Bayer Process – the refining of bauxite to alumina. Due to the high organic concentrations (e.g. tree roots) in the bauxite deposits in Western Australia, the Bayer Liquor accumulates these organics which inhibit the Bayer Process. Hence from the patent it seems ALCOA may consider it favourable to use this spent Bayer liquor for geopolymer production and replenish the plant with fresh sodium hydroxide solution. Recently the author with co-authors published results showing that a viable geopolymer paste could be produced using the Bayer Liquor as the alkali hydroxide source,

[8] DISCLAIMER: These prices are subject to market fluctuations, minimum quantities and other commercial terms; Minimum quantities would be on the order of 20 kT of each feedstock.

producing pastes of 43 MPa (van Riessen et al., 2013). The $CO_{2\text{-eq}}$ emissions from this material would be very low however, especially if it is considered as waste product enabling the emissions and embodied energy to be considered 0. The embodied energy of this 43 MPa paste was calculated at 0.9 GJ/t and 0.27 GJ/t when including and excluding respectively the initial embodied energy of the sodium hydroxide and alumina (Jamieson et al., 2015). The direct energy to process the liquor to a usable state was 0.78 GJ/t of processed liquor (Jamieson et al., 2015), which assuming the energy is supplied as electric power would produce 202 kg of CO_2-eq per tonne of processed liquor, making it very appealing as a substitute for sodium hydroxide. The emissions for sodium hydroxide at the same concentration as in the Bayer liquor (400 g/L of NaOH) would emit approximately 850 kg of CO_2-eq per tonne of sodium hydroxide solution.

5.5.3. Cost of carbon in the future

In the future the carbon tax rate may increase, possibly to $40 per tonne of CO_2-eq in real terms (Garnaut, 2011). Although any values are speculative it is worth considering the effect of a very high carbon tax value. Using an excessively high carbon tax value of $500 per tonne of $CO_{2\text{-eq}}$, Figure 5-19 shows the effect on the price compared to a more contemporary carbon tax value ($40 per tonne $CO_{2\text{-eq}}$ Figure 5-18). The excessive carbon tax modifies the cost-formulation relationship such that the cost is almost independent of Si/Al ratio. The Na/Al is the dominate parameter because it directly affects the weight fraction of Na (added as NaOH and/or Na_2SiO_3), which has a high GHG emission rate of 3.2 or 0.6 tonne per tonne of dry NaOH or Na_2SiO_3, respectively. This calculation shows that the excessive carbon tax does change the cost-strength optimal formulation, as shown in Figure 5-20, however not dramatically. The figure also shows with sensible changes in carbon price $0 to $40 per tonne CO2-eq expected in the next few years has only a small impact on the optimum geopolymer formulation which is unlikely to be sufficient to justify the business case to change formulation in a geopolymer production factory.

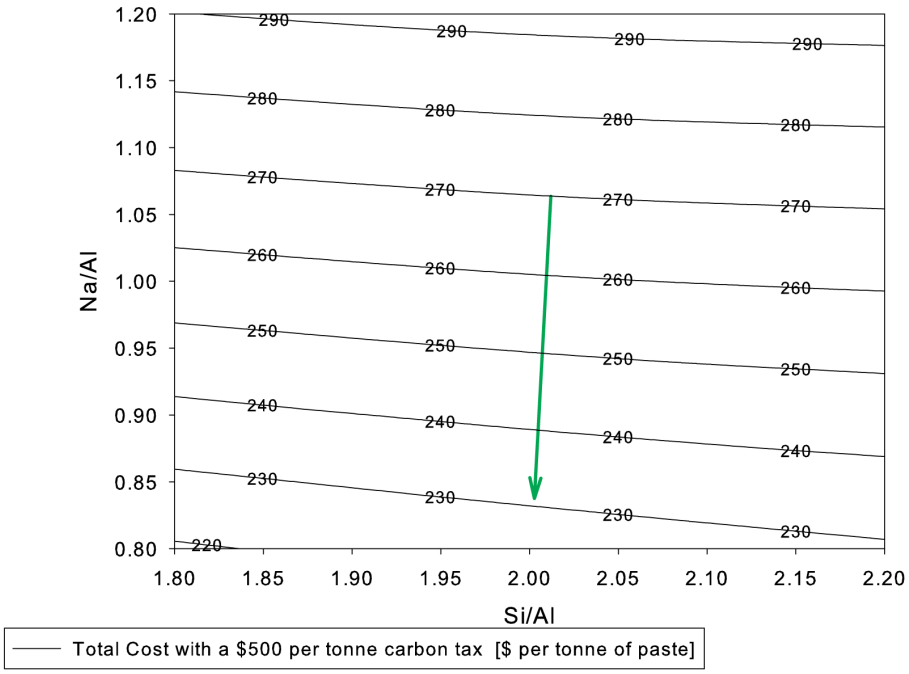

Figure 5-19 The total of cost of geopolymer production per tonne of paste with an excessively high carbon tax of $500 per tonne of CO_2-eq. Note that the direction of decreasing cost has rotated 45° anti-clockwise compared to Figure 5-18; this indicates that with a ridiculously high carbon tax the key parameter to optimise for lower cost is the Na/Al ratio, the Si/Al ratio now has almost no effect on the cost.

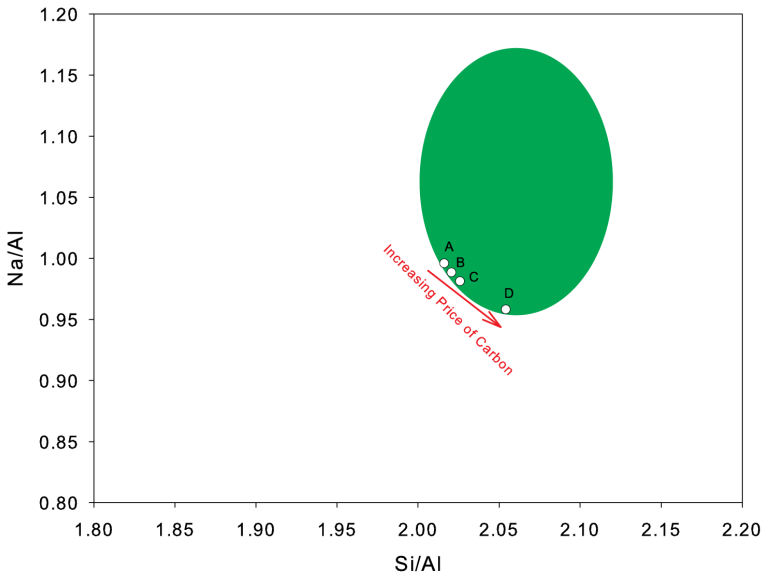

Figure 5-20 The effect of increasing price on carbon on the optimal geopolymer composition. The following prices of carbon were used: A = no carbon tax; B = $20 t^{-1}; C = $40 t^{-1} and D = $500 t^{-1}; Assuming the shaded area is a constraint based on suitable physical specifications and then finding the lowest cost after applying the carbon tax.

5.6. CHAPTER CONCLUSIONS

A geopolymer formulation that is optimised for stable compressive strength and minimum cost is insensitive to the additional cost burden of a reasonable carbon tax. As could have been expected, the carbon tax per tonne of geopolymer paste has a linear increase with increasing Na/Al ratio and Si/Al ratio, but the former ratio having a greater impact. This relationship occurs due to the large GHG burden associate with sodium hydroxide and sodium silicate production.

It was found the mean GHG emission rate was 240(50) kg-CO_2-eq per tonne of geopolymer paste, the standard deviation is the variation associated with changing geopolymer composition. The relative standard deviation (21%) indicates the GHG metric should be calculated on a case specific basis rather trying to use one value for geopolymers.

The mean carbon tax liability per tonne of paste was calculated as \$5(1) and \$7(1) for carbon taxes of \$20 and \$30 per tonne-CO_2-eq, respectively. The burden of the mean carbon tax liability as fraction of the unburdened cost of production is low, 3.6% and 5.0% for the \$20 and \$30 per tonne-CO_2-eq, respectively. Although the impact of a carbon tax has been conducted in isolation on geopolymers, it would have the impact of making geopolymers more competitive relative to OPC. The increased competitiveness of geopolymer would in turn drive increased innovation in further reducing the emissions from geopolymer.

CHAPTER 6: QUANTIFICATION OF THE EXTENT OF REACTION OF METAKAOLIN BASED GEOPOLYMERS USING XRD, SEM AND EDS.

This chapter is a typescript version of a published article:

Williams, R. P., R. D. Hart and A. van Riessen (2011) "Quantification of the extent of reaction of metakaolin based geopolymers using XRD, SEM and EDS." Journal of the American Ceramic Society **DOI: 10.1111/j.1551-2916.2011.04410.x.**

6.1. ABSTRACT

This study presents four independent methods to determine the fraction of metakaolin dissolution in geopolymers. Two quantitative XRD results agreed with two independent techniques using scanning electron microscopy (SEM). The fraction of the metakaolin consumed varied from 10(8) to 75(3) wt% for geopolymers with compressive strengths varying from 3.1(2) to 67(17) MPa, respectively. It is proposed that the increase in strength with higher consumption of metakaolin is primarily due to the resultant changes in the matrix chemistry rather than changes in the quantity of matrix. Input Si/Al ratios of 1.5, 1.9, 2.5 and 3.0 resulted in matrix Si/Al ratios of 1.7, 2.3, 3.8 and 21. As anticipated the fraction of metakaolin dissolved was found to vary with OH^- concentration. The area ratio method (ARM) and the partial or no known crystal structure method (PONKCS) have been identified as suitable for analysis of geopolymerisation by time resolved XRD. The shift in the amorphous peak or 'hump' was found to be insensitive and increased nonlinearly with the degree of reaction.

6.2. INTRODUCTION

The empirical formulations of geopolymers made with dehydroxylated kaolin (metakaolin) have been investigated by many researchers (Barbosa et al., 2000, Davidovits, 1987, Duxson et al., 2005b, Latella et al., 2008, Rowles and O'Connor, 2003, Rowles and O'Connor, 2009, Steveson and Sagoe-Crentsil, 2005a, Subaer et al., 2002). The physical properties of the geopolymers depend primarily on the ratio of Si/Al, M/Al and the water content (where M is often Na but may be K or other alkali elements) (Duxson et al., 2005b, Rowles and O'Connor, 2003). For example, the maximum compressive strength is generally achieved when the nominal composition of Si/Al = 1.8 to 2.2 and Na/Al = 0.9 to 1.2 (Rowles and O'Connor, 2003, Steveson and Sagoe-Crentsil, 2005a, Duxson et al., 2007a). However, alkali activation of the precursors to form geopolymer does not consume all the starting material as a result geopolymers are effectively composites consisting of the amorphous geopolymer matrix and a significant but undetermined amount of unreacted precursors.

A complication is that precursor kaolins, and the subsequent metakaolins, vary enormously and may, in part, be responsible for variations in results between materials made with effectively similar input chemistries. Kaolin particles vary from euhedral and platy to anhedral and may be tubular or even spherical. Platy particle widths may vary from 0.02 to 0.2 μm, while thickness can vary from 5 to 50 nm and N_2-BET specific surface areas ranging from 5 to 147 m^2/g have been recorded (Hart et al., 2002, Hughes et al., 2009). Tubular particles can have diameters from 30-150 nm and lengths from 0.1 to 0.53 μm. Mixtures of particle sizes and shapes within a single deposit are often common (Hart et al., 2003, Varajão et al., 2001). Properties such as particle size, shape and surface area will affect the degree and speed of dissolution of metakaolin and these parameters are largely maintained in the conversion of kaolin to metakaolin (Roy et al., 1955). Studies by Granizo et al. (2000) of NaOH dissolution of metakaolin from two only slightly different precursor kaolins demonstrated distinctly different degrees of dissolution. The calcination temperature is also significant; Wang

et al. (2010) showed the compressive strength of geopolymer varied from 73(2) MPa to 117(2) MPa by increasing the kaolin calcination temperature from 800°C to 900°C (4 hour soak time), where the value in brackets is the uncertainty in the last digit. While Subaer et al. (2002) demonstrated that residual metakaolin within a geopolymer will retain its morphology. Determining the extent of reaction of the metakaolin within a geopolymer is an important step in determining the chemistry of the geopolymer matrix.

The limitation of not knowing how much of the precursor has been consumed during the reaction and thus the final composition of the geopolymer matrix significantly limits understanding of the true compositional differences between materials, the different kinetics of geopolymer mixes or the bonding within geopolymers. The bulk composition does not correlate to the micro chemistry of the geopolymer matrix as a result of incomplete dissolution of solid feedstocks. The ‘degree of reaction’ has been investigated via: acid leaching (Fernández-Jiménez et al., 2006, Songpiriyakij et al., 2010); NMR analysis (Rowles et al., 2007); Energy dispersive spectroscopy (Rowles and O'Connor, 2009); FTIR (Rees et al., 2007a, Rees et al., 2007b), AC impedance spectroscopy (Provis et al., 2008), calorimetry (Granizo et al., 2000), in situ EDXRD (Provis and van Deventer, 2007b) and computer modelling (Provis and van Deventer, 2007a, Provis et al., 2010, Yunsheng et al., 2009). These methods measure a range of complementary information that relate to the ‘degree of reaction’, including the amount of dissolution of the solid starting materials; the formation of intermediate amorphous polymer phases; and conversion of the intermediate phases into the final amorphous geopolymer phases.

Rowles and O’Connor (2009) reported incongruent dissolution of Al and Si from metakaolin, however this was based on energy dispersive spectroscopy (EDS) of unreacted metakaolin particles. Their result cannot be reconciled with the EDS results of the geopolymer matrix in the same study and the authors’ NMR studies (Rowles et al., 2007). Careful reanalysis of the EDS data for the geopolymer matrix, rather than unreacted particles, of Rowles and O’Connor (2009) suggests there was congruent metakaolin dissolution. Their lower than expected Na content can be explained as alkali is leached

out in water during polishing (Ly et al., 2006, Rowles and O'Connor, 2003). The unreacted metakaolin composition measured by Rowles and O'Connor (2009) with EDS of Si/Al > 1, rather than the expected Si/Al =1, could be an artefact of measuring particles of a similar size to the information volume of EDS surrounded by a matrix with Si/Al > 1.

XRD patterns of metakaolin and geopolymers display diffuse scattering, sometimes referred to as broad amorphous humps. For metakaolin the hump is asymmetric with a peak maximum at approximately d ≈ 4 Å (22° 2θ for Cu Kα) while the geopolymer hump is symmetric with a peak maximum at d ≈ 3.2 Å (27-28° 2θ for Cu Kα). While many have noted that the peak shift demonstrates the reaction has occurred, to date, deconvolution of the precursor and product geopolymer peaks has proven difficult. For example, Provis and van Deventer (2007b) studied geopolymerisation kinetics with *in situ* energy dispersive diffraction and calculated the relative extent of reaction using a linear combination of the initial geopolymer pattern and the final geopolymer pattern.

Quantitative analysis of metakaolin dissolution and geopolymer formation has proved challenging due to the poor likelihood of any geopolymer standard consisting of pure geopolymer and the difficulty of determining how much of the material is geopolymer and how much is precursor metakaolin. We present two XRD methods to quantify the metakaolin content in the geopolymer. The first method is similar that of standard additions, where pure metakaolin is added to the geopolymer. The second XRD method is the partial or no known crystal structure (PONKCS) method (Scarlett and Madsen, 2006). This method requires a pure specimen of the phase with unknown structure or a specimen for which all the other phases can be readily quantified. Essentially a calibration constant is calculated for that phase compared to an internal standard, where the constant is usually proportional to the atomic mass per unit cell for crystalline materials. We also use two scanning electron microscope (SEM) based methods namely point counting to quantify the metakaolin content in the geopolymer sample and energy dispersive x-ray spectroscopy (EDS) to determine the composition of the resulting geopolymer matrix.

6.3. MATERIALS AND METHODS

6.3.1. Sample preparation

Sodium silicate solutions were prepared by dissolving silica fume (Australian Fused Materials) in sodium hydroxide solution (AR Grade, Sigma-Aldrich) at 70°C for 24 hours. Metakaolin was prepared by the dehydroxylation of kaolin (SnoBright 65, Unimin Pty Ltd, Welshpool, WA, Australia) by heating to 750°C and soaking at this temperature for 24 hours. Geopolymer samples were formed by mixing metakaolin and sodium silicate solution, then curing in sealed containers at 70°C for 24 hours. The amounts of NaOH, SiO_2, metakaolin and water were chosen to achieve input ratios of Si/Al, Na/Al and H/Si, detailed in Table 6-1, calculated using the equations described by Williams and van Riessen (2010) and in Chapter 4. Following 7 day compressive strength testing, fractured samples were crushed using a tungsten carbide ring mill. Weighed aliquots, corresponding to spikes of 10, 20, 40, 70 and 100% metakaolin, of the precursor metakaolin were added, before packing into flat plate holders for XRD analysis.

6.3.2. Compressive strength testing

Compressive strength testing was carried out approximating the methodology of ASTM C39 for concrete specimens. Cylindrical samples with a 2:1 height to diameter ratio were cut with a precision diamond blade such that the ends were perpendicular to the sides. A minimum of 4 samples per batch were tested. Following demoulding, the samples were air dried for 1 day prior to compressive strength testing. An EZ50 (Lloyd Instruments Ltd, West Sussex, United Kingdom) was used to apply a constant stress rate of 0.25 MPa/s, after a 50 N preload, until failure. The load and extension from preload (thus stress and strain) were recorded for analysis. Note: The Young's modulus were determined by the gradient of the stress-strain curve during compressive testing, it is repeatable between samples, but is an order of magnitude less that literature values, see section 3.7 for more details

6.3.3. XRD data collection

X-ray diffraction patterns were obtained using Cu Kα radiation with a Bruker D8 Advance diffractometer equipped with a LynxEye detector (Bruker-AXS, Karlsruhe, Germany). Powder patterns for the area ratio method (ARM) analysis were collected from 10-90° 2θ with a nominal step size of 0.03° at 1.0 step/s, using a 0.3° divergence slit and 2.5° primary and secondary Soller slits. The XRD patterns with ~5 wt% fluorite internal standard for PONKCS analysis were measured with the same settings except with a nominal step size of 0.02°. A knife edge collimator and tight detector discriminator settings were applied to reduce air scatter and iron fluorescence signals.

6.3.4. XRD analysis

The XRD data were modelled using TOPAS 4.2 software (Bruker-AXS, Karlsruhe, Germany). The quality of the fit of the refined structure models to the data was determined by visual inspection of the difference plot and statistically by figures of merit and the estimated standard deviation of individual parameters. The figures of merit monitored in this case were the weighted profile factor (R_{wp}) and the goodness of fit (GOF).

6.3.5. Area ratio method analysis

The Bragg peaks from anatase and quartz were modelled using structural models and the diffuse scattering from the metakaolin and geopolymer phases were each modelled with a split pseudo Voigt peak (SPV, i.e. asymmetric pseudo Voigt). The backgrounds were modelled with first order Chebychev polynomials. Each set of six diffraction patterns was refined simultaneously giving a parametric refinement (Stinton and Evans, 2007). This reduces the parameter correlation of the peak shape parameters and the background parameters. Thus the metakaolin and geopolymer peaks for each dataset of six diffraction patterns were constrained to have the same refined peak position and refined shape parameters (left and right half width at half maximum, and left and right Lorentzian/Gaussian mixing parameters). The crystalline phases were allowed to refine independently in each dataset.

The measured areas of metakaolin and geopolymer (A_{MK} and A_{GP}) can be predicted by equations 6.1 and 6.2, where S_{MK} is the weight percent of metakaolin spike added to the sample and k_{MK} and k_{GP} are the constants for metakaolin and geopolymer phases. The k constants are similar to the $I/I_{corundum}$ and ZMV (average atomic number (Z) x mass (M) x volume (V) of unit cell) values used for crystalline phases when using the reference intensity ratio or Rietveld methods to account for the different scattering strength of each phase. $C_{MK/MK}$ and $C_{MK/GP}$ are the weight fractions of metakaolin in the original metakaolin and geopolymers, respectively. These areas can be combined using equation 6.3 to calculate the metakaolin content (Y_{MK} as wt%). Combining equations 6.1, 6.2 and 6.3 and setting $C_{MK/MK}$ = 1 (i.e. 100%) yields Equation 6.4, the $C_{MK/GP}$ of the original sample is given by y-intercept of a linear regression of Y_{MK} and S_{MK}. *Note:* the gradient plus this intercept should be equal to one.

$$A_{MK} = \frac{C_{MK/MK}S_{MK} + C_{MK/GP}(1 - S_{MK})}{k_{MK}} \quad (6.1)$$

$$A_{GP} = \frac{(1 - C_{\frac{MK}{MK}})S_{MK} + (1 - C_{\frac{MK}{GP}})(1 - S_{MK})}{k_{GP}} \quad (6.2)$$

$$Y_{MK} = \frac{k_{MK}A_{MK}}{k_{MK}A_{MK} + k_{GP}A_{GP}} \quad (6.3)$$

$$Y_{MK} = (1 - C_{MK/GP})S_{MK} + C_{MK/GP} \quad (6.4)$$

This method could also be applied to time resolved diffraction data of geopolymer curing; allowing the relative degree of metakaolin dissolution or the concentration of other amorphous phases to be determined as a function of time. The ARM analysis could be applied in a standardless fashion to time resolved diffraction data to determine the formation and conversion kinetics of the intermediate reaction products. An intermediate phase of interest is amorphous aluminosilicate polymer which converts to geopolymer matrix, as predicted by kinetic modelling (Provis and van Deventer, 2007a) and observed by ex situ NMR studies (Fernández-Jiménez et al., 2005).

6.3.6. PONKCS method analysis

The PONKCS method requires the calibration of the phase with an unknown structure by measuring the diffraction pattern of the phases with an internal standard of known concentration. The calibration constant in TOPAS is referred to as ZM as it is usually the atomic mass per unit cell for a crystalline phase. The diffraction data of the metakaolin with 5 wt% fluorite was loaded into TOPAS, and then the fluorite, quartz and anatase were modelled with structural models and the metakaolin was modelled using a Pawley model (i.e. space group, no structure). For metakaolin, the space group was C1, and the starting lattice parameters were those published by White et al. (2010), the crystallite size and intensity of each reflection were allowed to refine. This approach resulted in too many reflections being generated, creating a high degree of parameter correlation. To overcome this reflections with large errors in the intensity (>20%) were removed and the refinement repeated – 20 reflections were used. The choice of space group has no impact on this method as it is essentially just a way of linking the intensities together in the modelling software. The intensity of the reflections, crystallite size and lattice parameters were fixed, an overall phase scale was allowed to refine which equalled approximately 1.000. The ZM value for the metakaolin ZM_{MK} was calculated using Equation 6.5 (Scarlett and Madsen, 2006). Where W and S are the known weights and the intensity scale factors for each phase, shown by the subscripts MK and S for metakaolin and the internal standard respectively. The ZM_{MK} value in this case has no physical meaning as the scale factor for the metakaolin is artificially equal to 1. The ZM_{MK} value was added to the metakaolin phase in TOPAS and saved for the analysis of the geopolymer samples.

$$(ZMV)_{MK} = \frac{W_{MK}}{W_S}\frac{S_S}{S_{MK}}(ZMV)_S \tag{6.5}$$

The diffraction pattern of the geopolymer samples with 5 wt% fluorite were loaded into TOPAS, and as before, the fluorite, quartz, anatase and any zeolites, if present, were modelled using structural models. The metakaolin

phase was modelled with the model calibrated above, the geopolymer phase(s) (also amorphous) was modelled with a single Voigt peak, the intensity of this peak was not used for any further calculations but it was required to fit the metakaolin phase properly. A Rietveld refinement combined with the use of an internal standard gave the absolute phase abundances of the metakaolin and geopolymer.

6.3.7. Determination of water content

To allow the calculation of the input concentration of metakaolin in the geopolymer samples the water loss must be determined. The degree of dehydration of the samples between synthesis and testing by XRD/SEM was measured thermo-gravimetrically. The samples were dehydrated and dehydroxylated by heating to 600°C for 30 minutes and the mass loss recorded. Assuming that all the water and other hydroxyls will decompose at this temperature the water loss prior to this step can now be determined.

6.3.8. Energy dispersive spectroscopy

Polished samples of the geopolymers (<1 μm finish), were investigated using a Zeiss Neon cross beam scanning electron microscope (SEM) (Carl-Ziess, Oberkochen, Germany). Energy dispersive spectra were collected at 5,000-10,000 counts per second for 100 live seconds on an Oxford instruments INCA-350 system (Oxford Instruments, Abingdon, Oxfordshire, U.K.) using a 15 keV primary electron beam. The EDS results were calibrated against well characterised kaolinite and feldspar samples covering the range of Na, Al and Si observed in these samples. Weight fractions were normalised to 100% and oxygen calculated. Molar ratios were obtained by dividing by the atomic weight.

6.3.9. Point counting analysis

SEM micrographs of the polished samples were collected with the in-lens secondary electron detector. Point counting was used to determine the unreacted metakaolin in the geopolymer matrix using a procedure modified

from ASTM C 1356 M. A similar method was employed by Feng et al. (2004b) to determine the degree of hydration in cement pastes. A grid was superimposed on the SEM image, and the phases were determined and counted at a magnification setting of 1,000-5,000X, which corresponds to an image field of view of 30 to 60 μm. A 13 x 9 grid was used giving 117 points per image, and approximately 30 images per sample, were examined so that 3000 points of geopolymer were counted per sample, allowing for pores and other impurities. Metakaolin was recognisable by its generally higher brightness and different texture to the geopolymer matrix when using secondary electron imaging.

6.3.10. Calculation of fraction of metakaolin reacted

The fraction of metakaolin that reacted in the original geopolymer sample can be calculated as the complement of the concentration of unreacted metakaolin in the geopolymer ($C_{MK/GP}$) divided by the input amount of metakaolin used to produce the geopolymer after correcting for sample dehydration.

6.4. RESULTS AND DISCUSSION

6.4.1. XRD data analysis

The XRD patterns for metakaolin and the geopolymer samples are shown in Figure 6-1 and the series of XRD patterns from the metakaolin spiked geopolymers of sample 1 are shown in Figure 6-2. In the XRD patterns both the original metakaolin and subsequent geopolymer contain minor amounts of quartz and anatase. The general trend of the amorphous peak to shift to lower 2-theta with increasing metakaolin spike is clear, while the presence of a distinguishable hump due to metakaolin is only apparent for large amounts (≥70%) of added metakaolin. A small broad peak from the 100% metakaolin samples at approximately 20° 2θ corresponds to the sawtooth hk0 reflection of disordered kaolin (Roy et al., 1955). This remaining reflection suggests that some residual structural order exists in the two dimensional sheet of the aluminosilicate material which appears to be completely disrupted by the reaction to form geopolymer. The disordered kaolin reflection was modelled using a Voigt peak, to ensure that it did not affect the modelling of the other peaks.

Table 6-1. The bulk geopolymer sample composition (elemental ratio), compressive strength, strain at maximum stress, Young's Modulus and the dehydration between synthesis and measurement.

Geopolymer Sample number	Si/Al	Na/Al	H/Si	Solution Si/Na	Solution H_2O (wt%)	Compressive strength (MPa)	Strain at max stress (%)	Young's Modulus (GPa)	Dehydration (wt%)
S1	1.92	1.00	5.53	0.84	53.1	67(17)	5.0(9)	2.0(1)	9.2(3)
S2	2.50	1.26	6.09	1.1	51.8	33(6)	2.8(3)	1.76(6)	18.7(3)
S3	3.08	1.53	5.94	1.3	48.9	3.1(2)	2.5(1)	0.24(2)	9.1(3)
S4	1.55	1.07	6.47	0.45	58.5	14(4)	1.9(2)	1.0(1)	14.9(3)

Values in parentheses correspond to the least significant figure in the standard deviation to the left.

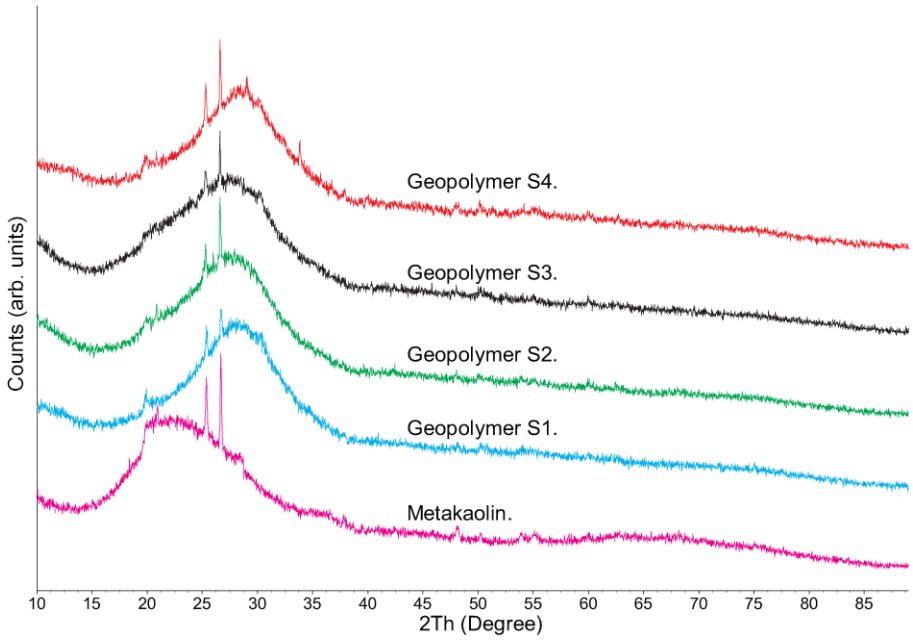

Figure 6-1 XRD patterns of metakaolin and the four geopolymer samples. Patterns have been offset for clarity.

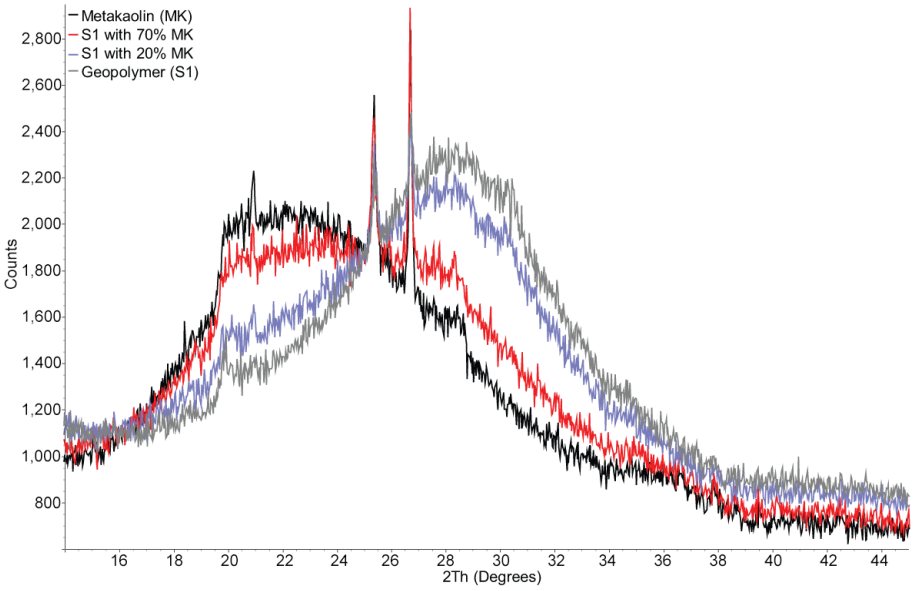

Figure 6-2 Selected XRD patterns of geopolymer sample 1 and the series of metakaolin spiked geopolymers (sample 1).

A common qualitative analysis of the degree of geopolymer reaction is to measure how far the amorphous hump shifts to higher 2θ. The diffuse scattering was modelled with only one peak for the geopolymer samples with

increasing metakaolin content. The curve for peak shift saturates quickly at amounts greater than 60% geopolymer, i.e. 40% metakaolin spike (Figure 6-3). This suggests that a simple peak shift method would be unresponsive to small amounts of metakaolin in geopolymer, and therefore, unable to be used to determine unreacted metakaolin in a system which has mostly reacted material. In this case, the position was measured by using one split pseudo Voigt peak refined independently for each pattern. Given that peak shift is nonlinear and is insensitive to changes in metakaolin content it will not be considered further. It was considered that that calculating the metakaolin content using the area of the metakaolin hump and geopolymer hump would have a linear response leading to the work in the subsequent sections.

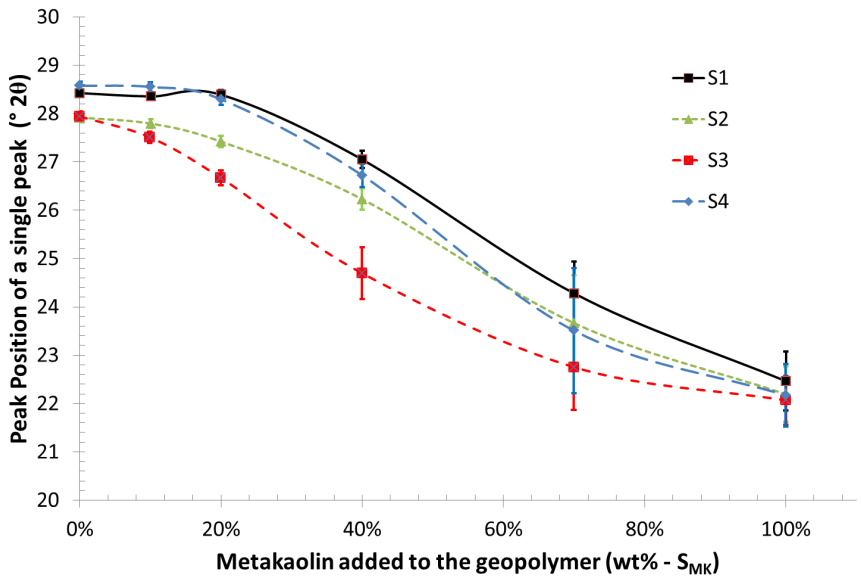

Figure 6-3 Peak shift of a single peak for all four series of geopolymer samples. Note the saturation of the peak shift when a <20 wt% metakaolin is added.

6.4.2. Area ratio method analysis (x-ray diffraction)

The XRD patterns and associated area ratio method (ARM) modelling from 14-45° 2θ are shown in Figure 6-4. The refined patterns show the changes in the diffuse scattering intensity (decreasing geopolymer, increasing

metakaolin) as metakaolin is added, the Bragg peaks for anatase and quartz and the combined residual.

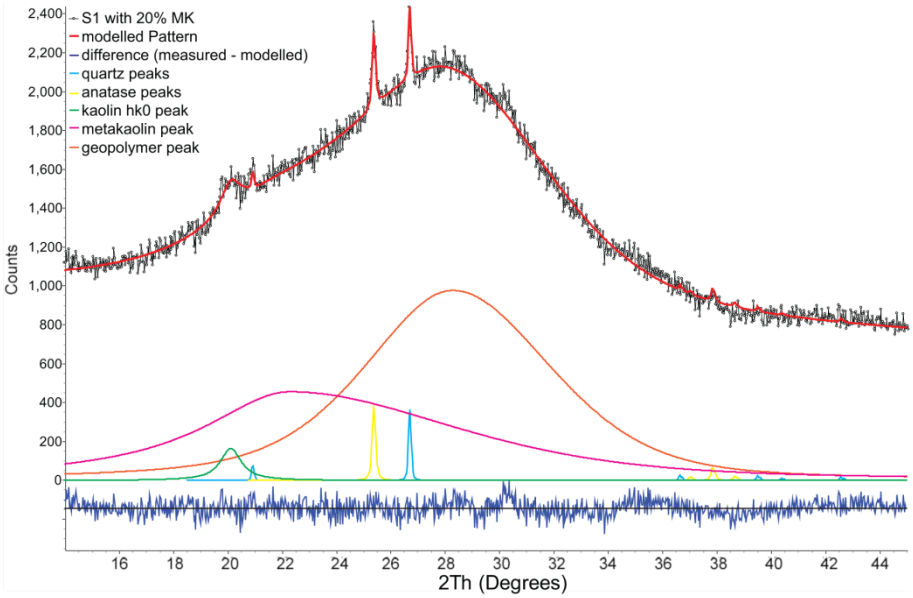

Figure 6-4 Typical area ratio method (ARM) XRD refinement – sample 1 (S1) with 20% metakaolin, modelled Bragg peaks for quartz and anatase and modelled diffuse peaks for metakaolin spiked geopolymer samples.

The refined positions of the metakaolin and geopolymer peaks are shown in Table 6-3. The peak areas were normalised to the maximum area of each peak type using Equation 6.3. The mean of four determinations was calculated for metakaolin at 4.02(2) Å or 22.0(1)° 2θ and geopolymer at 3.18(3) Å, or 27.7(3)° 2θ for Cu Kα radiation.

Figure 6-5 shows the calculated mass fraction of metakaolin (Y_{MK}) in the spiked sample versus the mass fraction of metakaolin added as a spike (S_{MK}), yielding a linear relationship. The y-intercept is the weight concentration of unreacted metakaolin in the original geopolymer sample ($C_{MK/GP}$), shown in Table 6-3. The quantity of metakaolin added to the sample, after corrections for dehydration, are provided along with the calculated fraction of reaction are also in Table 6-3. The result is highly linear for all determinations, with a small error and very high coefficient of variation (R^2) (Table 6-2).

Table 6-2. Linear regression data of measured metakaolin concentration (Y_{MK}) in the spiked sample vs. concentration of metakaolin spike (S_{MK}). The Y_{MK} intercept is equal to the concentration of metakaolin remaining in the geopolymer sample.

Sample No.	Line of best fit. (const = wt fraction of metakaolin)	R^2	M+C (ideal is 1)
S1	Y_{MK} = 0.876(10) S_{MK} + 0.129(5)	0.9995	1.005(12)
S2	Y_{MK} = 0.796(16) S_{MK} + 0.183(8)	0.9984	0.98(2)
S3	Y_{MK} = 0.731(41) S_{MK} + 0.257(22)	0.9878	0.99(5)
S4	Y_{MK} = 0.891(31) S_{MK} + 0.126(16)	0.9953	1.02(3)

Values in parentheses correspond to the least significant figure in the standard error from the refinement

Table 6-3. Refined geopolymer and metakaolin peak positions, dehydration corrected input metakaolin concentration (i.e. quantity of metakaolin added to sample), calculated concentration of unreacted metakaolin in the geopolymer and ($C_{MP/GP}$) and the fraction of original metakaolin that reacted.

				Concentration of unreacted metakaolin $C_{MK/GP}$ (wt%)			Fraction of MK Reacted (wt%)		
Sample No	Peak Metakaolin position (Å)	Peak Geopolymer position (Å)	Input Corrected metakaolin (wt%)	XRD (ARM)	XRD (PONKCS)	SEM (Point count)	XRD (ARM)	XRD (PONKCS)	SEM (Point count)
S1	3.99(1)	3.155(7)	43.8(2)	12.9(5)	13.5(2)	13.2(4)	71(1)	69.2(5)	69.8(9)
S2	4.03(2)	3.220(6)	38.0(2)	18.3(8)	20.0(2)	18.3(7)	52(2)	47.4(6)	52(2)
S3	4.04(2)	3.210(6)	28.6(2)	26(2)	27.7(1)	25.1(11)	10(8)	3.3(6)	12(4)
S4	4.02(1)	3.152(7)	51.1(2)	13(2)	9.8(2)	9.7(3)	75(3)	80.8(4)	81(1)

Values in parentheses correspond to the least significant figure in the standard error from the refinement

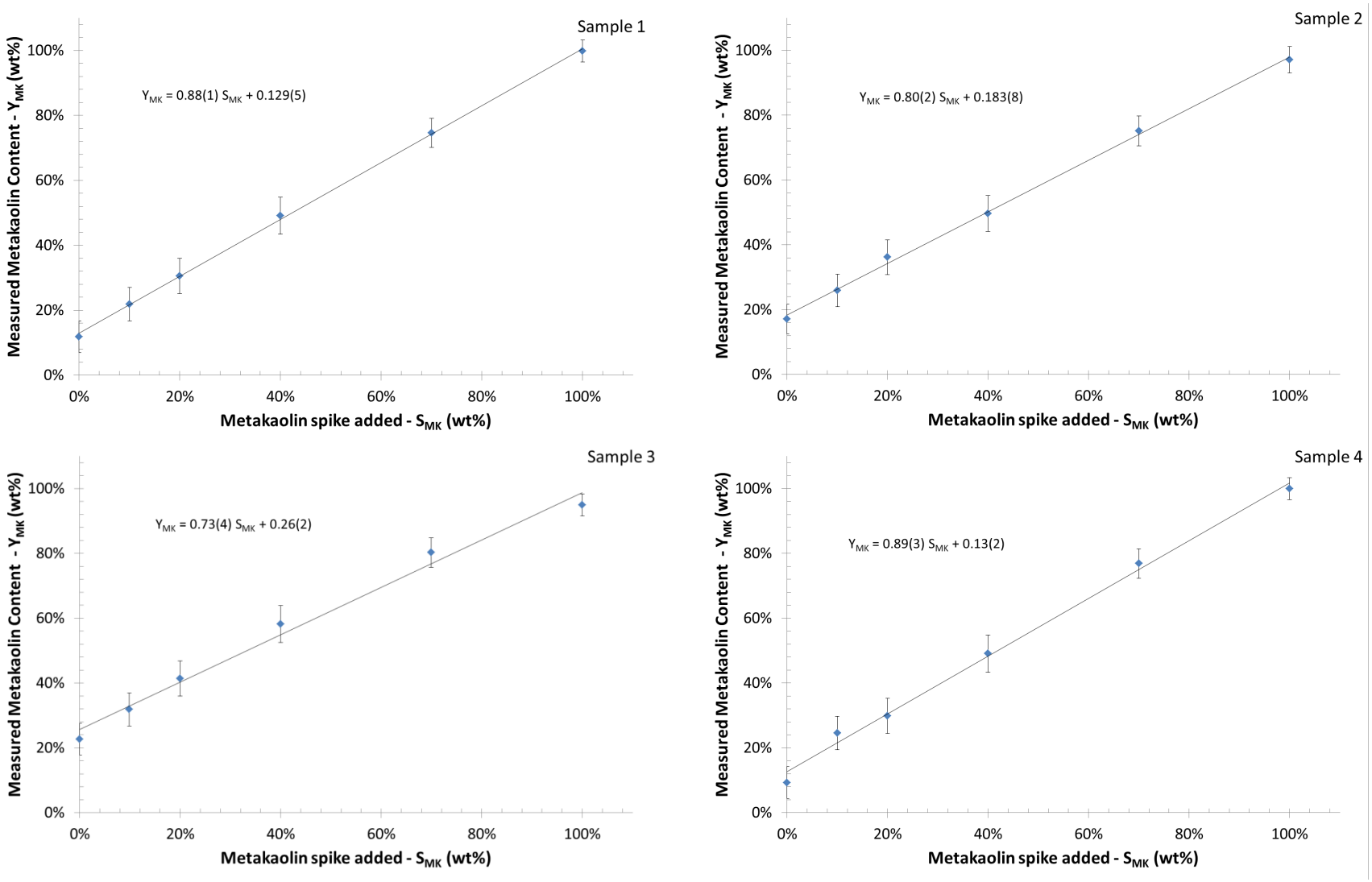

Figure 6-5 Calculated mass fraction of metakaolin (YMK) vs. mass fraction of metakaolin spike (SMK). The y-intercept indicates the concentration of metakaolin remaining in the geopolymer (CMK/GP).

The linearity of the S_{MK} vs Y_{MK} curves indicates that the ratio of k_{MK} to k_{GP} is appropriately estimated when the area of each peak type is normalised, hence a $k_{MK}/k_{GP} = 1$ was used. The correction factors k_{MK} and k_{GP} are not calculated; they are accounted for by normalising the peak areas. If the ratio of the assumed correction factors k_{MK^*} and k_{GP^*} were not equal to the ratio of the physical correction factors k_{MK} and k_{GP}, they will not cancel out and hence would not lead to a linear equation (Equation 6.6).

$$Y_{MK} = \frac{-\left((1-C_{\frac{MK}{GP}})S_{MK} + C_{\frac{MK}{GP}}\right) * {k^*_{MK}}/{k_{GP}}}{\left(k^*_{MK}k_{GP}\left(C_{\frac{MK}{GP}}-1\right) + k^*_{GP}k_{MK}\left(1-C_{\frac{MK}{GP}}\right)\right)S_{MK} - k^*_{MK}k_{GP}C_{\frac{MK}{GP}} - k^*_{GP}k_{MK}\left(1+C_{\frac{MK}{GP}}\right)} \quad (6.6)$$

The sum of the intercept and the gradient (both dimensionless quantities) should be equal to $C_{MK/MK}$ or one (100%), providing a check for self-consistency. For all sample series, this quantity is equal to one within experimental uncertainties (Table 6-2).

6.4.3. PONKCS method analysis (x-ray diffraction)

The results using the PONKCS XRD method are shown in Table 6.3, the calculated $C_{MK/GP}$ values agree with those calculated by the ARM XRD within 2 standard errors for geopolymer samples 1 to 3, and within 3 standard errors for geopolymer sample 4.

6.4.4. Point counting analysis (scanning electron microscopy)

Figure 6-6 shows electron micrographs of geopolymer sample 1. The 15 keV secondary electron images show the unreacted metakaolin as a brighter material. EDS analysis confirmed this was metakaolin by lack of sodium and a Si/Al ~ 1 which is consistent with the composition of the starting metakaolin ($Al_2Si_2O_5$). Similarly, geopolymer was confirmed by the presence of sodium and increased Si/Al ratios.

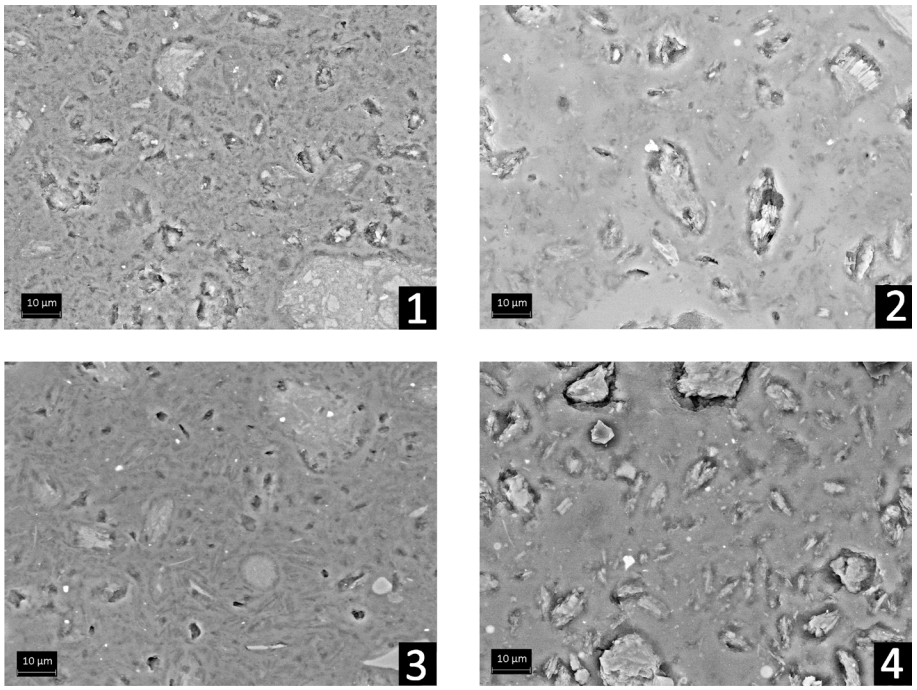

Figure 6-6 Typical microstructure of geopolymer samples 1 to 4. The unreacted metakaolin is encapsulated by the glassy geopolymer matrix.

A series of micrographs from each geopolymer mix was used to determine the concentration of unreacted metakaolin ($C_{MK/GP}$) using a point counting technique, with quartz, anatase and pores being ignored (Table 6-3). The agreement between the volume fractions of unreacted metakaolin found by point counting is close to the values for weight fraction determined by ARM XRD analysis and PONKCS analysis (Table 6-3). Conversion of the volume fraction to weight fraction using the density was not conducted due to the wide differences in the literature for values of density of both metakaolins and geopolymers. However, the broad agreement between XRD and SEM point counting supports the XRD results. If there were sodium silicate solution or solid in the pore space it would be ignored which would not affect the calculation of the extent of reaction, however would bias the estimates of matrix composition. The estimated Si/Al and Na/Al ratio would be higher than the true values if there were a large fraction of sodium silicate in the pores.

6.4.5. Calculation of fraction of metakaolin reacted

The unreacted metakaolin in the geopolymer ($C_{MK/GP}$) values determined from the ARM analysis, PONKCS analysis and the point counting were used to calculate the fraction of metakaolin consumed, as described above, with results shown in Table 6-3. There is excellent agreement between the PONKCS XRD, ARM XRD and SEM point counting methods. Assuming congruent Al and Si dissolution of the metakaolin, this data can also be used to calculate the average elemental ratio of the geopolymer matrix formed. These results explain why there is such a large variation in compressive strength between different samples. Sample 3 had a compressive strength of only 3.1(2) MPa, because only a very small fraction of the precursor metakaolin reacted producing a small amount of matrix to bind the unreacted particles while the matrix that did form had such high Si/Al and Na/Al ratios that it was intrinsically weak.

Examination of the concentration of OH^- ions in the activating solutions reveals, unsurprisingly the fraction of metakaolin that dissolves depends strongly on [OH^-], see Figure 6-7. This indicates that the metakaolin may stop dissolving as the [OH^-] concentration drops during the reaction. This is directly affected by the Si/Na ratio of the activating solution, (Figure 6-8) as increasing the Si content decreases OH^- of the solution. This provides an insight to why increased Si/Al ratio decreases the extent of reaction.

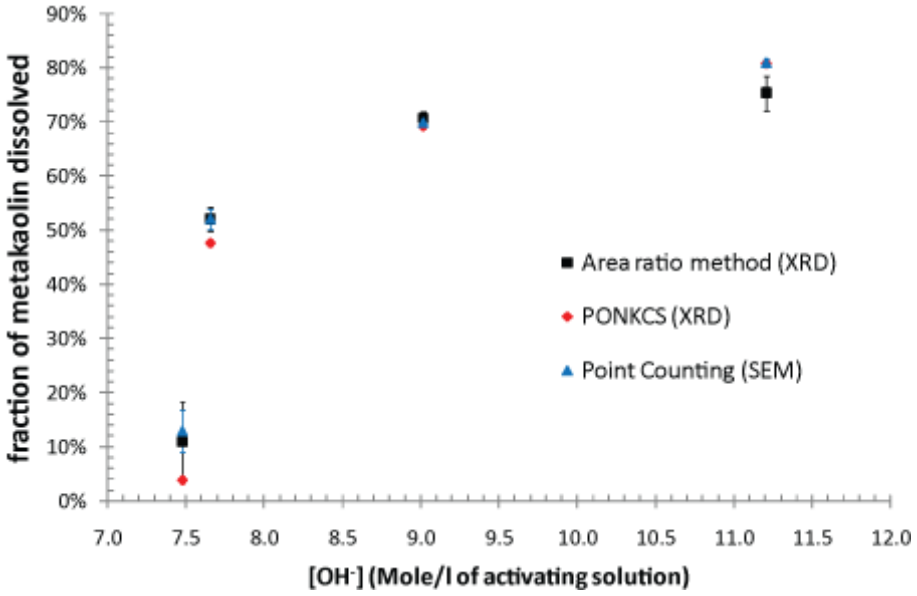

Figure 6-7 Degree of dissolution of the metakaolin compared to OH^- concentration (Mole/l) of the activating solution.

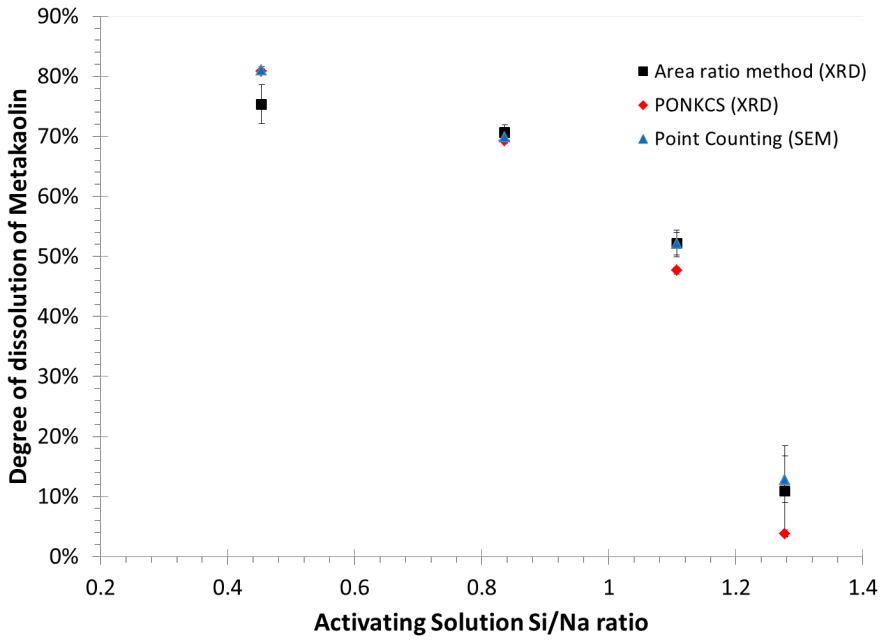

Figure 6-8 Degree of dissolution of the metakaolin compared to Si/Na ratio of the activating solution.

Table 6-4. The calculated elemental ratio for the bulk sample (as synthesised) and the resulting calculated matrix composition as determined by the area ratio method (ARM) XRD, PONKCS XRD method and SEM point counting. The geopolymer matrix composition was corrected for dehydration (Table 1) prior to measurement and the fraction of metakaolin that reacted (Table 6-3). Sensible EDS data could not be collected for sample 3, as the regions of geopolymer matrix were much smaller than the information volume of the EDS analysis.

	Bulk Sample			Geopolymer matrix estimated from ARM XRD		Geopolymer matrix estimated from PONKCS XRD		Geopolymer matrix estimated from point counting		Geopolymer matrix measured by EDS	
Sample	**Si/Al**	**Na/Al**	**H/Si**	**Si/Al**	**Na/Al**	**Si/Al**	**Na/Al**	**Si/Al**	**Na/Al**	**Si/Al**	**Na/Al**
S1	1.92	1.00	5.53	2.28	1.41	2.26	1.44	2.29	1.43	2.09	1.34
S2	2.50	1.26	6.09	3.84	2.42	3.98	2.64	3.84	2.42	2.81	1.49
S3	3.08	1.53	5.94	20.6	14.7	51.95	39.84	17.52	12.4	-	-
S4	1.55	1.07	6.47	1.72	1.42	1.66	1.32	1.67	1.32	1.74	1.34

6.4.6. Energy dispersive spectroscopy (scanning electron microscopy)

Energy Dispersive Spectroscopy (EDS) performed on each sample (with multiple (>20) analyses of the geopolymer matrix) show that for sample 1, the Si/Al ratio is 2.09 and the Na/Al ratio is 1.34, which is similar to the expected

Si/Al = 2.28 and Na/Al = 1.41, calculated from the fraction of metakaolin using the ARM XRD method, which is clearly different from the input Si/Al ratio of 1.92. Similar data were obtained for sample 4, where Si/Al was found to be 1.74 (1.72 from ARM XRD) and Na/Al = 1.34 (1.42 from ARM XRD). For sample 2, the Si/Al and Na/Al ratio of 2.81 and 1.49, respectively measured by EDS is significantly less than the predicted Si/Al and Na/Al ratio from ARM, PONCKS and Point Counting and much closer to the bulk composition. The most likely reason is that there were small unreacted fragments of unreacted metakaolin within the matrix, adding Si and Al in equal proportions to the information volume of the EDS determinations, reducing both the Si/Al and Na/Al ratio from the actual matrix composition.

The values of the geopolymer matrix for sample 3 were not obtained as there were no regions of geopolymer free from metakaolin larger than the EDS information volume. Limited determinations found Si/Al values of approximately 4.0, well below the ARM XRD determined value of 20 but well above the input ratio of 2.00. The 99% information depth for Si, Al and Na x-rays using a 15 keV excitation beam in geopolymer matrix, determined using Casino (Drouin et al., 2007) is approximately 2.2 μm for the calculated geopolymer matrix for all samples.

The difficulty in obtaining reliable EDS data even for samples where a large fraction of the metakaolin has reacted (>70%) can be seen in Figure 6-9 where sample 1 has been sectioned using the focussed ion beam (FIB) revealing the surface perpendicular to the polished sample surface. The geopolymer region is on the right and the corresponding metakaolin on the left. Typical geopolymer only regions were no greater than 2-3 μm which is of a similar size to the information volume of x-rays generated by 15 keV electrons, resulting in a high probability that the EDS spectrum contains information from regions of geopolymer matrix and unreacted metakaolin. The area contains many pores; two main size distributions are typically observed: large elongated pores 1-2 μm long by 0.1 μm wide and a much finer range typically <10 nm. The estimated thickness of unreacted metakaolin is 0.5 to 2 μm, which is smaller than the information depth hence, accurate EDS analysis cannot be conducted on the unreacted metakaolin

because the EDS spectrum will have contributions from the metakaolin and the geopolymer matrix beneath.

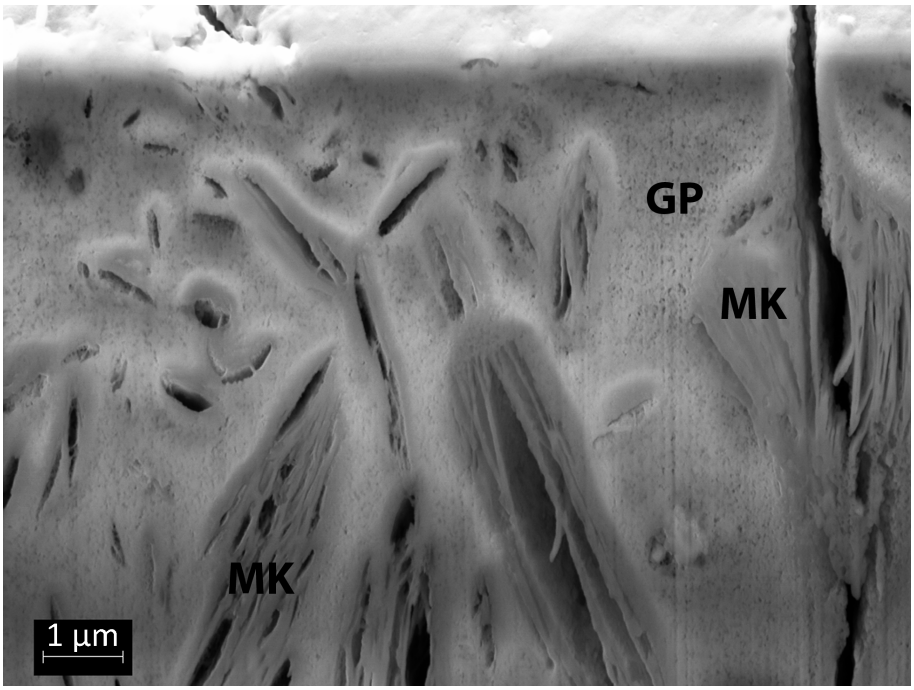

Figure 6-9 A cross section view of the sample 1, this surface has been exposed by milling with a focused ion beam (FIB). The image illustrates the difficulty with quantitative EDS of geopolymer, although there may appear to be no unreacted particles from the surface there are very few regions of 2x2 µm below the surface without metakaolin, hence EDS measurement of only matrix (GP) or only metakaolin (MK) will be unlikely.

6.4.7. Sampling volume

The four methods presented here provide similar results, particularly the two XRD and point counting methods. The main factors to consider in deciding which method is most suitable for continued use for such heterogeneous samples must be: (1) the variability, (2) the sampling volume, (3) possibility of systematic errors and (4) the cost or time taken for the analysis. The time taken to obtain results using point counting was considerably longer than the time required to obtain the XRD results while the amount of material examined using XRD is much greater and more likely to be more representative of the bulk materials. Similarly to point counting, the time taken to obtain SEM/EDS results was considerably longer than the time

required to obtain the XRD results and again the EDS analyses only examine a very small volume of the geopolymer material. The fraction of material examined is also compromised as there are very few areas of geopolymer large enough to obtain a spectrum free from interference by intruding metakaolin or other partially reacted materials. The information volume calculated with assistance of AbsorbDX v1.1.4 (Bruker-AXS, Germany) for an XRD measurement for these samples is approximately $4x10^{-9}$ m^3 for a single XRD measurement, compared to $4x10^{-16}$ m^3 for point counting and $8x10^{-17}$ m^3 for EDS analysis (20 spectra), calculated with CASINO. The XRD methods have information volumes 7 to 8 orders of magnitude larger than the SEM based techniques, making it far more representative of the bulk sample than the SEM based techniques. A source of systematic error that could prove problematic for both the microscopy techniques is the polishing, in particular the relief of geopolymer matrix compared to the unreacted metakaolin because the geopolymer matrix is softer than the metakaolin, possibly exposing more unreacted particles than is representative of the bulk. The polishing also has the potential of removing sodium from the surface layer.

6.4.8. Total matrix content

There is only a ±9 wt% deviation in the quantity of alkali aluminosilicate liquid (the sum of all solutions and dissolved products) available to form the geopolymer matrix, i.e. 86.5(2), 80.0(7), 72.3(1), 90.2(2) wt% for samples 1 to 4, respectively, and a large deviation in compressive strengths (Figure 6-10). Considering this, the dominant effect on geopolymer matrix formation and sample strength of the incomplete dissolution of the metakaolin is the impact of the geopolymer matrix chemistry rather than the quantity of alkali aluminosilicate liquid available.

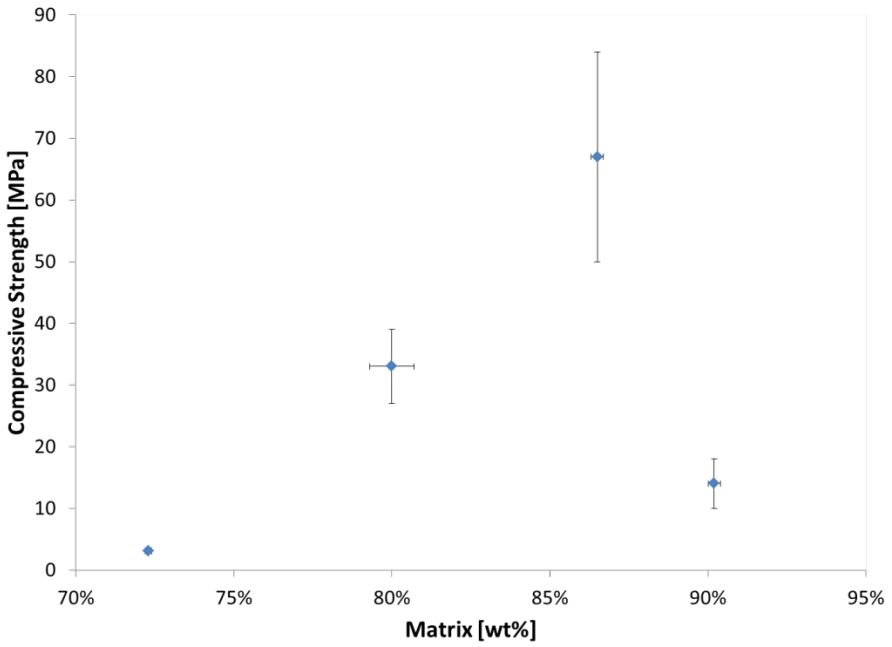

Figure 6-10 the compressive strength compared to matrix mass fraction. The matrix mass fraction is the sum of solution plus dissolved solids.

6.5. CHAPTER CONCLUSIONS

The area ratio method (ARM) and the PONCKS method have both been found to be robust and suitable analysis methods for *in situ* x-ray diffraction of geopolymer curing.

The fraction of metakaolin dissolution has been determined quantitatively for four geopolymer samples using two XRD methods and point counting by scanning electron microscopy. These techniques showed good agreement and general consensus with qualitative microchemistry results from energy dispersive spectroscopy. The compositions varied significantly from the bulk to the matrix composition; for Si/Al it varied from 1.5, 1.9, 2.5 and 3.1 to 1.7, 2.3, 4.0 and 52, respectively.

The fraction of reacted metakaolin varied with only small changes in bulk chemistry from 10(8) to 75(3) % for geopolymers with compressive strengths varying from 3.1(2) to 67(17) MPa.

These results provided an insight as to why the compressive strength of geopolymers drops off quickly with variation from the optimum chemistry. A decrease in the fraction of reacted metakaolin results in poor properties primarily due to the resultant changes in the matrix chemistry and to a much lesser extent on the reduction in the amount of geopolymer matrix available to bind the unreacted particles.

CHAPTER 7: THE FIRST 20 HOURS OF GEOPOLYMERISATION: AN IN SITU WAXS STUDY OF FLYASH BASED GEOPOLYMERS

7.1. ABSTRACT

This study followed the first 20 hours of flyash geopolymerisation at 70°C using time resolved Wide Angle X-ray Scattering (WAXS). The extent of dissolution of the amorphous phase of the flyash was determined to range from 29% to 54% for the different formulations trialled. The dissolution rate of the flyash significantly reduced after the first 5 hours for all samples. During the formation stage of the geopolymer there were significant temporal variations in the chemistry of the dissolved solution due to the rate of flyash dissolution, with a relative standard deviation of 20%, 57% and 24% for the Si/Al, Na/Al and H/Si ratios, respectively. Utilising the Power Law, scattering in the low angle region of the WAXS pattern combined with the geopolymer peak area yielded a measure which correlated with the compressive strength – providing a new method to measure the flyash dissolution and geopolymer formation processes independently. The evolution of several zeolite phases was followed, noting there are different formation mechanisms involved even within the same sample. Four samples were examined with compressive strengths ranging from 14(2) – 50(9) MPa, each was synthesised with flyash from Collie Power Station (Western Australia) activated with sodium silicate solution of varying concentrations.

7.2. INTRODUCTION

7.2.1. Geopolymer kinetics

Utilising x-ray diffraction the growth/dissolution kinetics of the crystalline phases can be readily studied (Provis and van Deventer, 2007b, Madsen et al., 2012). However, the amorphous (non-crystalline) phases can also be quantified (Chapter 6) allowing kinetics of amorphous phase(s) dissolution/growth to be quantified (Kern et al., 2012, Madsen et al., 2011).

As discussed in Section 2.2, there are several reported studies on the kinetics of geopolymerisation, utilising energy dispersive x-ray diffraction (Provis and van Deventer, 2007b), Attenuated Total Reflection Fourier Transform Infrared spectroscopy (ATR-FTIR) (Rees et al., 2007b), differential scanning calorimetry (DSC) (Rahier et al., 2003) and AC Impedance Spectroscopy (ACIS) (Provis et al., 2008). Although in situ SAXS and WAXS has been applied to track zeolite formation by many (Panzarella et al., 2007, de Moor et al., 1998, Dokter et al., 1994, Walton et al., 2000, Norby and Hanson, 1998), in situ SAXS and WAXS has only been applied in a limited way to the early kinetics studies of metakaolin geopolymers (Jozić et al., 2012).

De Silva et al. (2007) in a study of metakaolin geopolymer kinetics found setting times increased with increasing Si/Al until Si/Al = 2 then decreased with further increases to Si/Al. Zhang et al. (2012, 2013) found in a Isothermal Conduction Calorimetry (ICC) study of sodium hydroxide and sodium silicate activated metakaolin geopolymer that the extent of reaction increased with Na/Al between 0.74 to 1.47, but also increased the zeolite or zeolite-type phase crystallisation rates. They also found that increases in curing temperature from 25 to 40°C increased the rate of reaction and the extent of reaction, the sensitivity of extent of reaction to temperature was less for sodium hydroxide activated samples with a Na/Al >1. However, for sodium silicate activated samples they found the extent of reaction was maximised at an intermediate temperature (35°C). A sample cured at 40°C had a higher extent of reaction in the first 5 hours, but reached a plateau, leading to the useful conclusion that the fast formation of geopolymer can in

fact hinder the dissolution process thus decreasing the overall extent of reaction.

Jozić et al. (2012) studied kinetics of metakaolin geopolymer with in situ SAXS and WAXS. The geopolymer material studied appears to have a composition dissimilar to other geopolymers discussed in this study, the composition was Si/Al = 1.6 and 2.1; Na/Al = 0.9 and 1.72 and H/Si = 1.34 and 2.1; the key difference being the low H/Si, whereas typical values are 4-7 for structural geopolymers. This coupled with the electron micrograph of the microstructure showing a sparsely agglomerated material, which is more consistent with a very weak geopolymer. The finding of Jozić et al. (2012) for two geopolymer samples were that the fractal dimension of the geopolymer reduced from 2.9 to 2.4 after about 4 hours at 70°C for one sample and reduced from 3.3 to 2.3 after about 8 hours.

Steins et al. (2014) studied ageing of metakaolin geopolymer with ex situ SAXS, USAXS, SANS and nitrogen sorption. Steins et al. found that a fraction of the porosity transformed from open to closed porosity and after about 1 month the water in the pores dehydrates and is replaced by air.

Studying well cured metakaolin geopolymers, Maitland et al. (2011) found that USANS/SANS was predominantly from Power law scattering from open pores and the scatter was insensitive to geopolymer composition. In addition to the SANS and USANS data, Maitland et al. provided electron microscopy data to support the bimodal classification of the pores, designated level 1 and level 2 pores. The level 2 pores are <10 nm pores, also observed by others with TEM (Kriven et al., 2004, Bell and Kriven, 2004, Duxson et al., 2005b). Steins et al. (2014) utilising SANS and BET found that the pore volume decreased over a 6 month time scale for both sodium and potassium silicate activated metakaolin. Additionally, Steins et al. (2014) found the pore size distribution range was 5–20 nm for sodium silicate activated and 2.5-8.5 nm for potassium silicate activated metakaolin after 6 months. Phair et al. (2003) applied USANS to alkali activated flyash and slags, however the size scale probed was on the order of 500-5000 nm which is essentially probing the size and shape of agglomerates of the smaller subunits rather than subunits themselves.

7.3. MATERIALS AND METHODS

7.3.1. Geopolymer synthesis

The flyash used in this study was from Collie Power station, Western Australia. The flyash used was representatively sampled from the same 20 kg samples characterised in a Chapter 4. The geopolymer compositions were chosen to be within uncertainties of those for which compressive strength data was previously collected in Chapter 5. The compositions and physical properties are summarised in Table 7-1, only the amorphous component of the flyash is considered in the formulation, the crystalline species were considered inert. The amorphous and crystalline composition of the flyash is presented in Table 4.5 and 4.6.

Table 7-1 Composition of geopolymer samples, compressive strength (CS) and Young's Modulus (YM). Calculations of the elemental ratio only consider the amorphous composition of the flyash, i.e. the crystalline component was considered inert and the values indicate the target final composition assuming 100% reaction of the amorphous component of the flyash.

Sample Name	Si/Al	Na/Al	H/Si	CS [MPa]	YM [GPa]
CFA-1.8-0.8-5.5	1.8	0.8	5.5	14(2)	2.2(4)
CFA-2.0-0.8-5.5	2.0	0.8	5.5	35(3)	2.91(8)
CFA-2.0-1.2-5.5	2.0	1.2	5.5	50(9)	3.4(3)
CFA-2.2-0.8-5.5	2.2	0.8	5.5	40(7)	3.01(7)

The geopolymers were formulated for the matrix compositions in Table 7-1. The amorphous composition of the flyash was used to formulate the mixtures using Equation 3.6 to produce 10 g of sample, the other starting materials were sodium silicate solution (PQ Australia, Grade D); sodium hydroxide (Chem-Supply, AR grade) and deionised water.

The solutions were mixed together and allowed to rest at ambient temperature overnight in a 25 mL polypropylene vial. The flyash was quickly added to this vial and mixed at high speed using a mixing head on a Dremel rotary tool for 1 minute. The sample slurry was then sucked into a 100 mm long section of PEEK tubing using a 1 mL syringe for suction. The ends of the tubing were then sealed using 1.6 mm diameter steel nails. The tubes of samples were then placed in an ice bucket until 6 samples were prepared

then the samples were loaded into the 35 position sample changer of the WAXS instrument with temperature set at 25°C. Initial patterns were collected before the capillary temperature was increased to 70°C, as measured by a type-K thermocouple placed inside PEEK tubing loaded as a dummy sample in the sample changer. More information is provided in Section 3.4.7.

7.3.2. WAXS data Collection

The in situ experiment was conducted on the SAXS/WAXS beamline at the Australian Synchrotron, the optics are described in detail in Section 3.4.7, essentially the beam line has an in-vacuum undulator, double crystal monochromators and K-B (Kirkpatrick-Baez) focusing mirrors. A 20.000 keV photon beam was focused to a ~100 μm symmetrical spot. A MAR-165 camera was used to measure the patterns at a camera length of approximately 231 mm with the camera placed such that the beam centre was near the edge of the detector to maximise the angular range. Using these conditions the measured useful angular range was 1 to 25° 2θ, which is equivalent to a q-range of approximately 0.18 to 4.4 $Å^{-1}$ or equivalent to 2.5 to 65° 2θ with copper Kα radiation. A 35 capillary sample holder, with water-bath heating, was used to hold the samples at 70° C.

Selecting the correct capillaries for this experiment was challenging. The capillary needs to be resistant to concentrated sodium hydroxide solution at 70°C for 24 hours, as well as being available as thin tubing with an appropriate wall thickness to allow high x-ray transmission. Polyetheretherketone (PEEK) was found to meet these requirements. PEEK is highly resistant to hot caustic solutions, has a low atomic number and is available as a 1.59 mm diameter capillary with 0.01 mm wall thickness (SUPERLCO Analytical, USA).

7.3.3. WAXS data Processing

The exact values of camera length and camera tilt were obtained by using Fit2d (V12.012, European Synchrotron Radiation Facility (ESRF), France) to refine a pattern of LaB_6 (SRM 660b, NIST, USA). The sample 2D diffraction

datasets for the flyashes were filtered using a script in MATLAB (The Mathworks, MA, USA). The 2D diffraction patterns exhibited the expected sharp ring patterns from the mullite, secondary quartz and crystalline iron oxides. The patterns also had superimposed multiple spot patterns from the much larger crystallite size of primary quartz (Williams and van Riessen, 2010), a number of which saturated the detector. The absolute intensity of any point on the ring is low compared to the intensity of primary quartz spot patterns, which are produced by only a relatively small number of very large crystallites (10-50 μm). The spots were found by thresholding intensity values above 4,000 units, then expanding the size of each cluster of high intensity pixels by convolving a circle of 27 pixels diameter, this was used to generate a mask, which was used to set all affected pixels to an intensity of 65535. The patterns were normalised to the incident beam intensity; corrected for the transmission factor of each sample and the PEEK capillary 'blank' was subtracted. To account for the measured transmission factor of each sample an empty capillary was used to subtract the capillary diffraction signal.

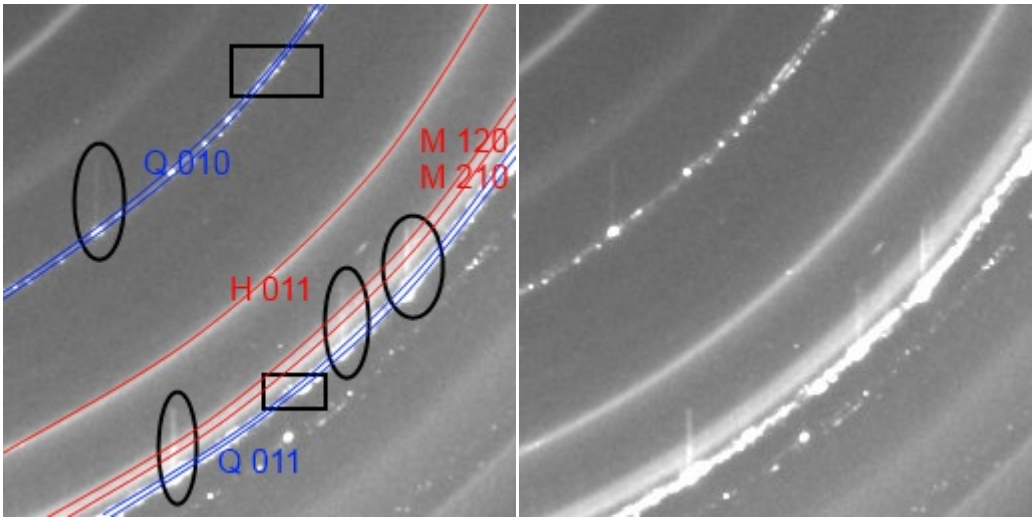

Figure 7-1 Cropped view of the 2D WAXS diffraction pattern from a geopolymer sample. The circled annotations on the left image show the pixel overflow in the columns where a large quartz (Q) crystal saturated the detector, overflowing into adjacent pixels. This effect was reduced by applying the masking process to remove saturated pixels. The square annotations show the quartz peaks where it is clear there is a distribution of quartz d-spacings. Note the hematite (H 011) and mullite (M 120 and M 210) peaks are smooth continuous rings, indicating the crystallite size is small compared to the diffraction information volume, hence there are thousands to millions of crystallites.

The filtered and normalised patterns were loaded into Fit2d, where the threshold value to mask out saturated pixels was set at 65534, and then

radially averaged applying the calibration for camera length and tilt. The filtering process improved the smoothness of the quartz peak intensity versus time.

7.3.4. WAXS phase Identification

A MATLAB script was used to visualise the diffraction patterns as a function of time using 2D colour plots; these were used to select 3 to 5 representative diffraction patterns to perform phase search/match. The search/match was conducted using EVA 15.0 (Bruker-AXS, Germany) with the Powder Diffraction File database (PDF 4+ 2009). The phases identified were exported such that accurate phase markers could be displayed on the MATLAB output. The identified phases were used to find the most suitable crystal structures for use in the subsequent Rietveld refinements using the ICSD (2010/1), PDF 4+ (2009) and American Mineralogist crystal structure databases.

7.3.5. WAXS data Analysis

A model was refined to the data using TOPAS 4.2 (Bruker-AXS, Germany), in launch (script) mode. The Bragg peaks from crystalline phases were modelled using the crystal structures (i.e. Rietveld method), whereas the diffuse scattering from the amorphous phases were modelled using a split pseudo Voigt (SPV) function per phase. The intended refinement method attempted is referred to as a parametric refinement (Stinton and Evans, 2007, Müller et al., 2009), that is to say all the patterns (per sample) were simultaneously opened and many parameters were linked together between patterns to reduce the number of refined parameters using analytical functions with a few refinable parameters. However, selecting the analytical functions to get a good fit of the data was not achieved, so the more typical and basic method of setting global variables for some parameters was required. The refined parameters are summarised in Table 7-2, when the parameter is refined in common, it means that the variable are analytically linked such that one variable is refined per pattern or phase, reducing the number of variables refined. The instrument resolution function (IRF) was

modelled using a convolution model described by Müller et al. (2009), refined with the LaB_6 (NIST SRM 660b) data.

Refining a common peak position and shape for the amorphous materials in the flyash and a common peak position shape for the geopolymer allows the degree of flyash dissolution to be determined using the area ratio of the geopolymer and flyash peaks (Chapter 6.5). This also allows the amorphous peak position of the geopolymer to be determined; the method was shown to be more accurate than using the measured shift in a single peak (Chapter 6).

The 'background' was modelled as required using Equation 7.1, where X is 2θ; and a, b, c and d are refinable parameters. The c parameter from herein will be referred to as the Power Law Pre-factor.

$$I(X) = a + bX + \frac{c}{X^d} \qquad (7.1)$$

The phase concentrations can be presented on an absolute scale with mullite being used as an 'internal standard' to the calibrate system. The mullite concentrations in the flyash were determined previously (Williams and van Riessen 2010) where it was demonstrated that mullite did not react significantly in any of the samples making it a suitable internal standard. It was noted that the mullite patterns exhibited small variations of periodic nature which correlated with other phases indicating that the use of an internal standard was suitable.

The Rietveld analysis was conducted with TOPAS in launch mode using the 'conserve_memory' directive to allow refinement with all ~500 datasets simultaneously.

The relative concentrations of geopolymer, flyash and the Power Law pre-factor were calculated by normalising each signal such that the range was between 0-100%.

Table 7-2 The parameter scheme used in the refinement. Note: GP represents geopolymer and FA flyash

	Overall		Per pattern	
Parameter	**Common**	**Each phase**	**Common**	**Per phase**
Background	-	-	X	-
Camera length error	X	-	-	-
Phase scale factor	-	-	-	X
Crystallite Size	-	-	-	X
Lattice Parameters	-	X	-	-
GP peak position	X	-	-	-
GP peak shape	X	-	-	-
GP peak intensity	-	-	X	-
FA peak position	X	-	-	-
FA peak shape	X	-	-	-
FA peak intensity	-	-	X	-

7.3.6. SAXS data Collection

The same capillaries were sent back to the SAXS/WAXS beamline and the beamline scientist, Nigel Kirby, generously collected SAXS data from the same sample capillaries 1 month after the WAXS experiments. The SAXS pattern was collected on the Pilatus 1M (DECTORIS Ltd., Switzerland) detector with beam energy of 15.0 keV and a camera length of approximately 1576 mm. The data was collected at 2 and 5 second exposure times. Data were collected at ambient pressure and temperature. The data collection range was approximately 0.01 – 0.7 $Å^{-1}$.

7.3.7. SAXS data processing

The camera length, camera tilt and absolute intensity calibrations were refined using beamline software 15-ID SAXS/WAXS ver3.299 (Australian Synchrotron, Melbourne, Australia) using an AgBEH standard. The sample datasets were radially averaged to produce a 1D pattern. The intensity and error were the average and standard deviation of each radial sector. The patterns were normalised to the incident beam intensity; corrected for the transmission factor of each sample and the PEEK capillary 'blank' was

subtracted. The power law fit was performed using Matlab Curve fitting toolbox using Equation 7.2 from Q = 0.02 and 0.10 $Å^{-1}$

$$I(Q) = \frac{a}{Q^b} \quad (7.2)$$

7.4. RESULTS AND DISCUSSION

7.4.1. WAXS results

Visual inspection of how the 2D diffraction patterns change with time reveals a ring pattern with sharp rings and diffuse rings, which are analogous to Bragg peaks and diffuse peaks from amorphous phases in conventional XRD patterns, both slowly varying as the reaction proceeds. The sharp rings were from zeolite-type phases which form suddenly after an induction time for the sample CFA-1.8-0.8-5.5, the zeolites in the other samples formed more gradually. The diffuse rings from the amorphous phases gradually increase in diameter. The sharp ring patterns from the mullite, iron oxides and newly formed zeolites are radially homogeneous, indicating a very small crystallite size relative to the diffraction information volume, i.e. thousands to millions of crystallites in the beam.

Superimposed on the rings are primary quartz spot patterns that move in position from pattern to pattern for a period of time and then stop moving. During the first part of the reaction the primary quartz spots randomly appear and disappear. The radius of the spots is slightly larger than the ring pattern of the secondary quartz, which is consistent with the previous findings that there are two populations of quartz in the flyash (Chapter 4). These spots cause a data processing challenge as the mean intensity is very imprecise because there are not a large number of crystals contributing to the spot, but can be dealt with, as detailed in Section 7.3.3. However, considering the spots appear and disappear because they are in rotational motion relative to the beam, provides an opportunity for a measure of setting time (i.e. cessation of liquid motion in the slurry) which is when the spot positions stop changing. The setting time was measured as the diffraction pattern where the spots don't significantly move for more than 3 patterns in a row. The measure of setting time is shown in Table 7-3. These values are unsupported by corresponding physical testing to assess accuracy of the determination.

The search and match results revealed the same phases as previously found in the flyashes (Chapter 4), but with the addition of some zeolite or zeolite-type phases that could not be uniquely identified. The phases could not be

identified as there were very few peaks and they did not match well with the peak positions for possible phases in the Powder Diffraction File or in specific zeolite collections (Treacy and Higgins, 2007). The zeolites found in the geopolymer probably have a high degree of interstitial substitution which has shifted the d-spacing away from the more pure zeolites in the databases.

Table 7-3 Setting time as measured by the time that the quartz spot positions stopped changing.

Sample Name	Setting time (min)
CFA-1.8-0.8-5.5	24
CFA-2.0-0.8-5.5	25
CFA-2.0-1.2-5.5	32
CFA-2.2-0.8-5.5	64

Visual inspection of the diffraction data time series as 2D colour contour images (Figure 7-2 to Figure 7-5), where intensity shown by colour scale, reveals several new crystalline phases which form with time. After an induction period, there was an increase in the low angle (Q < 1 $Å^{-1}$) intensity and a 'shift' in the diffuse scattering peak to higher angle. The induction time and reaction rates vary between geopolymer formulations.

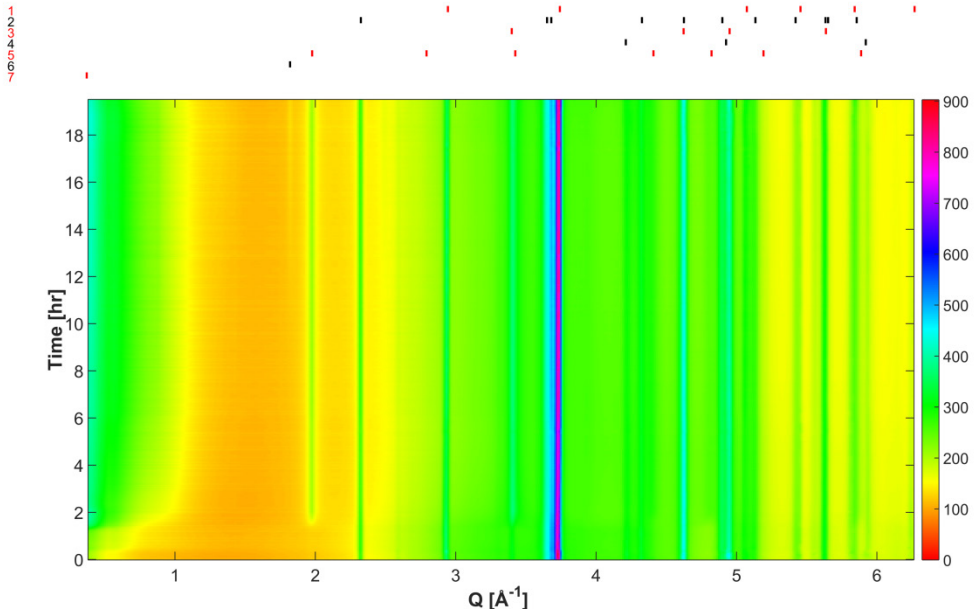

Figure 7-2 Time resolved diffraction pattern of CFA-1.8-0.8-5.5. Features include the evolution of low angle intensity (Q < 1 $Å^{-1}$), formation of two zeolite phases and the 'shift' in the amorphous peak position. The peak positions of significant identified phases are shown at the top of the figure for [1] Quartz (SiO_2), [2] Mullite ($Al_{4.64}5Si_{1.36}O_{9.68}$), [3] Hematite ($Fe_2O_3$), [4] Magnetite ($Fe_3O_4$), [5] unspecified zeolite 1, [6] unspecified zeolite 2 and [7] small angle scattering.

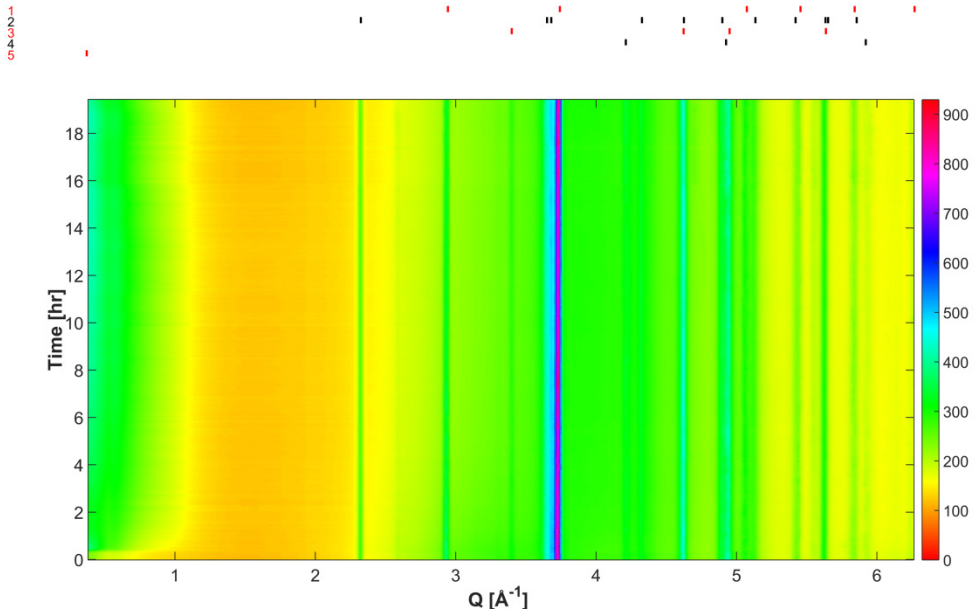

Figure 7-3 Time resolved diffraction pattern of CFA-2.0-0.8-5.5. Features include the evolution of low angle intensity (Q < 1 Å^{-1}) and the 'shift' in the amorphous peak position. The peak positions of significant identified phases are shown at the top of the figure for [1] Quartz (SiO_2), [2] Mullite ($Al_{4.64}5Si_{1.36}O_{9.68}$), [3] Hematite ($Fe_2O_3$), [4] Magnetite ($Fe_3O_4$) and [5] small angle scattering.

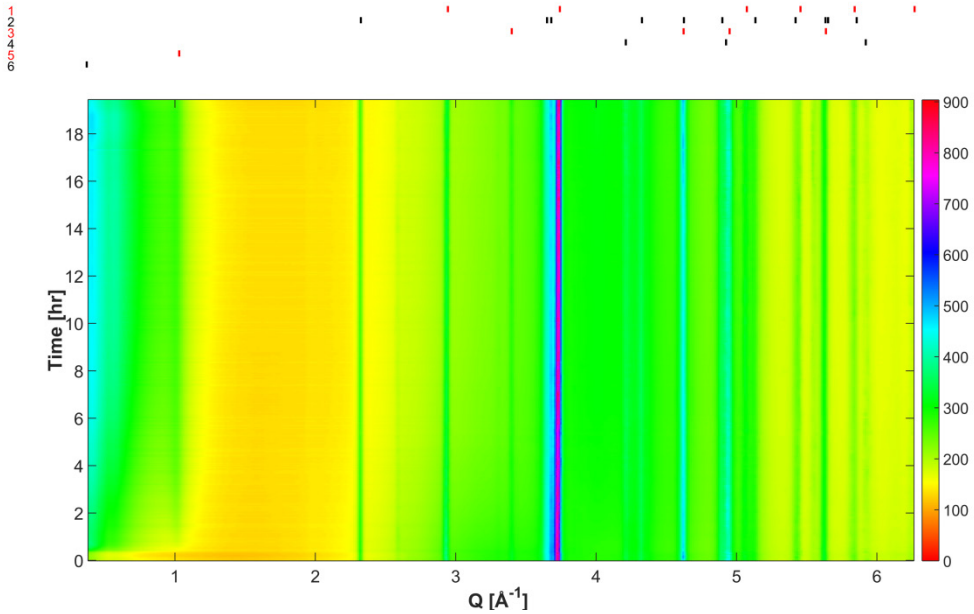

Figure 7-4 Time resolved diffraction pattern of CFA-2.0-1.2-5.5. Features include the evolution of low angle intensity (Q < 1 Å^{-1}), formation of a zeolite phase and the 'shift' in the amorphous peak position. The peak positions of significant identified phases are shown at the top of the figure for [1] Quartz (SiO_2), [2] Mullite ($Al_{4.64}5Si_{1.36}O_{9.68}$), [3] Hematite ($Fe_2O_3$), [4] Magnetite ($Fe_3O_4$), [5] unspecified zeolite 3 and [6] small angle scattering.

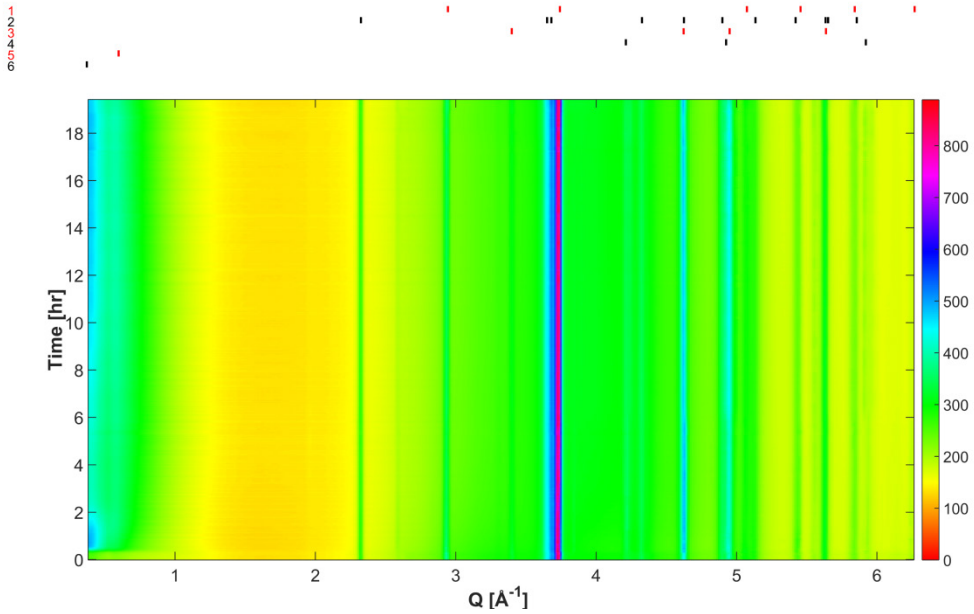

Figure 7-5 Time resolved diffraction pattern of CFA-2.0-0.8-5.5. Features include the evolution of low angle intensity (Q < 1 Å^{-1}), formation of a zeolite phase and the 'shift' in the amorphous peak position. The peak positions of significant identified phases are shown at the top of the figure for [1] Quartz (SiO_2), [2] Mullite ($Al_{4.64}5Si_{1.36}O_{9.68}$), [3] Hematite ($Fe_2O_3$), [4] Magnetite ($Fe_3O_4$), [5] unspecified zeolite 4 and [6] small angle scattering.

Using only the WAXS data, it could not be confirmed that the increase in intensity at low angle (Q < 1 Å^{-1}) was either broad Bragg peaks from large zeolite-type structures or a small angle scattering phenomenon, hence additional SAXS data was collected from the same capillaries 1 month after the initial experiment. The SAXS data in Figure 7-6 shows that, although there are some Bragg peaks from zeolite-type phases in the low angle region of the WAXS patterns (Q = 0.18 to 0.53 Å^{-1}), it is not the significant source of intensity. The SAXS patterns are analysed further in Section 7.4.2.

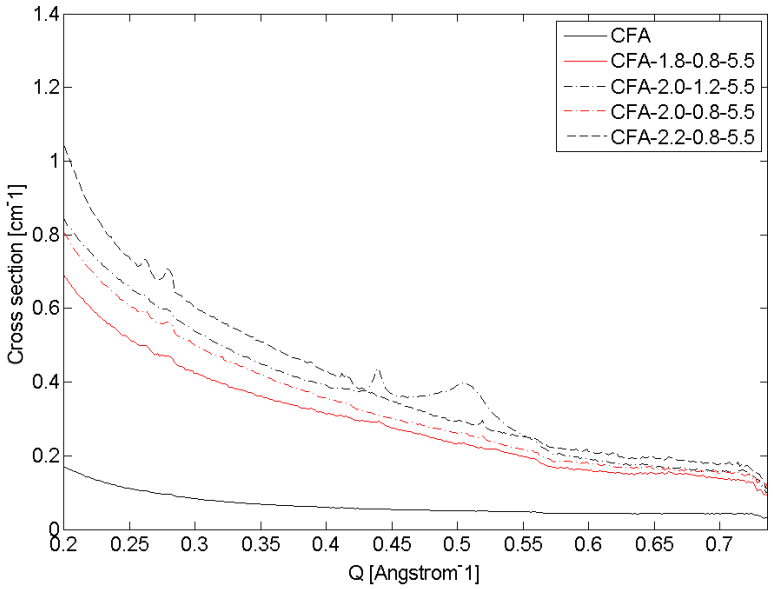

Figure 7-6 SAXS patterns confirm that the increased intensity at low angle (<3° 2θ) seen in the WAXS data is from small angle scattering phenomenon rather than a broad Bragg peak of a large zeolite. The useful limit of the WAXS data was Q = 0.18 $Å^{-1}$. Although there are Bragg peaks in the SAXS data, they are not source of the majority of the intensity. Note: cross section is a calibrated representation of intensity.

The peak shapes of the zeolite phases were fitted using Lorentzian peaks. Figure 7-7 shows peak area and a non-calibrated measure of crystallite size or coherently scattering domain size, by the integral breadth method (Balzar, 2000), for the major zeolite phase peak (Q = 1.97 $Å^{-1}$) in CFA-1.8-0.8-5.5. It shows that after an induction time, the concentration and crystallite size rapidly increases and plateaus out. This supports the understanding that during the induction time many crystallite seeds form and the phase concentration increases via crystal growth. Conversely, the other unidentified zeolite phase in the same sample which has an induction period of around 12 hours, Figure 7-8, shows different formation behaviour. The crystallite size instantaneously increases to a plateau value, while the peak intensity is still low (20% of maximum), and then the intensity continues to increase and the crystallite size slightly decreases. This indicates the crystal growth rate is much faster than the nucleation rate for the second zeolite.

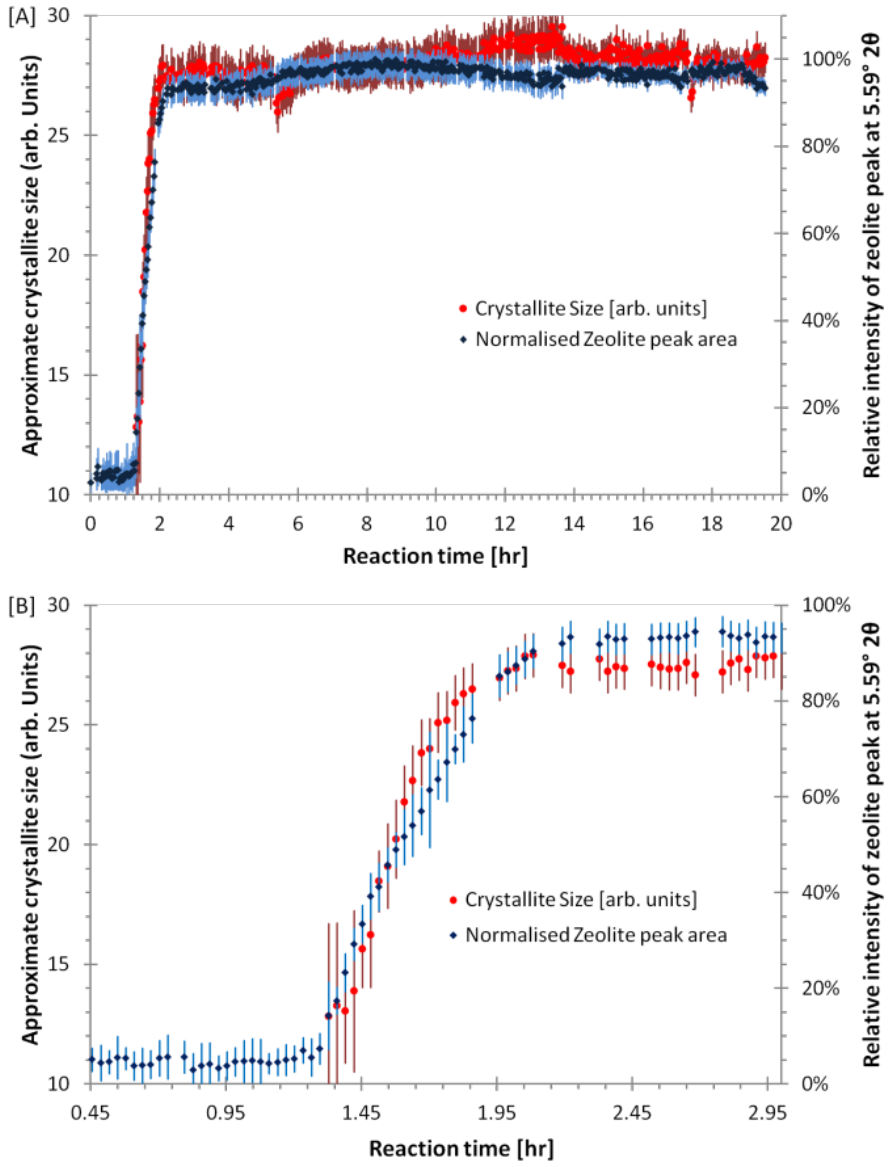

Figure 7-7 [A] The relative peak area and crystallite size for a zeolite peak at Q = 1.97 $Å^{-1}$for sample CFA-1.8-0.8-5.5. The plateau of the crystallite size as the relative peak intensity reach ~90% indicates there is nucleation period like the formation of typical zeolites, but with no crystal growth subsequently. Note: It is a fitting artifact that crystallite size randomly fluctuates when relative peak area is <5%, as there is insufficient intensity to fit the peak, hence the peaks are omitted for clarity. [B] Is zoomed in on 0.45 to 3 hr region. The error bars represent 1 estimated standard error from the refinement process.

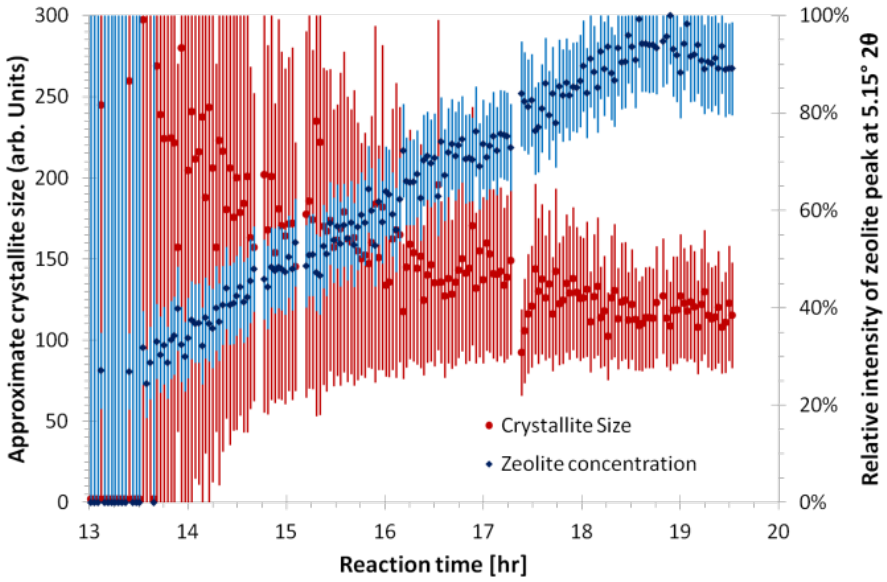

Figure 7-8 Relative peak area and crystallite sizes of a zeolite peak at Q = 1.82 Å^{-1} for sample CFA-1.8-0.8-5.5. The peak is of low intensity compared to the background, hence the noisy signal. The error bars represent 1 estimated standard error from the refinement process.

The quantitative phase results obtained from Rietveld refinement are shown in Figure 7-9. The quartz concentration for all samples is variable, as discussed above. The amorphous flyash content decreased smoothly with time and is summarised in Table 7-4.

It was found that the extent of flyash amorphous phase dissolution does not correlate with the physical properties. For all samples, the phase quantified as hematite decreased in the first few hours by approximately 50%. It is unlikely that hematite would dissolve in the high pH environment, which indicates that a portion of the quantified hematite is actually a soluble spinel phase with a very similar diffraction pattern. With the current datasets, given the low concentration of the phase (1-2 wt% in the samples) it is not possible to draw stronger conclusions. The peak positions of the amorphous phases are shown in Table 7-5. The peak positions of the geopolymer amorphous phase are at slightly lower angles than found for metakaolin geopolymers using a similar modelling method (Chapter 6) which was between 3.15 and 3.22 Å for metakaolin geopolymer compared to 2.92 to 3.06 Å for these flyash geopolymers.

Table 7-4 Summary of the flyash amorphous phase concentration; initial concentration was calculated from mix formulation and QPA results of the starting flyash (Chapter 4) and the final concentration was determined by the refinement of the WAXS data. The Compressive strength (CS) and Young's Modulus (YM) has been shown again for comparison.

Sample Name	Initial [wt%]	Final [wt%]	Extent of dissolution [%]	CS [MPa]	YM [GPa]
CFA-1.8-0.8-5.5	46	33	29	14(2)	2.2(4)
CFA-2.0-0.8-5.5	44	20	54	35(3)	2.91(8)
CFA-2.0-1.2-5.5	43	27	38	50(9)	3.4(3)
CFA-2.2-0.8-5.5	42	24	42	40(7)	3.01(7)

Table 7-5 d-spacings of the flyash and geopolymer amorphous phase peaks. The geopolymer amorphous phase peak positions are smaller than found for the metakaolin geopolymer (Chapter 6) which were between 3.15 and 3.22 Å. The flyash amorphous phase peak position was allowed vary between samples in the refinement.

Sample Name	Flyash amorphous phase [Å]	Geopolymer amorphous phase [Å]
CFA-1.8-0.8-5.5	3.96	2.92
CFA-2.0-0.8-5.5	4.00	3.02
CFA-2.0-1.2-5.5	4.08	2.99
CFA-2.2-0.8-5.5	4.03	3.06

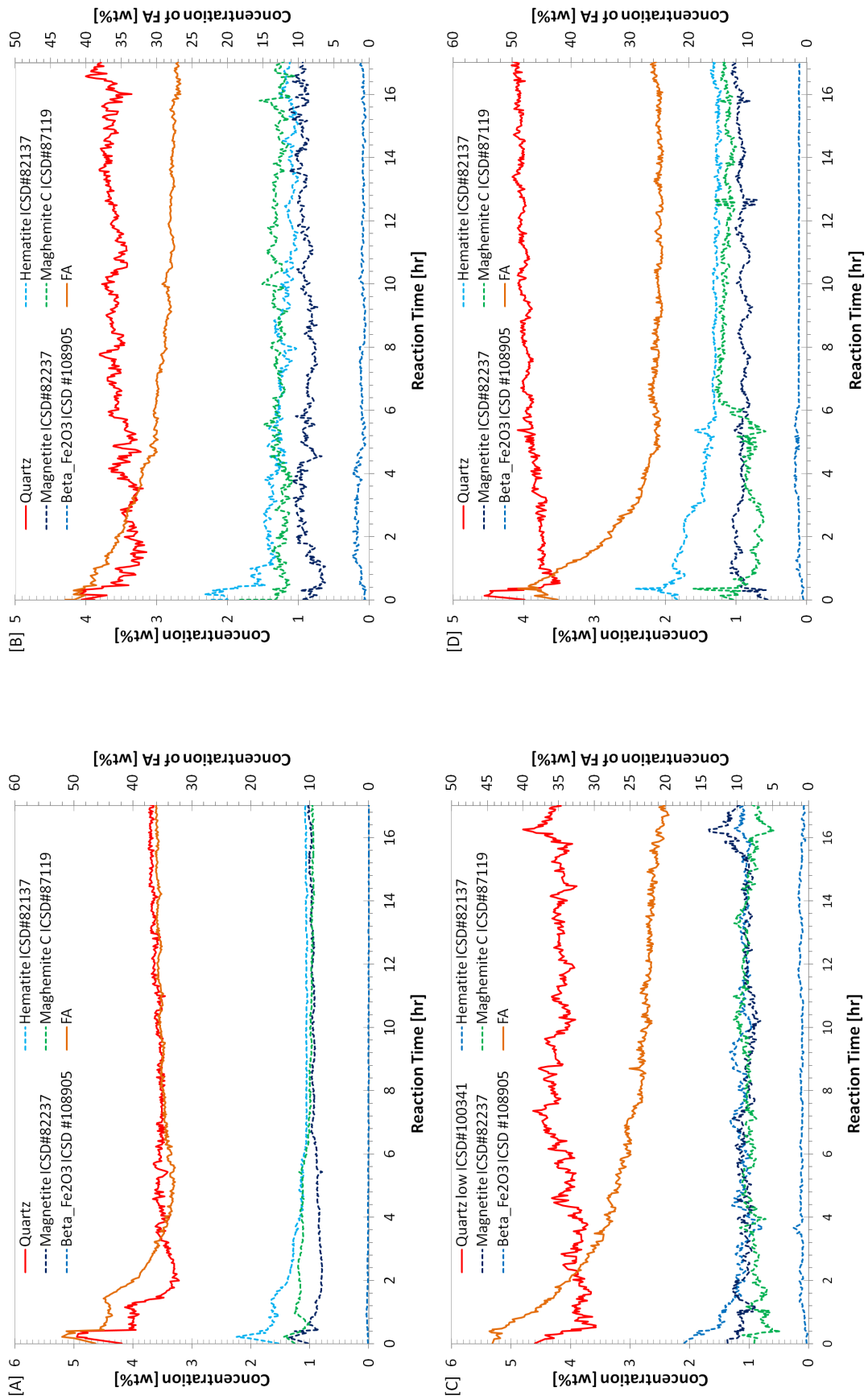

Figure 7-9 Quantitative phase results from the refinement[A] CFA-1.8-0.8-5.5 [B] CFA-2.0-1.2-5.5 [C] CFA-2.0-0.8-5.5 [D] CFA-2.2-0.8-5.5. The concentration of the flyash (FA) amorphous phase is shown on the right hand side axis.

Using the extent of dissolution of the flyash amorphous phase the Si/Al, Na/Al and H/Si of the reaction product can be calculated as a function of time, see Figure 7-10. The composition of geopolymer phase and zeolite phase(s) are not explicitly known, hence were not subtracted. The dissolution of the flyash amorphous component was assumed to be congruent, as discussed in Section 2.1.1 and Section 6.2. The amorphous SiO_2 and Al_2O_3 contents of this flyash was 32(3) wt% and 16(2) wt%, respectively of total of 64(4) wt% amorphous (Williams and van Riessen, 2010). As expected, the elemental concentrations in solution available for geopolymer formation varied significantly during the geopolymer growth phase, as dissolution of the flyash amorphous phase continues during the geopolymer formation. The mean and standard deviation of the elemental ratio are shown in Table 7-6. The statistics were calculated when the relative geopolymer concentrations were between 10 and 90%.

The relative standard deviation of H/Si ratio in solution during the formation stage correlates inversely with compressive strength (Figure 7-11). This correlation indicates strong geopolymer phases may only form when the conditions are within a specific range. The measured parameter which influences the calculated standard deviation of the calculated H/Si ratio is the dissolution rate of the amorphous fraction of flyash dissolution during the time the geopolymer forming. The results indicate if the flyash is dissolving a high rate during geopolymer formation the resulting geopolymer will be of lesser strength. The large variation of the solution composition in which geopolymer forms does prompt the question whether there is a similar variation in the actual composition of the geopolymer matrix. The quantitative EDS work of Rowles and O'Connor (2009) of metakaolin geopolymer found the standard deviation of Si/Al and Na/Al was orders of magnitude less; for example the matrix composition of the strongest sample was Si/Al = 3.2(1) and Na/Al = 1.36(6) which is a relative standard deviation of 3% and 4% respectively compared to mean relative standard deviations in this study of 20% and 56% for Si/Al and Na/Al, respectively.

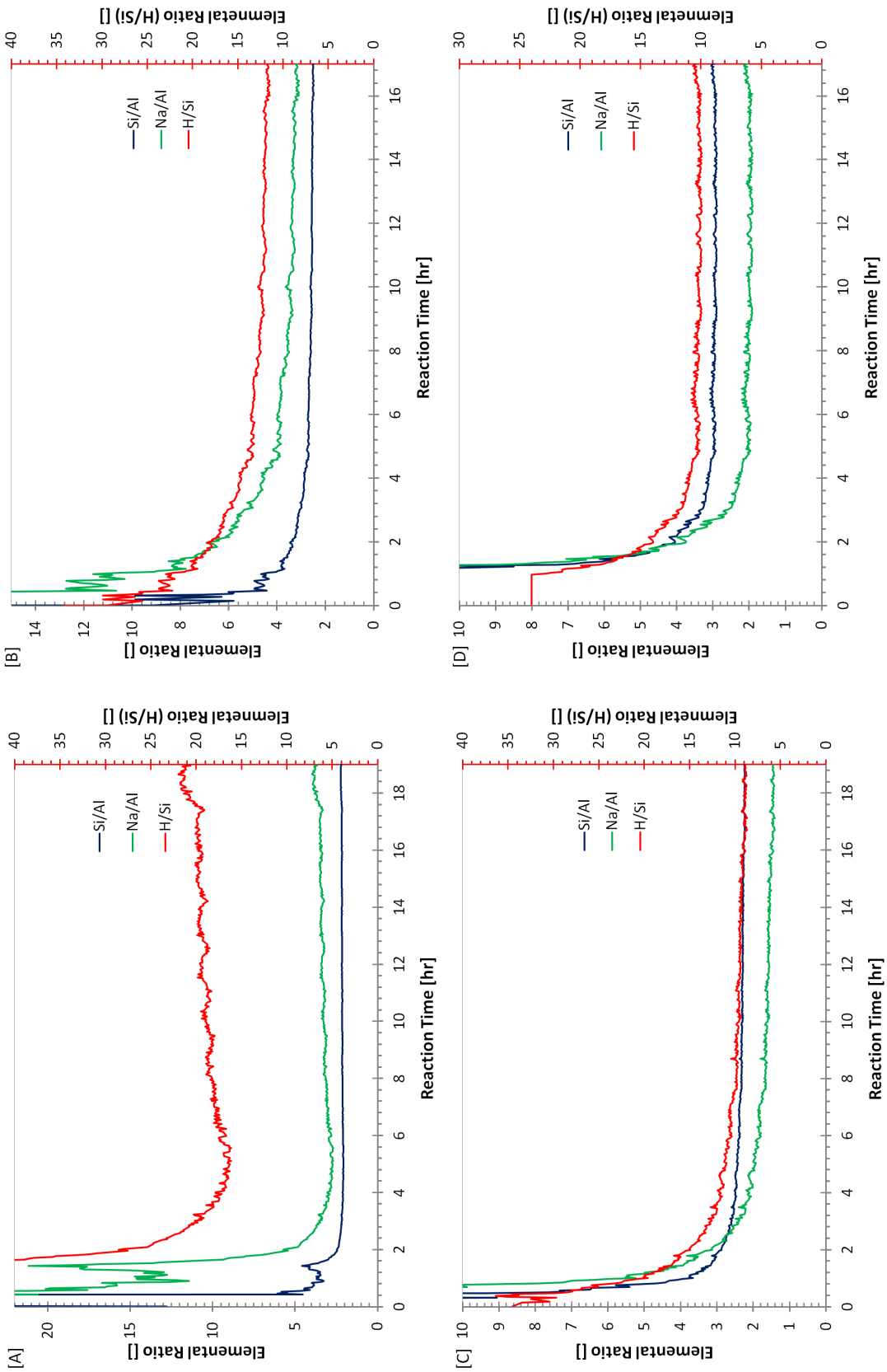

Figure 7-10 Elemental ratios of the reaction products as function of time [A] CFA-1.8-0.8-5.5 [B] CFA-2.0-1.2-5.5 [C] CFA-2.0-0.8-5.5 [D] CFA-2.2-0.8-5.5. Note: that the elemental ratio levels out 4-5 hours into the reaction.

Table 7-6 The calculated atomic ratio in the solution during geopolymer phase growth (between 10% and 90% of relative GP concentration), the mean and standard deviation were weighted by time. The final extent ratios are calculated from the final extent of the flyash dissolution, it is the mean of the last 15 patterns. Note: The formation of geopolymer and zeolite phases was not accounted for as the specific chemistry was not known.

	Solution during reaction			Final Extent		
Sample Name	**Si/Al**	**Na/Al**	**H/Si**	**Si/Al**	**Na/Al**	**H/Si**
CFA-1.8-0.8-5.5	2.3(4)	4.4(28)	22.5(77)	2.23(2)	3.9(2)	21.6(6)
CFA-2.0-0.8-5.5	2.5(6)	2.2(16)	11.2(33)	2.24(1)	1.46(4)	8.9(2)
CFA-2.0-1.2-5.5	2.8(4)	4.3(17)	13.8(26)	2.51(3)	3.2(1)	11.7(3)
CFA-2.2-0.8-5.5	3.2(8)	2.3(12)	10.8(16)	3.0(1)	2.1(2)	10.4(5)

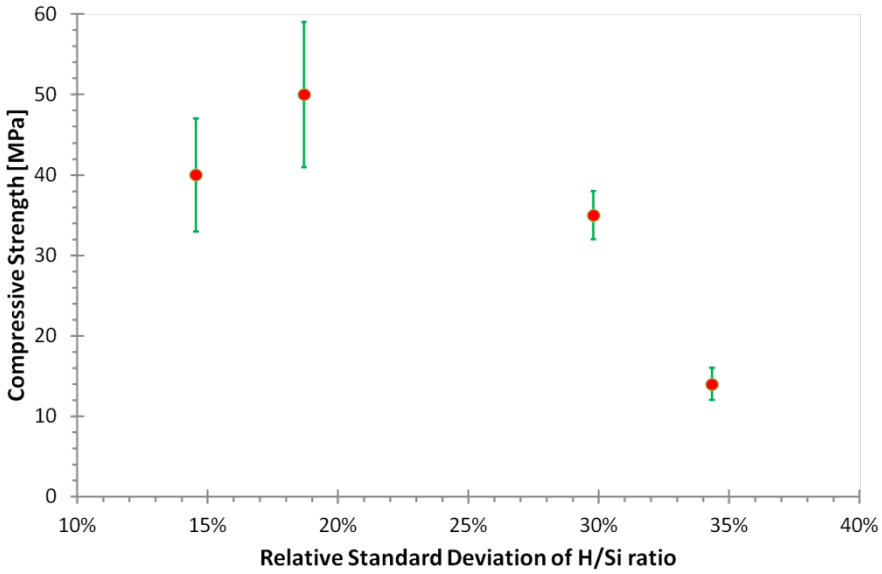

Figure 7-11 The relative standard deviation of calculated atomic H/Si in solution during geopolymer phase growth (between 10% and 90% of relative GP concentration). Note: The formation of geopolymer and zeolite phases was not accounted for and the inverse correlation between compressive strength and the variability of the solution.

Figure 7-12 shows the dissolution of the flyash amorphous phase and evolution of the geopolymer amorphous phase and the Power Law pre-factor. Both are displayed as a fraction between their minimum and maximum values. The Power Law pre-factor is correlated to the specific surface area of the sample and in this case indicates the presence of very small species; both the small geopolymer species and other small species resulting from the dissolution of the amorphous fraction of the flyash (Provis and van Deventer, 2007a) and the nanoporosity. Once the geopolymer has solidified, surface area would also have a major contribution from the porosity. Quantification of

the surface area from the SAXS data was beyond the scope of this study. The relative concentration of flyash in Figure 7-12a increases after 6 hours, this probably an indication that another amorphous phase with diffuse peak in a similar position to flyash has formed, rather than a geopolymer phase.

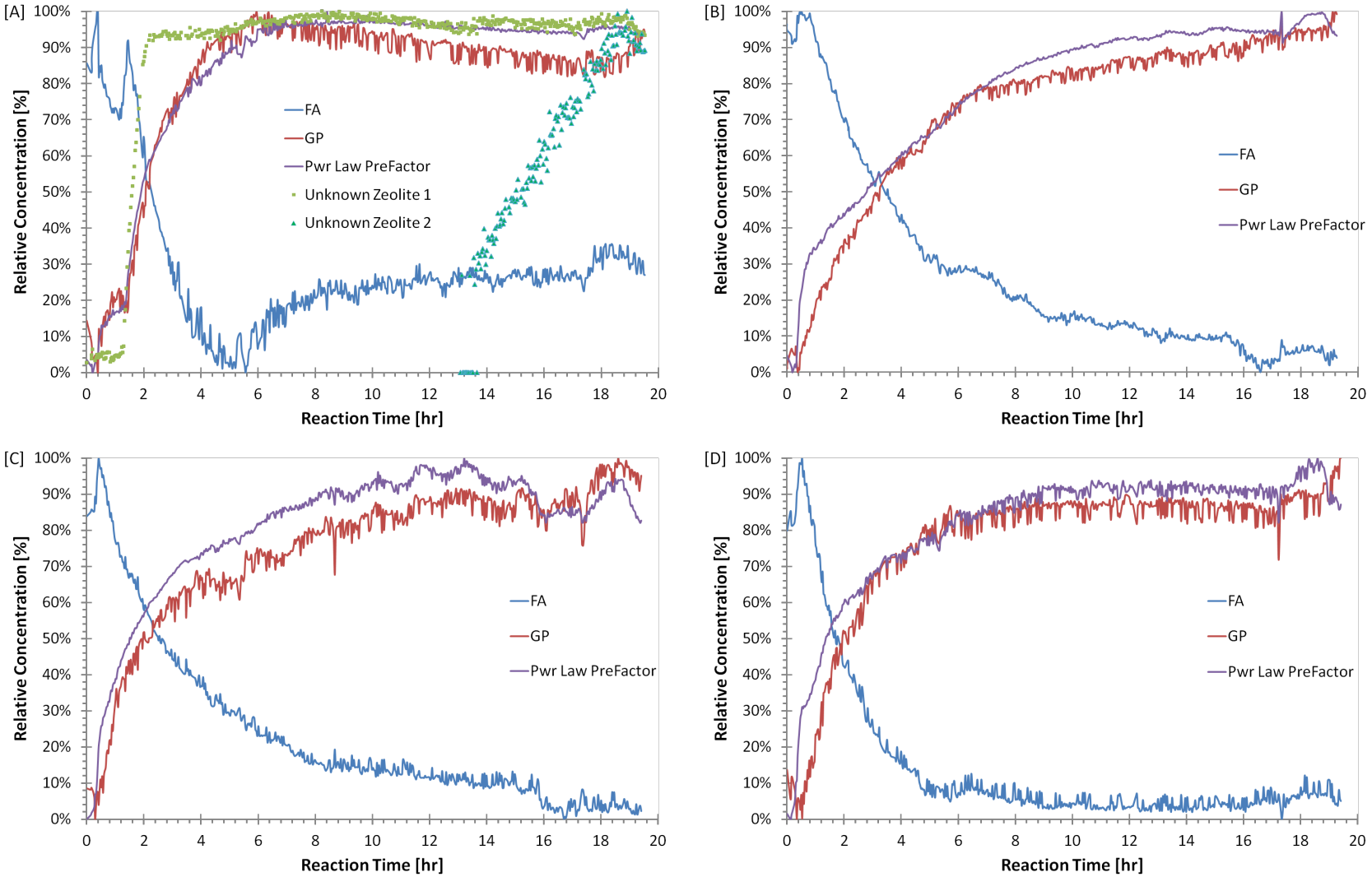

Figure 7-12 Refined output from WAXS data for samples: [A] CFA-1.8-0.8-5.5; [B] CFA-2.0-1.2-5.5 [C] CFA-2.0-0.8-5.5 [D] CFA-2.2-0.8-5.5; the time evolution of the diffuse scattering peaks of flyash (FA) and geopolymer (GP) compared with the Power Law pre factor. Note for plot [A], that the induction period for zeolite 1 and geopolymer are approximately equal.

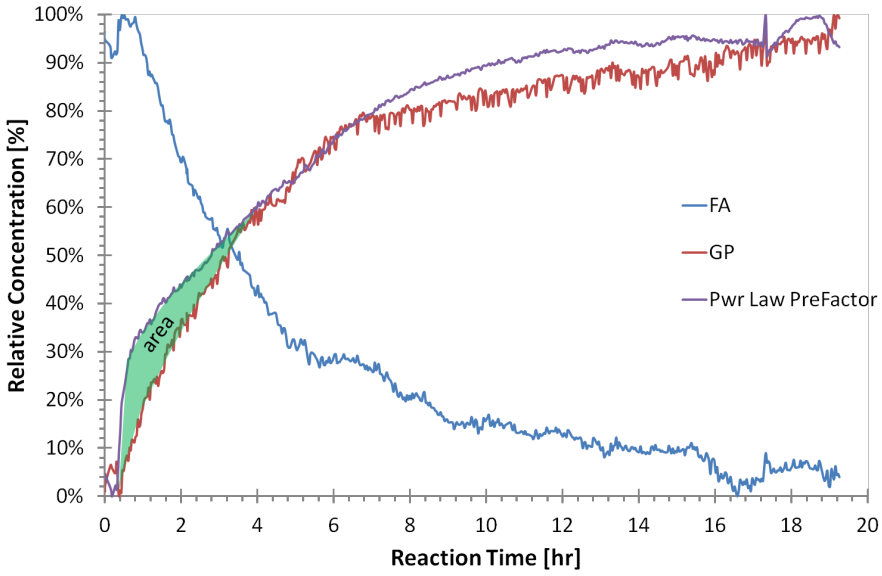

Figure 7-13 Integrating the area between the geopolymer formation and Power Law pre-factor, between approximately 15 minutes and the first intercept, results in a parameter that correlates with compressive strength.

The area between the curves of the relative intensities of the Power Law pre-factor and geopolymer signal correlates strongly with the mean compressive strength of the geopolymer samples. The area was determined by two methods; the first the area between the geopolymer and Power Law pre-factor from start of the reaction until the first incept of those curves (Figure 7-13). The second method was the area between the curves for the time between when the geopolymer had a relative concentration of 10% and 75%. The second method provides an improved correlation to the mean compressive strength of the sample. Given the Power Law pre-factor is likely correlated with the sum of dissolved aluminosilicates and geopolymer species; and the geopolymer signal is correlated with the geopolymer species; the area should be correlated to the quantity of flyash dissolved before significant geopolymerisation occurs. This supports the findings of Zhang et al. (2012, 2013) that the strength is maximised by prolonging the dissolution stage compared to the start of the geopolymerisation. This method has significant value for future experiments as it allows the dissolution and geopolymer formation (polycondensation) steps to be optimised separately. However, although the method would be predictive of

strength, the mechanism could also be related to porosity which also effects strength (Maitland et al., 2011).

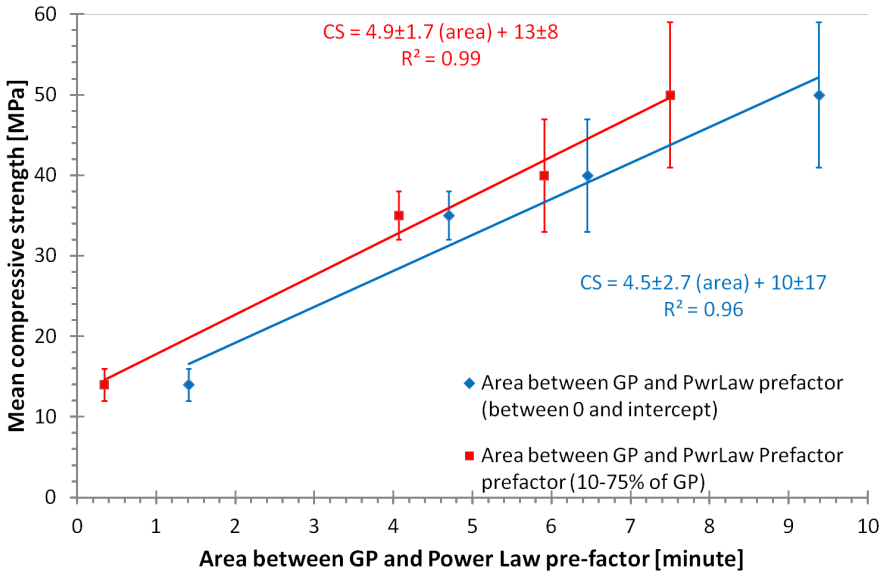

Figure 7-14 Relationship between the area between geopolymer formation and Power Law pre-factor (WAXS data), as measured by two metrics. This limited data set (n=4) does have a strong positive linear relationship for both methods of determining the area, indicating good correlation between the integrated area and the compressive strength. As described in the text, the area should be correlated to the quantity of flyash dissolved before significant geopolymerisation occurs, this supports the findings of Zhang et al. (2012, 2013) that the strength is maximised by prolonging the dissolution stage compared to the start of the geopolymerisation.

7.4.2. SAXS results

From the SAXS patterns (Figure 7-15) it can be seen that there is a significant difference in the intensity between the flyash and the geopolymer samples. A Power Law equation was fitted between q = 0.02 and 0.10 $Å^{-1}$, the fitted parameters are shown in Table 7-7. The fitted parameters were compared to the compressive strength result, (Figure 7-16) but no significant correlation was found.

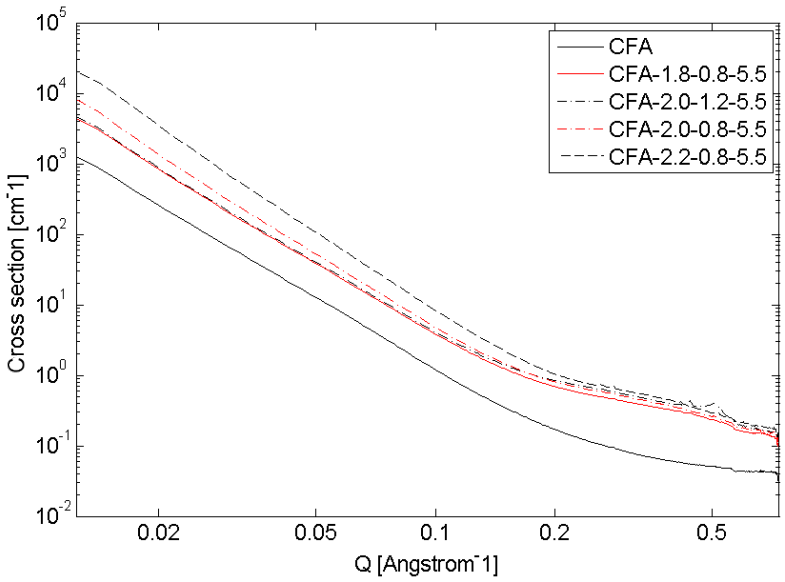

Figure 7-15 The SAXS patterns of the samples and the original flyash.

Table 7-7 Power Law fit results for the flyash and geopolymer samples. The SAXS data was fitted between q = 0.02 and 0.10Å-1. *a* is the pre-factor and *b* is the exponent.

Sample Name	a	b	R^2
CFA	0.00063(3)	-3.31(1)	1.0000
CFA-1.8-0.8-5.5	0.0014(2)	-3.41(3)	0.9999
CFA-2.0-0.8-5.5	0.0010(1)	-3.61(3)	0.9999
CFA-2.0-1.2-5.5	0.00139(2)	-3.41(3)	0.9999
CFA-2.2-0.8-5.5	0.0008(1)	-3.91(4)	0.9999

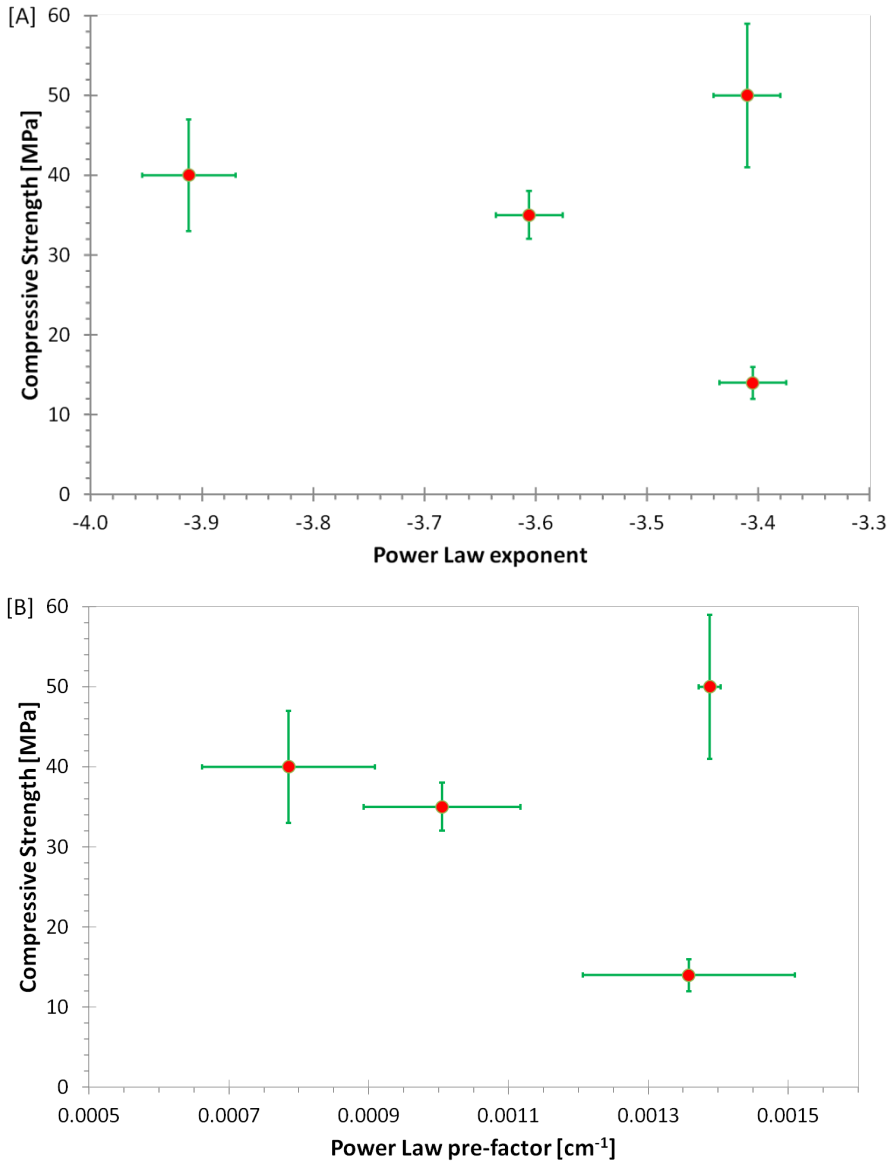

Figure 7-16 [A] Power Law exponent from the SAXS data compared with the compressive strength of the samples. [B] Power Law pre-factor – a, compared to the compressive strength of the samples. The SAXS data was fitted between Q = 0.02 and 0.10 Å^{-1}. There is no significant correlation between the exponent or the pre-factor with the compressive strength.

7.5. CHAPTER CONCLUSIONS

In this study in situ WAXS has been used to follow the reaction of flyash dissolution and subsequent geopolymerisation yielding:

- Confirmation that there are multiple mechanisms of zeolite formation even within the same geopolymer sample.
- A new method has been identified to separately measure the progress of feedstock dissolution and geopolymer formation in situ, which will allow a large number of optimisation experiments to be completed in the future.
- Identification of significant temporal variation in the composition of the solution from which the geopolymer forms; the relative standard deviation of the H/Si ratio during formation was correlated to the physical properties.
- A new method has been found, albeit time consuming, to measure the setting time of geopolymer paste formation.

The ex situ SAXS study of geopolymer at 1 month age have did not reveal anything significant when compared to the WAXS and compressive strength data.

CHAPTER 8: DEVELOPMENT OF ALKALI ACTIVATED BOROSILICATE INORGANIC POLYMERS (AABSIP)

Ross P Williams and Arie van Riessen

This chapter is a typescript version of the published article:

Williams, R. P. and A. van Riessen (2011) "Development of Alkali activated borosilicate inorganic polymers (AABSIP)." Journal of the European Ceramic Society **31**:8 1513-1516 **DOI: 10.1016/j.jeurceramsoc.2011.02.021**

8.1. ABSTRACT

A new class of materials is presented namely, alkali activated borosilicate inorganic polymers (AABSIP), which are similar to alkali activated aluminosilicate polymers (geopolymers). The pastes made with this new material ($Na_{1.10}BSi_{1.70}O_{8.88}.4.65(H_2O)$) were found to have a compressive strength of up to 56(7) MPa and a Young's Modulus of 1.95(7) GPa. The microstructure is composed of a glassy matrix with many sub-micron pores and some remnant precursor material. The AABSIP materials have been identified as suitable for structural and non-structural applications, particularly neutron shielding.

8.2. INTRODUCTION

Alkali activated aluminosilicate inorganic polymers or geopolymers have been the focus of many investigations (Barbosa et al., 2000, Davidovits, 1987, Duxson et al., 2007a, Duxson et al., 2005b, Fernández-Jiménez and Palomo, 2005, Keyte, 2008, Latella et al., 2008, Rowles and O'Connor, 2003, Rowles and O'Connor, 2009, Sindhunata et al., 2006, Skvara et al., 2005, Steveson and Sagoe-Crentsil, 2005b, Steveson and Sagoe-Crentsil, 2005a, Subaer et al., 2002, Williams and van Riessen, 2010) for applications varying from Portland cement replacement, radioactive waste containment, fireproof barriers, ceramic precursors and biological implants. Despite many groups worldwide producing reliable products from feedstocks such as flyash, the fundamental structure of geopolymers and formation mechanisms are not completely understood. In model clay based geopolymer systems the basic reaction mechanisms can be mathematically modelled (Provis et al., 2005). This process can be simplified to a dissolution-reorientation-solidification process. The physical properties of the geopolymers depend primarily on the ratio of Si/Al, Na/Al and the water content (Duxson et al., 2005b, Rowles and O'Connor, 2003). Often these ratios are investigated indirectly, for example, by varying the activation solution to solids ratio. The metakaolin geopolymer formulations optimised for maximum compressive strength are achieved when the nominal composition is Si/Al = 1.8 to 2.2 and Na/Al = 0.9 to 1.2 (Duxson et al., 2007a, Rowles and O'Connor, 2003, Steveson and Sagoe-Crentsil, 2005a). Therefore a typical geopolymer might be $NaAlSi_2O_6$-$5.5(H_2O)$.

We have substituted boron for aluminium in the inorganic polymer structure to produce a new class of material. The challenge was finding a form of B to use that had suitable composition, coordination chemistry and alkali dissolution kinetics. There are a number of choices for the B feedstock, the most available being boric acid (H_3BO_3) and borax ($Na_2B_4O_7.10H_2O$) which can be converted to boron oxide (B_2O_3) or borax with varying degrees of hydration. It should be noted that inorganic boron has been added to geopolymers previously but in this case to control setting time (Nicholson and

Fletcher, 2005), where there was no attempt to eliminate Al from the structure and so produced a boroaluminosilicate material.

Typically a geopolymer is synthesised by alkali activating an aluminosilicate solid with an alkali silicate solution. However, this method is not overly suitable for this study as the boron containing feedstocks typically have a high water content; boric acid and borax have 43 wt% and 47 wt% water, respectively. This high water content can be problematic when designing geopolymer mixtures as the bound water is not available initially, making the mixture unworkable (very dry and stiff). One alternative is to add the extra water required to have a workable mixture, however ultimately there is too much water, resulting in low pH in the solution and subsequently a weak solid. Another problem identified with borax-like materials is that the Na/B = 0.5, thus if the geopolymers are to have charge balancing (i.e. Na/B = 1), half the Na is supplied by the borax, meaning the solution pH will be lower than if it was wholly supplied by sodium hydroxide solution. Dehydration of borax decahydrate ($Na_2B_4O_7.10H_2O$) to borax pentahydrate ($Na_2B_4O_7.5H_2O$) is preferred as half the structural water has been removed, reducing the structural water content to 31 wt%. Although this process reduces the amount of structural water, the mix still maintains a starting Na/B = 0.5. The borax pentahydrate can be further heated to dehydroxylate it to anhydrous borax ($Na_2B_4O_7$) at 300°C. Although the boron in borax is both 3-fold and 4-fold coordinated, it is likely to reorganise during the reorientation stage of the geopolymerisation reaction; resulting in 4-fold coordinated boron in the inorganic polymer. If a sodium borate solution is used, the boron can more readily reorder during the polymerisation reaction.

Adequate neutron shielding is required for facilities such as medical linear accelerators, cyclotrons, synchrotrons, nuclear research facilities and nuclear power stations. The most suitable composition for neutron shielding depends on the neutron energy. Low atomic mass isotopes are best at slowing down high energy neutrons as they have high microscopic removal cross sections. In contrast, the isotopes that best capture lower energy (thermal) neutrons are those with high microscopic absorption cross-sections, however this property does not vary smoothly with atomic mass (NCRP, 1971, El-Khayatt

and El-Sayed Abdo, 2009). Elements with stable isotopes with particularly high absorption cross-sections include (Rauch and Waschkowski, 2003): B, Rh, Cd, In, Pm, Sm, Eu, Gd, Dy, Er, Tm, Hf, Ir, Au, Hg, Pa, Np. Hydrogenous material is often used to slow down high energy (fast) neutrons so that they can interact with the other isotopes in the shielding. Boron-10 is extensively used to capture thermal neutrons as it has a high capture cross-section and is abundant (19.4% of naturally occurring boron (Rauch and Waschkowski, 2003)). The macroscopic cross-section for both removal of fast neutrons and absorption of thermal neutrons is the product of the relevant microscopic cross-section and the number of atoms per unit volume of each isotope, this value can then be summed for all isotopes in a material.

8.3. MATERIALS AND METHODS

The boron starting materials utilised to manufacture AABSIP were borax ($Na_2B_4O_7.10H_2O$) and anhydrous borax ($Na_2B_4O_7$). The anhydrous borax was produced by dehydrating borax at 150°C for 30 minutes followed by further dehydration at 300°C for 15 hours. The diffraction pattern of the anhydrous borax is shown in Figure 8-1. The formulations of the AABSIP samples are presented in Table 8-1. Given the solubility of borax in sodium hydroxide solution, a formulation of $Na_{1.10}BSi_{1.70}O_{8.88}.4.65(H_2O)$ was selected for both mix 1 and mix 2. The boron containing feedstocks were dissolved in the sodium hydroxide solution. This solution was then mixed with silica fume in an ARE-250 Orbital Planetary Mixer (Thinky, Japan) at 1300 rpm for 5 minutes followed by a deaeration cycle of 2100 rpm for 0.5 minute. The resulting slurry was cured at 70°C for 24 hours in 24 mm diameter polypropylene vials. Compressive strength testing was conducted after cutting sample ends perpendicular to the long axis and air drying for approximately 1 hour prior to testing. An EZ50 (Lloyds, England) was used to apply a constant stress rate of 0.25 MPa/s, after a 50 N preload until the samples failed. Note: The Young's modulus were determined by the gradient of the stress-strain curve during compressive testing, it is repeatable between samples, but is an order of magnitude less that literature values, see section 3.7 for more details

Table 8-1 Formulations of the AABSIP samples.

Material	Supplier	Mix 1	Mix 2
Silica Fume SF98	Australian Fused Materials	40.5 wt%	40.5 wt%
Borax	Sigma Aldrich	-	37.1 wt%
Anhydrous Borax	Sigma Aldrich, then Heated at 300°C	19.5 wt%	-
NaOH (AR Grade)	ChemSupply	9.3 wt%	9.3 wt%
Deionised water		30.6 wt%	13.1 wt%

The ring milled fracture pieces were drifted into top loading plastic XRD sample holders. The x-ray diffraction patterns were collected on a D8 Advance (Bruker-AXS, Germany) with copper anode (40 kV, 40 mA) with a position sensitive detector (covering 3° 2θ). The patterns were collected from 10° to 100° 2θ with a nominal step size of 0.02° at 0.5 seconds/step. The

Bragg peaks from the crystalline phases were identified by search/match using EVA 11 (Bruker-AXS, Germany) to search the JCPDF Database. The morphology of the fracture surfaces were analysed with a Zeiss EVO-40 (Carl-Zeiss, Germany) scanning electron microscope (SEM).

8.4. RESULTS AND DISCUSSION

The anhydrous borax dissolved more rapidly than the hydrated borax in the sodium hydroxide solution and with a lower viscosity. The geopolymer slurry of mix 1 resulted in a lower viscosity than mix 2. After 7 days the samples from mix 1 and mix 2 produced samples that appeared dense, with a smooth surface finish and khaki colour. The compressive strength testing indicated that samples underwent elastic deformation followed by brittle fracture similar to behaviour exhibited by geopolymer pastes (Williams and van Riessen, 2010). The compressive strength and Young's modulus of both mixes were equal within uncertainties, Table 8-2. The strength and deformation mode indicate that this new class of material would be suitable for structural applications, similar to that of Portland cement or geopolymers. The spread of compressive strength results for mix 2 was significantly greater than for mix 1, believed to be caused by increased heterogeneity of mix 2.

Table 8-2 Compressive strength and Young's modulus of AABSIP samples. Uncertainties quoted are the standard deviation of 4 replicate samples.

	Compressive Strength (MPa)	Young's Modulus (GPa)
Mix 1	56(7)	1.95(7)
Mix 2	45(16)	1.71(7)

The microstructure of the AABSIP samples is similar to that of geopolymers; a glassy matrix with some pores (Barbosa et al., 2000, Rowles and O'Connor, 2003, Steveson and Sagoe-Crentsil, 2005a, Williams and van Riessen, 2010). Figure 8-2 illustrates the microstructure of a fracture surface of mix 1 which is also typical of mix 2. The micrograph shows a porous glassy matrix with some undissolved silica fume spheres and a ~3 μm borax crystal (assumed from morphology, EDS and the XRD results).

The samples were found to be predominantly x-ray amorphous with minor concentrations of borax (Figure 8-1). Samples from both mixes had similar x-ray diffraction patterns. The XRD data indicates that there has been a reaction, as the patterns of the AABSIP samples are not a linear combination of the calcined borax (amorphous) and the silica fume (amorphous).

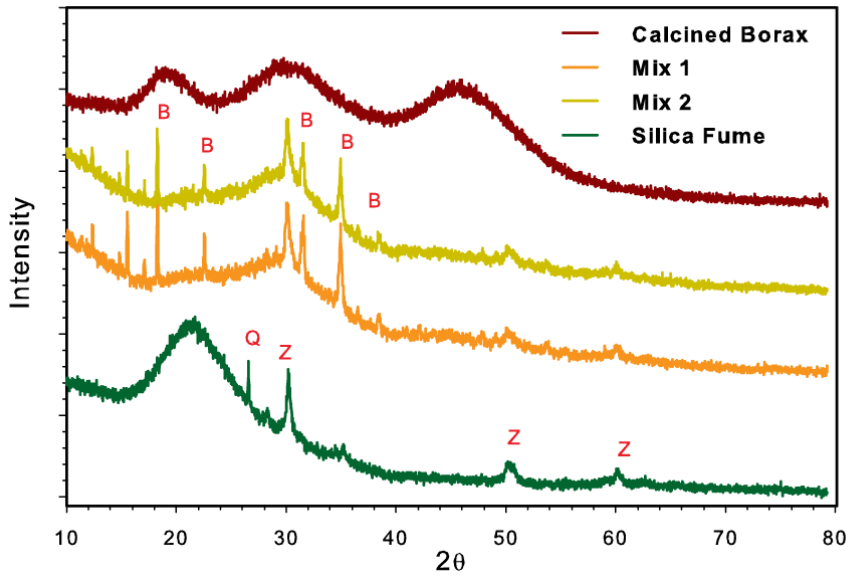

Figure 8-1 X-ray diffraction patterns of the silica fume and the anhydrous borax feedstocks that were used to produce the AABSIP samples mix 1 and mix 2. The crystalline peaks in the silica fume are zirconia (Z) and quartz (Q). The crystalline phase formed in the AABSIP samples was Borax decahydrate (B). Patterns offset for visibility.

The AABSIP samples were sound materials with high strength indicating a useful novel material has been developed. It is considered that the reaction mechanisms for AABSIP materials are similar to that of geopolymers (alkali activated aluminosilicate inorganic polymer) and alkali activated boroaluminosilicate (Nicholson and Fletcher, 2005). In the alkali activated boroaluminosilicate materials the boron was incorporated into the geopolymer matrix in Q4 sites (Nicholson and Fletcher, 2005). Synthesis of a strong stable material implies that boron was incorporated into a stable structure alongside the alkali and silicate, suggesting that B can substitute for Al.

This new class of material, AABSIP, is ideal for neutron shielding: castable, strong and with relatively high macroscopic neutron cross-sections for both fast and thermal neutrons. Table 8-3 shows the macroscopic cross-section for absorption and removal of thermal and fast neutrons respectively. An increase in macroscopic cross-sections results in more effective neutron shielding. For thermal neutrons the AABSIP samples have comparable abilities (per unit length) to that of borated polyethylene and superior to that

of water. For fast neutrons the AABSIP samples have comparable abilities to both borated polyethylene and water.

Table 8-3 Comparison of the calculated neutron shielding properties of the AABSIP and other shielding materials. Increased macroscopic cross-section results in improved neutron stopping power. References are for the composition of the material. The cross-section data is from published data (NCRP, 1971, Rauch and Waschkowski, 2003).

	(Thermal) macroscopic absorption cross-section (cm^{-1})	(Fast) macroscopic removal cross-section (cm^{-1})
AABSIP	2.8	0.11
AABSIP (50% dehydroxilation)	3.3	0.10
AABSIP (100% dehydroxilation)	4.1	0.08
Magnetite Concrete (El-Khayatt and El-Sayed Abdo, 2009)	0.06	0.11
Borated Polyethylene (NCRP, 1971) (8 wt% B_4C)	2.6	0.13
Borated Polyethylene (2007) (SWX-207HD5)	3.8	0.06
Water	0.02	0.11

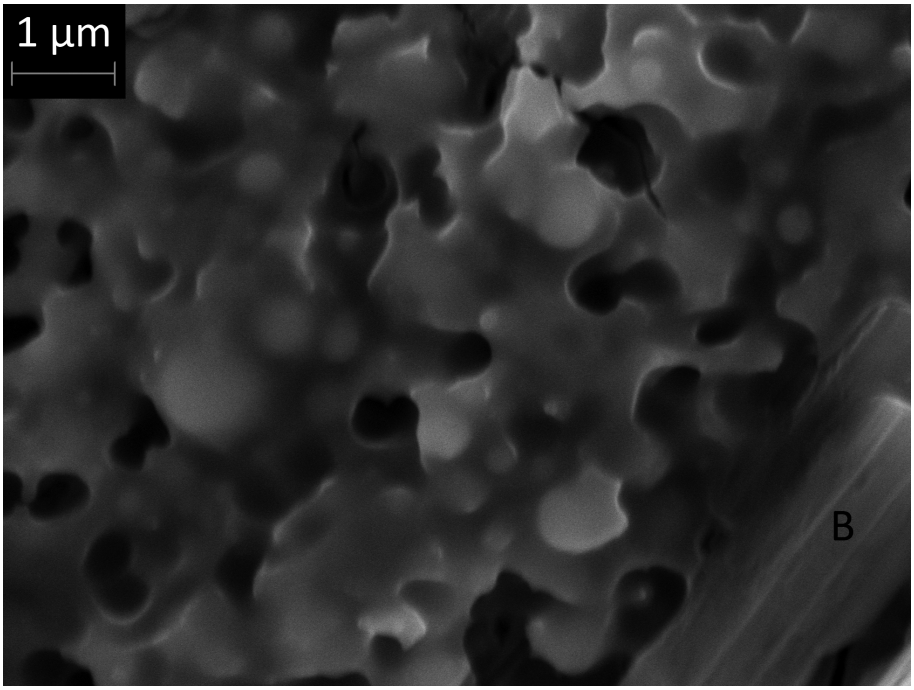

Figure 8-2 Microstructure of mix 1, a porous glassy matrix, with a crystallised borax crystal (B).

The bound water content of the AABSIP is useful to moderate (slow down) the fast neutrons, although in some situations the water will need to be removed from the structure when radiolitic hydrogen is problematic. Removal

of the water from the samples will reduce the effectiveness of shielding fast neutrons but increase the effectiveness of shielding thermal neutrons. The maximum working temperature of AABSIP is likely to be significantly higher than that of borated polyethylene (<90°C); this will be investigated in future work. AABSIP can be cast into moulds of various shapes and sizes, it can even be cast in situ making it one of the most versatile neutron shielding materials available. The material's high compressive strength indicates that structural walls can be constructed with AABSIP, making this material ideal for outer walls of nuclear facilities. AABSIP also has the advantage that it will not become significantly radioactive from neutron activation, reducing the need for secondary shielding for gamma radiation, particularly if potassium is substituted for sodium (Rauch and Waschkowski, 2003).

8.5. CHAPTER CONCLUSIONS

A new class of material has been presented – alkali activated borosilicate inorganic polymer (AABSIP). The microstructure is composed of a glassy matrix with many sub-micron pores and with some remnant precursor material. It has been identified as suitable for structural and non-structural applications, particularly for neutron shielding applications, based on the compressive strength and boron content.

CHAPTER 9: CONCLUDING REMARKS

9.1. CONCLUSIONS

This thesis aimed to improve the understanding on how to formulate geopolymers. In Chapter 4 a method was developed to accurately quantify what portion of the flyash should be used in formulation calculations. In Chapter 5 the effect of the formulation on strength, cost and green-house-gas emissions was investigated. In Chapter 6, several methods were compared to determine how much of the solid feedstock actually reacts. Chapter 7 extended the work in Chapter 4 and 6 to quantify the kinetics of the solid feedstock dissolution. Chapter 8 investigated the possibility of new material by replacing the aluminium with boron in an alkali activated inorganic polymer.

In Chapter 4, it was demonstrated that if only the amorphous component of the flyash is considered in formulating geopolymer, the compositions that yield strong geopolymer pastes are similar in composition to that of metakaolin geopolymers. Therefore for geopolymers, regardless of the source aluminosilicate, there is a common composition that results in good mechanical properties.

It was found that Collie and Port Augusta flyashes had disparate bulk compositions, with Si/Al of 1.65(1) and 1.30(1), respectively. While the determined amorphous compositions were equal, within uncertainties, in concentration, 65(4) wt% and 67(3) wt% respectively, and Si/Al ratio 1.7(2) for both. When the amorphous content was used to formulate geopolymer with a Si/Al = 2.0, Na/Si = 1.0 and H/Si = 5.5: Collie, Port Augusta and metakaolin geopolymer had equal compressive strengths within experimental uncertainties, on a 95% confidence interval. However, Bayswater flyash, with much higher bulk and amorphous Si/Al ratios of 2.34(2) and 4.3(3), respectively, the same did not hold. This is probably due to the fact Bayswater flyash was activated with sodium aluminate solution rather than sodium silicate to achieve the correct composition. While sodium aluminate activation can yield strong geopolymer, the incomplete dissolution of the flyash/metakaolin has a different effect, assuming congruent dissolution of Si and Al from the solid. For a sodium silicate activated geopolymer, incomplete

dissolution results in a binding matrix with a higher than designed Si/Al and Na/Al ratios. Whereas for a sodium aluminate activated geopolymer, the incomplete dissolution will result in a binding matrix with a lower than planned Si/Al ratio and higher than planned Na/Al ratio. Hence because the planned matrix composition does not account for incomplete dissolution the actual composition of matrix would not even approximately be equal for sodium silicate and sodium aluminate activated geopolymers of the same planned matrix composition.

In Chapter 5, it was found the GHG emission rate was 240(50) kg-CO_2-eq per tonne of geopolymer paste, the standard deviation is the variation associated with changing geopolymer composition. The relative standard deviation (21%) indicates the GHG metric should be calculated on a case specific basis rather trying to use one value for all geopolymers.
As expected it was found that the GHG emissions is most sensitive to changes in the sodium hydroxide and sodium silicate content of geopolymer, as the emission rate for these are orders of magnitude higher than that of the flyash. However it is clear that if the flyash requires transportation over very large distances (i.e. 1000's of km), then the contribution to GHG must be carefully assessed.

In Chapter 6, an extension of the PONCKS methods provided a novel method to determine the degree of dissolution of metakaolin in geopolymers. This method provided significant insight into why the compressive strengths of geopolymers are so sensitive to changes in composition. The significant effect that the incomplete dissolution of the metakaolin has on strength is that matrix chemistry differs from optimal rather than the effect of the reduced quantity of matrix.
The degree of dissolution of the metakaolin varied from 3.3(6) to 80.8(4) % for geopolymers with compressive strengths varying from 3.1(2) to 67(17) MPa. However, it was found that the compressive strength did not correlate with the quantity of matrix available for binding.

Chapter 7 combined the methodologies of Chapters 4 and 6 in a time resolved experiment on the early stages of flyash geopolymerisation. The result was a novel method to separately measure the dissolution of flyash and subsequent formation of geopolymer matrix during the initial stages of the reaction. The temporal variations of the solution H/Si ratio were found to impact the final physical properties.
The degree of dissolution of the flyash was found to be 29%, 54%, 38% and 42% after 22 hours, which is less than the degree of dissolution of metakaolin in metakaolin geopolymers after 28 days in Chapter 6.
It was confirmed that there are more than one mechanism of zeolite formation even within the same sample.

In Chapter 8, a novel class of material has been developed – alkali activated borosilicate inorganic polymer (AABSIP). This material has a compressive strength of 56(7) MPa, making it suitable for structural applications. Both the fast and thermal neutron shielding properties for AABSIP are comparable to commercially available products, such as borate polyethylene.

The combination of findings from chapters 4, 6 and 7 reveal that to better understand geopolymer formulation the following must be quantified:

- Quantity of reactive material in the solid feedstocks
- Extent to which the reactive material actually reacts
- Temporal variations in the reaction rates in the first few hours

The above has a significant effect on the physical properties of the geopolymer as it would impact on the specific chemical speciation of the resulting geopolymer matrix.

Chapter 5 reveals that there is scope to slightly de-optimise the mixture design for maximum physical properties in favour of optimising for reductions in green-house-gas emissions and costs. Chapter 8 discusses the possibility of using more than just alkali aluminosilicates, namely substituting boron containing feedstocks for the typically used Al containing feedstocks.

9.2. SIGNIFICANCE OF THE THESIS

The outcomes of the result chapters (4, 5, 6, 7 and 8) each have independently provided a significant contribution to the field of study. Perhaps the most significant contributions are from Chapter 6, 7 and 8; with two new analysis methods having been developed and a new class of material discovered.

The extended PONCKS method was shown to allow the quantification of the amorphous metakaolin in the presence of amorphous geopolymer matrix which provides a powerful analytical method. This method will be beneficial to other researchers studying metakaolin or flyash geopolymers and related alkali activated cements.

Similarly, the time resolved analysis method presented in the analysis of the early stages of flyash geopolymerisation is likely to be useful to researchers needing to monitor their specific geopolymerisation process. The quantification of the flyash amorphous content remaining and geopolymer matrix formed are likely to be very helpful in understanding the early stages of both flyash and metakaolin geopolymerisation.

The new class of material, AABSIP, creates a new application for geopolymer like materials, namely structural neutron shielding.

9.3. FUTURE WORK

The scope of future works include:

Utilise the PONCKS method of XRD analysis method used Chapter 6 to investigate other factors that influence the degree of dissolution of either metakaolin or flyash during geopolymerisation, such formulation, curing temperature, additives such as borate, calcium compounds, salts etc. that have been investigated with other methods to determine the degree of reaction.

Utilise the in situ method used in Chapter 7 investigate a wider range of flyash and metakaolin geopolymer formulations, and factors as per the above paragraph. The small angle x-ray scatter region is of interest and further investigation is warranted, it would be wise to plan the experiment next time such as to collect the SAXS and WAXS simultaneously. This may allow a better understanding of physical phenomena being observed to be developed.

The alkali activated borosilicate inorganic polymers (AABSIP) described in Chapter 8 deserves much attention. The AABSIP's must be tested as mortars and concretes, both with traditional concrete aggregates, such as silica sands and basalt rocks; but also with aggregates typically reserved for radiation shielding such as lead or steel shot; and/or borated plastic fibres. The speciation could be studied with a technique such as NMR or ATR-FTIR, which would increase the understanding of how this class of material relates to geopolymers.

Alternatively, as has already commenced by other researchers inspired by this work, investigate activation of flyash with alkali borate solutions.

CHAPTER 10: REFERENCES

ABARE. 2008. *Energy Update 2008 - Table F: Australian energy consumption, by industry and fuel type* [Online]. Canberra: Australian Bureau of Agricultural and Resource Economics. Available: http://www.abare.gov.au [Accessed July 20th 2009].
ABS 2006. Survey of Motor Vehicle Use Australia (12 months ended 31 October 2006). *In:* STATISTICS, A. B. O. (ed.). Canberra: Australian Bureau of Statistics.
ALINTA ENERGY 2015. Flinders Operations Closure Update. https://alintaenergy.com.au/about-us/news/flinders-operations-closure-update.
ALKALI MANUFACTURERS' ASSOCIATION OF INDIA 2012. Industry Review. Alkali Manufactures' Assoication of India.
ALLAHVERDI, A. & SKVARA, F. 2001a. Nitric acid attack on hardened paste of geopolymeric cements part 1. *Ceramics-Silikaty,* 45**, 3,** 81-88
ALLAHVERDI, A. & SKVARA, F. 2001b. Nitric acid attack on hardened paste of geopolymeric cements: Part 2. *Ceramics-Silikaty,* 45**, 4,** 143-149
ALLEN, A. J., THOMAS, J. J. & JENNINGS, H. M. 2007. Composition and density of nanoscale calcium-silicate-hydrate in cement. *Nature Materials,* 6**, 4,** 311-6.http://dx.doi.org/10.1038/nmat1871
ALLWOOD, J., CULLEN, J. & MILFORD, R. 2010. Options for Achieving a 50% Cut in Industrial Carbon Emissions by 2050. *Environmental Science & Technology,* 44**, 6,** 1888-94.http://dx.doi.org/10.1021/es902909k
APPELBAUM CONSULTING GROUP 2007. Australian Transport Facts 2007. Melbourne, Victoria: Australian Transport Energy data and Analysis Centre.
ASTM INTERNATIONAL 2015. C618 - 15: Standard Specification for Coal Fly Ash and Raw or Calcined Natural Pozzolan for Use in Concrete.
AUSTRALIAN STANDARDS AS 3582.1 - 1998. Supplementary cementitious materials for use with portland and blended cements, Part 1: Fly ash. *Australian Standards.* Standards Association of Australia.
BAKHAREV, T. 2005. Resistance of geopolymer materials to acid attack. *Cement and Concrete Research,* 35**, 4,** 658.http://dx.doi.org/10.1016/j.cemconres.2004.06.005
BALZAR, D. 2000. Voigt-Function Model in Diffraction Line-Broadening Analysis. *In:* SNYDER, R., FIALA, J. & BUNGE, H. J. (eds.) *Defect and Microstructure Analysis by Diffraction.* Oxford University Press.
BAN, T. & OKADA, K. 1992. Structure Refinement of Mullite by the Rietveld Method and a New Method for Estimation of Chemical Composition. *Journal of the American Ceramic Society,* 75**, 1,** 227-230.http://dx.doi.org/10.1111/j.1151-2916.1992.tb05473.x
BARBOSA, V. F. F. & MACKENZIE, K. J. D. 2003. Synthesis and thermal behaviour of potassium sialate geopolymers. *Materials Letters,* 57**, 9-10,** 1477.http://dx.doi.org/10.1016/S0167-577X(02)01009-1
BARBOSA, V. F. F., MACKENZIE, K. J. D. & THAUMATURGO, C. 2000. Synthesis and characterisation of materials based on inorganic polymers of alumina and silica: sodium polysialate polymers. *International Journal of Inorganic Materials,* 2**, 4,** 309.http://dx.doi.org/10.1016/S1466-6049(00)00041-6
BAUER, A. & BERGER, G. 1998. Kaolinite and smectite dissolution rate in high molar KOH solutions at 35° and 80°C. *Applied Geochemistry,* 13**, 7,** 905-916.http://dx.doi.org/10.1016/S0883-2927(98)00018-3
BAUER, A., VELDE, B. & BERGER, G. 1998. Kaolinite transformation in high molar KOH solutions. *Applied Geochemistry,* 13**, 5,** 619-629.http://dx.doi.org/10.1016/S0883-2927(97)00094-2
BELL, J. L., DRIEMEYER, P. E. & KRIVEN, W. M. 2009a. Formation of Ceramics from Metakaolin-Based Geopolymers. Part II: K-Based Geopolymer. *Journal of the American Ceramic Society,* 92**, 3,** 607-615.http://dx.doi.org/10.1111/j.1551-2916.2008.02922.x
BELL, J. L., DRIEMEYER, P. E. & KRIVEN, W. M. 2009b. Formation of Ceramics from Metakaolin-Based Geopolymers: Part I - Cs-Based Geopolymer. *Journal of the American Ceramic Society,* 92**, 1,** 1-8.http://dx.doi.org/10.1111/j.1551-2916.2008.02790.x
BELL, J. L. & KRIVEN, W. M. 2004. Nanoporosity in Aluminosilicate, Geopolymeric Cements. *Microscopy and Microanalysis,* 10**, Supplement S02,** 590.http://dx.doi.org/10.1017/S1431927604884496
BELL, J. L. & KRIVEN, W. M. 2009. Preparation of Ceramic Foams from Metakaolin-Based Geopolymer Gels. *Developments in Strategic Materials,* 29**, 10,** 97-111
BLACKFORD, M. G., HANNA, J. V., PIKE, K. J., VANCE, E. R. & PERERA, D. S. 2007. Transmission Electron Microscopy and Nuclear Magnetic Resonance Studies of Geopolymers for Radioactive Waste Immobilization. *Journal of the American Ceramic Society,* 90**, 4,** 1193-1199.http://dx.doi.org/10.1111/j.1551-2916.2007.01532.x
BRINDLEY, G. W. 1945. XLV. The effect of grain or particle Size on x-ray reflections from mixed powders and alloys, considered in relation to the quantitative determination of crystalline substances by x-ray methods. *The London, Edinburgh, and Dublin Philosophical Magazine and Journal of Science,* 36**, 256,** 347-369.10.1080/14786444508520918
BROUWERS, H. J. H. & VAN EIJK, R. J. 2002. Fly ash reactivity: Extension and application of a shrinking core model and thermodynamic approach. *Journal of Materials Science,* 37**, 10,** 2129-2141.http://dx.doi.org/10.1023/A:1015206305942
BRUKER AXS 2008. TOPAS V4: General profile and structure analysis software for powder diffraction data. Karlsruhe, Germany.: Bruker AXS.
BULLARD, J. W., JENNINGS, H. M., LIVINGSTON, R. A., NONAT, A., SCHERER, G. W., SCHWEITZER, J. S., SCRIVENER, K. L. & THOMAS, J. J. 2011. Mechanisms of cement hydration. *Cement and Concrete Research,* 41**, 12,** 1208-1223.http://dx.doi.org/10.1016/j.cemconres.2010.09.011
CAMERON, W. E. 1977. Composition and Cell Dimensions of Mullite. *American Ceramic Society Bulletin,* 56**, 11,** 1003
CHANG, E. H., SARKER, P. K., LLOYD, N. & RANGAN, B. V. Year. Shear Behaviour of Reinforced Fly Ash-Based Geopolymer Concrete Beams. *In:* Proceedings of the Concrete Institute of Australia 23rd Biennial Conference, October 18 - 20 2007 Adelaide, Australia. 679 - 687.
CHEARY, R. W. & COELHO, A. 1992. A fundamental parameters approach to X-ray line-profile fitting. *Journal of Applied Crystallography,* 25**, 2,** 109-121.http://dx.doi.org/10.1107/s0021889891010804
CHEARY, R. W., COELHO, A. A. & CLINE, J. P. 2004. Fundamental Parameters Line Profile Fitting in Laboratory Diffractometers. *Journal of Research of the National Institute of Standards and Technology,* 109**, 1,** 1-25

CHEN-TAN, N. W., RIESSEN, A. V., LY, C. V. & SOUTHAM, D. C. 2009. Determining the Reactivity of a Fly Ash for Production of Geopolymer. *Journal of the American Ceramic Society,* 92**, 4,** 881-887.http://dx.doi.org/10.1111/j.1551-2916.2009.02948.x
CIF 2008. CIF Annual Report to Greenhouse Challenge Plus - 2007/08. Canberra: Cement Industry Foundation.
CIF 2013. Industry Report 2013. Cement Industry Federation.
COMMONWEALTH OF AUSTRALIA. 2011. *Carbon Pollution Reduction Scheme* [Online]. Available: http://www.climatechange.gov.au/government/initiatives/cprs.aspx [Accessed 3 April 2011 2011].
CSRP 2010. Cooperative Research Centre for Sustainable Resource Processing: ACHIEVEMENTS 2003 – 2010; Our contribution to the sustainable processing of minerals and metals. Perth, Western Australia: Cooperative Research Centre for Sustainable Resource Processing (CSRP).
CULLITY, B. D. & WEYMOUTH, J. W. 1957. Elements of X-Ray Diffraction. *American Journal of Physics,* 25**, 6,** 394-395.http://dx.doi.org/10.1119/1.1934486
DAVIDOVITS, J. 1987. Properties of geopolymer cements. *Concrete International,* 9**,** 23-35
DAVIDOVITS, J. 1989. Geopolymers and geopolymeric materials. *Journal of Thermal Analysis and Calorimetry,* 35**, 2,** 429-41.http://dx.doi.org/10.1007/BF01904446
DAVIDOVITS, J. 1991. Geopolymers: Inorganic polymeric new materials. *Journal of Thermal Analysis (UK),* 37**, 8,** 1633.http://dx.doi.org/10.1007/BF01912193
DAVIDOVITS, J. 1993. Geopolymer cements to minimise carbon dioxide greenhouse warming. *Ceramic Transactions,* 37**,** 165-182
DAVIDOVITS, J. 1994. Global warming impact on the cement and aggregates industries. *World Resource Review,* 6**, 2,** 263
DAVIDOVITS, J. 2002. Environmentally driven geopolymer cement applications. *In:* WILLIAMS, J. R. (ed.) *Geopolymer 2002 3rd International Conference: Turning potential into profit.* Melbourne: Geopolymer Institute.
DAVIDOVITS, J. & DAVIDOVICS, M. 1991. Geopolymer - Ultra-High Temperature Tooling Material for the Manufacture of Advanced Composites. *36th International Sampe Symposium and Exhibition, Book 1 and 2.*
DAVIDOVITS, J. & SAWYER, J. L. 1985. *EARLY HIGH-STRENGTH MINERAL POLYMER*. United States of America patent application 582279.
DAVIDOVITS, J., SCHMITT, R.-E. & FRIEHMELT, V. 1993. Microwave processing of geopolymer-cement based waste forms. *Ceramic Transactions,* 36**,** 61-72
DAVIDOVITS, N., DAVIDOVICS, M. & DAVIDOVITS, J. 1989. *CERAMIC-CERAMIC COMPOSITE MATERIAL AND PRODUCTION METHOD*. United States of America patent application 218286.
DE MOOR, P.-P. E. A., BEELEN, T. P. M., KOMANSCHEK, B. U. & VAN SANTEN, R. A. 1998. Nanometer scale precursors in the crystallization of Si-TPA-MFI. *Microporous and Mesoporous Materials,* 21**, 4–6,** 263-269.http://dx.doi.org/10.1016/S1387-1811(98)00008-0
DE SILVA, P., SAGOE-CRENSTIL, K. & SIRIVIVATNANON, V. 2007. Kinetics of geopolymerization: Role of Al2O3 and SiO2. *Cement and Concrete Research,* 37**, 4,** 512-518.http://dx.doi.org/10.1016/j.cemconres.2007.01.003
DITRDLG 2008. Australian transport statistics, June 2008. *In:* DEPARTMENT OF INFRASTRUCTURE, T., REGIONAL DEVELOPMENT AND LOCAL GOVERNMENT (ed.). Canberra, Australia: Australian Government.
DOKTER, W. H., BEELEN, T. P. M., VAN GARDEREN, H. F., VAN SANTEN, R. A., BRAS, W., DERBYSHIRE, G. E. & MANT, G. R. 1994. Simultaneous monitoring of amorphous and crystalline phases in silicalite precursor gels. An in situ hydrothermal and time-resolved small- and wide-angle X-ray scattering study. *Journal of Applied Crystallography,* 27**, 6,** 901-906.http://dx.doi.org/10.1107/S0021889894004693
DOMBROWSKI, K., BUCHWALD, A. & WEIL, M. 2007. The influence of calcium content on the structure and thermal performance of fly ash based geopolymers. *Journal of Materials Science,* 42**, 9,** 3033-3043.http://dx.doi.org/10.1007/s10853-006-0532-7
DROUIN, D., COUTURE, A. R., JOLY, D., TASTET, X., AIMEZ, V. & GAUVIN, R. 2007. CASINO V2.42 - A Fast and Easy-to-use Modeling Tool for Scanning Electron Microscopy and Microanalysis Users. *Scanning,* 29**, 3,** 92-101
DUXSON, P. 2006. *The structure and thermal evolution of metakaolin geopolymers.* PhD PhD, The University of Melbourne.
DUXSON, P., LUKEY, G. C., SEPAROVIC, F. & VAN DEVENTER, J. S. J. 2005a. Effect of alkali cations on aluminum incorporation in geopolymeric gels. *Industrial & Engineering Chemistry Research,* 44**, 4,** 832-839.http://dx.doi.org/10.1021/ie0494216
DUXSON, P., MALLICOAT, S. W., LUKEY, G. C., KRIVEN, W. M. & VAN DEVENTER, J. S. J. 2007a. The effect of alkali and Si/Al ratio on the development of mechanical properties of metakaolin-based geopolymers. *Colloids and Surfaces, A: Physicochemical and Engineering Aspects,* 292**, 1,** 8-20.http://dx.doi.org/10.1016/j.colsurfa.2006.05.044
DUXSON, P., PROVIS, J. L., LUKEY, G. C., MALLICOAT, S. W., KRIVEN, W. M. & VAN DEVENTER, J. S. J. 2005b. Understanding the relationship between geopolymer composition, microstructure and mechanical properties. *Colloids and Surfaces A: Physicochemical and Engineering Aspects,* 269**, 1-3,** 47-58.http://dx.doi.org/10.1016/j.colsurfa.2005.06.060
DUXSON, P., PROVIS, J. L., LUKEY, G. C., SEPAROVIC, F. & VAN DEVENTER, J. S. J. 2005c. 29Si NMR Study of Structural Ordering in Aluminosilicate Geopolymer Gels. *Langmuir,* 21**, 7,** 3028-3036.http://dx.doi.org/10.1021/la047336x
DUXSON, P., PROVIS, J. L., LUKEY, G. C. & VAN DEVENTER, J. S. J. 2007b. The role of inorganic polymer technology in the development of `green concrete'. *Cement and Concrete Research,* 37**, 12,** 1590-1597.http://dx.doi.org/10.1016/j.cemconres.2007.08.018
DUXSON, P., PROVIS, J. L., LUKEY, G. C., VAN DEVENTER, J. S. J., SEPAROVIC, F. & GAN, Z. H. 2006. K-39 NMR of free potassium in geopolymers. *Industrial & Engineering Chemistry Research,* 45**, 26,** 9208-9210.http://dx.doi.org/10.1021/le060838g

EL-KHAYATT, A. M. & EL-SAYED ABDO, A. 2009. MERCSF-N: A program for the calculation of fast neutron removal cross sections in composite shields. *Annals of Nuclear Energy,* 36**,** **6,** 832-836.http://dx.doi.org/10.1016/j.anucene.2009.01.013
EUROPEAN COMMISSION 2013. The EU Emissions Trading System (EU ETS). *In:* PUBLICATIONS OFFICE (ed.) *http://dx.doi.org/10.2834/55480*.
FAWER, M., POSTLETHWAITE, D. & KLÜPPEL, H. 1998. Life cycle inventory for the production of zeolite a for detergents. *The International Journal of Life Cycle Assessment,* 3**,** **2,** 71-74.http://dx.doi.org/10.1007/BF02978490
FENG, D., TAN, H. & VAN DEVENTER, J. S. J. 2004a. Ultrasound enhanced geopolymerisation. *Journal of Materials Science,* 39**,** **2,** 571.http://dx.doi.org/10.1023/B:JMSC.0000011513.87316.5c
FENG, X., GARBOCZI, E. J., BENTZ, D. P., STUTZMAN, P. E. & MASON, T. O. 2004b. Estimation of the degree of hydration of blended cement pastes by a scanning electron microscope point-counting procedure. *Cement and Concrete Research,* 34**,** **10,** 1787-1793.http://dx.doi.org/10.1016/j.cemconres.2004.01.014
FERNÁNDEZ-JIMÉNEZ, A., DE LA TORRE, A. G., PALOMO, A., LOPEZ-OLMO, G., ALONSO, M. M. & ARANDA, M. A. G. 2006. Quantitative determination of phases in the alkaline activation of fly ash. Part II: Degree of reaction. *Fuel,* 85**,** **14-15,** 1960-1969.http://dx.doi.org/10.1016/j.fuel.2010.03.051
FERNÁNDEZ-JIMÉNEZ, A. & PALOMO, A. 2005. Composition and microstructure of alkali activated fly ash binder: Effect of the activator. *Cement and Concrete Research,* 35**,** **10,** 1984-1992.10.1016/j.cemconres.2005.03.003
FERNÁNDEZ-JIMÉNEZ, A., PALOMO, A. & CRIADO, M. 2005. Microstructure development of alkali-activated fly ash cement: a descriptive model. *Cement and Concrete Research,* 35**,** **6,** 1204.http://dx.doi.org/10.1016/j.cemconres.2004.08.021
FERNANDEZ JIMINEZ, A. M., LACHOWSKI, E. E., PALOMO, A. & MACPHEE, D. E. 2004. Microstructural characterisation of alkali-activated PFA matrices for waste immobilisation. *Cement and Concrete Composites,* 26**,** **8,** 1001-1006.http://dx.doi.org/10.1016/j.cemconcomp.2004.02.034
FLETCHER, R. A., MACKENZIE, K. J. D., NICHOLSON, C. L. & SHIMADA, S. 2005. The composition range of aluminosilicate geopolymers. *Journal of the European Ceramic Society,* 25**,** **9,** 1471.http://dx.doi.org/10.1016/j.jeurceramsoc.2004.06.001
FLOWER, D. & SANJAYAN, J. 2007. Green house gas emissions due to concrete manufacture. *The International Journal of Life Cycle Assessment,* 12**,** **5,** 282-288.http://dx.doi.org/10.1065/lca2007.05.327
FRIEDLINGSTEIN, P., HOUGHTON, R. A., MARLAND, G., HACKLER, J., BODEN, T. A., CONWAY, T. J., CANADELL, J. G., RAUPACH, M. R., CIAIS, P. & LE QUERE, C. 2010. Update on CO2 emissions. *Nature Geosci,* 3**,** **12,** 811-812.http://dx.doi.org/10.1038/ngeo1022
GARNAUT, R. 2011. Update Paper six: Carbon pricing and reducing Australia's emissions. *Garnaut Climate Change Review – Update 2011*.
GOMES, S. & FRANCOIS, M. 2000. Characterization of mullite in silicoaluminous fly ash by XRD, TEM, and 29Si MAS NMR. *Cement and Concrete Research,* 30**,** **2,** 175-181.http://dx.doi.org/10.1016/S0008-8846(99)00226-4
GOOGLE. 2015. *Google Maps* [Online]. Available: maps.google.com.au [Accessed].
GOURLEY, J. & JOHNSON, G. Year. Developments in geopolymer precast concrete. *In:* World Congress Ceopolymer, 2005. 139-143.
GRANIZO, M. L., BLANCO-VARELA, M. T. & PALOMO, A. 2000. Influence of the starting kaolin on alkali-activated materials based on metakaolin. Study of the reaction parameters by isothermal conduction calorimetry. *Journal of Materials Science,* 35**,** **24,** 6309.http://dx.doi.org/10.1023/A:1026790924882
HAJIMOHAMMADI, A., PROVIS, J. L. & VAN DEVENTER, J. S. J. 2010. Effect of Alumina Release Rate on the Mechanism of Geopolymer Gel Formation. *Chemistry of Materials,* 22**,** **18,** 5199-5208.10.1021/cm101151n
HARDJITO, D., WALLAH, S. E., SUMAJOUW, D. M. J. & RANGAN, B. V. 2004. On the development of fly ash-based geopolymer concrete. *ACI Materials Journal,* 101**,** **6,** 467-472
HARSH, S., SHEN, Z. & DARWIN, D. 1990. Strain-Rate Sensitive Behavior of Cement Paste and Mortar in Compression. *ACI Materials Journal,* 87**,** **5,** 508-516
HART, R. D., LOWE, J. L., SOUTHAM, D. C., PERERA, D. S., WALLS, P., VANCE, E. R., GOURLEY, T. & WRIGHT, K. 2006. Aluminosilicate inorganic polymers from waste materials. *Publications of the Australasian Institute of Mining and Metallurgy,* 3/2006**,** **Green Processing 2006,** 93-103
HART, R. D., PIERRE, T. G. S., GILKES, A. J., MCKINLEY, A. J., SIRADZ, S. & BALWANT, S. 2002. Iron in soil kaolins from Indonesia and Western Australia. *Clay Minerals,* 37**,** 671.http://dx.doi.org/10.1180/0009855023740069
HART, R. D., WIRIYAKITNATEEKUL, W. & GILKES, R. J. 2003. Properties of soil kaolins from Thailand. *Clay Minerals,* 38**,** **1,** 71-94.http://dx.doi.org/10.1180/0009855033810080
HEELEY, P. 2003. Ash utilisation in Australia: a market study. Brisbane, Australia: Cooperative Research Centre for Coal in Sustainable Development.
HEIDRICH, C., HINCZAK, I. & RYAN, B. 2005. Case study: CCP's potential to lower greenhouse gas emissions for Australia. *World of Coal Ash.* Lexington, Kentucky, USA: American Coal Ash Association.
HUGHES, J. C., GILKES, R. J. & HART, R. D. 2009. Intercalation of reference and soil kaolins in relation to physico-chemical and structural properties. *Applied Clay Science,* 45**,** **1-2,** 24-35.http://dx.doi.org/10.1016/j.clay.2009.04.006
HUNTZINGER, D. N. & EATMON, T. D. 2009. A life-cycle assessment of Portland cement manufacturing: comparing the traditional process with alternative technologies. *Journal of Cleaner Production,* 17**,** **7,** 668-675.http://dx.doi.org/10.1016/j.jclepro.2008.04.007
ICIS 2008. Sodium silicate. *ICIS Chemical Business,* 273**,** **12,** 38-39
IEA 2008. CO_2 emissions from fuel combustion. Paris, France: International Energy Agency.
JAMIESON, E., MCLELLAN, B., VAN RIESSEN, A. & NIKRAZ, H. 2015. Comparison of embodied energies of Ordinary Portland Cement with Bayer-derived geopolymer products. *Journal of Cleaner Production,* 99**,** 112-118.http://dx.doi.org/10.1016/j.jclepro.2015.03.008

JAMIESON, E. J. 2008. *Method for management of contaminants in alkaline process liquors* Australia patent application 2007283446.
JÄMSTORP, E., FORSGREN, J., BREDENBERG, S., ENGQVIST, H. & STRØMME, M. 2010. Mechanically strong geopolymers offer new possibilities in treatment of chronic pain. *Journal of Controlled Release,* 146**, 3,** 370-377.http://dx.doi.org/10.1016/j.jconrel.2010.05.029
JOZIĆ, D., ZORICA, S., TIBLJAŠ, D. & BERNSTORFF, S. Year. Insitu SAXS/WAXS study of the developing process of geopolymer structures. *In:* 15th European Conference on Composite Materials, 2012 2012.
KERN, A., MADSEN, I. & SCARLETT, N. Y. 2012. Quantifying Amorphous Phases. *In:* KOLB, U., SHANKLAND, K., MESHI, L., AVILOV, A. & DAVID, W. I. F. (eds.) *Uniting Electron Crystallography and Powder Diffraction.* Springer Netherlands.
KEYTE, L. 2008. *What's wrong with Tarong? The importance of coal fly ash glass chemistry in inorganic polymer synthesis.* Doctor of Philosophy, The University of Melbourne.
KIRKUP, L. 1994. *Experimental methods :an introduction to the analysis and presentation of data.,* Brisbane, John Wiley & Sons.
KÖHLER, S. J., DUFAUD, F. & OELKERS, E. H. 2003. An experimental study of illite dissolution kinetics as a function of ph from 1.4 to 12.4 and temperature from 5 to 50°C. *Geochimica et Cosmochimica Acta,* 67**, 19,** 3583-3594.http://dx.doi.org/10.1016/S0016-7037(03)00163-7
KRIVEN, W. M., BELL, J. L. & GORDON, M. 2004. Geopolymer refractories for the glass manufacturing industry. *Ceramic Engineering and Science Proceedings,* 25**, 1,** 57-79.http://dx.doi.org/10.1002/9780470294857.ch5
KRIVENKO, P. Year. Development of alkaline cements supported by theory and practice. *In:* International Workshop on Geopolymer Cements and Concretes, 2005 Perth, Western Australia.
KURDOWSKI, W. 2014. *Cement and Concrete Chemistry*, Springer Netherlands.
LATELLA, B., PERERA, D., DURCE, D., MEHRTENS, E. & DAVIS, J. 2008. Mechanical properties of metakaolin-based geopolymers with molar ratios of Si/Al ≈ 2 and Na/Al ≈ 1. *Journal of Materials Science,* 43**, 8,** 2693-2699.http://dx.doi.org/10.1007/s10853-007-2412-1
LECOMTE, I., LIEGEOIS, M., RULMONT, A., CLOOTS, R. & MASERI, F. 2003. Synthesis and characterization of new inorganic polymeric composites based on kaolin or white clay and on ground-granulated blast furnace slag. *Journal of Materials Research,* 18**, 11,** 2571-2579.http://dx.doi.org/10.1557/JMR.2003.0360
LI, J. F., LI, L. & STOTT, F. H. 2004. Crystallographical analysis of surface layers of refractory ceramics formed using combined flame spray and simultaneous laser treatment. *Journal of the European Ceramic Society,* 24**, 10-11,** 3129-3138.http://dx.doi.org/10.1016/j.jeurceramsoc.2003.11.002
LI, Z. J. & LIU, S. F. 2007. Influence of slag as additive on compressive strength of fly ash-based geopolymer. *Journal of Materials in Civil Engineering,* 19**, 6,** 470-474.http://dx.doi.org/10.1061/(Asce)0899-1561(2007)19:6(470)
LIPPIATT, B. C. & AHMAD, S. 2004. Measuring the life-cycle environmental and economic performance of concrete: the BEES approach. *International workshop on sustainable development and concrete technology*. Beijing, China: Iowa State University.
LY, L., VANCE, E. R., PERERA, D. S., ALY, Z. & OLUFSON, K. 2006. Leaching of Geopolymers in Deionised Water. *Advances in Technology of Materials Processing Journal,* 8**, 2,** 236-247.http://dx.doi.org/10.2240/azojomo0238
MACKENZIE, K., RAHNER, N., SMITH, M. & WONG, A. 2010. Calcium-containing inorganic polymers as potential bioactive materials. *Journal of Materials Science,* 45**, 4,** 999-1007.http://dx.doi.org/10.1007/s10853-009-4031-5
MACKENZIE, K. J. D. & O'LEARY, B. 2009. Inorganic polymers (geopolymers) containing acid-base indicators as possible colour-change humidity indicators. *Materials Letters,* 63**, 2,** 230-232.http://dx.doi.org/10.1016/j.matlet.2008.09.053
MADSEN, I. C. & SCARLETT, N. V. Y. 2008. Quantitative Phase Analysis. *In:* DINNEBIER, R. E. & BILLINGE, S. (eds.) *Powder diffraction : theory and practice* Cambridge: Royal Society of Chemistry.
MADSEN, I. C., SCARLETT, N. V. Y. & KERN, A. 2011. Description and survey of methodologies for the determination of amorphous content via X-ray powder diffraction. *Zeitschrift für Kristallographie Crystalline Materials.*
MADSEN, I. C., SCARLETT, N. V. Y., RILEY, D. P. & RAVEN, M. D. 2012. Quantitative Phase Analysis Using the Rietveld Method. *Modern Diffraction Methods.* Wiley-VCH Verlag GmbH & Co. KGaA.
MAITLAND, C. F., BUCKLEY, C. E., O'CONNOR, B. H., BUTLER, P. D. & HART, R. D. 2011. Characterization of the pore structure of metakaolin-derived geopolymers by neutron scattering and electron microscopy. *Journal of Applied Crystallography,* 44**, 4,** 697-707.http://dx.doi.org/10.1107/s0021889811021078
MASI, G., RICKARD, W. D. A., BIGNOZZI, M. C. & VAN RIESSEN, A. 2015. The effect of organic and inorganic fibres on the mechanical and thermal properties of aluminate activated geopolymers. *Composites Part B: Engineering,* 76**, 0,** 218-228.http://dx.doi.org/10.1016/j.compositesb.2015.02.023
MCLELLAN, B. C., WILLIAMS, R. P., LAY, J., VAN RIESSEN, A. & CORDER, G. D. 2011. Costs and carbon emissions for geopolymer pastes in comparison to ordinary portland cement. *Journal of Cleaner Production,* 19**, 9–10,** 1080-1090.http://dx.doi.org/10.1016/j.jclepro.2011.02.010
MÜLLER, M., DINNEBIER, R. E., JANSEN, M., WIEDEMANN, S. & PLÜG, C. 2009. Kinetic analysis of the phase transformation from α- to β-copper phthalocyanine: A case study for sequential and parametric Rietveld refinements. *Powder Diffraction,* 24**, 03,** 191-199.http://dx.doi.org/10.1154/1.3194111
MYERS, R. J., BERNAL, S. A., GEHMAN, J. D., VAN DEVENTER, J. S. J. & PROVIS, J. L. 2015. The Role of Al in Cross-Linking of Alkali-Activated Slag Cements. *Journal of the American Ceramic Society,* 98**, 3,** 996-1004.10.1111/jace.13360
NAZARI, A., MAGHSOUDPOUR, A. & SANJAYAN, J. G. 2014. Characteristics of boroaluminosilicate geopolymers. *Construction and Building Materials,* 70**, 0,** 262-268.http://dx.doi.org/10.1016/j.conbuildmat.2014.07.087
NAZARI, A., MAGHSOUDPOUR, A. & SANJAYAN, J. G. 2015a. Boroaluminosilicate geopolymers: role of NaOH concentration and curing temperature. *RSC Advances,* 5**, 16,** 11973-11979.http://dx.doi.org/10.1039/C4RA11665H

NAZARI, A., MAGHSOUDPOUR, A. & SANJAYAN, J. G. 2015b. Flexural strength of plain and fibre-reinforced boroaluminosilicate geopolymer. *Construction and Building Materials,* 76**, 0,** 207-213.http://dx.doi.org/10.1016/j.conbuildmat.2014.12.002
NCRP 1971. NCRP Report No. 38 - Protection against Neutron Radiation. *Recommendation of the National Council on Radiation Protection and Measurernents.* WASHINGTON D.C.
NETMOTION INC. . 2003. *Properties of PEEK, polyetheretherketone* [Online]. Available: http://www.netmotion.com/htm_files/wh_properties.htm [Accessed 2010].
NICHOLSON, C. L. & FLETCHER, R. A. 2005. *Geopolymers and Methods for Their Production*. New Zealand patent application WO 2005/019130 A1. 22.08.2003.
NISBETT, M. 2002. Life Cycle Inventory of Portland Cement Manufacture. Portland Cement Association.
NORBY, P. & HANSON, J. C. 1998. Hydrothermal synthesis of the microporous aluminophosphate CoAPO-5; in situ time-resolved synchrotron X-ray powder diffraction studies. *Catalysis Today,* 39**, 4,** 301-309.http://dx.doi.org/10.1016/S0920-5861(97)00118-1
O'BRIEN, K., MÉNACHÉ, J. & O'MOORE, L. 2009. Impact of fly ash content and fly ash transportation distance on embodied greenhouse gas emissions and water consumption in concrete. *The International Journal of Life Cycle Assessment*.http://dx.doi.org/10.1007/s11367-009-0105-5
OELKERS, E. H. & GISLASON, S. R. 2001. The mechanism, rates and consequences of basaltic glass dissolution: I. An experimental study of the dissolution rates of basaltic glass as a function of aqueous Al, Si and oxalic acid concentration at 25°C and pH = 3 and 11. *Geochimica et Cosmochimica Acta,* 65**, 21,** 3671-3681.http://dx.doi.org/10.1016/s0016-7037(01)00664-0
OELKERS, E. H., SCHOTT, J. & DEVIDAL, J.-L. 1994. The effect of aluminum, pH, and chemical affinity on the rates of aluminosilicate dissolution reactions. *Geochimica et Cosmochimica Acta,* 58**, 9,** 2011-2024.http://dx.doi.org/10.1016/0016-7037(94)90281-x
OKADA, K., IMASE, A., ISOBE, T. & NAKAJIMA, A. 2011. Capillary rise properties of porous geopolymers prepared by an extrusion method using polylactic acid (PLA) fibers as the pore formers. *Journal of the European Ceramic Society,* 31**, 4,** 461-467.http://dx.doi.org/10.1016/j.jeurceramsoc.2010.10.035
OKADA, K., OOYAMA, A., ISOBE, T., KAMESHIMA, Y., NAKAJIMA, A. & MACKENZIE, K. J. D. 2009. Water retention properties of porous geopolymers for use in cooling applications. *Journal of the European Ceramic Society,* 29**, 10,** 1917-1923.http://dx.doi.org/10.1016/j.jeurceramsoc.2008.11.006
OUALIT, M., JAUBERTHIE, R., RENDELL, F., MELINGE, Y. & ABADLIA, M. T. 2012. External corrosion to concrete sewers: a case study. *Urban Water Journal,* 9**, 6,** 429-434.10.1080/1573062X.2012.668916
OUDADESSE, H., DERRIEN, A. C., LEFLOCH, M. & DAVIDOVITS, J. 2007a. MAS-NMR studies of geopolymers heat-treated for applications in biomaterials field. *Journal of Materials Science,* 42**, 9,** 3092-3098.http://dx.doi.org/10.1007/s10853-006-0524-7
OUDADESSE, H., DERRIEN, A. C., MAMI, M., MARTIN, S., CATHELINEAU, G. & YAHIA, L. 2007b. Aluminosilicates and biphasic HA-TCP composites: studies of properties for bony filling. *Biomedical Materials,* 2**, 1,** S59.http://dx.doi.org/10.1088/1748-6041/2/1/S09
PACHECO-TORGAL, F., CASTRO-GOMES, J. & JALALI, S. 2008. Alkali-activated binders: A review: Part 1. Historical background, terminology, reaction mechanisms and hydration products. *Construction and Building Materials,* 22**, 7,** 1305-1314.http://dx.doi.org/10.1016/j.conbuildmat.2007.10.015
PALOMO, A. & LOPEZ DE LA FUENTE, J. I. 2003. Alkali-activated cementitous materials: Alternative matrices for the immobilisation of hazardous wastes: Part I. Stabilisation of boron. *Cement and Concrete Research,* 33**, 2,** 281.http://dx.doi.org/10.1016/S0008-8846(02)00963-8
PANZARELLA, B., TOMPSETT, G., CONNER, W. C. & JONES, K. 2007. In Situ SAXS/WAXS of Zeolite Microwave Synthesis: NaY, NaA, and Beta Zeolites. *ChemPhysChem,* 8**, 3,** 357-369.http://dx.doi.org/10.1002/cphc.200600496
PARMENTIER, J., VILMINOT, S. & DORMANN, J. L. 1999. Fe- and Cr-substituted mullites: Mössbauer spectroscopy and rietveld structure refinement. *Solid State Sciences,* 1**, 5,** 257-265.http://dx.doi.org/10.1016/S1293-2558(00)80080-1
PERERA, D. S., CASHION, J. D., BLACKFORD, M. G., ZHANG, Z. M. & VANCE, E. R. 2007. Fe speciation in geopolymers with Si/Al molar ratio of similar to 2. *Journal of the European Ceramic Society,* 27**, 7,** 2697-2703.http://dx.doi.org/10.1016/j.jeurceramsoc.2006.10.006
PETEK GURSEL, A., MASANET, E., HORVATH, A. & STADEL, A. 2014. Life-cycle inventory analysis of concrete production: A critical review. *Cement and Concrete Composites,* 51**, 0,** 38-48.http://dx.doi.org/10.1016/j.cemconcomp.2014.03.005
PHAIR, J. W., SCHULZ, J. C., BERTRAM, W. K. & ALDRIDGE, L. P. 2003. Investigation of the microstructure of alkali-activated cements by neutron scattering. *Cement and Concrete Research,* 33**, 11,** 1811.http://dx.doi.org/10.1016/S0008-8846(03)00199-6
PIETERSEN, H. S., FRAAY, A. L. A. & BIJEN, J. M. Year. Reactivity of Fly ash at High pH, in Fly Ash and Coal Conversion By-Products: Characterization, Utilization and Disposal VI. *In:* GLASSER, F. P. & DAY, R. L., eds. Materials Research Society Symposium Proceedings, 1989. Materials Research Society, 139.
POPOVIC, J., TKALCEC, E., GRZETA, B., KURAJICA, S. & SCHMAUCH, J. 2007. Cobalt incorporation in mullite. *American Mineralogist,* 92**, 2-3,** 408-411.http://dx.doi.org/10.2138/am.2007.2114
PROVIS, J. L. 2014. Geopolymers and other alkali activated materials: why, how, and what? *Materials and Structures,* 47**, 1-2,** 11-25.http://dx.doi.org/10.1617/s11527-013-0211-5
PROVIS, J. L., DUXSON, P., HARREX, R. M., YONG, C.-Z. & VAN DEVENTER, J. S. J. 2009. Valorisation of fly ashes by geopolymerisation. *Global NEST Journal,* 11**, 2,** 147
PROVIS, J. L., DUXSON, P., VAN DEVENTER, J. S. J. & LUKEY, G. C. 2005. The role of mathematical modelling and gel chemistry in advancing geopolymer technology. *Chemical Engineering Research and Design,* 83**, A7,** 853-860.http://dx.doi.org/10.1205/cherd.04329
PROVIS, J. L. & VAN DEVENTER, J. S. J. 2007a. Geopolymerisation kinetics. 2. Reaction kinetic modelling. *Chemical Engineering Science,* 62**, 9,** 2318-2329.http://dx.doi.org/10.1016/j.ces.2007.01.028
PROVIS, J. L. & VAN DEVENTER, J. S. J. 2007b. Geopolymerization kinetics. 1. In situ energy-dispersive X-ray diffractometry. *Chemical Engineering Science,* 62**, 9,** 2309-2317.http://dx.doi.org/10.1016/j.ces.2007.01.027

PROVIS, J. L. & VAN DEVENTER, J. S. J. (eds.) 2009. *Geopolymers : structure, processing, properties and industrial applications,* Oxford: Woodhead Publishing.
PROVIS, J. L., WALLS, P. A. & VAN DEVENTER, J. S. J. 2008. Geopolymerisation kinetics. 3. Effects of Cs and Sr salts. *Chemical Engineering Science,* 63**, 18,** 4480-4489.http://dx.doi.org/10.1016/j.ces.2008.06.008
PROVIS, J. L., WHITE, C. E. & VAN DEVENTER, J. S. J. 2010. Discussion of Y. Zhang et al., "Study of ion cluster reorientation process of geopolymerisation reaction using semi-empirical AM1 calculations," Cem Concr Res 39(12): 1174-1179; 2009. *Cement and Concrete Research,* 40**, 5,** 827-828.http://dx.doi.org/10.1016/j.cemconres.2010.01.009
PRUSINSKI, J. R., MARCEAU, M. L. & VANGEEM, M. G. 2006. Life cycle inventory of slag cement concrete. *Eighth CANMET / ACI International conference on recent advances in concrete technology.* Montreal, Canada: American Concrete Institute.
PURDON, A. O. 1940. The action of alkalis on blastfurance slag. *Transactions and communications of Journal of the Society of Chemical Industry,* 59**, 53,** 191-202.http://dx.doi.org/10.1002/jctb.5000595310
RAHIER, H., DENAYER, J. F. & VAN MELE, B. 2003. Low-temperature synthesized aluminosilicate glasses Part IV Modulated DSC study on the effect of particle size of metakaolinite on the production of inorganic polymer glasses. *Journal of Materials Science,* 38**, 14,** 3131.http://dx.doi.org/10.1023/A:1024733431657
RAHIER, H., SIMONS, W., VAN MELE, B. & BIESEMANS, M. 1997. Low-temperature synthesized aluminosilicate glasses: Part III Influence of the composition of the silicate solution on production, structure and properties. *Journal of Materials Science,* 32**, 9,** 2237.http://dx.doi.org/10.1023/A:1018563914630
RANGAN, B. V. 2008. Studies on fly ash-based geopolymer concrete. *Malaysian Construction Research Journal,* 3**, 2,** 1
RAUCH, A. & WASCHKOWSKI, W. 2003. Neutron Scattering Lengths. *In:* DIANOUX, A.-J. & LANDER, G. (eds.) *Neutron Data Booklet.* 2nd ed. Grenoble, France.
REES, C. A., PROVIS, J. L., LUKEY, G. C. & VAN DEVENTER, J. S. J. 2007a. Attenuated Total Reflectance Fourier Transform Infrared Analysis of Fly Ash Geopolymer Gel Aging. *Langmuir,* 23**, 15,** 8170-8179.http://dx.doi.org/10.1021/la700713g
REES, C. A., PROVIS, J. L., LUKEY, G. C. & VAN DEVENTER, J. S. J. 2007b. In Situ ATR-FTIR Study of the Early Stages of Fly Ash Geopolymer Gel Formation. *Langmuir,* 23**, 17,** 9076-9082.http://dx.doi.org/10.1021/la701185g
REES, C. A., PROVIS, J. L., LUKEY, G. C. & VAN DEVENTER, J. S. J. 2008. The mechanism of geopolymer gel formation investigated through seeded nucleation. *Colloids and Surfaces A: Physicochemical and Engineering Aspects,* 318**, 1-3,** 97-105.http://dx.doi.org/10.1016/j.colsurfa.2007.12.019
RICKARD, W. D. A., VAN RIESSEN, A. & WALLS, P. 2010. Thermal Character of Geopolymers Synthesized from Class F Fly Ash Containing High Concentrations of Iron and a-Quartz. *International Journal of Applied Ceramic Technology,* 7**, 1,** 81-88.http://dx.doi.org/10.1111/j.1744-7402.2008.02328.x
RICKARD, W. D. A., WILLIAMS, R., TEMUUJIN, J. & VAN RIESSEN, A. 2011. Assessing the suitability of three Australian fly ashes as an aluminosilicate source for geopolymers in high temperature applications. *Materials Science and Engineering: A,* 528**, 9,** 3390-3397.http://dx.doi.org/10.1016/j.msea.2011.01.005
RONCHETTI, S., PIANA, M., DELMASTRO, A., SALIS, M. & MAZZA, D. 2001. Synthesis and characterization of Fe and P substituted 3:2 mullite. *Journal of the European Ceramic Society,* 21**, 14,** 2509-2514.http://dx.doi.org/10.1016/S0955-2219(01)00272-2
ROWLES, M. & O'CONNOR, B. 2003. Chemical optimisation of the compressive strength of aluminosilicate geopolymers synthesised by sodium silicate activation of metakaolinite. *Journal of Materials Chemistry,* 13**, 5,** 1161.http://dx.doi.org/10.1039/B212629J
ROWLES, M. R., HANNA, J. V., O'CONNOR, B. H., PIKE, K. J., SMITH, M. E. & VANCE, E. R. 2007. A ^{29}Si, ^{27}Al and ^{23}Na3 MAS NMR study of bonding character in aluminosilicate inorganic polymers. *Applied Magnetic Resonance,* 32**,** 663 - 689.http://dx.doi.org/10.1007/s00723-007-0043-y
ROWLES, M. R. & O'CONNOR, B. H. 2009. Chemical and Structural Microanalysis of Aluminosilicate Geopolymers Synthesized by Sodium Silicate Activation of Metakaolinite. *Journal of the American Ceramic Society,* 92**, 10,** 2354.http://dx.doi.org/10.1111/j.1551-2916.2009.03191.x
ROWLES, M. R. & O'CONNOR, B. H. 2009. Chemical and Structural Microanalysis of Aluminosilicate Geopolymers Synthesized by Sodium Silicate Activation of Metakaolinite. *Journal of the American Ceramic Society,* 92**, 10,** 2354.http://dx.doi.org/10.1111/j.1551-2916.2009.03191.x
ROY, R., ROY, D. M. & FRANCIS, E. E. 1955. New Data on Thermal Decomposition of Kaolinite and Halloysite. *Journal of the American Ceramic Society,* 38**, 6,** 198-205.http://dx.doi.org/10.1111/j.1151-2916.1955.tb14929.x
SAMARIN, A. 1999. Utilisation of waste from coal-fired power plants - an important factor in the abatement of greenhouse gas emissions. *ATSE Focus.* Canberra: Australian Academy of Technological Sciences and Engineering.
SCARLETT, N. V. Y. & MADSEN, I. C. 2006. Quantification of phases with partial or no known crystal structures. *Powder Diffraction,* 21**, 4,** 278-284.http://dx.doi.org/10.1154/1.2362855
SCHNEIDER, H. & KOMARNENI, S. 2005. *Mullite,* Weinheim Wiley-VCH.
SEARATES LP. 2015. *Sea Rates: Route Explorer* [Online]. Available: http://www.searates.com/services/routes-explorer/ [Accessed 5th of July 2015 2015].
SHIELDWERX 2007. Neutron Shielding - SWX-207HD & 207HD5. *In:* SHIELDWERX™ - A DIVISION OF BLADEWERX LLC (ed.) *www.shieldwerx.com.* Rio Rancho, New Mexico, USA.
SINDHUNATA, VAN DEVENTER, J. S. J., LUKEY, G. C. & XU, H. 2006. Effect of Curing Temperature and Silicate Concentration on Fly-Ash-Based Geopolymerization. *Industrial & Engineering Chemistry Research,* 45**, 10,** 3559-3568.http://dx.doi.org/10.1021/ie051251p
SKVARA, F., JILEK, T. & KOPECKY, L. 2005. Geopolymer materials based on fly ash. *Ceramics Silikaty,* 49**, 3,** 195-204
SKVÁRA, F., KOPECKÝ, L., SMILAUER, V. & BITTNAR, Z. 2009. Material and structural characterization of alkali activated low-calcium brown coal fly ash. *Journal of Hazardous Materials,* 168**, 2-3,** 711-720.http://dx.doi.org/10.1016/j.jhazmat.2009.02.089

SONGPIRIYAKIJ, S., KUBPRASIT, T., JATURAPITAKKUL, C. & CHINDAPRASIRT, P. 2010. Compressive strength and degree of reaction of biomass- and fly ash-based geopolymer. *Construction and Building Materials,* 24**, 3,** 236-240.http://dx.doi.org/10.1016/j.conbuildmat.2009.09.002
STEINS, P., POULESQUEN, A., FRIZON, F., DIAT, O., JESTIN, J., CAUSSE, J., LAMBERTIN, D. & ROSSIGNOL, S. 2014. Effect of aging and alkali activator on the porous structure of a geopolymer. *Journal of Applied Crystallography,* 47**, 1,** 316-324.http://dx.doi.org/10.1107/s160057671303197x
STEVESON, M. & SAGOE-CRENTSIL, K. 2005a. Relationships between composition, structure and strength of inorganic polymers. Part 1: Metakaolin-derived inorganic polymers. *Journal of Materials Science,* 40**, 8,** 2023.http://dx.doi.org/10.1007/s10853-005-1226-2
STEVESON, M. & SAGOE-CRENTSIL, K. 2005b. Relationships between composition, structure and strength of inorganic polymers. Part 2: Fly ash-derived inorganic polymers. *Journal of Materials Science,* 40**, 16,** 4247.http://dx.doi.org/10.1007/s10853-005-2794-x
STINTON, G. W. & EVANS, J. S. O. 2007. Parametric Rietveld refinement. *Journal of Applied Crystallography,* 40**, 1,** 87-95.http://dx.doi.org/10.1107/s0021889806043275
SUBAER & VAN RIESSEN, A. 2007. Thermo-mechanical and microstructural characterisation of sodium-poly(sialate-siloxo) (Na-PSS) geopolymers. *Journal of Materials Science,* 42**, 9,** 3117-3123.http://dx.doi.org/10.1007/s10853-006-0522-9
SUBAER, VAN RIESSEN, A., O'CONNOR, B. H. & BUCKLEY, C. E. 2002. Compressive strength and microstructural character of aluminosilicate geopolymers. *Journal of the Australasian ceramic society,* 38**, 1,** 83
SUMAJOUW, D. M. J., HARDJITO, D., WALLAH, S. E. & RANGAN, B. V. 2007. Fly ash-based geopolymer concrete: study of slender reinforced columns. *Journal of Materials Science,* 42**, 9,** 3124-3130.http://dx.doi.org/10.1007/s10853-006-0523-8
TAYLOR, H. F. W. 1997. *Cement Chemistry,* London, Thomas Telford Publishing.
TEMUUJIN, J., MINJIGMAA, A., RICKARD, W., LEE, M., WILLIAMS, I. & VAN RIESSEN, A. 2010. Fly ash based geopolymer thin coatings on metal substrates and its thermal evaluation. *Journal of Hazardous Materials,* 180**, 1-3,** 748-752.http://dx.doi.org/10.1016/j.jhazmat.2010.04.121
TEMUUJIN, J., MINJIGMAA, A., RICKARD, W. & VAN RIESSEN, A. 2012. Thermal properties of spray-coated geopolymer-type compositions. *Journal of Thermal Analysis and Calorimetry,* 107**, 1,** 287-292.http://dx.doi.org/10.1007/s10973-011-1766-4
TEMUUJIN, J., VAN RIESSEN, A. & WILLIAMS, R. 2009. Influence of calcium compounds on the mechanical properties of fly ash geopolymer pastes. *Journal of Hazardous Materials,* 167**, 1–3,** 82-88.http://dx.doi.org/10.1016/j.jhazmat.2008.12.121
TREACY, M. M. & HIGGINS, J. B. 2007. *Collection of Simulated XRD Powder Patterns for Zeolites Fifth (5th) Revised Edition*, Elsevier.
TSAI, Y.-L., HANNA, J. V., LEE, Y.-L., SMITH, M. E. & CHAN, J. C. C. 2010. Solid-state NMR study of geopolymer prepared by sol-gel chemistry. *Journal of Solid State Chemistry,* 183**, 12,** 3017-3022.http://dx.doi.org/10.1016/j.jssc.2010.10.008
UNITED NATIONS 1998. Report of the conference of the parties on its third session, held at Kyoto from 1 to 11 Decemeber 1997. *Framework convention of Climate change: Conference of the Parties.* Kyoto.
UNSTATS 2010. Greenhouse gas emissions by sector (absolute values). *United Nations Statistical Division;.*
US DEPARTMENT OF ENERGY. 2015. *Hydrogen Production* [Online]. Available: http://www.hydrogen.energy.gov/production.html [Accessed 14/06/2015 2015].
USGS 2005. Mineral commodity summaries 2005. *Mineral Commodities Summaries.* Reston, VA.
USGS 2007. Mineral commodity summaries 2007. *Mineral Commodities Summaries.* Reston, VA.
USGS 2009. Mineral commodity summaries 2009. *Mineral Commodities Summaries.* Reston, VA.
USGS 2011. Mineral commodity summaries 2011. *Mineral Commodities Summaries.* Reston, VA.
USGS 2013a. *Cement Statistics 2012,* Reston, VA.
USGS 2013b. Mineral commodity summaries 2013. *Mineral Commodities Summaries.* Reston, VA.
USGS 2015a. Mineral commodity summaries 2015. *Mineral Commodities Summaries.* Reston, VA.
USGS. 2015b. *The Water Cycle: The Oceans* [Online]. Available: http://water.usgs.gov/edu/watercycleoceans.html [Accessed 14/06/2015 2015].
VAN DEVENTER, J. S. J., PROVIS, J. L. & DUXSON, P. 2012. Technical and commercial progress in the adoption of geopolymer cement. *Minerals Engineering,* 29**,** 89-104.http://dx.doi.org/10.1016/j.mineng.2011.09.009
VAN JAARSVELD, J. G. S., VAN DEVENTER, J. S. J. & LUKEY, G. C. 2003. The characterisation of source materials in fly ash-based geopolymers. *Materials Letters,* 57**, 7,** 1272
VAN RIESSEN, A., JAMIESON, E., KEALLEY, C. S., HART, R. D. & WILLIAMS, R. P. 2013. Bayer-geopolymers: An exploration of synergy between the alumina and geopolymer industries. *Cement and Concrete Composites,* 41**, 0,** 29-33.http://dx.doi.org/10.1016/j.cemconcomp.2013.04.010
VAN RIESSEN, A., RICKARD, W. & SANJAYAN, J. 2009. Thermal properties of geopolymers. *In:* PROVIS, J. L. & DEVENTER, J. S. J. V. (eds.) *Geopolymers: Structure, processing, properties and industrial applications.* Cambridge: Woodhead Publishing Limited.
VAN SANTEN, R. 1998. Industrial Gases in Australia. Available: http://www.chemlink.com.au/caustic_asia98.pdf [Accessed 8th July, 2009].
VARAJÃO, A. F. D. C., GILKES, R. J. & HART, R. D. 2001. The relationships between kaolinite crystal properties and the origin of materials for a Brazilian kaolin deposit. *Clays and Clay Minerals,* 49**, 1,** 44-59
VASSILEV, S. V. & VASSILEVA, C. G. 1996. Occurrence, abundance and origin of minerals in coals and coal ashes. *Fuel Processing Technology,* 48**, 2,** 85-106.http://dx.doi.org/10.1016/S0378-3820(96)01021-1
VICKERS, L. 2015. *Development of Geopolymer Systems for High Temperature Applications.* PHD, Curtin University.
VICKERS, L., VAN RIESSEN, A. & RICKARD, W. D. A. 2015. *Fire-Resistant Geopolymers - Role of Fibres and Fillers to Enhance Thermal Properties*, Springer.
VIJAI, K., KUMUTHA, R. & VISHNURAM, B. G. 2012. Properties of glass fibre reinforced geopolymer concrete composites. *Asian Journal fo Civil Engineering (Building and Housing),* 13**, 4,** 511-520

VON DREELE, R. B. & RODRIGUEZ-CARVAJAL, J. 2008. Chapter 3 The Intensity of a Bragg Reflection. *Powder Diffraction: Theory and Practice.* The Royal Society of Chemistry.
WALLAH, S., HARDJITO, D., SUMAJOUW, D. & RANGAN, B. 2005. Sulfate and acid resistance of fly ash-based geopolymer concrete. *In:* STEWART, M. & DOCKRILL, B. (eds.) *Australian Structural Engineering Conference 2005* Sydney, NSW, Australia.
WALLAH, S. & RANGAN, B. V. 2006. Low-Calcium Fly Ash-Based Geopolymer Concrete: Long-term Properties. *Research Report GC 2, Faculty of Engineering.* Perth, Australia: Curtin University of Technology.
WALTON, R. I., MILLANGE, F., O'HARE, D., DAVIES, A. T., SANKAR, G. & CATLOW, C. R. A. 2000. An in Situ Energy-Dispersive X-ray Diffraction Study of the Hydrothermal Crystallization of Zeolite A. 1. Influence of Reaction Conditions and Transformation into Sodalite. *The Journal of Physical Chemistry B,* 105**, 1,** 83-90.http://dx.doi.org/10.1021/jp002711p
WANG, M. R., JIA, D. C., HE, P. G. & ZHOU, Y. 2010. Influence of calcination temperature of kaolin on the structure and properties of final geopolymer. *Materials Letters,* 64**, 22,** 2551-2554.http://dx.doi.org/10.1016/j.matlet.2010.08.007
WARD, C. R. & FRENCH, D. 2006. Determination of glass content and estimation of glass composition in fly ash using quantitative X-ray diffractometry. *Fuel,* 85**, 16,** 2268-2277.http://dx.doi.org/10.1016/j.fuel.2005.12.026
WBCSD 2012. Getting the Numbers Right Project: Reporting CO2. *Global Cement Database on CO_2 and Energy Information.* http://www.wbcsdcement.org/GNR-2012/index.html.
WEIL, M., DOMBROWSKI, K. & BUCHWALD, A. 2009. Life-cycle analysis of geopolymers. *In:* PROVIS, J. L. & VAN DEVENTER, J. S. J. (eds.) *Geopolymers: structures, processing, properties and industrial applications.* Cambridge, England: Woodhead Publishing Limited.
WELLS, O. C. 1974. *Scanning electron microscopy,* New York, New York : McGraw-Hill.
WHITE, C. E., DAEMEN, L. L., HARTL, M. & PAGE, K. 2015. Intrinsic differences in atomic ordering of calcium (alumino)silicate hydrates in conventional and alkali-activated cements. *Cement and Concrete Research,* 67**, 0,** 66-73.http://dx.doi.org/10.1016/j.cemconres.2014.08.006
WHITE, C. E., PROVIS, J. L., PROFFEN, T., RILEY, D. P. & VAN DEVENTER, J. S. J. 2010. Density Functional Modeling of the Local Structure of Kaolinite Subjected to Thermal Dehydroxylation. *Journal of Physical Chemistry A,* 114**, 14,** 4988-4996.http://dx.doi.org/10.1021/Jp911108d
WILLIAMS, R. P. & VAN RIESSEN, A. 2008. Data processing of diffraction data from the MYTHEN detector system on the Powder Diffraction beamline at the Australian Synchrotron using MyHST. *CMR Technical Note: 001.* Bentley: Curtin University of Technology.
WILLIAMS, R. P. & VAN RIESSEN, A. 2010. Determination of the reactive component of fly ashes for geopolymer production using XRF and XRD. *Fuel,* 89**, 12,** 3683-3692.http://dx.doi.org/10.1016/j.fuel.2010.07.031
WILLIAMS, R. P. & VAN RIESSEN, A. 2011. Development of alkali activated borosilicate inorganic polymers (AABSIP). *Journal of the European Ceramic Society,* 31**, 8,** 1513-1516.http://dx.doi.org/10.1016/j.jeurceramsoc.2011.02.021
WILSON, B. & JONES, B. 1994. Life cycle assessment of domestic laundry detergent builders. Landbank, UK.
WINBURN, R. S., GRIER, D. G., MCCARTHY, G. J. & PETERSON, R. B. 2000. Rietveld quantitative X-ray diffraction analysis of NIST fly ash standard reference materials. *Powder Diffraction,* 15**, 3,** 163-171.http://dx.doi.org/10.1017/S0885715600011015
WORRELL, E., PRICE, L., MARTIN, N., HENDRIKS, C. & MEIDA, L. O. 2001. Carbon dioxide emissions from the global cement industry. *Annual Review of Energy and the Environment,* 26**, 1,** 303-329.http://dx.doi.org/10.1146/annurev.energy.26.1.303
YIP, C. K., LUKEY, G. C. & VAN DEVENTER, J. S. J. 2005. The coexistence of geopolymeric gel and calcium silicate hydrate at the early stage of alkaline activation. *Cement and Concrete Research,* 35**, 9,** 1688-1697.http://dx.doi.org/10.1016/j.cemconres.2004.10.042
YUNSHENG, Z., YANTAO, J., WEI, S. & ZONGJIN, L. 2009. Study of ion cluster reorientation process of geopolymerisation reaction using semi-empirical AM1 calculations. *Cement and Concrete Research,* 39**, 12,** 1174-1179.http://dx.doi.org/10.1016/j.cemconres.2009.07.022
ZHANG, Z., PROVIS, J. L., WANG, H., BULLEN, F. & REID, A. 2013. Quantitative kinetic and structural analysis of geopolymers. Part 2. Thermodynamics of sodium silicate activation of metakaolin. *Thermochimica Acta,* 565**, 0,** 163-171.http://dx.doi.org/10.1016/j.tca.2013.01.040
ZHANG, Z., WANG, H., PROVIS, J. L., BULLEN, F., REID, A. & ZHU, Y. 2012. Quantitative kinetic and structural analysis of geopolymers. Part 1. The activation of metakaolin with sodium hydroxide. *Thermochimica Acta,* 539**, 0,** 23-33.http://dx.doi.org/10.1016/j.tca.2012.03.021

Every reasonable effort has been made to acknowledge the owners of copyright material. I would be pleased to hear from any copyright owner who has been omitted or incorrectly acknowledged.

APPENDIX 1 – MYHIST CMR TECH NOTE

CMR Technical Note: 001

Title:
Data processing of diffraction data from the MYTHEN detector system on the Powder Diffraction beamline at the Australian Synchrotron using MyHST.

Authors: Ross P Williams and Arie van Riessen
Contact Email: ross.williams@curtin.edu.au

Introduction

Currently the Powder Diffraction beamline at the Australian Synchrotron is equipped with a MYTHEN detector system (**m**icrostrip s**y**stem for **t**ime r**e**solved experime**n**ts), acquired from the SLS Detector group at the Paul Scherrer Institut (Switzerland). The MYTHEN detector system at the PD beamline consists of 16 MYTHEN detector modules (Figure 1), each covering approximately 4.8° 2θ with approximately 0.2° 2θ gap between modules. The current setup on the PD beamline results in each pixel covering approximately 0.00375° (2θ) resulting in a total collection angle ~80°. To overcome the gap between modules the diffraction pattern is collected as two or more histograms, the second histogram is collected after moving the detector an arbitrary angle x, such that 0.2°<x<4.8°. If more than 80° 2θ is required subsequent histograms are collected at higher angles. There is also a very minor artefact in the data which manifests itself with a slight increase in signal in the first and last few pixel of the each module (Figure 3).

This detector system is primarily designed, as it name suggests, for time resolved experiments. Due to its design the resolution and instrumental signal to noise ratio is rather low compared to more traditional single or double monochromator detector systems, with well defined detector slits. The benefit of this detector system is excellent counting statistics due to the parallel angular collection, which results in typical acquisition times of between 2 and 1800 seconds, depending on the application.

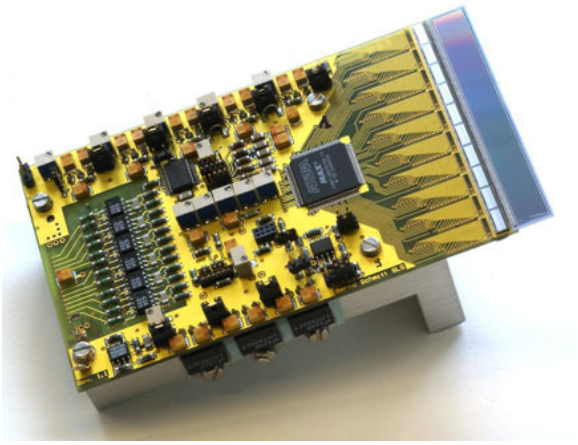

Figure 1 Photograph of a typical MYTHEN detector module, similar to that used on PD beamline at the Australian Synchrotron [1]

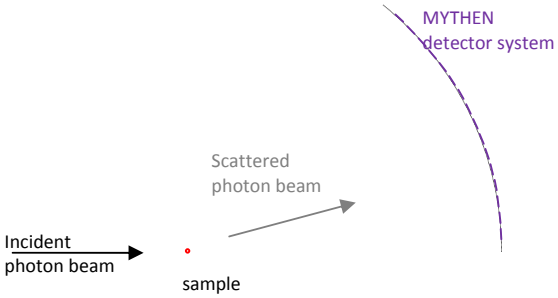

Figure 2 A schematic of the MYTHEN detector system showing the 16 MYTHEN detector modules in a linear array collecting approximately 80° 2θ with 0.2° 2θ gaps between modules

Currently the software provided at the beamline to join the histogram pairs together is under-developed. Mathew Rowles, CSRIO Minerals (Clayton Victoria, Australia), has written code in JAVA to join the histogram files but three limiting factors of his code has prompted me to provide my own solution. The limiting factors are:

- Command line driven, making it harder for users not familiar with batch file writing.
- Manual correction for the relative zero offset between histograms
- Does not account for extra signal artefacts near the edges.

Initially flood fill and angular corrections/calibrations are applied to the data at the beamline, producing data files for each of the histograms. These data files (.xy) are whitespace (one space) delimited ASCII text files, ie they can be opened directly in notepad or excel. More specifically, there is no header, with angle in the first column and counts in the second, with the angle being recorded as a floating point number (with 6 decimal point precision, unknown accuracy) and counts as an integer. It is not known if the data type of each column is signed or unsigned nor if the counts are exported as a long integer – both of which determine the maximum allowable count. Due to the nature of the angular calibration the step size is irregular (~0.00375°).

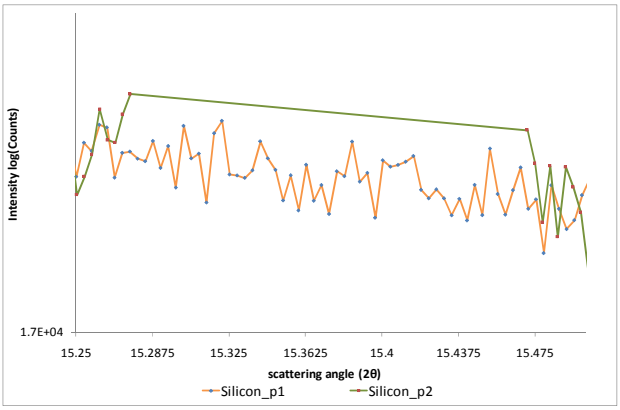

Figure 3 Powder diffraction data of a small region showing the gap in the second histogram (silicon_p2-green line). The sample is NIST SRM 640, there is no Bragg peak near this angle. Note the increase in the signal close to the edges of gap in the data.

A Solution - MyHST

A small application has been written using IDL Workbench (ITT Visual Information Solutions) to align the histograms and join the data. It is has been named the **MY**THEN detector system **h**istogram **s**plice **t**ool (MyHST). The data can be joined by filling the gaps (plus a little overlap) in the first histogram from the second histogram, cut and paste style.

More specifically, initially the data is interpolated (by default linearly) onto a common grid with constant step size of 0.00375° step size. The cross-correlation product is then calculated for a 'lag' of -50 to 50 pixels, the position of the maximum value for this function represent the relative zero-offset between histograms for which there is maximum cross correlation. The maximum value is determined by fitting a Gaussian to the cross correlation product as a function of pixel 'lag', this allows a relative zero error to be determined with better than a pixel precision. This zero offset correction can be manually forced to zero in the case that either the correction does not work, that is the zero does not converge < 0.0001 or the user

does not want this type of correction.. This calculated relative zero offset is applied to the raw data of the second histogram, then interpolated again on the same constant step size grid as histogram 1. The gaps (plus overlap of 0.05°) are filled with data from the histogram 2.

Instructions

1. Either download the .zip file or access the supplied cd.
2. Open if it doesn't automatically open, run "myhst_ver1_7.exe".
3. Click "Run MyHST version 1.7"

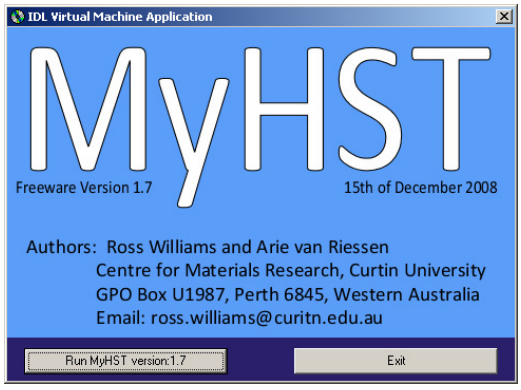

4. Click "Click to continue" then, "ok" to the welcome screen.

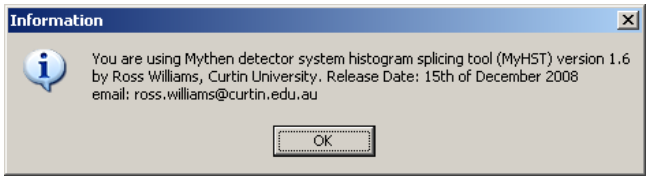

5. Choose "Yes" to apply the relative zero offset error correction to align the two data sets, or "No" to just merge the raw data sets

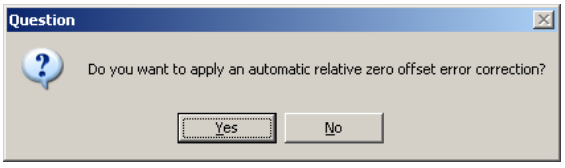

6. Select the files you want to join together; you only need to select the "_p1" file of each data group. It will automatically open the second histogram by changing the "_p1" in the filename to "_p2" in the filename.

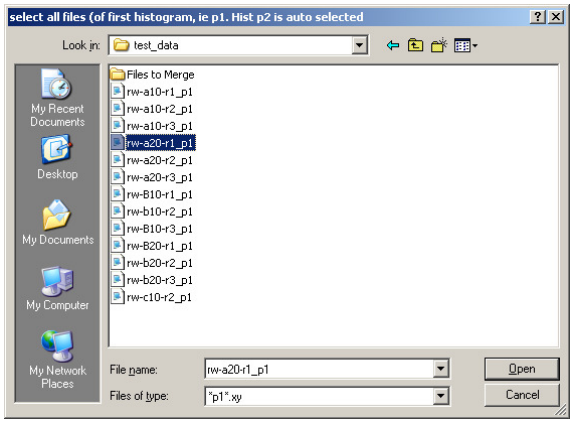

7. When using the cross correlation method to align the two data sets inspect the output. If the two diffraction patterns look ok and the "Cross Correlation" graph has a definite peak then the data should be ok. If the zero did not converge to less than 0.0001° then the script will popup an error. It is recommended you click "No" to this error and do not continue to try to align the datasets.

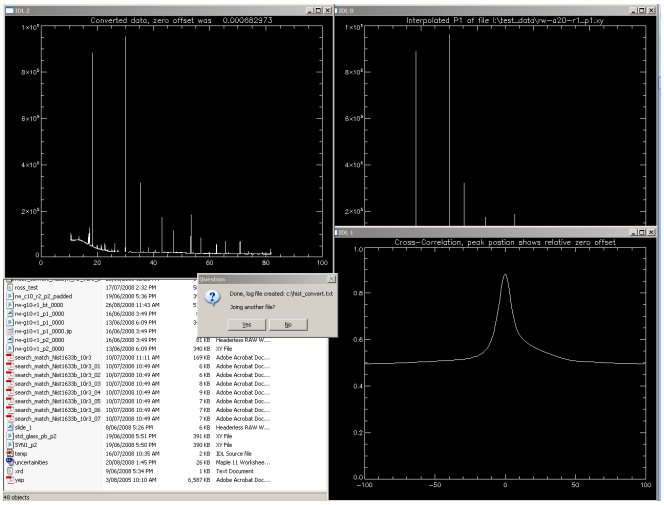

8. If the displayed pattern is unacceptable, or you are not happy with the joining, start again and choose "No" to the "…Apply relative zero offset correction..." question (ie go back to step 4).

9. The joined file is saved in the same directory as the original files, with the "p1" changed to "bt".

   Filename example:

   You selected "i:\powder_data_01_p1_00001.xy"

   Program automatically joins it with "i:\powder_data_01_p2_00001.xy"

   Generating the join file "i:\powder_data_01_bt_00001.xy"

   A log file is also created, "c:\hist_convert.txt", the file is a table, showing the filename, alignment method, initial relative zero offset and the final zero offset.

```
i:\powder_data_01_bt_00001.xy cross_correlation   0.000682973 -2.33600e-005
```

Current known limitations of this code:

- If "_p1" is in the base filename the program will fail, as it will look for the "_p2" file. ie if the filenames are 'sam_p13432_p1_00000.xy' and 'sam_p13432_p2_00000.xy' the program will fail as the first "_p1" is replaced with "_p2". The work around is to rename the files so that this does not happen.
- Dead pixels are not detected; it uses an interpolated value in its place, with no accounting for uncertainties.
- Fitting a Gaussian peak to the centre of the cross-correlation distribution is not very robust and can fail, in particular it fails if the diffraction pattern is FCC and one of the dominate peaks is in a gap, this makes the cross-correlation distribution skewed and the central peak (and maximum value) is not equivalent to the actual relative zero offset. Also if there is a single high symmetry phase, and the gaps fall on the major peaks the process will fail.

References:

1. Bernd.Schmitt. *SLS Detector Group - MYTHEN*. [cited; Available from: http://pilatus.web.psi.ch/mythen.htm.

APPENDIX 2 – COPYRIGHT CLEARANCES

ELSEVIER LICENSE
TERMS AND CONDITIONS

Mar 21, 2011

This is a License Agreement between Ross P Williams ("You") and Elsevier ("Elsevier") provided by Copyright Clearance Center ("CCC"). The license consists of your order details, the terms and conditions provided by Elsevier, and the payment terms and conditions.

All payments must be made in full to CCC. For payment instructions, please see information listed at the bottom of this form.

Supplier	Elsevier Limited The Boulevard,Langford Lane Kidlington,Oxford,OX5 1GB,UK
Registered Company Number	1982084
Customer name	Ross P Williams
Customer address	Bld 301, Curtin University
	Perth, WA, other 6845
License number	2633910580510
License date	Mar 21, 2011
Licensed content publisher	Elsevier
Licensed content publication	Fuel
Licensed content title	Determination of the reactive component of fly ashes for geopolymer production using XRF and XRD
Licensed content author	Ross P. Williams, Arie van Riessen
Licensed content date	December 2010
Licensed content volume number	89
Licensed content issue number	12
Number of pages	10
Start Page	3683
End Page	3692
Type of Use	reuse in a thesis/dissertation
Portion	full article
Format	both print and electronic
Are you the author of this Elsevier article?	Yes
Will you be translating?	No
Order reference number	
Title of your thesis/dissertation	Optimising Geopolymer Formation
Expected completion date	May 2011
Estimated size (number of pages)	200
Elsevier VAT number	GB 494 6272 12
Permissions price	0.00 USD
VAT/Local Sales Tax	0.0 USD / 0.0 GBP
Total	0.00 USD
Terms and Conditions	

INTRODUCTION

1. The publisher for this copyrighted material is Elsevier. By clicking "accept" in connection with completing this licensing transaction, you agree that the following terms and conditions apply to this transaction (along with the Billing and Payment terms and conditions established by Copyright Clearance Center, Inc. ("CCC"), at the time that you opened your Rightslink account and that are available at any time at http://myaccount.copyright.com).

GENERAL TERMS

2. Elsevier hereby grants you permission to reproduce the aforementioned material subject to the terms and conditions indicated.

3. Acknowledgement: If any part of the material to be used (for example, figures) has appeared in our publication with credit or acknowledgement to another source, permission must also be sought from that source. If such permission is not obtained then that material may not be included in your publication/copies. Suitable acknowledgement to the source must be made, either as a footnote or in a reference list at the end of your publication, as follows:

"Reprinted from Publication title, Vol /edition number, Author(s), Title of article / title of chapter, Pages No., Copyright (Year), with permission from Elsevier [OR APPLICABLE SOCIETY COPYRIGHT OWNER]." Also Lancet special credit - "Reprinted from The Lancet, Vol. number, Author(s), Title of article, Pages No., Copyright (Year), with permission from Elsevier."

4. Reproduction of this material is confined to the purpose and/or media for which permission is hereby given.

5. Altering/Modifying Material: Not Permitted. However figures and illustrations may be altered/adapted minimally to serve your work. Any other abbreviations, additions, deletions and/or any other alterations shall be made only with prior written authorization of Elsevier Ltd. (Please contact Elsevier at permissions@elsevier.com)

6. If the permission fee for the requested use of our material is waived in this instance, please be advised that your future requests for Elsevier materials may attract a fee.

7. Reservation of Rights: Publisher reserves all rights not specifically granted in the combination of (i) the license details provided by you and accepted in the course of this licensing transaction, (ii) these terms and conditions and (iii) CCC's Billing and Payment terms and conditions.

8. License Contingent Upon Payment: While you may exercise the rights licensed immediately upon issuance of the license at the end of the licensing process for the transaction, provided that you have disclosed complete and accurate details of your proposed use, no license is finally effective unless and until full payment is received from you (either by publisher or by CCC) as provided in CCC's Billing and Payment terms and conditions. If full payment is not received on a timely basis, then any license preliminarily granted shall be deemed automatically revoked and shall be void as if never

granted. Further, in the event that you breach any of these terms and conditions or any of CCC's Billing and Payment terms and conditions, the license is automatically revoked and shall be void as if never granted. Use of materials as described in a revoked license, as well as any use of the materials beyond the scope of an unrevoked license, may constitute copyright infringement and publisher reserves the right to take any and all action to protect its copyright in the materials.

9. Warranties: Publisher makes no representations or warranties with respect to the licensed material.

10. Indemnity: You hereby indemnify and agree to hold harmless publisher and CCC, and their respective officers, directors, employees and agents, from and against any and all claims arising out of your use of the licensed material other than as specifically authorized pursuant to this license.

11. No Transfer of License: This license is personal to you and may not be sublicensed, assigned, or transferred by you to any other person without publisher's written permission.

12. No Amendment Except in Writing: This license may not be amended except in a writing signed by both parties (or, in the case of publisher, by CCC on publisher's behalf).

13. Objection to Contrary Terms: Publisher hereby objects to any terms contained in any purchase order, acknowledgment, check endorsement or other writing prepared by you, which terms are inconsistent with these terms and conditions or CCC's Billing and Payment terms and conditions. These terms and conditions, together with CCC's Billing and Payment terms and conditions (which are incorporated herein), comprise the entire agreement between you and publisher (and CCC) concerning this licensing transaction. In the event of any conflict between your obligations established by these terms and conditions and those established by CCC's Billing and Payment terms and conditions, these terms and conditions shall control.

14. Revocation: Elsevier or Copyright Clearance Center may deny the permissions described in this License at their sole discretion, for any reason or no reason, with a full refund payable to you. Notice of such denial will be made using the contact information provided by you. Failure to receive such notice will not alter or invalidate the denial. In no event will Elsevier or Copyright Clearance Center be responsible or liable for any costs, expenses or damage incurred by you as a result of a denial of your permission request, other than a refund of the amount(s) paid by you to Elsevier and/or Copyright Clearance Center for denied permissions.

LIMITED LICENSE

The following terms and conditions apply only to specific license types:

15. **Translation**: This permission is granted for non-exclusive world **English** rights only unless your license was granted for translation rights. If you licensed translation rights you may only translate this content into the languages you requested. A professional translator must perform all translations and reproduce the content word for word preserving the integrity of the article. If this license is to re-use 1 or 2 figures then

permission is granted for non-exclusive world rights in all languages.

16. **Website**: The following terms and conditions apply to electronic reserve and author websites:
Electronic reserve: If licensed material is to be posted to website, the web site is to be password-protected and made available only to bona fide students registered on a relevant course if:
This license was made in connection with a course,
This permission is granted for 1 year only. You may obtain a license for future website posting,
All content posted to the web site must maintain the copyright information line on the bottom of each image,
A hyper-text must be included to the Homepage of the journal from which you are licensing athttp://www.sciencedirect.com/science/journal/xxxxx or the Elsevier homepage for books athttp://www.elsevier.com , and
Central Storage: This license does not include permission for a scanned version of the material to be stored in a central repository such as that provided by Heron/XanEdu.

17. **Author website** for journals with the following additional clauses:

All content posted to the web site must maintain the copyright information line on the bottom of each image, and
he permission granted is limited to the personal version of your paper. You are not allowed to download and post the published electronic version of your article (whether PDF or HTML, proof or final version), nor may you scan the printed edition to create an electronic version,
A hyper-text must be included to the Homepage of the journal from which you are licensing athttp://www.sciencedirect.com/science/journal/xxxxx , As part of our normal production process, you will receive an e-mail notice when your article appears on Elsevier's online service ScienceDirect (www.sciencedirect.com). That e-mail will include the article's Digital Object Identifier (DOI). This number provides the electronic link to the published article and should be included in the posting of your personal version. We ask that you wait until you receive this e-mail and have the DOI to do any posting.
Central Storage: This license does not include permission for a scanned version of the material to be stored in a central repository such as that provided by Heron/XanEdu.

18. **Author website** for books with the following additional clauses:
Authors are permitted to place a brief summary of their work online only.
A hyper-text must be included to the Elsevier homepage at http://www.elsevier.com

All content posted to the web site must maintain the copyright information line on the bottom of each image
You are not allowed to download and post the published electronic version of your chapter, nor may you scan the printed edition to create an electronic version.
Central Storage: This license does not include permission for a scanned version of the material to be stored in a central repository such as that provided by Heron/XanEdu.

19. **Website** (regular and for author): A hyper-text must be included to the Homepage of the journal from which you are licensing at http://www.sciencedirect.com/science/journal/xxxxx. or for books to the Elsevier homepage at http://www.elsevier.com

20. **Thesis/Dissertation**: If your license is for use in a thesis/dissertation your thesis may be submitted to your institution in either print or electronic form. Should your thesis be published commercially, please reapply for permission. These requirements include permission for the Library and Archives of Canada to supply single copies, on demand, of the complete thesis and include permission for UMI to supply single copies, on demand, of the complete thesis. Should your thesis be published commercially, please reapply for permission.

21. **Other Conditions**:

JOHN WILEY AND SONS LICENSE
TERMS AND CONDITIONS

Mar 21, 2011

This is a License Agreement between Ross P Williams ("You") and John Wiley and Sons ("John Wiley and Sons") provided by Copyright Clearance Center ("CCC"). The license consists of your order details, the terms and conditions provided by John Wiley and Sons, and the payment terms and conditions.

All payments must be made in full to CCC. For payment instructions, please see information listed at the bottom of this form.

License Number	2633911129172
License date	Mar 21, 2011
Licensed content publisher	John Wiley and Sons
Licensed content publication	Journal of the American Ceramic Society
Licensed content title	Quantification of the Extent of Reaction of Metakaolin-Based Geopolymers using X-Ray Diffraction, Scanning Electron Microscopy, and Energy-Dispersive Spectroscopy
Licensed content author	Ross P. Williams,Robert D. Hart,Arie van Riessen
Licensed content date	Mar 1, 2011
Start page	no
End page	no
Type of use	Dissertation/Thesis
Requestor type	Author of this Wiley article
Format	Print and electronic
Portion	Full article
Will you be translating?	No
Order reference number	
Total	0.00 USD
Terms and Conditions	

TERMS AND CONDITIONS

This copyrighted material is owned by or exclusively licensed to John Wiley & Sons, Inc. or one of its group companies (each a "Wiley Company") or a society for whom a Wiley Company has exclusive publishing rights in relation to a particular journal (collectively "WILEY"). By clicking "accept" in connection with completing this licensing transaction, you agree that the following terms and conditions apply to this transaction (along with the billing and payment terms and conditions established by the Copyright Clearance Center Inc., ("CCC's Billing and Payment terms and conditions"), at the time that you opened your Rightslink account (these are available at any time at http://myaccount.copyright.com)

Terms and Conditions

1. The materials you have requested permission to reproduce (the "Materials") are protected by copyright.

2. You are hereby granted a personal, non-exclusive, non-sublicensable, non-transferable, worldwide, limited license to reproduce the Materials for the purpose specified in the licensing process. This license is for a one-time use only with a maximum distribution equal to the number that you identified in the licensing process. Any form of republication granted by this licence must be completed within two years of the date of the grant of this licence (although copies prepared before may be distributed thereafter). The Materials shall not be used in any other manner or for any other purpose. Permission is granted subject to an appropriate acknowledgement given to the author, title of the material/book/journal and the publisher and on the understanding that nowhere in the text is a previously published source acknowledged for all or part of this Material. Any third party material is expressly excluded from this permission.

3. With respect to the Materials, all rights are reserved. Except as expressly granted by the terms of the license, no part of the Materials may be copied, modified, adapted (except for minor reformatting required by the new Publication), translated, reproduced, transferred or distributed, in any form or by any means, and no derivative

works may be made based on the Materials without the prior permission of the respective copyright owner. You may not alter, remove or suppress in any manner any copyright, trademark or other notices displayed by the Materials. You may not license, rent, sell, loan, lease, pledge, offer as security, transfer or assign the Materials, or any of the rights granted to you hereunder to any other person.

4. The Materials and all of the intellectual property rights therein shall at all times remain the exclusive property of John Wiley & Sons Inc or one of its related companies (WILEY) or their respective licensors, and your interest therein is only that of having possession of and the right to reproduce the Materials pursuant to Section 2 herein during the continuance of this Agreement. You agree that you own no right, title or interest in or to the Materials or any of the intellectual property rights therein. You shall have no rights hereunder other than the license as provided for above in Section 2. No right, license or interest to any trademark, trade name, service mark or other branding ("Marks") of WILEY or its licensors is granted hereunder, and you agree that you shall not assert any such right, license or interest with respect thereto.

5. NEITHER WILEY NOR ITS LICENSORS MAKES ANY WARRANTY OR REPRESENTATION OF ANY KIND TO YOU OR ANY THIRD PARTY, EXPRESS, IMPLIED OR STATUTORY, WITH RESPECT TO THE MATERIALS OR THE ACCURACY OF ANY INFORMATION CONTAINED IN THE MATERIALS, INCLUDING, WITHOUT LIMITATION, ANY IMPLIED WARRANTY OF MERCHANTABILITY, ACCURACY, SATISFACTORY QUALITY, FITNESS FOR A PARTICULAR PURPOSE, USABILITY, INTEGRATION OR NON-INFRINGEMENT AND ALL SUCH WARRANTIES ARE HEREBY EXCLUDED BY WILEY AND ITS LICENSORS AND WAIVED BY YOU.

6. WILEY shall have the right to terminate this Agreement immediately upon breach of this Agreement by you.

7. You shall indemnify, defend and hold harmless WILEY, its Licensors and their respective directors, officers, agents and employees, from and against any actual or threatened claims, demands, causes of action or proceedings arising from any breach of this Agreement by you.

8. IN NO EVENT SHALL WILEY OR ITS LICENSORS BE LIABLE TO YOU OR ANY OTHER PARTY OR ANY OTHER PERSON OR ENTITY FOR ANY SPECIAL, CONSEQUENTIAL, INCIDENTAL, INDIRECT, EXEMPLARY OR PUNITIVE DAMAGES, HOWEVER CAUSED, ARISING OUT OF OR IN CONNECTION WITH THE DOWNLOADING, PROVISIONING, VIEWING OR USE OF THE MATERIALS REGARDLESS OF THE FORM OF ACTION, WHETHER FOR BREACH OF CONTRACT, BREACH OF WARRANTY, TORT, NEGLIGENCE, INFRINGEMENT OR OTHERWISE (INCLUDING, WITHOUT LIMITATION, DAMAGES BASED ON LOSS OF PROFITS, DATA, FILES, USE, BUSINESS OPPORTUNITY OR CLAIMS OF THIRD PARTIES), AND WHETHER OR NOT THE PARTY HAS BEEN ADVISED OF THE POSSIBILITY OF SUCH DAMAGES. THIS LIMITATION SHALL APPLY NOTWITHSTANDING ANY FAILURE OF ESSENTIAL PURPOSE OF ANY LIMITED REMEDY PROVIDED HEREIN.

9. Should any provision of this Agreement be held by a court of competent jurisdiction to be illegal, invalid, or unenforceable, that provision shall be deemed amended to achieve as nearly as possible the same economic effect as the original provision, and the legality, validity and enforceability of the remaining provisions of this Agreement shall not be affected or impaired thereby.

10. The failure of either party to enforce any term or condition of this Agreement shall not constitute a waiver of either party's right to enforce each and every term and condition of this Agreement. No breach under this agreement shall be deemed waived or excused by either party unless such waiver or consent is in writing signed by the party granting such waiver or consent. The waiver by or consent of a party to a breach of any provision of this Agreement shall not operate or be construed as a waiver of or consent to any other or subsequent breach by such other party.

11. This Agreement may not be assigned (including by operation of law or otherwise) by you without WILEY's prior written consent.

12. Any fee required for this permission shall be non-refundable after thirty (30) days from receipt.

13. These terms and conditions together with CCC's Billing and Payment terms and conditions (which are incorporated herein) form the entire agreement between you and WILEY concerning this licensing transaction and (in the absence of fraud) supersedes all prior agreements and representations of the parties, oral or written. This Agreement may not be amended except in writing signed by both parties. This Agreement shall be binding upon and inure to the benefit of the parties' successors, legal representatives, and authorized assigns.

14. In the event of any conflict between your obligations established by these terms and conditions and those established by CCC's Billing and Payment terms and conditions, these terms and conditions shall prevail.

15. WILEY expressly reserves all rights not specifically granted in the combination of (i) the license details provided by you and accepted in the course of this licensing transaction, (ii) these terms and conditions and (iii) CCC's Billing and Payment terms and conditions.

16. This Agreement will be void if the Type of Use, Format, Circulation, or Requestor Type was misrepresented during the licensing process.

17. This Agreement shall be governed by and construed in accordance with the laws of the State of New York, USA, without regards to such state's conflict of law rules. Any legal action, suit or proceeding arising out of or relating to these Terms and Conditions or the breach thereof shall be instituted in a court of competent jurisdiction in New York County in the State of New York in the United States of America and each party hereby consents and submits to the personal jurisdiction of such court, waives any objection to venue in such court and consents to service of

process by registred or certified mail, return receipt requested, at the last known address of such party. . BY CLICKING ON THE "I ACCEPT" BUTTON, YOU ACKNOWLEDGE THAT YOU HAVE READ AND FULLY UNDERSTAND EACH OF THE SECTIONS OF AND PROVISIONS SET FORTH IN THIS AGREEMENT AND THAT YOU ARE IN AGREEMENT WITH AND ARE WILLING TO ACCEPT ALL OF YOUR OBLIGATIONS AS SET FORTH IN THIS AGREEMENT.

v1.4

Gratis licenses (referencing $0 in the Total field) are free. Please retain this printable license for your reference. No payment is required.

If you would like to pay for this license now, please remit this license along with your payment made payable to "COPYRIGHT CLEARANCE CENTER" otherwise you will be invoiced within 48 hours of the license date. Payment should be in the form of a check or money order referencing your account number and this invoice number RLNK10954180.
Once you receive your invoice for this order, you may pay your invoice by credit card. Please follow instructions provided at that time.

Make Payment To:
Copyright Clearance Center
Dept 001
P.O. Box 843006
Boston, MA 02284-3006

For suggestions or comments regarding this order, contact Rightslink Customer Support:customercare@copyright.com or +1-877-622-5543 (toll free in the US) or +1-978-646-2777.

ELSEVIER LICENSE
TERMS AND CONDITIONS

Mar 22, 2011

This is a License Agreement between Ross P Williams ("You") and Elsevier ("Elsevier") provided by Copyright Clearance Center ("CCC"). The license consists of your order details, the terms and conditions provided by Elsevier, and the payment terms and conditions.

All payments must be made in full to CCC. For payment instructions, please see information listed at the bottom of this form.

Supplier	Elsevier Limited The Boulevard,Langford Lane Kidlington,Oxford,OX5 1GB,UK
Registered Company Number	1982084
Customer name	Ross P Williams
Customer address	Bld 301, Curtin University Perth, WA, other 6845
License number	2634391408513
License date	Mar 22, 2011
Licensed content publisher	Elsevier
Licensed content publication	Journal of the European Ceramic Society
Licensed content title	Development of alkali activated borosilicate inorganic polymers (AABSIP)
Licensed content author	Ross P. Williams, Arie van Riessen
Licensed content date	8 March 2011
Licensed content volume number	n/a
Licensed content issue number	n/a
Number of pages	1
Start Page	
End Page	
Type of Use	reuse in a thesis/dissertation
Intended publisher of new work	other
Format	both print and electronic
Are you the author of this Elsevier article?	Yes
Will you be translating?	No
Order reference number	
Title of your	Optimising Geopolymer Formation

thesis/dissertation	
Expected completion date	May 2011
Estimated size (number of pages)	200
Elsevier VAT number	GB 494 6272 12
Permissions price	0.00 USD
VAT/Local Sales Tax	0.00 USD / GBP
Total	0.00 USD
Terms and Conditions	

any conflict between your obligations established by these terms and conditions and those established by CCC's Billing and Payment terms and conditions, these terms and conditions shall control.
14. Revocation: Elsevier or Copyright Clearance Center may deny the permissions described in this License at their sole discretion, for any reason or no reason, with a full refund payable to you. Notice of such denial will be made using the contact information provided by you. Failure to receive such notice will not alter or invalidate the denial. In no event will Elsevier or Copyright Clearance Center be responsible or liable for any costs, expenses or damage incurred by you as a result of a denial of your permission request, other than a refund of the amount(s) paid by you to Elsevier and/or Copyright Clearance Center for denied permissions.

LIMITED LICENSE

The following terms and conditions apply only to specific license types:
15. **Translation**: This permission is granted for non-exclusive world **English** rights only unless your license was granted for translation rights. If you licensed translation rights you may only translate this content into the languages you requested. A professional translator must perform all translations and reproduce the content word for word preserving the integrity of the article. If this license is to re-use 1 or 2 figures then permission is granted for non-exclusive world rights in all languages.
16. **Website**: The following terms and conditions apply to electronic reserve and author websites:
Electronic reserve: If licensed material is to be posted to website, the web site is to be password-protected and made available only to bona fide students registered on a relevant course if:
This license was made in connection with a course,
This permission is granted for 1 year only. You may obtain a license for future website posting,
All content posted to the web site must maintain the copyright information line on the bottom of each image,
A hyper-text must be included to the Homepage of the journal from which you are licensing at http://www.sciencedirect.com/science/journal/xxxxx or the Elsevier homepage for books at http://www.elsevier.com , and
Central Storage: This license does not include permission for a scanned version of the material to be stored in a central repository such as that provided by Heron/XanEdu.
17. **Author website** for journals with the following additional clauses:
All content posted to the web site must maintain the copyright information line on the bottom of each image, and
he permission granted is limited to the personal version of your paper. You are not allowed to download and post the published electronic version of your article (whether PDF or HTML, proof or final version), nor may you scan the printed edition to create an electronic version,
A hyper-text must be included to the Homepage of the journal from which you are licensing at http://www.sciencedirect.com/science/journal/xxxxx , As part of our normal production process, you will receive an e-mail notice when your article appears on Elsevier's online service ScienceDirect (www.sciencedirect.com). That e-mail will include the article's Digital Object Identifier (DOI). This number provides the electronic link to the published article and should be included in the posting of your personal version. We ask that you wait until you receive this e-mail and have the DOI to do any posting.
Central Storage: This license does not include permission for a scanned version of the material to be stored in a central repository such as that provided by Heron/XanEdu.
18. **Author website** for books with the following additional clauses:
Authors are permitted to place a brief summary of their work online only.
A hyper-text must be included to the Elsevier homepage at http://www.elsevier.com
All content posted to the web site must maintain the copyright information line on the bottom of each image
You are not allowed to download and post the published electronic version of your chapter, nor may you scan the printed edition to create an electronic version.
Central Storage: This license does not include permission for a scanned version of the material to be stored in a central repository such as that provided by Heron/XanEdu.

19. **Website** (regular and for author): A hyper-text must be included to the Homepage of the journal from which you are licensing at http://www.sciencedirect.com/science/journal/xxxxx. or for books to the Elsevier homepage at http://www.elsevier.com
20. **Thesis/Dissertation**: If your license is for use in a thesis/dissertation your thesis may be submitted to your institution in either print or electronic form. Should your thesis be published commercially, please reapply for permission. These requirements include permission for the Library and Archives of Canada to supply single copies, on demand, of the complete thesis and include permission for UMI to supply single copies, on demand, of the complete thesis. Should your thesis be published commercially, please reapply for permission.
21. **Other Conditions**:

v1.6

Gratis licenses (referencing $0 in the Total field) are free. Please retain this printable license for your reference. No payment is required.

If you would like to pay for this license now, please remit this license along with your payment made

payable to "COPYRIGHT CLEARANCE CENTER" otherwise you will be invoiced within 48 hours of the license date. Payment should be in the form of a check or money order referencing your account number and this invoice number RLNK0.
Once you receive your invoice for this order, you may pay your invoice by credit card. Please follow instructions provided at that time.

Make Payment To:
Copyright Clearance Center
Dept 001
P.O. Box 843006
Boston, MA 02284-3006

For suggestions or comments regarding this order, contact Rightslink Customer Support: customercare@copyright.com or +1-877-622-5543 (toll free in the US) or +1-978-646-2777.

ELSEVIER LICENSE
TERMS AND CONDITIONS

Aug 31, 2015

This is a License Agreement between Ross P Williams ("You") and Elsevier ("Elsevier") provided by Copyright Clearance Center ("CCC"). The license consists of your order details, the terms and conditions provided by Elsevier, and the payment terms and conditions.

All payments must be made in full to CCC. For payment instructions, please see information listed at the bottom of this form.

Supplier	Elsevier Limited The Boulevard,Langford Lane Kidlington,Oxford,OX5 1GB,UK
Registered Company Number	1982084
Customer name	Ross P Williams
Customer address	Curtin University Perth, WA 6845
License number	3699180282445
License date	Aug 31, 2015
Licensed content publisher	Elsevier
Licensed content publication	Journal of Hazardous Materials
Licensed content title	Material and structural characterization of alkali activated low-calcium brown coal fly ash
Licensed content author	František Škvára,Lubomír Kopecký,Vít Šmilauer,Zdeněk Bittnar
Licensed content date	15 September 2009
Licensed content volume number	168
Licensed content issue number	2-3
Number of pages	10
Start Page	711
End Page	720
Type of Use	reuse in a thesis/dissertation
Intended publisher of new work	other
Portion	figures/tables/illustrations
Number of figures/tables/illustrations	1
Format	both print and electronic
Are you the author of this Elsevier article?	No
Will you be translating?	No
Original figure numbers	Figure 7
	Optimising Geopolymer Formation

Title of your thesis/dissertation	
Expected completion date	Nov 2015
Estimated size (number of pages)	220
Elsevier VAT number	GB 494 6272 12
Permissions price	0.00 USD
VAT/Local Sales Tax	0.00 USD / 0.00 GBP
Total	0.00 USD
Terms and Conditions	

INTRODUCTION

1. The publisher for this copyrighted material is Elsevier. By clicking "accept" in connection with completing this licensing transaction, you agree that the following terms and conditions apply to this transaction (along with the Billing and Payment terms and conditions established by Copyright Clearance Center, Inc. ("CCC"), at the time that you opened your Rightslink account and that are available at any time at http://myaccount.copyright.com).

GENERAL TERMS

2. Elsevier hereby grants you permission to reproduce the aforementioned material subject to the terms and conditions indicated.

3. Acknowledgement: If any part of the material to be used (for example, figures) has appeared in our publication with credit or acknowledgement to another source, permission must also be sought from that source. If such permission is not obtained then that material may not be included in your publication/copies. Suitable acknowledgement to the source must be made, either as a footnote or in a reference list at the end of your publication, as follows:

"Reprinted from Publication title, Vol /edition number, Author(s), Title of article / title of chapter, Pages No., Copyright (Year), with permission from Elsevier [OR APPLICABLE SOCIETY COPYRIGHT OWNER]." Also Lancet special credit - "Reprinted from The Lancet, Vol. number, Author(s), Title of article, Pages No., Copyright (Year), with permission from Elsevier."

4. Reproduction of this material is confined to the purpose and/or media for which permission is hereby given.

5. Altering/Modifying Material: Not Permitted. However figures and illustrations may be altered/adapted minimally to serve your work. Any other abbreviations, additions, deletions and/or any other alterations shall be made only with prior written authorization of Elsevier Ltd. (Please contact Elsevier at permissions@elsevier.com)

6. If the permission fee for the requested use of our material is waived in this instance, please be advised that your future requests for Elsevier materials may attract a fee.

7. Reservation of Rights: Publisher reserves all rights not specifically granted in the combination of (i) the license details provided by you and accepted in the course of this licensing transaction, (ii) these terms and conditions and (iii) CCC's Billing and Payment terms and conditions.

8. License Contingent Upon Payment: While you may exercise the rights licensed immediately upon issuance of the license at the end of the licensing process for the transaction, provided that you have disclosed complete and accurate details of your proposed use, no license is finally effective unless and until full payment is received from you (either by publisher or by CCC) as provided in CCC's Billing and Payment terms and conditions. If full payment is not received on a timely basis, then any license preliminarily granted shall be deemed automatically revoked and shall be void as if never granted. Further, in the event that you breach any of these terms and conditions or any of CCC's Billing and Payment terms and conditions, the license is automatically revoked and shall be void as if never granted. Use of materials as described in a revoked license, as well as any use of the materials beyond the scope of an unrevoked license, may constitute copyright infringement and publisher reserves the right to take any and all action to protect its copyright in the materials.

9. Warranties: Publisher makes no representations or warranties with respect to the licensed material.

10. Indemnity: You hereby indemnify and agree to hold harmless publisher and CCC, and their respective officers, directors, employees and agents, from and against any and all claims arising out of your use of the licensed material other than as specifically authorized pursuant to this license.

11. No Transfer of License: This license is personal to you and may not be sublicensed, assigned, or transferred by you to any other person without publisher's written permission.

12. No Amendment Except in Writing: This license may not be amended except in a writing signed by both parties (or, in the case of publisher, by CCC on publisher's behalf).

13. Objection to Contrary Terms: Publisher hereby objects to any terms contained in any purchase order, acknowledgment, check endorsement or other writing prepared by you, which terms are inconsistent with these terms and conditions or CCC's Billing and Payment terms and conditions. These terms and conditions, together with CCC's Billing and Payment terms and conditions (which are incorporated herein), comprise the entire agreement between you and publisher (and CCC) concerning this licensing transaction. In the event of any conflict between your obligations established by these terms and conditions and those established by CCC's Billing and Payment terms and conditions, these terms and conditions shall control.

14. Revocation: Elsevier or Copyright Clearance Center may deny the permissions described in this License at their sole discretion, for any reason or no reason, with a full refund payable to you. Notice of such denial will be made using the contact information provided by you. Failure to receive such notice will not alter or invalidate the denial. In no event will Elsevier or Copyright Clearance Center be responsible or liable for any costs, expenses or damage incurred by you as a result of a denial of your permission request, other than a refund of the amount(s) paid by you to Elsevier and/or Copyright Clearance Center for denied permissions.

LIMITED LICENSE

The following terms and conditions apply only to specific license types:

15. **Translation**: This permission is granted for non-exclusive world **English** rights only unless your license was granted for translation rights. If you licensed translation rights you may only translate this content into the languages you requested. A professional translator

must perform all translations and reproduce the content word for word preserving the integrity of the article. If this license is to re-use 1 or 2 figures then permission is granted for non-exclusive world rights in all languages.

16. **Posting licensed content on any Website**: The following terms and conditions apply as follows: Licensing material from an Elsevier journal: All content posted to the web site must maintain the copyright information line on the bottom of each image; A hyper-text must be included to the Homepage of the journal from which you are licensing at http://www.sciencedirect.com/science/journal/xxxxx or the Elsevier homepage for books at http://www.elsevier.com; Central Storage: This license does not include permission for a scanned version of the material to be stored in a central repository such as that provided by Heron/XanEdu.

Licensing material from an Elsevier book: A hyper-text link must be included to the Elsevier homepage at http://www.elsevier.com . All content posted to the web site must maintain the copyright information line on the bottom of each image.

Posting licensed content on Electronic reserve: In addition to the above the following clauses are applicable: The web site must be password-protected and made available only to bona fide students registered on a relevant course. This permission is granted for 1 year only. You may obtain a new license for future website posting.

17. **For journal authors:** the following clauses are applicable in addition to the above:

Preprints:

A preprint is an author's own write-up of research results and analysis, it has not been peer-reviewed, nor has it had any other value added to it by a publisher (such as formatting, copyright, technical enhancement etc.).

Authors can share their preprints anywhere at any time. Preprints should not be added to or enhanced in any way in order to appear more like, or to substitute for, the final versions of articles however authors can update their preprints on arXiv or RePEc with their Accepted Author Manuscript (see below).

If accepted for publication, we encourage authors to link from the preprint to their formal publication via its DOI. Millions of researchers have access to the formal publications on ScienceDirect, and so links will help users to find, access, cite and use the best available version. Please note that Cell Press, The Lancet and some society-owned have different preprint policies. Information on these policies is available on the journal homepage.

Accepted Author Manuscripts: An accepted author manuscript is the manuscript of an article that has been accepted for publication and which typically includes author-incorporated changes suggested during submission, peer review and editor-author communications.

Authors can share their accepted author manuscript:

- immediately
    - via their non-commercial person homepage or blog
    - by updating a preprint in arXiv or RePEc with the accepted manuscript

- via their research institute or institutional repository for internal institutional uses or as part of an invitation-only research collaboration work-group
- directly by providing copies to their students or to research collaborators for their personal use
- for private scholarly sharing as part of an invitation-only work group on commercial sites with which Elsevier has an agreement

– after the embargo period

- via non-commercial hosting platforms such as their institutional repository
- via commercial sites with which Elsevier has an agreement

In all cases accepted manuscripts should:

– link to the formal publication via its DOI

– bear a CC-BY-NC-ND license - this is easy to do

– if aggregated with other manuscripts, for example in a repository or other site, be shared in alignment with our hosting policy not be added to or enhanced in any way to appear more like, or to substitute for, the published journal article.

Published journal article (JPA): A published journal article (PJA) is the definitive final record of published research that appears or will appear in the journal and embodies all value-adding publishing activities including peer review co-ordination, copy-editing, formatting, (if relevant) pagination and online enrichment.

Policies for sharing publishing journal articles differ for subscription and gold open access articles:

Subscription Articles: If you are an author, please share a link to your article rather than the full-text. Millions of researchers have access to the formal publications on ScienceDirect, and so links will help your users to find, access, cite, and use the best available version.

Theses and dissertations which contain embedded PJAs as part of the formal submission can be posted publicly by the awarding institution with DOI links back to the formal publications on ScienceDirect.

If you are affiliated with a library that subscribes to ScienceDirect you have additional private sharing rights for others' research accessed under that agreement. This includes use for classroom teaching and internal training at the institution (including use in course packs and courseware programs), and inclusion of the article for grant funding purposes.

Gold Open Access Articles: May be shared according to the author-selected end-user license and should contain a CrossMark logo, the end user license, and a DOI link to the formal publication on ScienceDirect.

Please refer to Elsevier's posting policy for further information.

18. **For book authors** the following clauses are applicable in addition to the above: Authors are permitted to place a brief summary of their work online only. You are not allowed to download and post the published electronic version of your chapter, nor may you

scan the printed edition to create an electronic version. **Posting to a repository:** Authors are permitted to post a summary of their chapter only in their institution's repository.

19. **Thesis/Dissertation**: If your license is for use in a thesis/dissertation your thesis may be submitted to your institution in either print or electronic form. Should your thesis be published commercially, please reapply for permission. These requirements include permission for the Library and Archives of Canada to supply single copies, on demand, of the complete thesis and include permission for Proquest/UMI to supply single copies, on demand, of the complete thesis. Should your thesis be published commercially, please reapply for permission. Theses and dissertations which contain embedded PJAs as part of the formal submission can be posted publicly by the awarding institution with DOI links back to the formal publications on ScienceDirect.

Elsevier Open Access Terms and Conditions

You can publish open access with Elsevier in hundreds of open access journals or in nearly 2000 established subscription journals that support open access publishing. Permitted third party re-use of these open access articles is defined by the author's choice of Creative Commons user license. See our open access license policy for more information.

Terms & Conditions applicable to all Open Access articles published with Elsevier:

Any reuse of the article must not represent the author as endorsing the adaptation of the article nor should the article be modified in such a way as to damage the author's honour or reputation. If any changes have been made, such changes must be clearly indicated.

The author(s) must be appropriately credited and we ask that you include the end user license and a DOI link to the formal publication on ScienceDirect.

If any part of the material to be used (for example, figures) has appeared in our publication with credit or acknowledgement to another source it is the responsibility of the user to ensure their reuse complies with the terms and conditions determined by the rights holder.

Additional Terms & Conditions applicable to each Creative Commons user license:

CC BY: The CC-BY license allows users to copy, to create extracts, abstracts and new works from the Article, to alter and revise the Article and to make commercial use of the Article (including reuse and/or resale of the Article by commercial entities), provided the user gives appropriate credit (with a link to the formal publication through the relevant DOI), provides a link to the license, indicates if changes were made and the licensor is not represented as endorsing the use made of the work. The full details of the license are available at http://creativecommons.org/licenses/by/4.0.

CC BY NC SA: The CC BY-NC-SA license allows users to copy, to create extracts, abstracts and new works from the Article, to alter and revise the Article, provided this is not done for commercial purposes, and that the user gives appropriate credit (with a link to the formal publication through the relevant DOI), provides a link to the license, indicates if changes were made and the licensor is not represented as endorsing the use made of the work. Further, any new works must be made available on the same conditions. The full details of the license are available at http://creativecommons.org/licenses/by-nc-sa/4.0.

CC BY NC ND: The CC BY-NC-ND license allows users to copy and distribute the Article, provided this is not done for commercial purposes and further does not permit distribution of the Article if it is changed or edited in any way, and provided the user gives appropriate credit (with a link to the formal publication through the relevant DOI), provides a link to the license, and that the licensor is not represented as endorsing the use made of the work. The full details of the license are available at http://creativecommons.org/licenses/by-nc-nd/4.0. Any commercial reuse of Open Access articles published with a CC BY NC SA or CC BY NC ND license requires permission from Elsevier and will be subject to a fee.

Commercial reuse includes:

- Associating advertising with the full text of the Article
- Charging fees for document delivery or access
- Article aggregation
- Systematic distribution via e-mail lists or share buttons

Posting or linking by commercial companies for use by customers of those companies.

20. **Other Conditions**:

v1.7

Questions? customercare@copyright.com or +1-855-239-3415 (toll free in the US) or +1-978-646-2777.

SPRINGER LICENSE
TERMS AND CONDITIONS

Dec 07, 2010

This is a License Agreement between Ross P Williams ("You") and Springer ("Springer") provided by Copyright Clearance Center ("CCC"). The license consists of your order details, the terms and conditions provided by Springer, and the payment terms and conditions.

All payments must be made in full to CCC. For payment instructions, please see information listed at the bottom of this form.

License Number	2563461311192
License date	Dec 07, 2010
Licensed content publisher	Springer
Licensed content publication	Applied Magnetic Resonance
Licensed content title	^{29}Si, ^{27}Al, ^{1}H and ^{23}Na MAS NMR Study of the Bonding Character in Aluminosilicate Inorganic Polymers
Licensed content author	M. R. Rowles
Licensed content date	Jan 1, 2007
Volume number	32
Issue number	4
Type of Use	Thesis/Dissertation
Portion	Figures
Author of this Springer article	No
Order reference number	
Title of your thesis / dissertation	Improving the understanding of silicate inorganic polymers
Expected completion date	Jan 2011
Estimated size(pages)	200
Total	0.00 USD
Terms and Conditions	

Introduction

The publisher for this copyrighted material is Springer Science + Business Media. By clicking "accept" in connection with completing this licensing transaction, you agree that the following terms and conditions apply to this transaction (along with the Billing and Payment terms and conditions established by Copyright Clearance Center, Inc. ("CCC"), at the time that you opened your Rightslink account and that are available at any time at http://myaccount.copyright.com).

Limited License

With reference to your request to reprint in your thesis material on which Springer Science and Business Media control the copyright, permission is granted, free of charge, for the use indicated in your enquiry. Licenses are for one-time use only with a maximum distribution equal to the number that you identified in the licensing process.

This License includes use in an electronic form, provided it is password protected or on the university's intranet, destined to microfilming by UMI and University repository. For any other electronic use, please contact Springer at (permissions.dordrecht@springer.com or permissions.heidelberg@springer.com)

The material can only be used for the purpose of defending your thesis, and with a maximum of 100 extra copies in paper.

Although Springer holds copyright to the material and is entitled to negotiate on rights, this license is only valid, provided permission is also obtained from the (co) author (address is given with the article/chapter) and provided it concerns original material which does not carry references to other sources (if material in question appears with credit to another source, authorization from that source is required as well). Permission free of charge on this occasion does not prejudice any rights we might have to charge for reproduction of our copyrighted material in the future.

Altering/Modifying Material: Not Permitted
However figures and illustrations may be altered minimally to serve your work. Any other abbreviations, additions, deletions and/or any other alterations shall be made only with prior written authorization of the author(s) and/or Springer Science + Business Media. (Please contact Springer at permissions.dordrecht@springer.com or permissions.heidelberg@springer.com)

Reservation of Rights
Springer Science + Business Media reserves all rights not specifically granted in the combination of (i) the license details provided by you and accepted in the course of this licensing transaction, (ii) these terms and conditions and (iii) CCC's Billing and Payment terms and conditions.

Copyright Notice:
Please include the following copyright citation referencing the publication in which the material was originally published. Where wording is within brackets, please include verbatim.
"With kind permission from Springer Science+Business Media: <book/journal title, chapter/article title, volume, year of publication, page, name(s) of author(s), figure number(s), and any original (first) copyright notice displayed with material>."

Warranties: Springer Science + Business Media makes no representations or warranties with respect to the licensed material.

Indemnity
You hereby indemnify and agree to hold harmless Springer Science + Business Media and CCC, and their respective officers, directors, employees and agents, from and against any and all claims arising out of your use of the licensed material other than as specifically authorized pursuant to this license.

No Transfer of License
This license is personal to you and may not be sublicensed, assigned, or transferred by you to any other person without Springer Science + Business Media's written permission.

No Amendment Except in Writing
This license may not be amended except in a writing signed by both parties (or, in the case of Springer Science + Business Media, by CCC on Springer Science + Business Media's behalf).

Objection to Contrary Terms

Springer Science + Business Media hereby objects to any terms contained in any purchase order, acknowledgment, check endorsement or other writing prepared by you, which terms are inconsistent with these terms and conditions or CCC's Billing and Payment terms and conditions. These terms and conditions, together with CCC's Billing and Payment terms and conditions (which are incorporated herein), comprise the entire agreement between you and Springer Science + Business Media (and CCC) concerning this licensing transaction. In the event of any conflict between your obligations established by these terms and conditions and those established by CCC's Billing and Payment terms and conditions, these terms and conditions shall control.

Jurisdiction
All disputes that may arise in connection with this present License, or the breach thereof, shall be settled exclusively by the country's law in which the work was originally published.

Other terms and conditions:

v1.2

Gratis licenses (referencing $0 in the Total field) are free. Please retain this printable license for your reference. No payment is required.

If you would like to pay for this license now, please remit this license along with your payment made payable to "COPYRIGHT CLEARANCE CENTER" otherwise you will be invoiced within 48 hours of the license date. Payment should be in the form of a check or money order referencing your account number and this invoice number RLNK10895440. Once you receive your invoice for this order, you may pay your invoice by credit card. Please follow instructions provided at that time.

Make Payment To:
Copyright Clearance Center
Dept 001
P.O. Box 843006
Boston, MA 02284-3006

If you find copyrighted material related to this license will not be used and wish to cancel, please contact us referencing this license number 2563461311192 and noting the reason for cancellation.

Questions? customercare@copyright.com or +1-877-622-5543 (toll free in the US) or +1-978-646-2777.

ELSEVIER LICENSE
TERMS AND CONDITIONS

Aug 31, 2015

This is a License Agreement between Ross P Williams ("You") and Elsevier ("Elsevier") provided by Copyright Clearance Center ("CCC"). The license consists of your order details, the terms and conditions provided by Elsevier, and the payment terms and conditions.

All payments must be made in full to CCC. For payment instructions, please see information listed at the bottom of this form.

Supplier	Elsevier Limited The Boulevard,Langford Lane Kidlington,Oxford,OX5 1GB,UK
Registered Company Number	1982084
Customer name	Ross P Williams
Customer address	Curtin University Perth, WA 6845
License number	3699171233242
License date	Aug 31, 2015
Licensed content publisher	Elsevier
Licensed content publication	Cement and Concrete Research
Licensed content title	Microstructure development of alkali-activated fly ash cement: a descriptive model
Licensed content author	A. Fernández-Jiménez,A. Palomo,M. Criado
Licensed content date	June 2005
Licensed content volume number	35
Licensed content issue number	6
Number of pages	6
Start Page	1204
End Page	1209
Type of Use	reuse in a thesis/dissertation
Portion	figures/tables/illustrations
Number of figures/tables/illustrations	1
Format	both print and electronic
Are you the author of this Elsevier article?	No
Will you be translating?	No
Original figure numbers	Figure 6
Title of your thesis/dissertation	Optimising Geopolymer Formation
Expected completion date	Nov 2015

Estimated size (number of pages)	220
Elsevier VAT number	GB 494 6272 12
Permissions price	0.00 AUD
VAT/Local Sales Tax	0.00 AUD / 0.00 GBP
Total	0.00 AUD

Terms and Conditions

INTRODUCTION

1. The publisher for this copyrighted material is Elsevier. By clicking "accept" in connection with completing this licensing transaction, you agree that the following terms and conditions apply to this transaction (along with the Billing and Payment terms and conditions established by Copyright Clearance Center, Inc. ("CCC"), at the time that you opened your Rightslink account and that are available at any time at http://myaccount.copyright.com).

GENERAL TERMS

2. Elsevier hereby grants you permission to reproduce the aforementioned material subject to the terms and conditions indicated.

3. Acknowledgement: If any part of the material to be used (for example, figures) has appeared in our publication with credit or acknowledgement to another source, permission must also be sought from that source. If such permission is not obtained then that material may not be included in your publication/copies. Suitable acknowledgement to the source must be made, either as a footnote or in a reference list at the end of your publication, as follows:

"Reprinted from Publication title, Vol /edition number, Author(s), Title of article / title of chapter, Pages No., Copyright (Year), with permission from Elsevier [OR APPLICABLE SOCIETY COPYRIGHT OWNER]." Also Lancet special credit - "Reprinted from The Lancet, Vol. number, Author(s), Title of article, Pages No., Copyright (Year), with permission from Elsevier."

4. Reproduction of this material is confined to the purpose and/or media for which permission is hereby given.

5. Altering/Modifying Material: Not Permitted. However figures and illustrations may be altered/adapted minimally to serve your work. Any other abbreviations, additions, deletions and/or any other alterations shall be made only with prior written authorization of Elsevier Ltd. (Please contact Elsevier at permissions@elsevier.com)

6. If the permission fee for the requested use of our material is waived in this instance, please be advised that your future requests for Elsevier materials may attract a fee.

7. Reservation of Rights: Publisher reserves all rights not specifically granted in the combination of (i) the license details provided by you and accepted in the course of this licensing transaction, (ii) these terms and conditions and (iii) CCC's Billing and Payment terms and conditions.

8. License Contingent Upon Payment: While you may exercise the rights licensed immediately upon issuance of the license at the end of the licensing process for the

transaction, provided that you have disclosed complete and accurate details of your proposed use, no license is finally effective unless and until full payment is received from you (either by publisher or by CCC) as provided in CCC's Billing and Payment terms and conditions. If full payment is not received on a timely basis, then any license preliminarily granted shall be deemed automatically revoked and shall be void as if never granted. Further, in the event that you breach any of these terms and conditions or any of CCC's Billing and Payment terms and conditions, the license is automatically revoked and shall be void as if never granted. Use of materials as described in a revoked license, as well as any use of the materials beyond the scope of an unrevoked license, may constitute copyright infringement and publisher reserves the right to take any and all action to protect its copyright in the materials.

9. Warranties: Publisher makes no representations or warranties with respect to the licensed material.

10. Indemnity: You hereby indemnify and agree to hold harmless publisher and CCC, and their respective officers, directors, employees and agents, from and against any and all claims arising out of your use of the licensed material other than as specifically authorized pursuant to this license.

11. No Transfer of License: This license is personal to you and may not be sublicensed, assigned, or transferred by you to any other person without publisher's written permission.

12. No Amendment Except in Writing: This license may not be amended except in a writing signed by both parties (or, in the case of publisher, by CCC on publisher's behalf).

13. Objection to Contrary Terms: Publisher hereby objects to any terms contained in any purchase order, acknowledgment, check endorsement or other writing prepared by you, which terms are inconsistent with these terms and conditions or CCC's Billing and Payment terms and conditions. These terms and conditions, together with CCC's Billing and Payment terms and conditions (which are incorporated herein), comprise the entire agreement between you and publisher (and CCC) concerning this licensing transaction. In the event of any conflict between your obligations established by these terms and conditions and those established by CCC's Billing and Payment terms and conditions, these terms and conditions shall control.

14. Revocation: Elsevier or Copyright Clearance Center may deny the permissions described in this License at their sole discretion, for any reason or no reason, with a full refund payable to you. Notice of such denial will be made using the contact information provided by you. Failure to receive such notice will not alter or invalidate the denial. In no event will Elsevier or Copyright Clearance Center be responsible or liable for any costs, expenses or damage incurred by you as a result of a denial of your permission request, other than a refund of the amount(s) paid by you to Elsevier and/or Copyright Clearance Center for denied permissions.

LIMITED LICENSE

The following terms and conditions apply only to specific license types:

15. **Translation**: This permission is granted for non-exclusive world **English** rights only unless your license was granted for translation rights. If you licensed translation rights you may only translate this content into the languages you requested. A professional translator must perform all translations and reproduce the content word for word preserving the

integrity of the article. If this license is to re-use 1 or 2 figures then permission is granted for non-exclusive world rights in all languages.

16. **Posting licensed content on any Website**: The following terms and conditions apply as follows: Licensing material from an Elsevier journal: All content posted to the web site must maintain the copyright information line on the bottom of each image; A hyper-text must be included to the Homepage of the journal from which you are licensing at http://www.sciencedirect.com/science/journal/xxxxx or the Elsevier homepage for books at http://www.elsevier.com; Central Storage: This license does not include permission for a scanned version of the material to be stored in a central repository such as that provided by Heron/XanEdu.

Licensing material from an Elsevier book: A hyper-text link must be included to the Elsevier homepage at http://www.elsevier.com . All content posted to the web site must maintain the copyright information line on the bottom of each image.

Posting licensed content on Electronic reserve: In addition to the above the following clauses are applicable: The web site must be password-protected and made available only to bona fide students registered on a relevant course. This permission is granted for 1 year only. You may obtain a new license for future website posting.

17. **For journal authors:** the following clauses are applicable in addition to the above:

Preprints:

A preprint is an author's own write-up of research results and analysis, it has not been peer-reviewed, nor has it had any other value added to it by a publisher (such as formatting, copyright, technical enhancement etc.).

Authors can share their preprints anywhere at any time. Preprints should not be added to or enhanced in any way in order to appear more like, or to substitute for, the final versions of articles however authors can update their preprints on arXiv or RePEc with their Accepted Author Manuscript (see below).

If accepted for publication, we encourage authors to link from the preprint to their formal publication via its DOI. Millions of researchers have access to the formal publications on ScienceDirect, and so links will help users to find, access, cite and use the best available version. Please note that Cell Press, The Lancet and some society-owned have different preprint policies. Information on these policies is available on the journal homepage.

Accepted Author Manuscripts: An accepted author manuscript is the manuscript of an article that has been accepted for publication and which typically includes author-incorporated changes suggested during submission, peer review and editor-author communications.

Authors can share their accepted author manuscript:

- immediately
    - via their non-commercial person homepage or blog
    - by updating a preprint in arXiv or RePEc with the accepted manuscript

- via their research institute or institutional repository for internal institutional uses or as part of an invitation-only research collaboration work-group
- directly by providing copies to their students or to research collaborators for their personal use
- for private scholarly sharing as part of an invitation-only work group on commercial sites with which Elsevier has an agreement

– after the embargo period

- via non-commercial hosting platforms such as their institutional repository
- via commercial sites with which Elsevier has an agreement

In all cases accepted manuscripts should:

– link to the formal publication via its DOI

– bear a CC-BY-NC-ND license - this is easy to do

– if aggregated with other manuscripts, for example in a repository or other site, be shared in alignment with our hosting policy not be added to or enhanced in any way to appear more like, or to substitute for, the published journal article.

Published journal article (JPA): A published journal article (PJA) is the definitive final record of published research that appears or will appear in the journal and embodies all value-adding publishing activities including peer review co-ordination, copy-editing, formatting, (if relevant) pagination and online enrichment.

Policies for sharing publishing journal articles differ for subscription and gold open access articles:

Subscription Articles: If you are an author, please share a link to your article rather than the full-text. Millions of researchers have access to the formal publications on ScienceDirect, and so links will help your users to find, access, cite, and use the best available version.

Theses and dissertations which contain embedded PJAs as part of the formal submission can be posted publicly by the awarding institution with DOI links back to the formal publications on ScienceDirect.

If you are affiliated with a library that subscribes to ScienceDirect you have additional private sharing rights for others' research accessed under that agreement. This includes use for classroom teaching and internal training at the institution (including use in course packs and courseware programs), and inclusion of the article for grant funding purposes.

Gold Open Access Articles: May be shared according to the author-selected end-user license and should contain a CrossMark logo, the end user license, and a DOI link to the formal publication on ScienceDirect.

Please refer to Elsevier's posting policy for further information.

18. **For book authors** the following clauses are applicable in addition to the above: Authors are permitted to place a brief summary of their work online only. You are not allowed to download and post the published electronic version of your chapter, nor may you

scan the printed edition to create an electronic version. **Posting to a repository:** Authors are permitted to post a summary of their chapter only in their institution's repository.

19. **Thesis/Dissertation**: If your license is for use in a thesis/dissertation your thesis may be submitted to your institution in either print or electronic form. Should your thesis be published commercially, please reapply for permission. These requirements include permission for the Library and Archives of Canada to supply single copies, on demand, of the complete thesis and include permission for Proquest/UMI to supply single copies, on demand, of the complete thesis. Should your thesis be published commercially, please reapply for permission. Theses and dissertations which contain embedded PJAs as part of the formal submission can be posted publicly by the awarding institution with DOI links back to the formal publications on ScienceDirect.

Elsevier Open Access Terms and Conditions

You can publish open access with Elsevier in hundreds of open access journals or in nearly 2000 established subscription journals that support open access publishing. Permitted third party re-use of these open access articles is defined by the author's choice of Creative Commons user license. See our open access license policy for more information.

Terms & Conditions applicable to all Open Access articles published with Elsevier:

Any reuse of the article must not represent the author as endorsing the adaptation of the article nor should the article be modified in such a way as to damage the author's honour or reputation. If any changes have been made, such changes must be clearly indicated.

The author(s) must be appropriately credited and we ask that you include the end user license and a DOI link to the formal publication on ScienceDirect.

If any part of the material to be used (for example, figures) has appeared in our publication with credit or acknowledgement to another source it is the responsibility of the user to ensure their reuse complies with the terms and conditions determined by the rights holder.

Additional Terms & Conditions applicable to each Creative Commons user license:

CC BY: The CC-BY license allows users to copy, to create extracts, abstracts and new works from the Article, to alter and revise the Article and to make commercial use of the Article (including reuse and/or resale of the Article by commercial entities), provided the user gives appropriate credit (with a link to the formal publication through the relevant DOI), provides a link to the license, indicates if changes were made and the licensor is not represented as endorsing the use made of the work. The full details of the license are available at http://creativecommons.org/licenses/by/4.0.

CC BY NC SA: The CC BY-NC-SA license allows users to copy, to create extracts, abstracts and new works from the Article, to alter and revise the Article, provided this is not done for commercial purposes, and that the user gives appropriate credit (with a link to the formal publication through the relevant DOI), provides a link to the license, indicates if changes were made and the licensor is not represented as endorsing the use made of the work. Further, any new works must be made available on the same conditions. The full details of the license are available at http://creativecommons.org/licenses/by-nc-sa/4.0.

CC BY NC ND: The CC BY-NC-ND license allows users to copy and distribute the Article, provided this is not done for commercial purposes and further does not permit distribution of the Article if it is changed or edited in any way, and provided the user gives appropriate credit (with a link to the formal publication through the relevant DOI), provides a link to the license, and that the licensor is not represented as endorsing the use made of the work. The full details of the license are available at http://creativecommons.org/licenses/by-nc-nd/4.0. Any commercial reuse of Open Access articles published with a CC BY NC SA or CC BY NC ND license requires permission from Elsevier and will be subject to a fee.

Commercial reuse includes:

- Associating advertising with the full text of the Article
- Charging fees for document delivery or access
- Article aggregation
- Systematic distribution via e-mail lists or share buttons

Posting or linking by commercial companies for use by customers of those companies.

20. **Other Conditions**:

v1.7

Questions? customercare@copyright.com or +1-855-239-3415 (toll free in the US) or +1-978-646-2777.

ELSEVIER LICENSE
TERMS AND CONDITIONS

Dec 07, 2010

This is a License Agreement between Ross P Williams ("You") and Elsevier ("Elsevier") provided by Copyright Clearance Center ("CCC"). The license consists of your order details, the terms and conditions provided by Elsevier, and the payment terms and conditions.

All payments must be made in full to CCC. For payment instructions, please see information listed at the bottom of this form.

Supplier	Elsevier Limited The Boulevard,Langford Lane Kidlington,Oxford,OX5 1GB,UK
Registered Company Number	1982084
Customer name	Ross P Williams
Customer address	Bld 301, Curtin University Perth, WA, other 6845
License number	2563460981712
License date	Dec 07, 2010
Licensed content publisher	Elsevier
Licensed content publication	International Journal of Inorganic Materials
Licensed content title	Synthesis and characterisation of materials based on inorganic polymers of alumina and silica: sodium polysialate polymers
Licensed content author	Valeria F. F. Barbosa, Kenneth J. D. MacKenzie, Clelio Thaumaturgo
Licensed content date	September 2000
Licensed content volume number	2
Licensed content issue number	4
Number of pages	9
Start Page	309
End Page	317
Type of Use	reuse in a thesis/dissertation
Portion	figures/tables/illustrations
Number of figures/tables/illustrations	1
Format	electronic
Are you the author of this Elsevier article?	No
Will you be translating?	No
Order reference number	
Title of your thesis/dissertation	Improving the understanding of silicate inorganic polymers
Expected completion date	Jan 2011

Expected completion date	Jan 2011
Estimated size (number of pages)	200
Elsevier VAT number	GB 494 6272 12
Permissions price	0.00 USD
Value added tax 0.0%	0.0 USD / 0.0 GBP
Total	0.00 USD
Terms and Conditions	

INTRODUCTION

1. The publisher for this copyrighted material is Elsevier. By clicking "accept" in connection with completing this licensing transaction, you agree that the following terms and conditions apply to this transaction (along with the Billing and Payment terms and conditions established by Copyright Clearance Center, Inc. ("CCC"), at the time that you opened your Rightslink account and that are available at any time at http://myaccount.copyright.com).

GENERAL TERMS

2. Elsevier hereby grants you permission to reproduce the aforementioned material subject to the terms and conditions indicated.

3. Acknowledgement: If any part of the material to be used (for example, figures) has appeared in our publication with credit or acknowledgement to another source, permission must also be sought from that source. If such permission is not obtained then that material may not be included in your publication/copies. Suitable acknowledgement to the source must be made, either as a footnote or in a reference list at the end of your publication, as follows:

"Reprinted from Publication title, Vol /edition number, Author(s), Title of article / title of chapter, Pages No., Copyright (Year), with permission from Elsevier [OR APPLICABLE SOCIETY COPYRIGHT OWNER]." Also Lancet special credit - "Reprinted from The Lancet, Vol. number, Author(s), Title of article, Pages No., Copyright (Year), with permission from Elsevier."

4. Reproduction of this material is confined to the purpose and/or media for which permission is hereby given.

5. Altering/Modifying Material: Not Permitted. However figures and illustrations may be altered/adapted minimally to serve your work. Any other abbreviations, additions, deletions and/or any other alterations shall be made only with prior written authorization of Elsevier Ltd. (Please contact Elsevier at permissions@elsevier.com)

6. If the permission fee for the requested use of our material is waived in this instance, please be advised that your future requests for Elsevier materials may attract a fee.

7. Reservation of Rights: Publisher reserves all rights not specifically granted in the combination of (i) the license details provided by you and accepted in the course of this licensing transaction, (ii) these terms and conditions and (iii) CCC's Billing and Payment terms and conditions.

8. License Contingent Upon Payment: While you may exercise the rights licensed immediately upon issuance of the license at the end of the licensing process for the transaction, provided that you have disclosed complete and accurate details of your proposed use, no license is finally effective unless

and until full payment is received from you (either by publisher or by CCC) as provided in CCC's Billing and Payment terms and conditions. If full payment is not received on a timely basis, then any license preliminarily granted shall be deemed automatically revoked and shall be void as if never granted. Further, in the event that you breach any of these terms and conditions or any of CCC's Billing and Payment terms and conditions, the license is automatically revoked and shall be void as if never granted. Use of materials as described in a revoked license, as well as any use of the materials beyond the scope of an unrevoked license, may constitute copyright infringement and publisher reserves the right to take any and all action to protect its copyright in the materials.

9. Warranties: Publisher makes no representations or warranties with respect to the licensed material.

10. Indemnity: You hereby indemnify and agree to hold harmless publisher and CCC, and their respective officers, directors, employees and agents, from and against any and all claims arising out of your use of the licensed material other than as specifically authorized pursuant to this license.

11. No Transfer of License: This license is personal to you and may not be sublicensed, assigned, or transferred by you to any other person without publisher's written permission.

12. No Amendment Except in Writing: This license may not be amended except in a writing signed by both parties (or, in the case of publisher, by CCC on publisher's behalf).

13. Objection to Contrary Terms: Publisher hereby objects to any terms contained in any purchase order, acknowledgment, check endorsement or other writing prepared by you, which terms are inconsistent with these terms and conditions or CCC's Billing and Payment terms and conditions. These terms and conditions, together with CCC's Billing and Payment terms and conditions (which are incorporated herein), comprise the entire agreement between you and publisher (and CCC) concerning this licensing transaction. In the event of any conflict between your obligations established by these terms and conditions and those established by CCC's Billing and Payment terms and conditions, these terms and conditions shall control.

14. Revocation: Elsevier or Copyright Clearance Center may deny the permissions described in this License at their sole discretion, for any reason or no reason, with a full refund payable to you. Notice of such denial will be made using the contact information provided by you. Failure to receive such notice will not alter or invalidate the denial. In no event will Elsevier or Copyright Clearance Center be responsible or liable for any costs, expenses or damage incurred by you as a result of a denial of your permission request, other than a refund of the amount(s) paid by you to Elsevier and/or Copyright Clearance Center for denied permissions.

LIMITED LICENSE

The following terms and conditions apply only to specific license types:

15. **Translation**: This permission is granted for non-exclusive world **English** rights only unless your license was granted for translation rights. If you licensed translation rights you may only translate this content into the languages you requested. A professional translator must perform all translations and reproduce the content word for word preserving the integrity of the article. If this license is to re-use 1 or 2 figures then permission is granted for non-exclusive world rights in all languages.

16. **Website**: The following terms and conditions apply to electronic reserve and author websites:

Electronic reserve: If licensed material is to be posted to website, the web site is to be password-protected and made available only to bona fide students registered on a relevant course if:
This license was made in connection with a course,
This permission is granted for 1 year only. You may obtain a license for future website posting,
All content posted to the web site must maintain the copyright information line on the bottom of each image,
A hyper-text must be included to the Homepage of the journal from which you are licensing at http://www.sciencedirect.com/science/journal/xxxxx or the Elsevier homepage for books at http://www.elsevier.com , and
Central Storage: This license does not include permission for a scanned version of the material to be stored in a central repository such as that provided by Heron/XanEdu.

17. **Author website** for journals with the following additional clauses:

All content posted to the web site must maintain the copyright information line on the bottom of each image, and
he permission granted is limited to the personal version of your paper. You are not allowed to download and post the published electronic version of your article (whether PDF or HTML, proof or final version), nor may you scan the printed edition to create an electronic version,
A hyper-text must be included to the Homepage of the journal from which you are licensing at http://www.sciencedirect.com/science/journal/xxxxx , As part of our normal production process, you will receive an e-mail notice when your article appears on Elsevier's online service ScienceDirect (www.sciencedirect.com). That e-mail will include the article's Digital Object Identifier (DOI). This number provides the electronic link to the published article and should be included in the posting of your personal version. We ask that you wait until you receive this e-mail and have the DOI to do any posting.
Central Storage: This license does not include permission for a scanned version of the material to be stored in a central repository such as that provided by Heron/XanEdu.

18. **Author website** for books with the following additional clauses:
Authors are permitted to place a brief summary of their work online only.
A hyper-text must be included to the Elsevier homepage at http://www.elsevier.com

All content posted to the web site must maintain the copyright information line on the bottom of each image
You are not allowed to download and post the published electronic version of your chapter, nor may you scan the printed edition to create an electronic version.
Central Storage: This license does not include permission for a scanned version of the material to be stored in a central repository such as that provided by Heron/XanEdu.

19. **Website** (regular and for author): A hyper-text must be included to the Homepage of the journal from which you are licensing at http://www.sciencedirect.com/science/journal/xxxxx. or for books to the Elsevier homepage at http://www.elsevier.com

20. **Thesis/Dissertation**: If your license is for use in a thesis/dissertation your thesis may be submitted to your institution in either print or electronic form. Should your thesis be published commercially, please reapply for permission. These requirements include permission for the Library

and Archives of Canada to supply single copies, on demand, of the complete thesis and include permission for UMI to supply single copies, on demand, of the complete thesis. Should your thesis be published commercially, please reapply for permission.

21. **Other Conditions**:

v1.6

Gratis licenses (referencing $0 in the Total field) are free. Please retain this printable license for your reference. No payment is required.

If you would like to pay for this license now, please remit this license along with your payment made payable to "COPYRIGHT CLEARANCE CENTER" otherwise you will be invoiced within 48 hours of the license date. Payment should be in the form of a check or money order referencing your account number and this invoice number RLNK10895438. Once you receive your invoice for this order, you may pay your invoice by credit card. Please follow instructions provided at that time.

Make Payment To:
Copyright Clearance Center
Dept 001
P.O. Box 843006
Boston, MA 02284-3006

If you find copyrighted material related to this license will not be used and wish to cancel, please contact us referencing this license number 2563460981712 and noting the reason for cancellation.

Questions? customercare@copyright.com or +1-877-622-5543 (toll free in the US) or +1-978-646-2777.